

Doctoral thesis

Doctoral theses at NTNU, 2023:295

Pia M. Vornewald

Orchestrating the intestinal epithelial niche: Intestinal smooth muscle tissue and cytokines in epithelial regulation

NTNU
Norwegian University of Science and Technology
Thesis for the Degree of
Philosophiae Doctor
Faculty of Medicine and Health Sciences
Department of Clinical and Molecular Medicine



Norwegian University of
Science and Technology

Pia M. Vornewald

Orchestrating the intestinal epithelial niche: Intestinal smooth muscle tissue and cytokines in epithelial regulation

Thesis for the Degree of Philosophiae Doctor

Trondheim, September 2023

Norwegian University of Science and Technology
Faculty of Medicine and Health Sciences
Department of Clinical and Molecular Medicine



Norwegian University of
Science and Technology

NTNU

Norwegian University of Science and Technology

Thesis for the Degree of Philosophiae Doctor

Faculty of Medicine and Health Sciences

Department of Clinical and Molecular Medicine

© Pia M. Vornewald

ISBN 978-82-326-7290-5 (printed ver.)

ISBN 978-82-326-7289-9 (electronic ver.)

ISSN 1503-8181 (printed ver.)

ISSN 2703-8084 (online ver.)

Doctoral theses at NTNU, 2023:295

Printed by NTNU Grafisk senter

Summary in Norwegian

Norsk tittel: *Orkestrering av tarmepitel-nisjen: Tarmens glatte muskelvev og cytokiner i epitelregulering*

Tarmforstyrrelser, som inflammatorisk tarmsykdom, blir stadig mer vanlige. For å utvikle bedre behandlingsmetoder, må vi forstå hvordan tarmen fungerer og hva som skjer på cellenivå når disse lidelsene oppstår. I denne studien avdekket vi hvordan spesifikke faktorer i tarmen bidrar til å opprettholde helse og helbrede skade i tarmslimhinnen (tarmepitel).

I et av våre hovedfunn viser vi at glatt muskelvev i tarmveggen spiller en betydelig og tidligere ukjent rolle i støtte til intestinale stamceller. Mer spesifikt fant vi at bone morphogenetic protein (BMP)-antagonister produsert av glatte muskelceller, er avgjørende for å holde stamcellene sunne og funksjonelle. Disse stamcellene er viktige for vedlikehold og reparasjon av tarmepitelet. Vi studerte også et annet protein produsert av glatte muskelceller, kalt Matrix metalloproteinase 17 (MMP17), involvert i modulering av ekstracellulær matriks. Ved å bruke en knock-out-musemodell som mangler MMP17, fant vi at dette proteinet er nødvendig for reparasjon av epitelet etter skade. Mus som manglet MMP17 var bedre rustet til å bekjempe infeksjoner med *Trichuris muris*, en type parasittisk orm. Vi tror at dette kan skyldes høyere nivåer av visse infeksjonsrelaterede effekter produsert av slimceller, sekretoriske celletyper i tarmene deres.

Videre undersøkte vi effektene av å eksponere laboratoriedyrkede mini-tarmer, kjent som organoider, for forskjellige cytokiner, signaleringsmolekyler som former immunresponsen mot infeksjoner. Cytokinene IL-13 og IL-22 førte til endringer i slimceller og tuftceller, en sensor-type-celle som er viktig i immunresponsen mot tarmparasitter. Dette førte til at vi oppdaget at BMP-signaler, en signalvei kjent for å bidra til cellenes modning, begrenser dannelsen av tuftceller i respons til IL-13. I tillegg observerte vi økt aktivitet i BMP-signalveien i MMP17-manglende mus, noe som antyder at et høyere antall modne slimceller kan forklare de høyere nivåene av effekter.

Oppsummert bidrar våre funn til økt forståelse av hvordan tarmepitelet reguleres, og kaster lys over rollene til og samspillet mellom glatt muskelvev, MMP17 og cytokiner. Den fremhever viktigheten av BMP-signalveien, og dens funksjon i å opprettholde homeostase og beskyttelse mot skade og infeksjoner i tarmen.

Kandidat: Pia Magdalena Vornewald

Institutt: Institutt for klinisk og molekylær medisin (IKOM)

Veileder(e): Menno Oudhoff, Mara Martin-Alonso

**Finansieringskilde: Senter for molekylær inflammasjonsforskning (CEMIR)
- Centre of Excellence (SFF) fra Norges Forskningsråd**

*Ovennevnte avhandling er funnet verdig til å forsvares offentlig for graden PhD i
Medisin og helsevitenskap. Disputas finner sted i Trondheim 22.09.2023, kl 12:15.*

Summary

Gut disorders, like inflammatory bowel disease, are becoming increasingly common. To develop better treatments, we need to understand how the gut works and what happens at the cellular level when these disorders occur. This study reveals new findings about how specific factors within the gut contribute to maintain the health of the gut lining (intestinal epithelium), manage immune responses, and help the epithelium heal after injury.

One of our key findings was that smooth muscle tissue, which is part of the gut wall, plays a significant and previously unknown role in supporting intestinal stem cells. These stem cells are vital for the maintenance and repair of the epithelium. Specifically, we found out that smooth muscle cells produce certain factors, called bone morphogenetic protein (BMP) antagonists, that are essential for keeping these stem cells healthy and functional. Our research then focused on a particular protein that is found in smooth muscle cells, called Matrix metalloproteinase 17 (MMP17), that belongs to a group of proteins involved in extracellular matrix modulation. Using a knock-out mouse model that lacks MMP17, we found that this protein is crucial for the repair of the epithelium after injury. Interestingly, mice lacking MMP17 were also better at clearing infections with *Trichuris muris*, a type of parasitic worm. We believe this may be due to higher levels of certain infection-related effectors, produced by goblet cells, secretory-type cells, in their guts.

We also examined the effects of exposing lab-grown mini-guts, known as organoids, to different cytokines, which are signaling molecules that shape the immune response to infections. The cytokines IL-13 and IL-22 led to changes in goblet cells and tuft cells, a sensor-type cell that is important during immune responses to gut parasites. In this context we discovered a new role of BMP signaling, a pathway known to encourage the maturation of cells, in limiting the formation of tuft cells in response to IL-13. Additionally, we detected more activity of the BMP pathway in MMP17-deficient mice, suggesting that a higher number of mature goblet cells could explain the higher levels of effectors.

In conclusion, this research helps us better understand how the intestinal epithelium is regulated, shedding light on the roles of smooth muscle tissue, MMP17, and cytokines. It highlights the importance of certain signaling processes, like BMP, in controlling how the intestine maintains homeostasis but also responds to injury and infections.

Acknowledgement

The work embodied in this thesis was carried out between 2019 and 2023 at the Department of Clinical and Molecular Medicine, Faculty of Medicine and Health Sciences, at the Norwegian University of Science and Technology (NTNU) in Trondheim. I am very grateful to the Faculty of Medicine and Health Sciences at NTNU and the Center of Molecular Inflammation Research (CEMIR), funded by the Research Council of Norway, for their financial support.

My profound thanks go to my supervisors, Menno Oudhoff and Mara Martín-Alonso. Menno, your guidance, support, and ever-present enthusiasm about my results have been invaluable throughout this journey. Mara, I am grateful for your wonderful mentorship in and out of the lab and your warm support that eased my path.

I want to express my sincere appreciation to both current and former lab members. Alberto, Andrew, Håvard, Jenny, Maria, Marion, Mei, Naveen, Rosalie, Rouan, Roos, and Shirin. – you have made the lab environment stimulating, and enjoyable. Your collaborative spirit, engaging discussions, and camaraderie have enriched this experience beyond measure.

I am also grateful to all our collaborators, without whom this work would not have been possible.

To my office mates, your company has been a source of inspiration and motivation. From our scientific discourses to our coffee walks, and from your emotional support to going out post-work, every moment has been cherished.

A big thank you to the warm and welcoming CEMIR community for being supportive and fostering an environment conducive to growth and learning. Additionally, I am grateful to the support facilities including CMIC, CoMed, and all the technicians who make our research possible.

I extend my deepest thanks to my family and friends for their unwavering support and encouragement. I especially want to acknowledge my parents for their love and belief in me.

Lastly, my thoughts go out to Sebi. You are missed every day.

For everyone who asked for my chocolate chip cookie recipe over the years:

Ingredients: 2 cups + 2 tablespoons flour, 1 tsp baking soda, 2 tsp cornstarch, 1 tsp salt, 170g butter (melted and cooled), 1 cup brown sugar, ½ cup white sugar, 2 eggs, 1 tsp vanilla sugar, 1 ½ cups chopped dark chocolate, plus more for topping

Instructions: Mix the butter, sugars, eggs, and vanilla sugar until combined. Add in the flour, baking soda, cornstarch, and salt. Mix briefly. Fold in the chopped chocolate. Refrigerate for min 30 min. Form cookies and set them on a baking sheet. Bake at 180 °C for 8-12 min. Press extra chocolate into the top to make them look pretty. Let cool. Enjoy!

Contents

Summary in Norwegian.....	i
Summary.....	iii
Acknowledgement.....	v
Contents.....	vii
List of Papers.....	ix
1 Introduction.....	1
1.1 The gastrointestinal tract.....	1
1.1.1 The gastrointestinal wall.....	1
1.2 The intestinal epithelium.....	3
1.2.1 Cells of the intestinal epithelium.....	3
1.2.2 Intestinal mucus layer.....	7
1.3 The intestinal stem cell (ISC) niche.....	8
1.3.1 Signaling pathways in the niche.....	8
1.3.2 Epithelial cell contribution to the ISC niche.....	11
1.3.3 Mesenchymal cell contribution to the ISC niche.....	12
1.3.4 Intestinal regeneration and plasticity.....	12
1.4 Extra cellular matrix (ECM) and its regulation.....	13
1.4.1 Intestinal ECM structure and composition.....	13
1.4.2 ECM as part of the ISC niche.....	14
1.4.3 MMPs as ECM regulators.....	15
1.4.4 Unique properties and functions of MMP17.....	16
1.5 Intestinal mucosal immune system.....	17
1.5.1 Epithelial immune defense mechanisms.....	17
1.5.2 Immune cells in the intestine.....	19
1.5.3 Immune responses in the intestine.....	23
1.6 Experimental models.....	24
1.6.1 GI tract in humans and mice – understanding similarities and differences.....	24

1.6.2	Modeling mucosal immunity to pathogenic bacteria with <i>Citrobacter rodentium</i>	26
1.6.3	Modeling mucosal immunity to parasitic infections with <i>Trichuris muris</i> and <i>Nippostrongylus brasiliensis</i>	27
1.6.4	DSS-induced colitis	29
1.6.5	Radiation induced injury model	30
1.6.6	Apc ^{Min} mouse model.....	31
1.6.7	Intestinal organoids.....	31
2	Aim of this work.....	35
3	Summary of Papers.....	37
4	Discussion.....	39
4.1	Intestinal smooth muscle tissue: A novel source of niche factors in the ISC niche	39
4.2	MMP17: A key regulator of ISC niche and epithelial repair processes via ECM modulation	41
4.3	Increased goblet cell-associated gene expression in <i>Mmp17</i> KO mice is not cytokine dependent.....	43
4.4	The multifaceted roles of BMP signaling in regulating epithelial differentiation and gene expression during homeostasis and inflammation...	44
4.5	Exploring the role of goblet cell effectors in the defense against intestinal pathogens	46
4.6	Translatability of results from mouse and organoid to human and into medical applications	48
5	Conclusion	53
6	List of Tables	55
7	List of Figures.....	57
8	List of Abbreviations	59
9	Bibliography	63

List of Papers

Articles included in this thesis:

Paper 1

Smooth muscle-specific MMP17 (MT4-MMP) regulates the intestinal stem cell niche and regeneration after damage

Mara Martín-Alonso, Sharif Iqbal, **Pia M. Vornewald**, Håvard T. Lindholm, Mirjam J. Damen, Fernando Martínez, Sigrid Hoel, Alberto Díez-Sánchez, Maarten Altelaar, Pekka Katajisto, Alicia G. Arroyo & Menno J. Oudhoff

Nat Commun. 2021 Nov 18. doi: 10.1038/s41467-021-26904-6

Paper 2

BMP signaling in the intestinal epithelium drives a critical feedback loop to restrain IL-13-driven tuft cell hyperplasia

Håvard T. Lindholm, Naveen Parmar, Claire Drurey, Marta Campillo Poveda, **Pia M. Vornewald**, Jenny Ostrop, Alberto Díez-Sánchez, Rick M. Maizels, Menno J. Oudhoff

Sci Immunol. 2022 May 13. doi: 10.1126/sciimmunol.abl6543

Paper 3

*Mmp17-deficient mice exhibit heightened goblet cell effector expression in the colon and increased resistance to chronic *Trichuris muris* infection*

Pia M. Vornewald, Ruth Forman, Rouan Yao, Naveen Parmar, Håvard T. Lindholm, Mara Martín-Alonso, Kathryn Else, Menno J. Oudhoff

Manuscript

Articles not included in this thesis:

Paper 4

IL4ra-independent vaginal eosinophil accumulation following helminth infection exacerbates epithelial ulcerative pathology of HSV-2 infection

Alisha Chetty, Matthew G. Darby, **Pia M. Vornewald**, Mara Martín-Alonso, Anna Filz, Manuel Ritter, Henry J. McSorley, Lindi Masson, Katherine Smith, Frank Brombacher, Matthew K. O'Shea, Adam F. Cunningham, Bernhard Ryffel, Menno J. Oudhoff, Benjamin G. Dewals, Laura E. Layland, William G. C. Horsnell

Cell Host Microbe. 2021 Apr 14. doi: 10.1016/j.chom.2021.02.004.

Paper 5

Intestinal-epithelial LSD1 controls goblet cell maturation and effector responses required for gut immunity to bacterial and helminth infection

Naveen Parmar, Kyle Burrows, **Pia M. Vornewald**, Håvard T. Lindholm, Rosalie T. Zwiiggelaar, Alberto Díez-Sánchez, Mara Martín-Alonso, Madeleine Fossli, Bruce A. Vallance, John Arne Dahl, Colby Zaph, Menno J. Oudhoff

PLoS Pathog. 2021 Mar 31. doi: 10.1371/journal.ppat.1009476

Paper 6 (commentary article)

Helminths get MIFfed by the tuft cell - ILC2 circuit

Pia M. Vornewald, Menno J. Oudhoff

Immunol Cell Biol. 2022 May. doi: 10.1111/imcb.12544

Paper 7 (Manuscript)

Early-life Intestinal Epithelial Maturation by LSD1 Dictates Local Gut Immune Cell Composition Independent from the Microbiota

Alberto Díez-Sánchez, Håvard T. Lindholm, **Pia M. Vornewald**, Jenny Ostrop, Naveen Parmar, Tovah N. Shaw, Mara Martín-Alonso, Menno J. Oudhoff

Manuscript currently under review at Science Immunology

1 Introduction

1.1 The gastrointestinal tract

The Gastrointestinal tract (GI) is a complex system that comprises several parts, including the oral cavity, pharynx, esophagus, stomach, small intestine (SI), and large intestine. The SI is further subdivided into duodenum, jejunum, and ileum, while the large intestine is subdivided into the cecum, appendix, colon, rectum, and anal canal (Figure 1). The primary function of the GI tract is to digest food and absorb essential nutrients, including carbohydrates, proteins, fats, minerals, and vitamins, while eliminating waste from the body. In this capacity, the GI tract relies on accessory organs of digestion, such as the salivary glands, liver, gallbladder, and pancreas.¹⁻³

1.1.1 The gastrointestinal wall

The gastrointestinal wall consists of four tissue layers. From the lumen (inner cavity of the intestine) outwards these are mucosa, submucosa, muscle layer (muscularis propria) and serosa (Figure 1).¹ These layers are interconnected by connective tissue, nerves, and vasculature, forming a complex network. While efficiently mediating nutrient absorption from lumen contents, the intestinal wall is exposed to a high load of luminal microbes. The intestinal immune system has to balance tolerance to normal microbiota while at the same time preserving the ability to recognize and eliminate pathogenic microbes to prevent infections.^{2,3}

The mucosa is structurally and functionally the most complex layer, fulfilling both the absorptive function and serving as a barrier. It can be subdivided into three parts: the epithelium, lamina propria, and muscularis mucosae (Figure 1). The inner most layer is the epithelium, a single layer of cells composed of several cell types. The structure and composition of the epithelium vary depending on the position and function along the GI tract. SI epithelium and colon epithelium will be described in detail in the next chapter. Below the epithelium is the lamina propria, which consists of connective tissue and contains blood and lymphatic vessels as well as lymphocytes and lymph nodules. Finally, the muscularis mucosae is a thin layer of smooth muscle cells that forms the boundary between the mucosa and the submucosa.²

2 Introduction

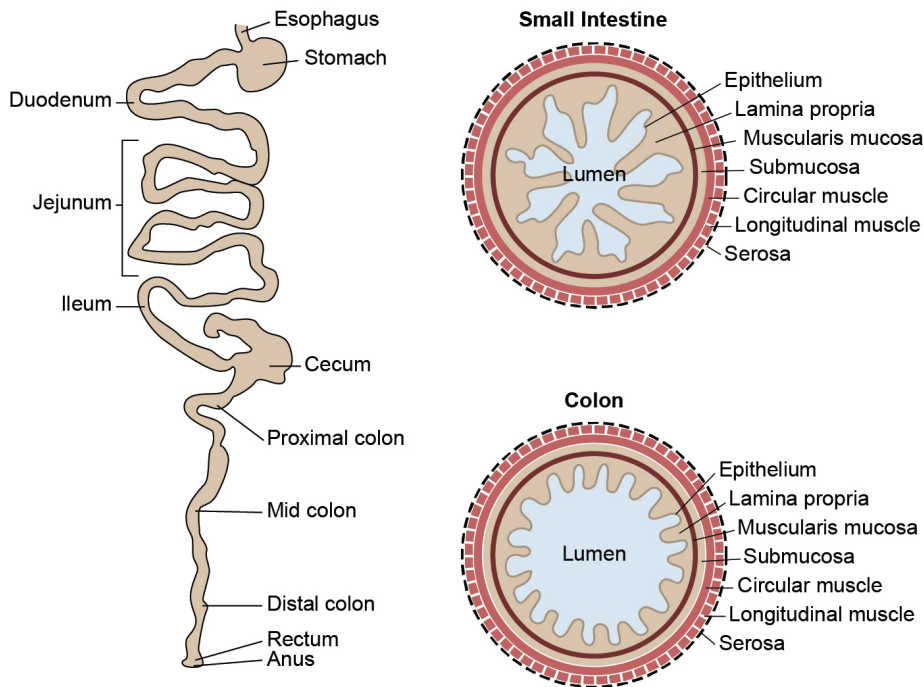


Figure 1: Mouse intestinal tract. Left: Depiction of mouse intestine, extracted at full length starting from stomach, small intestine subdivided into duodenum, jejunum, and ileum, followed by the large intestine subdivided into cecum, colon, and rectum, and finally the anus. Right: Schematic depiction of cross sections of small intestine and colon. Layers of the intestinal wall from lumen outwards are the mucosa (including epithelium, lamina propria and muscularis mucosa), submucosa, muscularis propria (including a circular and longitudinal muscle layer), and serosa, the most outer layer. This figure is partially based on Treuting, *et al.* ⁴

The submucosa is a layer of connective tissue containing blood vessels, lymphatics, and nerves, which supports the mucosa and provides flexibility to the GI tract.²

The muscularis propria, or muscle layer, has two sub-layers: an inner circular muscle layer and an outer longitudinal muscle layer. Separated by the intermuscular space, these layers contract in a coordinated manner to facilitate the movement of intestinal contents through the GI tract via peristalsis. The muscle also has an immunological function, helping to flush out pathogens like parasites from the gut through increased contractions.²

The outermost layer of the gastrointestinal wall is the serosa, comprising a thin layer of connective tissue and a simple squamous epithelium called the

mesothelium. The serosa serves as a protective barrier and provides lubrication, allowing for smooth movement of the GI tract in the abdominal cavity.²

In summary, the gastrointestinal tract is a sophisticated system with various interconnected layers and organs that work in harmony to digest food, absorb nutrients, and eliminate waste. Understanding its structure and function is crucial for studying and treating GI-related diseases and disorders. In this thesis, I will mostly focus on the epithelium and its regulation by smooth muscle tissue and cytokines during homeostasis, injury, and infection.

1.2 The intestinal epithelium

The intestinal epithelium forms the inner lining on the luminal side of both small and large intestine. It works as a physical barrier to external factors by maintaining tight intercellular junctions.⁵ The epithelium is a single layer of cells, with most being columnar surface cells that have different functions depending on their localization in the GI tract. The intestinal epithelium is renewed at a fast rate, with most epithelial cells being replaced every 3 to 5 days in mice.⁶

The epithelium is not a straight layer of cells but forms a three-dimensional structure with the goal to maximize surface area for absorption and protect the stem cells that enable constant renewal. The stem cells are located at the bottom of invaginations in the epithelium, called crypts and give rise to transit amplifying cells (rapidly dividing progenitor cells that differentiate into the mature intestinal epithelial cell types). Transit amplifying cells are pushed up and out of the crypt by the constant proliferation towards the intestinal surface. In the small intestine, the surface area is further increased by finger-like projections into the lumen, called villi, that contain the majority of differentiated cells. Once the epithelial cells reach the small intestinal villus tip or the colonic surface, they will eventually undergo anoikis and are shed into the intestinal lumen (Figure 2).^{7,8}

1.2.1 Cells of the intestinal epithelium

There are six different mature cell types in the intestinal epithelium that all derive from intestinal stem cells (ISC). Progenitor cells can commit to either an absorptive lineage, forming enterocytes and Microfold (M) cells, or a secretory lineage, resulting in goblet cells, tuft cells, Paneth cells or enteroendocrine cells (EECs) (Figure 2 and Figure 4).⁸

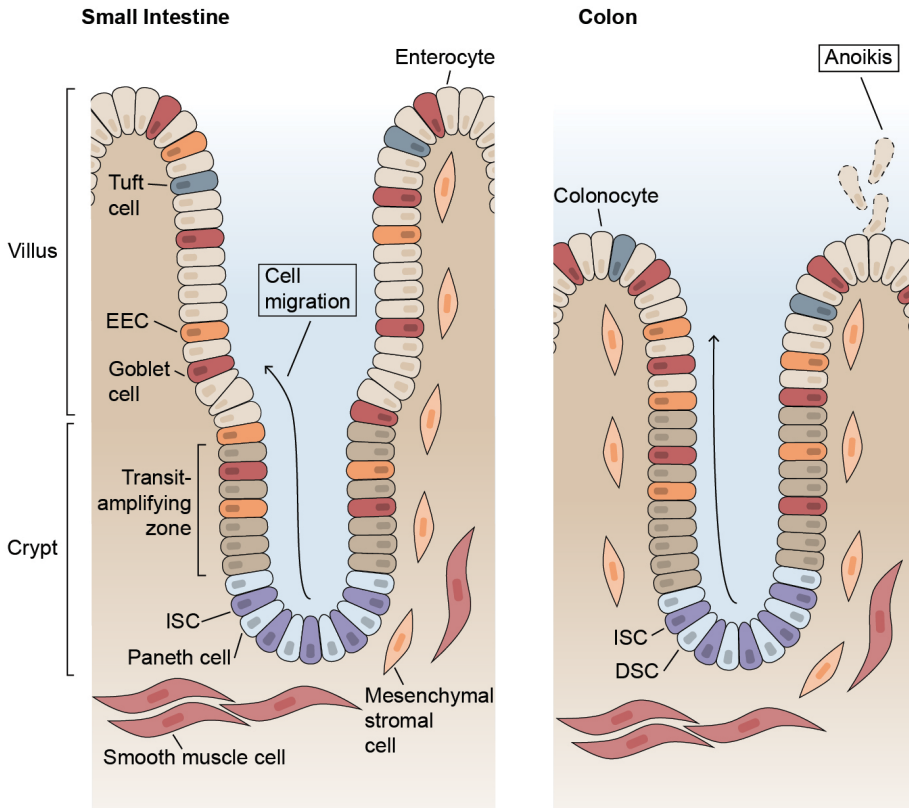


Figure 2: Structure and composition of the small intestinal and colon epithelial layer. Cell types are labeled in different colors. The small intestinal epithelium is divided into the crypt, which mostly contains intestinal stem cells (ISC) (purple) supported by Paneth cells (light blue), and progenitor cells in the transit amplifying zone (brown). The villus contains differentiated cell types including enterocytes (beige), enteroendocrine cells (EEC) (yellow), goblet cells (red), and tuft cells (dark blue). Right: The colon epithelium does not have villi, only crypts, and lack Paneth cells. Enterocytes in the colon are called colonocytes (beige). The role of Paneth cells is partially filled by deep crypt secretory cells (DSC). Microfold cells, found in both SI and colon, are not shown as they are only found in follicle-associated epithelium that sit above gut-associated lymphoid tissues (GALT). Most differentiated cells migrate up the crypt, once the cells have reached the villus tip/colonic surface they undergo anoikis and shed into the lumen (light blue background). In the lamina propria (beige background) there are multiple mesenchymal cell populations that provide factors necessary for the ISC niche, this includes the smooth muscle cells (light red) of the muscularis mucosa and different mesenchymal stromal cells (light yellow). This figure is based on Beumer and Clevers⁸.

ISCs were first described in the 1970s, when they were termed crypt-base columnar cells.⁹ In 2007, the Wnt target gene *Lgr5* became the universal marker for ISCs, after the discovery that Wnt/ β -catenin pathway was essential for its maintenance.¹⁰ Aside from the Wnt pathway, Notch and Epidermal Growth Factor (EGF) signaling are also active in ISCs, while Bone morphogenetic protein (BMP) signaling is suppressed. There are about 5-16 ISCs at the bottom of each crypt,

which constantly compete for niche occupancy. ISCs that are ‘pushed out’ of the stem cell zone, will immediately start to differentiate. The process of constant expansion and loss of ISC clones follows a pattern of neutral drift. These drift dynamics are heavily influenced by changes in the local niche.^{7,11} Aside from the fast-cycling *Lgr5*⁺ stem cells, +4 cells have been described as another population of ISCs. They are slow-cycling, damage resistant cells, named for their location in the crypt between the uppermost Paneth cell and the progenitor cells. +4 cells play an important role in intestinal regeneration and are considered “reserve ISCs”.^{7,12}

Enterocytes are the most abundant epithelial cell type in the GI tract, particularly in the small intestine. Their primary function is to carry out the final steps of digestion and absorption of nutrients in the small intestine and absorption of water in the colon. They produce various enzymes, such as disaccharidases and peptidases, to further break down nutrients for absorption through specialized receptors, transporters, or channels. Enterocytes possess a highly specialized apical membrane organized into microvilli, forming a brush border that increases the absorptive surface area. This brush border, combined with the crypt-villus-structure and intestinal folds, expands the absorptive surface area to approximately 30 m² in an adult human. Enterocytes also serve a protective function against infectious and immunogenic agents, with a dense layer of transmembrane mucins covering the brush border that acts as a diffusion barrier. This layer prevents bacteria from attaching to the epithelium while simultaneously allowing nutrients to pass through. Moreover, enterocytes can endocytose luminal antigens, process them, and present them to T-cell via MHC class II at the basolateral membrane. Enterocytes have also been reported to produce certain anti-microbial peptides (AMPs) like REG3 β and REG3 γ .^{8,13-15}

Goblet cells are present in both small and large intestine. They are specialized cells that primarily produce intestinal mucus and secrete antimicrobials. The mucus layer lubricates the intestinal lumen, facilitating the movement of food through the intestine, and protects the intestinal epithelium from physical damage and microbial invasion which will be explained in detail in chapter 1.2.2. Goblet cells, like enterocytes, are short-lived cells. Once formed, goblet cells migrate up the crypt-villus and crypt-surface axes, and are exfoliated upon reaching the tip of the villus or the colonic surface.⁸ Generally, goblet cells are distinguished from other epithelial cells by transcription factors that drive goblet cell differentiation, core mucus proteins, and specific proteins involved mucus protein biosynthesis and protein folding. Single cell RNA sequencing has revealed distinct sub-population among goblet cells. Two main subpopulations have been identified as canonical and non-canonical goblet cells. Canonical goblet cells are characterized by high expression of classical goblet cell markers like *Atoh1*, *Muc2*, *Fcgbp* and

Cla1. Non-canonical goblet cells, on the other hand, have a more enterocyte-like expression profile with higher levels of *Hes1*, *Dmbt1*, *Muc17*, and ion channels.¹⁶ A further distinction can be made in the colon between the large upper crypt goblet cells and the morphologically distinct, smaller inter-crypt goblet cells. Both upper-crypt goblet cells and inter-crypt goblet cells are responsible for producing the main mucus components.¹⁷

Paneth cells are located at the base of the crypts in the SI, interspersing intestinal stem cells. Paneth cells have a dual role in protecting and supporting stem cells. They secrete AMPs such as lysozyme and defensins that keep the crypt clear of microbiota. Additionally, they also play a role in stem cell maintenance in the SI by providing EGF, TGF- α , WNT3, and the Notch ligand, DLL4.¹⁸ The role of Paneth cells as part of the ISC niche and their colonic counterpart are described in chapter 1.3.2.

Tuft cells are characterized by their distinct elongated microvilli and can be found in both SI and colon. They play a critical role in the immune response against parasitic infections by sensing antigens produced by helminths in the intestinal lumen and alert the immune system by producing cytokines such as interleukin-25 (IL-25) (See chapters 1.5.1 and 1.6.3). Additionally, tuft cells contribute to maintaining intestinal homeostasis by sensing luminal contents and participating in the regulation of the gut microbiome.^{19,20}

Enteroendocrine cells (EEC) are present in both SI and large intestine. They comprise about 1 % of all epithelial cells. EECs secrete over 20 different hormones in response to nutrients in the lumen, regulating gastrointestinal activity, systemic metabolism, and appetite.⁸ There are multiple types of EEC subtypes, defined by their principle hormone product. The distribution of those subtypes changes greatly from proximal to the distal part of the intestinal tract.²¹

Microfold (M) cells are specialized cells that can only be found in the follicle-associated epithelium that sit in the epithelium above gut-associated lymphoid tissues (GALT). They take up antigens or bacteria from the intestinal lumen and transport them to antigen-presenting cells. This also makes them the site of entry for many viral and bacterial intestinal pathogens.⁸

In summary, the intestinal epithelium is a complex tissue that is comprised of several different cell types, each with unique functions. The integrity of this tissue is crucial for proper nutrient absorption, protection against harmful substances, and overall gut health.

1.2.2 Intestinal mucus layer

The apical side of intestinal epithelium is covered by a mucus layer. The mucus forms a selective barrier that has evolved to address the diverse challenges encountered in various compartments of the intestinal tract. Mucus thickness varies long the length of the intestinal tract and correlates with the density of goblet cells.⁵ In the SI, the mucus serves to protect the epithelium from harsh conditions caused by gastric acid, bile, and digestive enzymes, as well as mechanical forces from non-digested food. The mucus also restricts bacterial colonization while still allowing nutritional uptake. The large intestine has a significantly greater bacterial load than the SI, and its mucus must defend against mechanical forces caused by fecal matter, while still allowing the absorption and sensing of substances. In the SI, the mucus is loose and constantly renewed, which helps keep harmful substances away from the epithelium. In the large intestine, the mucus barrier is stratified into a dense layer directly above the epithelium, containing no commensals and a loose layer on the luminal side above that.¹⁷

The mucus forms a net-like three-dimensional structure that restricts diffusion of substances and prevents penetration by pathogens. The mucus layer is formed by molecules secreted from the epithelium, with goblet cells being the primary producers of mucus components. The core mucus components include mucin-2 (MUC2), Fc γ binding protein (FCGBP), and calcium-activated chloride channel regulator1 (CLCA1).¹⁷ The mucus also contains forms a scaffolding for retaining other molecules like AMPs secreted by various epithelial cells, as well as immunoglobulin A (IgA) produced by plasma cells. IgA binds and aggregate bacteria, while AMPs can actively lyse bacteria, thereby reinforcing the physical barrier. The secretion of mucus components by goblet cells happens under baseline condition or in response to stimulation.^{5,22}

Mucin glycans also serve as nutrients for some intestinal microbiota, which break them down into short chain fatty acids (SCFA). The SCFAs propionate and butyrate fuel intestinal epithelial cells. Other fermentation products such as acetate and lactate are toxic not some pathogenic bacteria, adding an additional layer to the immune defense provided by the intestinal mucus.⁵

The mucus layer is dynamic and responds to external cues, such as, microbiota and their metabolites, which impact the appearance and composition of the intestinal mucus layer. This is illustrated by the fact that the mucus layer in germ free mice is thinner than in conventionally housed mice.²³

1.3 The intestinal stem cell (ISC) niche

The concept of the stem cell niche was discovered upon the observation that adult stem cells often lose their “stemness” when removed from their normal environment in a tissue, leading to the hypothesis that the microenvironment around the stem cells provides cues that control the stem-cell numbers, division, self-renewal, and differentiation.²⁴ In the following text, I will provide an overview on the cell types and signaling pathways forming the intestinal epithelial niche.

1.3.1 Signaling pathways in the niche

Signaling Pathways are a crucial component of the ISC niche. Localized cell to cell signaling, as well as gradients of signaling molecules and inhibitors, work simultaneously both in maintaining ISCs and to drive differentiation into the different cell types that make up the intestinal epithelium (Figure 3 and Figure 4). The molecules that activate these signaling pathways are produced by both epithelial cells themselves and surrounding mesenchymal cells. In the following section, I will discuss the most important pathways in the intestinal epithelium: Wnt, Notch, EGF, and BMP and Hippo signaling. Additional signals that regulate stem cells include interleukins and nutrition.^{8,25,26}

Wnt signaling is essential in maintaining ISCs in homeostasis and during intestinal regeneration. Deregulation of the Wnt pathway leads to uncontrolled cell proliferation and promotes cancer. Wnt ligands are produced by Paneth cells (only in the small intestine) and mesenchymal cells surrounding the crypt. Wnt ligands bind to the Frizzled–LGR5–LRP6 receptor complex, this in turn inhibits the APC destruction complex and leads to accumulation of β -catenin, the key mediator of Wnt signals, and its translocation into the nucleus. In the nucleus β -catenin acts as a transcriptional co-factor for T-cell factor transcription factors (TCFs), inducing the transcription of Wnt target genes (Figure 3). The importance of Wnt signaling for the maintenance of ISCs is easily observable in intestinal organoids, where WNT3 secreted by Paneth cells within the organoid is essential to support small intestinal organoid growth.²⁷ Colon organoids, which lack Paneth cells, need exogenous supplementation of WNT3 or co-culture with mesenchymal cells in order to grow.^{7,28} Organoids as a model system for the intestinal epithelium and their culture are described in detail in chapter 1.6.7.

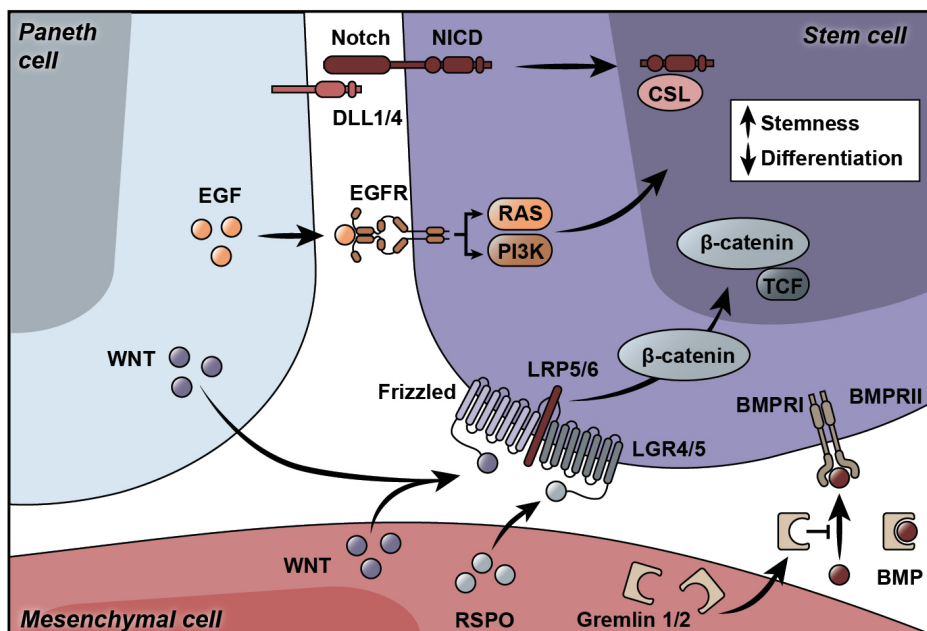


Figure 3: Signaling pathways in the intestinal stem cell niche. Interactions between intestinal stem cells (ISC) (purple), Paneth cells (light blue) and mesenchymal cells (red) through signaling pathways that support ISC survival. Top to bottom, Notch signaling (red), EGF signaling (yellow), Wnt signaling with enhancer RSPO (purple and light blue), and inhibition of BMP signaling through the BMP antagonists Gremlin 1/2 (beige). This figure is based on Meyer, et al.²⁹

R-spondins (RSPO) are an essential enhancer of Wnt signaling, acting directly through LGR5.³⁰ Complexes of RSPO and LGRs bind and inhibit E3 ligases that mark the receptors Frizzled (Wnt receptors) and LRP5/6 for endocytosis and degradation (Figure 3). This drastically increases Wnt signaling as more Wnt receptors are available on the cell surface. Increased expression of RSPOs can also drive cancer development, due to this strengthening of Wnt signaling.^{8,31}

EGF signaling is needed for intestinal proliferation; however, it is not essential for ISC maintenance. Overactive EGF signaling is a step towards cancer, while blocking EGF signaling in intestinal organoids stops organoid growth. EGF is expressed by Paneth cells (small intestine only) and in low levels by CD34+/PDGFR α stromal cells. Binding of EGF to the EGFR ErbB receptor, followed by receptor dimerization, induces various intracellular signaling cascades like MAPK, PI3K-AKT, and JAK-STAT (Figure 3).³²

Notch signaling together with Wnt signaling is important in maintaining ISC stemness, but also stirs the cell fate between secretory and absorptive cell lineages. Notch signaling is activated by membrane-to-membrane contact between two cells, where Notch ligands such as DLL1 or DLL4, which are expressed on the

surface of one cell, interact with Notch receptors such as NOTCH1, which are expressed on the surface of a second cell. Upon ligand binding, the Notch intracellular domain (NICD) of the receptor is released and translocates to the nucleus, where it binds the transcription factor CSL (Figure 3).²⁹ The main downstream effect of Notch signaling is the expression of the transcription factor HES1, which in turn represses the expression of transcription factor ATOH1. ATOH1 is needed to induce transcription of Notch ligands. Suppression of ATOH1 through Notch activation leads to a mechanism called lateral inhibition and causes a binary ‘on’ or ‘off’ state in a cell population, as a cell expressing Notch ligands suppresses the expression of Notch ligands in all surrounding cells it touches. Notch signaling plays an essential role in fate commitment in the intestine. Active Notch signaling suppresses differentiation into secretory lineage cells while favoring differentiation into absorptive lineage cells (Figure 4). Loss of ATOH1 leads to loss of all secretory cells, whereas over expression of ATOH1 leads to higher numbers of secretory cells.^{33,34} Thus, Notch signaling serves the dual purpose of maintaining the stem cells at the bottom of the crypt and regulating the ratio of cells of secretory and absorptive lineages.^{25,29}

BMP signaling suppresses stem cell signature genes and induces differentiation in the crypt. BMP belongs to the TGF- β ligand superfamily. In the intestine BMP2 and BMP4 are the main ligands for BMP receptors and are produced by mesenchymal cells. Binding of BMP facilitates the dimerization of type I and type II BMP receptors. This leads to phosphorylation and dimerization of rSMADs, which in turn bind common SMAD (cSMAD or SMAD4) in a complex which translocates to the nucleus. There, the SMAD complex regulates the expression of target genes. BMP signaling can be inhibited by BMP antagonists that sequester BMPs by forming a stable complex with BMPs that prevents receptor interaction (Figure 3). These antagonists such as Chordin-like 1 (CHRDL1), Gremlin 1 (GREM1), Gremlin 2 (GREM2), or Noggin are secreted by mesenchymal cells, mainly myofibroblasts located below intestinal crypts. The location of these cells creates a gradient from the bottom to the top of the crypt, allowing for increased BMP signaling towards the top of the crypt (Figure 4).^{35,36}

Hippo signaling is not essential during homeostasis but is critical for epithelial repair. Key components of the Hippo pathway include kinase cascades comprised of MST1/2, SAV1, LATS1/2, and MOB1A/B. The transcriptional co-activators YAP1 and TAZ are the downstream effectors of the Hippo pathway and are essential for intestinal regeneration after injury. Hippo signaling controls cell proliferation and apoptosis, while dysregulation of the pathway often leads to uncontrolled tissue growth and tumorigenesis. There are more than 20 upstream regulators of the Hippo pathway including cell polarity, contact inhibition, stress, mechanotransduction, cell attachment, hormones and growth factors.^{37,38}

Wnt, Notch, EGF, BMP, and Hippo signaling as well as cytokines and differences in nutrition, work together to maintain the intestinal epithelium. Figure 4 showcases the signaling gradients present in the ISC niche and explains the intestinal epithelial cell differentiation pathways induced by the different types of signaling.⁷ Infections and inflammatory context can also change epithelial cell differentiation and expression, which will be addressed in chapter 1.5.1 and in the discussion. The cellular sources of these signaling molecules are introduced in the next two chapters.

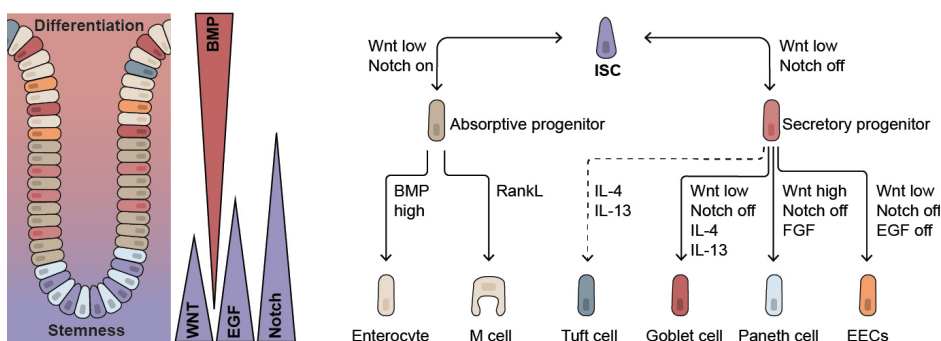


Figure 4: Signaling gradients and cell fate in the intestinal epithelial niche. Left: Most important signaling gradients in the intestinal crypt along the crypt-colon-surface-axis. Right: Cell fate in the intestinal crypt. Notch signaling is determining the fate towards an absorptive (Notch on) or secretory fate (Notch off). Cells of the absorptive lineage differentiate into Enterocytes by default, as BMP signaling increases. M cell develop in the follicle-associated epithelium in the presence of receptor activator of nuclear factor κ -B ligand (RankL). Secretory progenitors can mature into tuft cells, goblet cells, Paneth cells and different Enteroendocrine cell (EEC) subtypes. Goblet cell differentiation requires the inhibition of both Notch and Wnt-signaling pathways. Tuft cell differentiation is not fully understood, however IL4 and IL13 can induce both tuft cells and goblet cells. Goblet cell differentiation is the default pathway for secretory progenitors, when Wnt levels are low and Notch signaling is turned off. Paneth cells develop when Wnt levels are high in the presence of fibroblast growth factor (FGF). A combination of low Wnt levels, no Notch signaling and reduced epidermal growth factor (EGF) signaling leads to the maturation of EECs, the specification of the different EEC subtypes is not fully understood, yet. Part of this figure is adapted from Gehart and Clevers.^{7,8}

1.3.2 Epithelial cell contribution to the ISC niche

Differentiated epithelial cells form a part of the intestinal stem cell niche supported by mesenchymal stromal cells and the extracellular matrix (ECM). Specifically, Paneth cells, which are interspersed between ISCs, secrete WNT3, EGF, and the Notch ligands Delta-like 1 (DLL1) and DLL4, which in turn trigger the activation of NOTCH1 and NOTCH2 on ISCs.⁸ In the colon, where Paneth cells do not exist, part of their function is fulfilled by deep crypt secretory cells (DSC), marked by Reg4. While DSCs express the Notch ligands DLL1 and DLL4, they do not produce Wnt ligands, which are exclusively provided by mesenchymal cell populations in the colon.^{39,40}

1.3.3 Mesenchymal cell contribution to the ISC niche

Mesenchymal cell populations located below the intestinal epithelium are an essential part of the ISCs niche. The mesenchyme is made up of myofibroblast, fibroblasts, pericytes, endothelial cells, neural cells, and smooth muscle cells.⁴¹ Not only do these cells provide structural support, but they are also sources of essential signaling molecules such as Wnts, BMPs, BMP antagonists, and cytokines.⁴²⁻⁴⁴

Smooth Muscle cells, of the muscularis mucosa, have been described to express the BMP antagonists Gremlin 1 and Gremlin 2. This may indicate that smooth muscle cells contribute to the ISC niche in the intestine by decreasing BMP signaling and inhibiting differentiation in the lower crypt.⁴⁵

Mesenchymal stromal cells in the intestine, comprise a collection of non-epithelial, non-hematopoietic, non-endothelial, and non-neuronal cells that can produce growth factors, cytokines, and ECM components that are essential for normal development and homeostasis. They are located beneath the intestinal epithelium, and can be found in the lamina propria, submucosa, muscularis mucosae, muscularis propria, serosa and mesothelium. They are a diverse group of cells that includes telocytes, CD34⁺ fibroblasts, pericytes, Map3k2-Regulated Intestinal Stromal Cells (MRISCs), myocytes, interstitial cell of Cajal and mesothelial cells. Various markers such as vimentin, CD90, S100A4, α -smooth muscle actin and desmin have been employed to identify distinct subsets of mesenchymal stromal cell populations.⁴³

Recent research interest has focused on the physiological function of mesenchymal stromal cell. For instance, fibroblasts are thought to regulate intestinal homeostasis by providing Wnt enhancer R-spondin1 and BMP antagonists like Gremlin1, thus supporting the ISCs niche.⁴⁶ It has also been suggested that telocytes located within the villus regulate epithelial cells by producing essential Wnt ligands and BMPs.^{42,47}

In summary, both epithelial and mesenchymal cells- including SMCs- contribute to the establishment of a biochemical Wnt-BMP gradient, which facilitates the maintenance of ISCs and the differentiation of intestinal epithelial cells. The relative populations of differentiated epithelial cell types are fairly constant in homeostasis, however, this can quickly change upon injury or upon inflammation. Epithelial regeneration and plasticity will be discussed in the following section.

1.3.4 Intestinal regeneration and plasticity

The intestinal epithelium has a remarkable ability to regenerate upon damage. When acute injury leads to ISC loss, regenerative responses that restore the stem cell compartment are activated. Several cell types of the intestinal epithelium have

been discovered to be able to dedifferentiate to LGR5⁺ stem cells in order to repopulate the intestinal crypt after damage. The first cells to replace LGR5⁺ stem cells are quiescent stem cells from the +4 position from the crypt base. Additionally, both secretory and absorptive progenitor cells can dedifferentiate to repopulate the crypt. However, progenitor cells, as fast-dividing cells, are very susceptible towards chemotherapy treatment and irradiation and could therefore be too damaged to replace lost ISCs. Recent studies have suggested that even fully differentiated cell types like Paneth cells⁴⁸, certain subpopulation of tuft cells⁴⁹, and perhaps enteroendocrine cells⁵⁰, may be able to dedifferentiate and contribute to the repopulation of the crypt after ISC loss.^{12,29} Plasticity of the intestinal epithelium is controlled through upregulation of the same pathways that support the ISCs niche during homeostasis, like Wnt and Notch. Wnt signaling is increased while BMP signaling is inhibited through elevated expression of BMP antagonists.²⁹

1.4 Extra cellular matrix (ECM) and its regulation

The ECM is a non-cellular component of tissues and organs that provides structural support and modulates cellular behavior. The ECM has a vital role in cell adhesion, migration, proliferation, and differentiation, thereby influencing tissue development, maintenance, and repair.

1.4.1 Intestinal ECM structure and composition

In the intestine the ECM can be divided into two distinct compartments, the basement membrane, situated directly beneath the basal side of the epithelial layer, and the interstitial matrix, which permeates the lamina propria, submucosa, smooth muscle and serosa layers. The ECM provides critical structural support to the intestinal tissue. Its components have unique properties, such as retaining water to maintain tissue hydration, forming a selective barrier, and providing tensile strength. Beyond these structural roles, the ECM also offers biochemical and biomechanical cues to the cells.⁵¹

The ECM comprises a complex network of hundreds of diverse proteins and polysaccharide molecules, known as glycosaminoglycans (GAGs). These GAGs in the ECM are linked to proteins to form proteoglycans (PGs). The composition of the ECM varies widely between tissues and is markedly heterogeneous. Epithelial and mesenchymal cells, including fibroblasts, myofibroblasts, and smooth muscle cells, produce and secrete the components of the ECM.

The basement membrane represents a specialized form of ECM, primarily composed of type IV collagen, laminins, nidogens, and perlecan. The interstitial

matrix, on the other hand, predominantly consists of collagens, fibronectin, elastin, decorin, and hyaluronan. The ECM facilitates cell adhesion and via specific ECM receptors, such as integrins.

The ECM is highly dynamic and undergoes constant remodeling. This remodeling is facilitated by proteases that cleave the matrix components and tightly controlled by inhibitors. Dysregulation of this balance can lead to various diseases. In the event of injury, the ECM undergoes rapid degradation and reorganization, facilitating the migration of cells towards the site of injury. In inflammatory context, the ECM also modulates the recruitment and activity of immune cells.⁵¹

1.4.2 ECM as part of the ISC niche

The ECM plays an essential role in regulating ISC behavior, by providing biomechanical and biochemical signals that modulate stem cell proliferation, differentiation, and self-renewal. The ECM can influence ISC behavior through cell-ECM interaction, as well as soluble or ECM-bound factors. These can be growth factors, cytokines, and other signaling molecules that interact with cell-surface receptors.⁵²

Integrins, a large family of heterodimeric transmembrane receptor, are the key receptors involved in ECM-ISC interactions. At focal adhesion complexes, Integrins together with adaptors and signaling proteins connect the ECM to the intracellular cytoskeleton. This connection makes cells able to sense and respond to mechanical stimuli which can for example activate the Hippo pathway.⁵³ The sensitivity of the intestinal epithelium toward ECM stiffness is highlighted by experiments of intestinal organoids grown in different matrixes.⁵⁴ Integrins can also directly regulate self-renewal and proliferation of stem cells by signaling through focal adhesion kinase or they can mediate signaling pathways, like Hedgehog signaling.^{52,55,56} Another way of ECM-cell interaction is through intrinsic growth-factor-like domains within ECM proteins. Laminins have been found to contain multiple EGF-like domains that are thought to bind to EGF receptors after proteolysis.⁵⁷ Additional to direct cell-ECM interactions, ECM components can bind growth factors, thus regulating their local availability. The ECM can function as a reservoir for growth factors, by binding to the ECM, they become insoluble and biologically inactive. Upon ECM remodeling through enzymes, like matrix metalloproteinases (MMPs), they become available again.⁵⁸ Further evidence for the importance of the ECM as part of the ISC niche is provided by experiments with decellularized tissues that can guide stem cell differentiation towards the tissue specific cell types the ECM was derived from.⁵⁹

In summary, the ECM forms an important part of the ISC niche through direct signaling and the binding and release of signaling molecules. Regulators of the

ECM need to be tightly controlled, as dysregulation can quickly lead to aberrant signaling and tumorigenesis. An important family of ECM regulators, MMPs, will be introduced in the following section.

1.4.3 MMPs as ECM regulators

Matrix metalloproteinases (MMPs) are a family of calcium-dependent zinc-containing endopeptidases that play a crucial role in the regulation of the ECM by degrading its components, including ECM proteins/glycoproteins, membrane receptors, cytokines, and growth factors. MMPs were first discovered in the context of the rapid tissue remodeling happening in amphibians during metamorphosis in 1962 by Gross and Lapiere.⁶⁰ Since then, over 20 MMPs have been identified in humans and mice, numbered in order of discovery. MMPs are involved in various physiological processes, including tissue remodeling, wound healing, angiogenesis, and cell migration and have been implicated in various diseases such as rheumatoid arthritis, cancer and in inflammatory bowel disease (IBD).^{61,62}

MMPs can be categorized into several subgroups by substrate specificity and structure (Figure 5): collagenases (MMP-1, MMP-8, MMP-13, and MMP-18), gelatinases (MMP-2 and MMP-9), stromelysins (MMP-3, MMP-10 and MMP-11), matrilysins (MMP-7 and MMP-26), and membrane-type MMPs (MT-MMPs). MT-MMPs are anchored to the cell membrane and can further be subdivided by their membrane tether, this can be a transmembrane domain (MMP-14, MMP-15, MMP-16, MMP-24), an amino terminal peptide (MMP-23A, MMP-23B) or a glycosylphosphatidylinositol (GPI) anchor (MMP17, MMP-25).⁶³

Regulation of MMP activity is essential for maintaining tissue homeostasis. MMPs are synthesized as inactive zymogens (proMMPs) and need proteolytic activation by other proteases. In addition, the activity of MMPs is controlled by endogenous tissue inhibitors of metalloproteinases (TIMPs), which bind the active site of MMPs and inhibit their enzymatic function.⁶⁴

Dysregulation of the tightly controlled MMP activity has been associated with various pathological conditions. In particular, overexpression or imbalanced activation of MMPs can lead to excessive ECM degradation, resulting in tissue destruction and inflammation. Consequently, MMPs have emerged as biomarkers and as potential therapeutic targets for various diseases.⁶¹

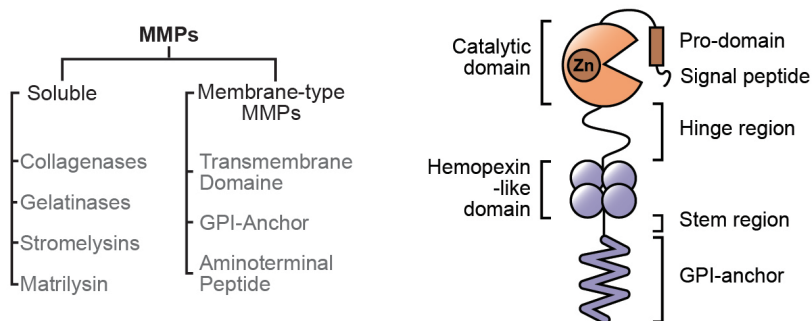


Figure 5: Classification of MMPs and structure of MMP17. Left: MMPs can be classed into soluble MMPs and membrane-type MMPs. Soluble MMPs are subdivided by their substrate specificity into collagenases, gelatinases, stromelysins and matrilysin, while membrane type MMPs are often subdivided by their membrane-anchor. Right: Domain structure of MMP17.

1.4.4 Unique properties and functions of MMP17

The MMP that captured our research interest is MMP17, also known as MT4-MMP. As an MT-MMP, MMP17 has unique properties and functions that distinguish it from other MMPs. Due to the membrane attachment, MMP17 is able to cleave membrane and membrane-associated proteins, as well as ECM components close to the membrane, thereby regulating the pericellular space. The membrane anchor of MMP17 is a GPI anchor, a feature that MMP17 only shares with MMP-25.⁶⁵ The structural domains of MMP17 include a signal peptide, a pro-domain, a catalytic domain with a zinc ion, a hinge region, a hemopexin-like domain, and a stem region which connects to the GPI membrane anchor (Figure 5).⁶⁶

The catalytic domain sequence homology of MMP17 with other MMPs is fairly low, which might explain its differences in activity. MMP17 hydrolyses very few classical ECM components, when compared to other MMPs. Only weak cleavage of gelatin, fibrin and fibrinogen has been shown experimentally. Activity towards other ECM and non-ECM substrates has been reported for proTNF, COMP, α -2-macroglobulin, LRP1, ADAMTS4, osteopontin, thrombospondin 4, and α M integrin.^{66,67} In addition, in cell lines overexpressing active MMP17, autocleavage of MMP17 has been reported.⁶⁸ Functionally, MMP17 has been associated with regulating cell migration, axonal growth, and immune cell recruitment, as well as promoting tumor growth and angiogenesis. MMP17 has both proteolytic and non-proteolytic functions. While MMP17s proteolytic activity appears to be necessary for pro-angiogenic and pro-metastatic effects, its effect on cell proliferation is not dependent on its proteolytic function.^{66,68,69}

To study MMP17 *in vivo*, a KO mouse strain was introduced by Rikimaru et al. in 2007. In this *Mmp17* KO mouse, the *Mmp17* genomic sequence is partially replaced by a LacZ cassette, that functions as a reporter of *Mmp17* promoter activation. This made it possible to observe MMP17 expression in various tissues and cell types. Prominent expression was seen in brain, lungs, and uterus, while lower levels were detected in spleen, stomach, intestine and testis. MMP17 has also been detected in immune cell types, e.g. macrophages, indicating a role during inflammation.⁷⁰ Interestingly, *Mmp17* expression correlated with the expression of alpha smooth muscle actin (α SMA), pointing towards the expression of *Mmp17* in smooth muscle cells throughout the mouse body. Despite the abundant presence of MMP17 in multiple tissues, mice lacking MMP17 develop normally and show normal appearance, behavior, life span, and fertility.

71

Pathological function of MMP17 has been studied more than its physiological function. MMP17 has been implicated in inflammatory processes, like cartilage ECM degradation in osteoarthritis. MMP17 is found in increased levels in several cancers, including breast cancer, head and neck cancer, gastric cancer, and colon cancer.⁶⁶ Although MMP17 has been linked to various physiological processes and pathologies, the underlying mechanisms of action of MMP17 remain unknown.

1.5 Intestinal mucosal immune system

In the intestine, epithelium and immune system work together to maintain the balance between immune tolerance to commensal microorganisms and food while maintaining an active defense against pathogens. Commensal microorganisms in the gut play an important role during intestinal infections, as the microbiota is the first point of contact for pathogens. A healthy microbiome has been shown to be able to limit the colonization and overgrowth of a pathogen, but commensals can also assist pathogens in colonization, for example by providing nutrients.⁷² In the following I will describe the epithelial and immune cellular contributions to the intestinal mucosal immune system.

1.5.1 Epithelial immune defense mechanisms

The epithelial surface forms a physical barrier that is a first layer of defense. The epithelial cells are interconnected by tight junctions, formed by complexes out of several members of the claudin and occludin families linked to the cytoskeleton of intestinal epithelial cells. These connection form a selective, semipermeable barrier between adjacent epithelial cells that, while allowing the passage of water, ions, and small solutes, prevents inflammatory agents, like pathogens, toxins, and

antigens, from reaching the underlying tissues.^{5,73} The epithelium also produces the mucus layer, a complex network of mucins and AMPs that covers the apical epithelial surface and provides additional protection by limiting microorganisms from coming in contact with the epithelial cells.⁷⁴ The structure and composition of the mucus layer was introduced in chapter 1.2.2.

The intestinal epithelial cells have a primary role in the innate defense against pathogens. Pattern recognition receptors (PRRs), like Toll-like receptors (TLRs) and NOD-like receptors (NLRs), recognize microbial-associated molecular patterns (MAMPs) or damage-associated molecular patterns (DAMPs), trigger signaling cascades that induce pro-inflammatory cytokines and chemokines and lead to immune cell recruitment. TLRs and NLRs activate NF κ B, which induces production of CCL1, CCL2, CXCL1, CXCL8 and CCL20 in epithelial cells that attract neutrophils, macrophages, and dendritic cells. Cellular damage can also activate an inflammasome leading to the production of IL-18 that activates myeloid cells and increases barrier integrity. PRRs on the apical surface of the epithelial cells are downregulated in the intestine to accommodate the presence of commensal microbiota and are mostly present in intracellular vesicles and in the cytosol.^{5,72,75}

Goblet cells are the main producer of mucus components, including the core mucus proteins MUC2, FCGBP, and CLCA1. The importance of the mucus in protecting the epithelial layer, becomes apparent in *Muc2*^{-/-} mice that develop spontaneous colitis at 5 weeks of age.⁷⁶ The secretion of mucus components by goblet cells is continuous under baseline condition. However, upon stimulation, goblet cells can rapidly release almost all the mucus stored in mucus granulae in a process called compound exocytosis.⁷⁷ This stimulation can be induced by bacterial products or cytokines like IL-22 or IFN- γ .^{74,78} This sudden release of large amount of mucus can flush pathogens away from the mucosal surface, limiting their levels at the epithelial surface and assisting in clearance.⁷⁹

Aside from mucus forming proteins, goblet cells also secrete other factors, that have antimicrobial properties or regulatory functions during homeostasis and immune responses. Among those are trefoil factor 3 (TFF3), resistin-like molecule β (RELM- β), zymogen granule protein 16 (ZG16), angiogenin 4 (ANG4), and small proline-rich protein (SPRR2A).⁸⁰ Trefoil factors are a family of cysteine-rich proteins that play a role in mucosal repair. TFF3 is expressed by goblet cells in the SI and colon and contributes to the maintenance and stabilization of the intestinal barrier function.⁸¹ RELM- β , mostly expressed in cecum and proximal colon, is induced upon Th2 immune responses, and has been demonstrated to have anti-bacterial and anti-helminth effects.^{82,83} ZG16 is a lectin-like protein that can aggregate Gram-positive bacteria, together with the mucus layer, this aggregation

keeps the bacteria further away from the epithelial surface.⁸⁴ ANG4 is an antimicrobial protein that is expressed by goblet cells in the large intestine. *Ang4* expression is induced by IL-13.⁸⁵ SPRR2A selectively kills Gram-positive bacteria and is induced by type 2 cytokines.⁸⁶

Goblet cells also act as luminal sensors that can deliver luminal antigens to innate immune cells via the formation of so-called goblet cell-associated antigen passages. Innate immune cells in the lamina propria can take up the antigens and deliver them to the lymph nodes where they induce adaptive immune responses.^{17,87}

Tuft cells play a key role in the defense against parasitic helminth. In 2016 they were identified as the source of IL-25. IL-25 is released by tuft cells upon sensing of helminth antigens in the lumen and activates group 2 innate lymphoid cells (ILC2s). Activated ILC2s increase the expression of IL-13 which induces epithelial progenitors towards secretory lineages, like goblet cells and tuft cells. This mechanism has been termed the tuft cell-ILC2 circuit. Aside from IL-25, tuft cells also express another type 2 epithelial cytokine, thymic stromal lymphopoietin (TSLP).⁸⁸ This makes tuft cells important regulators of the immune response.

In summary, epithelial cells play an important part in forming the first line of defense against pathogens. The mucus and the epithelial layer prevent harmful agents from entering the underlying tissue. Upon infection, sensing and uptake of luminal antigens, as well as the release of alarmins, help guiding the immune response of innate and adaptive immune cells, while increased mucus and AMP release assist in pathogen clearance. In the next section, I will present the different immune cells populations, their location in the intestine and their role during infections.

1.5.2 Immune cells in the intestine

The immune system in the in the intestine can be classed into inductive sites and effector sites. Inductive sites include the intestine-draining mesenteric lymph nodes (mLN) and the gut-associated lymphoid tissues (GALTs), where cells of the adaptive immune system are primed. The effective sites include the intestinal epithelium and lamina propria, where primed adaptive immune cells and innate immune cells are scattered throughout. GALTs are organized structures like Payer's patches in the SI, and isolated lymphoid follicles that that can be found distributed along the whole length of the intestine.⁸⁹ In the following I will present some of the most common types of adaptive (T cells, B cells) and innate (Macrophages, Dendritic cells, Innate lymphoid cells (ILCs)) immune cells in the intestine and their role in the immune defense.

T cells are a type of adaptive lymphoid cell that are defined by the presence of a T cell receptor (TCR) on their cell surface. The critical step in T cell maturation is the development of a functional TCR. Each mature T cell has a unique TCR, that is able to bind a specific antigen presented by the major histocompatibility complex (MHC) on cells. T cells have two major subtypes, CD4⁺ helper T cells and CD8⁺ cytotoxic T cells.⁹⁰

In the intestine T cells can be found intraepithelial and in the lamina propria. Intraepithelial lymphocytes (IEL) are mostly CD8⁺ and located between enterocytes of the epithelial layer. This places them in direct vicinity of the antigens within the lumen. IELs have both regulatory and effector capabilities and are almost exclusively T cells. Lamina propria T cells on the other hand are predominantly CD4⁺ with a 2:1 ratio of CD4⁺ T cells to CD8⁺ T cells.^{5,91}

T helper (Th) cells are a prominent and diverse class of immune cell in the gut. They get their name from their ability to polarize the immune response and other immune cells into a certain direction through secretion of cytokines. This is important as different pathogens require different immune responses. Th cells can be classed into several subtypes, the most prominent being Th1, Th2 and Th17. However, in recent years, additional Th subtypes have been discovered, for example Th9.^{90,92}

Naïve T cells differentiate into Th1 cells through IL-12 secreted by antigen-presenting cells. Th1 cells help in the defense against intracellular bacteria and viruses. They primarily produce interferon (IFN)- γ which activates macrophages and tumor necrosis factor (TNF) which directs cytotoxic CD8⁺ T cell responses. IFN- γ also promotes B cell class switching to induce opsonizing IgG antibody isotypes. Th2 cells promote the clearance of parasitic helminths. Their differentiation is driven by IL-4 expressed by innate immune cells. Th2 cells secrete IL-4, IL-5, and IL-13, which causes B cell class switching to IgE, priming basophils and mast cells for granule release, recruit eosinophils and enhance epithelial mucus production. IL-17 producing, Th17 cells regulate the clearance of extracellular bacteria and fungi and help maintaining commensal populations. IL17 recruits and activates neutrophils. Differentiation into Th17 cells is driven primarily by IL-6 and TGF- β and stabilized through IL-23 and IL-1 β .⁹²⁻⁹⁵

It is of note that the division of Th cells is not clean cut. Recently a great amount of plasticity has been observed between Th cell subtypes. Th cells can transition between subtypes or hybrid cells can express markers of two different subtypes.^{90,95-97}

Regulatory T cells (Tregs), a subset of CD4⁺ T cells characterized by the transcription factor (TF) FoxP3, are crucial for immune tolerance and maintaining

homeostasis. In the intestine the immune system is constantly exposed to various antigens from commensal microbes, dietary components, and potential pathogens. Tregs contain inflammatory immune responses to harmless antigens. They modulate the immune response mostly through expression of anti-inflammatory cytokines such as IL-10 and TGF- β . IL-10, the major effector cytokine of Tregs limits Th cell expansion, promotes ISC renewal, and induces IgA secretion by B cells. In addition, Tregs have been described to have important non-immunological roles as well, such as supporting epithelial barrier integrity and local tissue repair.⁹⁸

B cells, a class of adaptive immune cells, are the producers of antibody molecules and part of the humoral immunity. Humoral immunity plays a critical role in the intestinal tract, not only during infections but also at homeostasis. B cell responses in the gut are initiated in GALTs. In comparison to other tissues, the intestinal lamina propria contains a large number of plasma cells (activated B cells) in homeostasis, with increasing numbers towards both proximal and distal end of the intestinal tract. Plasma cells secrete large quantities of the secretory immunoglobulin isotype IgA, that are transported across the epithelium by polymeric immunoglobulin receptor into the lumen.⁹⁹ IgA in the mucus is an additional layer of defense and prevents commensals from encroaching on the epithelium.¹⁰⁰ While mucosal IgG levels are generally low, IgG is increased and has a protective role during infections.^{101,102}

There are many types of innate immune cells in the intestine. Macrophages and Dendritic cells are mononuclear phagocytes that can take up antigens and present them to cells of the adaptive immune system.

Macrophages are the most abundant leukocyte in the healthy intestinal lamina propria. Their role is to phagocytize and degrade microorganisms that breached the epithelium as well as dead cells. Macrophages secrete large amounts of anti-inflammatory IL-10, which prevents inflammation by blocking pro-inflammatory signals and promotes the survival of Tregs.⁹⁹

Dendritic cells (DCs) operate at the interface of innate and adaptive immunity. They maintain immune tolerance towards commensal, but also prime and polarize the immune responses towards pathogens. DCs in the intestinal lamina propria can sample antigens in different ways. Soluble antigens can reach DCs via transcellular or paracellular transport across the epithelium. Antigen-transporting M cells are an antigen entry site in the follicle-associated epithelium. Goblet cell-associated antigen passages formed by Goblet cells, can transport soluble and particulate antigens. Finally, DCs can also directly sample luminal antigens by extending paracellular trans-epithelial dendrites.¹⁰³

Innate lymphoid cells (ILCs) are often called the innate counterpart to T cells. They lack a T cell receptor but originate from the same common lymphoid progenitor as lymphocytes. Aside from cytotoxic ILCs (NK cells), there are 3 main groups of helper ILCs. Innate sensor cells, such as dendritic cells, macrophages, or epithelial cells, produce distinct cytokines upon sensing MAMPs, that in turn activate different subsets of ILCs.⁹⁵ ILCs act early in the immune response, produce cytokines quicker than T cells, and help polarize the immune response. ILCs are primarily tissue resident.¹⁰⁴

Table 1: Overview of type 1, 2, and 3 immunity and immune tolerance. This list is non exhaustive and the presented immune concepts do not occur in isolation.^{95,105}

<i>Immune function</i>	<i>Inducer cytokine</i>	<i>Innate cells</i>	<i>Adaptive counterpart</i>	<i>Transcription factors</i>	<i>Mediators</i>
Type 1 immunity: Tumors, Intracellular pathogens (bacteria, viruses, parasites)	IL-12, TNF α	ILC1 NK cells	CD4+ Th1 CD8+ CTL	T-bet	IFN- γ
Type 2 immunity: Large extra cellular parasites, Allergens	IL-2, IL-25, IL-33, PGD2, TL1A and TSLP	ILC2	CD4+ Th2	GATA-3, ROR α	IL-4, IL-5, IL-9, IL-13
Type 3 immunity: Extracellular microbes (bacteria, <i>fungi</i>)	IL-23	ILC3, LTi cells	CD4+ Th17	ROR γ T	IL-17 IL-22
Immune tolerance: Microbiota, Dietary antigens	Short-chain fatty acids TGF- β , IL-2	ILC3	CD4+ Tregs	Foxp3	IL-10 TGF- β IL-35

Helper ILCs are divided into three subsets: ILC1s, ILC2s, and ILC3s. The composition of ILCs within the intestinal mucosa is dependent on microbiota and pathogen exposure.⁵ The subsets are defined by the cytokines they secrete and the kind of immunity they promote. ILC1s adaptive counterpart are Th1 cells, like

them, ILC1s play a role in type 1 immunity towards intracellular bacteria and viruses. They express the transcription factor T-bet and can secrete IFN- γ . ILC2s express the transcription factors GATA-3 and ROR α and secrete IL-4, IL-5, and IL-13. They are part of a type 2 immune response, similar to Th2 cells, and help in the clearance of parasitic helminths.¹⁰⁶ Lastly, ILC3s express the transcription factor ROR γ T and secrete IL-17 and IL-22. They are involved in the defense against bacteria and fungi and are, like Th17 cells, part of type 3 immunity.^{95,107,108}

Table 1 lists the different immune functions, adaptive T cell counterparts, respective stimuli, transcription factors and cytokines of ILCs. The general concepts of type 1, type 2, and type 3 immunity are detailed in the following section.

1.5.3 Immune responses in the intestine

All parts of the mucosal immune system work together during an immune response. Broadly, the immune response can be classified into three categories depending on the cell types and cytokines involved: type 1, type 2 and type 3 immunity. Each is specific towards different types of immunogenic agent. Their dysregulation can also lead to different diseases.¹⁰⁹

Type 1 immune response, also called Th1 immune response, is primarily involved in protecting against intracellular pathogens, such as viruses and intracellular bacteria, as well as against tumor cells. This type of immune response is characterized by activation of Th1 cells, ILC1 cells, CD8+ cytotoxic T cells and NK cells. Th1 cells release the cytokines interferon-gamma (IFN- γ) and tumor necrosis factor-alpha (TNF- α), which activate macrophages and other immune cells to eliminate the infected cells and limit the spread of the pathogen. Dysregulation of type 1 immunity in the intestine is responsible for autoimmune diseases like IBD.^{91,94,95,109}

Type 2 immune response, or Th2 immunity, is responsible for defending the body against extracellular parasites, such as helminth. The response is mediated by the activation of Th2 cells, which release the cytokines IL-4, IL-5, and IL-13. These cytokines stimulate B cells to produce antibodies, particularly IgE, which opsonizes the pathogen and recruit eosinophils, mast cells and basophils to eliminate it. Type 2 immunity is also associated with allergic reactions, as excessive activation of type 2 response leads to inflammation and tissue damage.^{19,95,109}

Type 3 immune responses, also called Th17 immunity, is crucial in defending the body against extracellular bacteria and fungi. The immune response is started by the activation of Th17 cells, which produce cytokines like IL-17, IL-22 and IL-23. These cytokines stimulate the production of AMPs and recruit neutrophils to

the site of infection, promoting the clearance of the pathogens. Dysregulation of type 3 immunity can contribute to the development of autoimmune diseases and chronic inflammatory conditions.^{72,94,95,109}

Immune tolerance to food and commensal microbes is important in maintaining intestinal homeostasis. Central players in regulating immune tolerance are FoxP3⁺ Tregs, loss of them results in systemic autoimmunity. DCs induce Tregs by presenting antigens, their pro-regulatory and anti-inflammatory behavior is supported by factors including SCFAs from commensal bacteria, prostaglandin E2 produced by stromal cells, TSLP produced by epithelial cells, and IL-10 from macrophages and Tregs. Aside from IL-10, Tregs also express TGF- β , both anti-inflammatory cytokines further induce DCs towards a tolerogenic phenotype and suppress immune responses.^{5,91}

While I presented the types of immune responses as separate entities, the reality is not quite as clean cut. The types of immunity are not mutually exclusive. Just like Th cells can transition between and express markers of two different subtypes, aspects of more than one type of immunity can be present during an immune response and shift from one to another. Dysregulation of an immune response can lead to damage and chronic inflammation, while the wrong type of immune response or downregulation of an immune response can prevent clearance of a pathogen resulting in chronic infections.⁹⁵ In this thesis different mouse models were employed to study the different types of immune responses. The different models and their limitations will be presented in the following.

1.6 Experimental models

1.6.1 GI tract in humans and mice – understanding similarities and differences

While the goal of our research is understanding more about the intestine and its diseases to ultimately help humans, most of the research in this thesis is carried out in mice or using mouse cells. In order to translate this research to human conditions, we have to consider the similarities and differences between the human and mouse intestinal tract. Overall mammalian gastrointestinal tract anatomy is strongly conserved, there are however differences that reflect the differences in diets, feeding patterns, body sizes and metabolic requirements of the species.^{110,111}

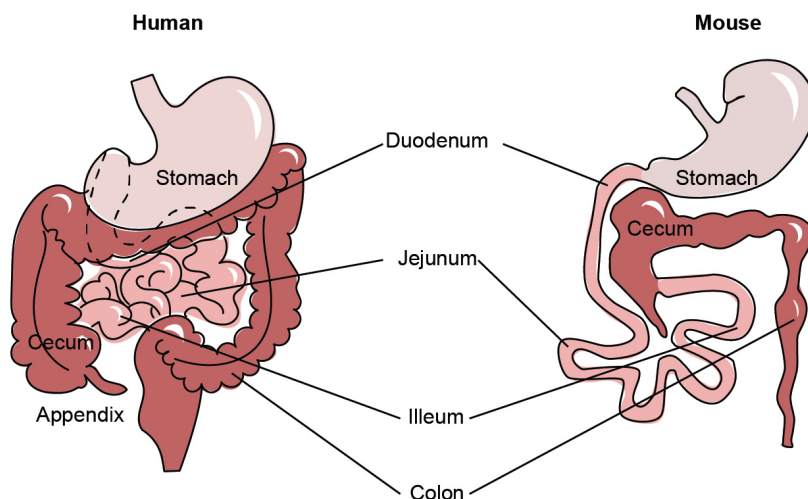


Figure 6: Human and mouse GI tract anatomy. The overall anatomy of the GI tract is the same between mice and humans, but there are some differences in morphology and relative size of distinct parts. Stomach (light pink), small intestine (pink) and large intestine (red). Schematic representation, not to scale. This figure is adapted from Nishiyama, et al.¹¹²

The overall anatomy of the intestines and the composition gut wall (see Figure 1) is the same between mice and humans, but there are some differences in morphology and relative size of distinct parts (Figure 6). In humans the surface ratio of small intestine:colon is 400 compared to 18 in mouse. Mouse villi are taller compared to human ones, thereby increasing the surface area of the small intestine. This might be compensating for the missing mucosal folds in the small intestine of mice. In mice a large cecum is the site of plant material fermentation and production of vitamins K and B, whereas in humans the cecum does not have a clear function and is much smaller relative to the size of the total GI tract. This expanded colon and cecum space is very likely due to the high content of indigestible fiber in the mouse diet.¹¹⁰ In addition, humans have an appendix that is attached to the cecum, it could just be a remnant of evolution, but might function as a repository for beneficial bacteria.¹¹³

There is also some microscopical differences in the structure of the epithelium. While the cell types in the intestinal epithelium are the same in both species, the distribution of goblet cells and Paneth cells are different. In humans, goblet cells are equally distributed from cecum to rectum, while in mice their numbers at the base of the crypt decrease towards the proximal end of the colon. In mice Paneth cells are only present in the small intestine, whereas in humans they can be found in the cecum and proximal colon as well.¹¹⁰

While there is some overlap in bacterial species, the overall composition of the microbiome is considerably different between mice and humans.¹¹¹

1.6.2 Modeling mucosal immunity to pathogenic bacteria with *Citrobacter rodentium*

Diarrheal diseases are the second leading cause of death in children under 5, accounting for 525 000 deaths every year. They are often caused by enteric bacteria that can be pathobionts (potentially harmful commensal organisms), opportunistic or primary pathogens. Infections are spread over contaminated drinking water or food and poor hygiene conditions. One of the leading pathogens causing diarrheal disease is *Salmonella spp.* a primary intestinal pathogen.¹¹⁴ *Escherichia coli* is a gram-negative bacterium that is part of the normal mammalian intestinal flora, most strains are harmless, but some can cause severe disease, like enteropathogenic *E. coli* (EPEC) and enterohaemorrhagic *E. coli* (EHEC).^{115,116}

The mouse model *Citrobacter rodentium* is a common model used to investigate human intestinal diseases, not only as a model for type 3 gram-negative bacterial infections like EPEC and EHEC, but also Crohn's disease, ulcerative colitis and colon tumorigenesis.¹¹⁶

In C57BL/6 mice, *C. rodentium* infection causes relatively mild self-limiting disease. The course of infection can be divided into four phases. After inoculation via oral gavage, *C. rodentium* colonizes the cecal lymphoid patch. About 4 days post infection (DPI), the expansion phase begins, where *C. rodentium* attaches to the intestinal epithelium in the distal colon and can even colonize the apex of the crypt. There *C. rodentium* begins to express virulence factors and proliferate rapidly. At about 8 DPI the infection enters a steady state. Pathogen shedding plateaus at around 10^8 - 10^9 colony forming units (CFUs) per gram fecal matter. Last is the clearance phase which starts at around 12 DPI. The host starts to clear the infection and bacterial shedding goes down.¹¹⁶

During early infection dendritic cells secrete IL-23, inducing type 3 innate lymphoid cells (ILC3s) to secrete IL-22 and IL-17. IL-22 induces IECs to secrete AMPs like REG3 β and REG3 γ . In the steady-state phase, tissue neutrophils also contribute to the IL-22 response. Clearance of *C. rodentium* is mediated through opsonization by IgG and engulfment by phagocytes. Th1 and Th17 cells secrete IL-22, IL-21, IFN- γ and IL-17. An over proliferation of transit amplifying cells causes crypt hyperplasia. The remaining bacteria in the lumen are then outcompeted by resident commensals.^{72,117,118} Figure 7 depicts the induction of the type 3 immune response during *C. rodentium* infection.

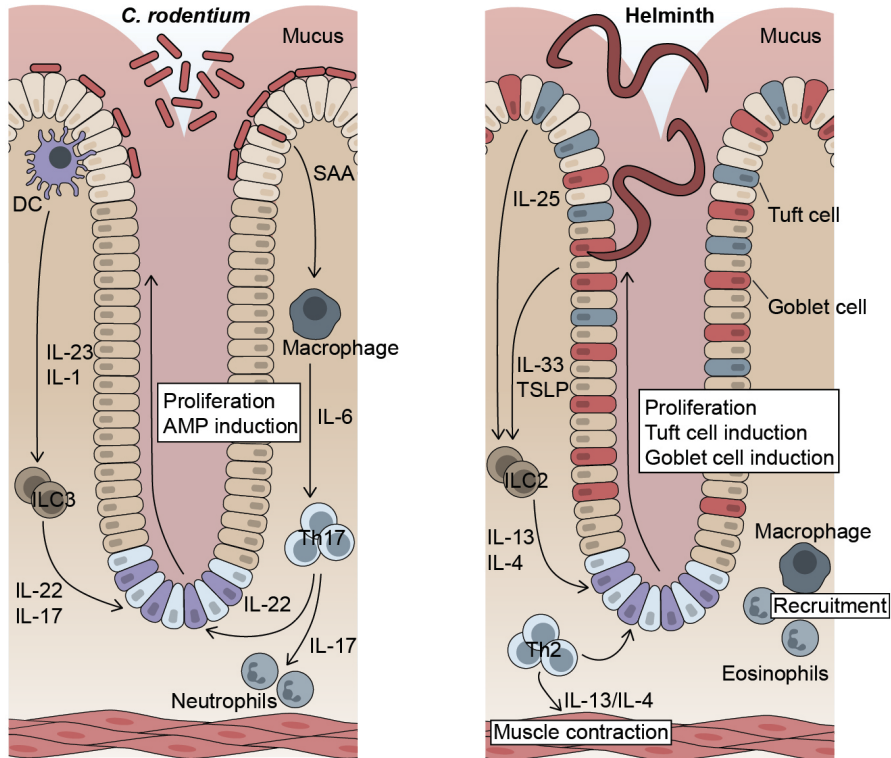


Figure 7: Colon mucosa immune responses to bacterial and parasitic infections. Left: Induction of type 3 immunity during *C. rodentium* infection. DCs secrete IL-23 and IL-1, inducing ILC3s to secrete proinflammatory IL-22 which induces the epithelium to secrete AMPs. Attachment of bacteria to enterocytes induces epithelial proliferation and upregulates production of serum amyloid A (SAA). SAA induces the production of IL-6 by macrophages and in turn expansion of Th17 cells and IL-17 production, which helps recruit neutrophils.^{117,118} Right: Induction of a protective type 2 immune response during helminth infection. The epithelium makes the first contact with the parasite, tuft cells detect the presence of helminth and release IL-25 and leukotrienes. Damage to the epithelial layer induces the release of alarmins, like IL-33 and TSLP. This activates innate effector cells, including ILC2s and induces production of IL-13, IL-4, and IL-5, inducing a type 2 immune response. ILC-2-derived cytokines induce various downstream effects, including activation of DCs that activate Th2 cells, recruitment of eosinophils, activation of macrophages, and inducing smooth-muscle hypercontractility. IL-13 and IL-4 have a direct effect on the epithelium causing increased proliferation and promotes tuft cell and goblet cell differentiation. Goblet cells will produced increased amounts of mucus and AMPs like RELM- β .¹¹⁹⁻¹²¹ Epithelial cell types are labeled the same as in Figure 2.

1.6.3 Modeling mucosal immunity to parasitic infections with *Trichuris muris* and *Nippostrongylus brasiliensis*

Infections with soil-transmitted helminths are among the most common infections worldwide. The main three types are roundworms (*Ascaris lumbricoides*), whipworms (*Trichuris trichiura*) and hookworms (*Necator*

americanus and *Ancylostoma duodenale*). An estimated 24% of the world population are affected, often in tropical or subtropical areas with poor access to clean water, sanitation, and hygiene. The morbidity of worm infections is related to the species and the intensity of infection (number of worms). This can range from no apparent symptoms to diarrhea, abdominal pain, malnutrition, and weakness. In children, helminths infections can cause impaired growth and physical development.^{122,123}

Recent research interest has been focused on how chronic helminth infections can influence pathogenesis of other diseases and infections. Infections with helminths appear to worsen the damage caused by other diseases, e.g. sexually transmitted viral infections like herpes simplex virus 2 or human papillomavirus, by inducing a type 2 immune profile in the female genital tract.¹²⁴

The general response that leads to the expulsion of intestinal parasitic worms is called a “weep and sweep” response induced by a type 2 immune response. This response includes three main mechanisms: increased epithelial cell turnover, increased mucin production by goblet cells and muscle hypercontractility.¹²⁰ The induction of a type 2 response towards helminths is depicted in Figure 7.

There are several established mouse models to study parasitic helminth infections. There are generally a lot of similarities in the immune responses to parasitic helminths, but there are some differences between different worm species depending on the infection cycle and virulence factors of the parasite. This thesis utilizes two different models. *Trichuris muris* is a mouse model for human whip worm infections, similar to *T. trichiura* in humans. While *Nippostrongylus brasiliensis* is a murine model for human hookworms, mimicking *N. americanus* infection in humans. Both of which will be explained in more detail.¹²⁵

When using models of parasite infections there are a few limitations to consider. The main differences between human infections and most laboratory models are the route of host entry and the infection dose. In endemic areas, constant low levels of parasites and re-infection are common, whereas in many experimental models a single high dose is administered.^{120,126}

T. muris infection occurs through ingestion of infective eggs that accumulate in the cecum, where the first larvae (L1) hatch after about 90 min. The hatching is induced by commensal bacteria. After hatching, L1 penetrate the wall of the cecum and proximal colon and remain in the epithelial layer for 3 more molts (L2-L4), until about 22 DPI. While the anterior end of the worm remains buried in the epithelium, the posterior end will stick out into the lumen. By day 32 DPI adult worms can be observed in the cecum and proximal colon and produce eggs that

leave the host with the feces. Those eggs need 2 months to embryonate before they become infective.¹²⁷

The type of immune response that is mounted upon *T. muris* infection can determine susceptibility or resistance. Generally, the development of a type 2 response is associated with resistance and worm clearance, whereas a type 1 response is linked to the establishment of a chronic infection. Susceptibility of mice against *T. muris* depends on the mouse strain, gender, infection dose and *T. muris* strain. For example, males are more susceptible to the infection than females. C57BL/6 mice are generally resistant to a high dose infection (around 400 eggs) of *T. muris* but develop a chronic infection upon low dose infection (less than 40 eggs). Due to this dose dependency, *T. muris* can be used to study both type 1 and type 2 immunity.^{128,129} Both innate and adaptive immune response work together to form a protective response against *T. muris*.¹³⁰

N. brasiliensis has a more complex life cycle when compared to *T. muris*, involving free-living and tissue migratory parasitic stages. *N. brasiliensis* larvae first hatch in soil and moult twice until they reach their infective stage. The infective L3 larvae penetrate the skin of the host and are carried through the blood stream to the airways. There they exit from the alveolar capillaries and crawl up the bronchial tree to reach the pharynx. From there *N. brasiliensis* larvae are subsequently swallowed and establish themselves in the small intestine. In contrast to *T. muris*, *N. brasiliensis* does not bury into the epithelium but resides in the intestinal lumen.¹²⁵ In experimental settings L3 larvae are often injected subcutaneously, to ensure infection.¹³¹ Most mouse strains are resistant to *N. brasiliensis* infection and clear the parasite after mounting a type 2 response.¹³²

1.6.4 DSS-induced colitis

Since its introduction in 1990 by Isao Okayasu¹³³, dextran sodium sulfate (DSS)-induced colitis has become the most extensively studied and most widely used model of chemical-induced colitis. The model is relatively simple and closely resembles human ulcerative colitis pathology. The DSS treatment causes erosion of the intestinal epithelium, inflammatory infiltration (neutrophils and macrophages), and dysbiosis of the intestinal microbiome (Figure 8). The inflammatory response in DSS-induced colitis is characterized by the expression of the cytokines TNF- α , IL-6, and IL-1 β and leads to increased intestinal permeability, goblet cell depletion, and increased adhesion of commensal microbes to the epithelium. While the exact mechanism via which DSS causes colitis is not fully understood, it is thought that DSS and medium-chain-length fatty acids in the colon form nano-lipid vesicles that fuse with the membranes of colonic epithelial cells. These nano-complexes in the cytoplasm could then activate intestinal inflammatory signaling pathways.¹³⁴⁻¹³⁶

For an acute colitis model with spontaneous recovery, DSS is orally administered via the drinking water for 4-7 days (5 days in the experiments included in this thesis), followed by several days of recovery with normal drinking water.^{137,138} The DSS-treated mice lose weight and develop diarrhea, rectal bleeding, and intestinal epithelial ulcers. For modeling chronic colitis, DSS has to be given in multiple cycles.¹³⁵

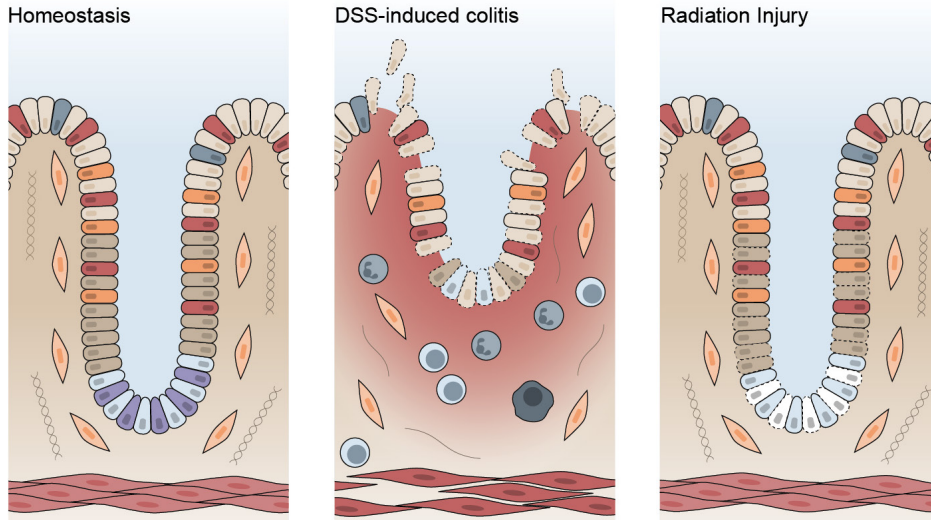


Figure 8: Epithelial injury models. Comparison of epithelial injury in acute DSS-induced colitis and radiation injury. DSS-treatment leads to epithelial damage with loss of ISCs, induction of an immune response with infiltration of immune cells. Radiation induces loss of LGR5+ ISCs and proliferating cells. Cell types are labeled the same as in Figure 2. Dotted cell borders indicate damaged/dying cells.

1.6.5 Radiation induced injury model

In contrast to DSS-induced colitis that involves the activation of immune cells and release of pro-inflammatory cytokines, radiation-induced injury does not trigger an inflammatory response. Radiation induced injury is primarily driven by DNA-damage and subsequent apoptosis. This makes it possible to study the epithelial response to damage and ISC-loss separate from inflammation. To induce intestinal epithelial injury in mice, γ -radiation doses of 8-15 Gy are necessary. Proliferating cells, like *Lgr5*+ stem cells and transit amplifying cells, are highly susceptible to ionizing radiation. The regenerative responses of the epithelium include an apoptotic phase, where the epithelium undergoes severe crypt loss and crypt shrinkage. After two to four days the proliferative phase begins: the few surviving ISCs start to proliferate while other cell types help replenish the ISCs through dedifferentiation (See chapter 1.3.4). Finally, in the normalization phase, crypt and villi length is restored to pre-radiation state.^{29,139}

1.6.6 Apc^{Min} mouse model

The Apc^{Min} mouse model is a well-established model for studying the development and progression of colorectal cancer.¹⁴⁰ The mice carry one copy of a mutated Adenomatous polyposis coli (APC) gene, a tumor suppressor with a crucial role in regulating the Wnt pathway, resulting in an increased Wnt pathway activation, that leads to epithelial tumor formation. Those heterozygous Apc^{Min} mice spontaneously develop polyp adenomas mainly in the small intestine through loss of heterozygosity.¹⁴¹

1.6.7 Intestinal organoids

Organoid technology has exploded in the last 10 years. Many different culture systems for several types of organs have been established. Organoids are described as a 3D structure grown from stem cells, that consist of organ-specific cell types that self-organize through cell sorting and spatially restricted lineage commitment. Organoids can be grown from two types of stem cells: 1. pluripotent embryonic stem cells and 2. organ-restricted adult-stem cells.¹⁴²

Various different organoid models can be established from pluripotent stem cells, each requiring a precise differentiation protocol. So far stomach, intestinal, lung, thyroid, liver, kidney, hippocampal, optic cup and cerebral organoids have been established. Certain organs also allow organoids to be grown from their adult stem cells. This is done by mimicking the conditions in stem cell niche during either homeostasis for fast-renewing tissues or otherwise during damage repair. Organoids derived from adult stem cells have been established among others for lung, small and large intestine, stomach, liver, pancreas, fallopian tubes and spleen. The necessary factors can be added as recombinant proteins or provided by feeder cell lines.^{142,143}

Organoids have many potential applications. They can be cultured long term similar to traditional cell culture, while providing a closer to *in vivo* view with the interplay of different cell types in a tissue. This allows the in-depth study of infectious diseases, hereditary diseases, toxicology, and cancer. Organoids are also a great tool for personalized medicine: Cells from a patient can be grown into organoids and treatment options can be tested and refined without subjecting the patient to side effects of ineffective treatments. This could also help minimize treatment costs. Finally, organoids can be a tool for regenerative medicine and gene therapy, where modified organoids can be grown and later transplanted into a patient.^{142,144,145}

Aside from those benefits for patients, using organoids for pharmacological tests and toxicology studies can help reduce the number of animals needed for experiments, making it a more ethical research approach. Organoids can be easily

expanded and therefore high throughput screenings with fast read-out can streamline research. Lastly, organoids give an isolated view of a tissue, this makes for a very controlled environment that can help in understanding the individual roles of certain cells in a tissue.¹⁴⁶ One of the first organoid models that was established from adult stem cells are intestinal, epithelial organoids, first reported by Sato et al. in 2009.¹⁴⁷

Intestinal epithelial organoids can be grown from LGR5+ stem cells, sitting at the bottom of the crypt of the SI and large intestine. SI organoids are grown in a 3D protein matrix, like Matrigel™, and need EGF, Noggin and RSPO added to the culture medium in order to maintain the stem cells and grow. This combination mimics the conditions in the intestinal stem cell niche, where most factors are provided by mesenchymal cells sitting below the epithelium. While in SI organoids, Wnt is produced by Paneth cells that intersperse the stem cells, colon epithelial organoids (colonoids) need external Wnt (in the form of WNT3a) added to the culture medium in order to thrive. The mentioned conditions apply to mouse organoids, as human intestinal organoids require some additional factors.^{147,148}

Intestinal organoids are great tools to study tissue homeostasis, cell-to-cell interactions, differentiation, and physiology, but there are some short comings compared to *in vivo* models that have to be considered. While intestinal organoids are comprised of all the different cell types that make up the intestinal epithelium, they only contain epithelial cell types (Figure 9). They lack other cells that are present in the intestine, like various mesenchymal cell types, vasculature and neurons, as well as immune cells and intestinal microbiota in the intestinal lumen. To mitigate those shortcomings of the organoid culture model, several groups have employed co-culture models to study interactions with specific cells or pathogens and the intestinal epithelium. As intestinal organoids form lumen-enclosed structures, access to the absorptive side of the epithelium is limited. This also leads to an accumulation of apoptotic cells inside the organoids, which is profoundly different *in vivo* where microbiota break down and feed on the shed cells and luminal contents are moving through the intestine constantly. Monolayer cultures are a way to have an accessible apical side of the epithelium, as well as organ-on-chip technology that allows for added perfusion of the tissue. Matrigel™, that is often used for intestinal organoid culture has a highly complex composition. Composition changes between batches and percentage of Matrigel™ used, change the mechanical properties of the matrix and have been shown to impact organoid growth. Recent studies have been working on more controlled substrate matrixes that could replace Matrigel™ in organoid culture applications.¹⁴⁹

In conclusion, organoids are a great model for studying the intestinal epithelium in a quick, cheaper, scalable, and more ethical way compared to *in vivo* models, like mice. It is, however, important to keep in mind the simplified nature of the model.

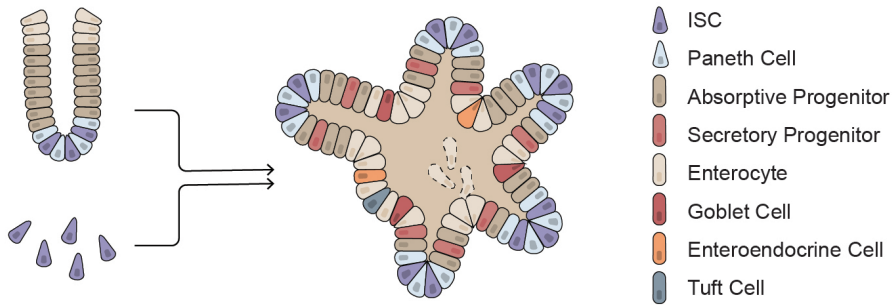


Figure 9: Generation and growth of intestinal organoids. Intestinal crypts or isolated ISCs can be grown into intestinal organoids. Differentiated intestinal organoids form crypts and contain most cell types of the intestinal epithelium.

2 Aim of this work

1. Investigate the role of the intestinal smooth muscle, and muscle-derived MMP17, in the context of the intestinal epithelial niche and epithelial repair.
2. Determine the role of MMP17 on the intestinal epithelial homeostasis and during immunity to intestinal bacterial and helminth infections.
3. Compare the effect of cytokines, related to different types of immune responses, on intestinal epithelial differentiation and gene expression patterns.

3 Summary of Papers

1. Smooth muscle-specific MMP17 (MT4-MMP) regulates the intestinal stem cell niche and regeneration after damage

This paper discusses the previously underappreciated role of the intestinal smooth muscle as part of the ISCs niche and highlights the role of MMP17 in epithelial repair after injury. One major finding is that smooth muscle cells, particularly those residing in the muscularis mucosa, are the primary source of BMP antagonists, like GREM1/2 and CHRDL1, which are crucial for ISC homeostasis. Further this paper stresses the important role of smooth muscle derived-MMP17 *in vivo*. *Mmp17* KO mice show a reduction of ISC associated genes in homeostasis, potentially due to increased levels of SMAD4 signaling in the crypts. MMP17 KO mice also show an impaired epithelial repair response to chemical and radiation injury and increased tumor formation. Periostin (POSTN) is a matricellular protein that is cleaved by MMP17 and induces repair-like features in the intestinal epithelium. The lack of cleaved POSTN in the intestinal epithelium could be the cause for the impaired regeneration capabilities of the intestinal epithelium.

2. BMP signaling in the intestinal epithelium drives a critical feedback loop to restrain IL-13-driven tuft cell hyperplasia

This study explores how different types of immune responses drive changes in the composition and expression of the intestinal epithelium, utilizing both organoid and mouse models. SI organoid cultures with IL-22 and IL-13 suggest that while both cytokines induce goblet cells, they induce different goblet cell gene signatures. While IL-13 induced goblet cells through classical Notch signaling, IL-22 uses an alternative route. Another focus of the study is on tuft cells that are regulators in intestinal health and play a critical role in the defense against parasitic helminths. IL-13 is known for inducing tuft cell expansion in the intestinal epithelium, but, as this paper presents, IL-13 also induces BMP signaling in the epithelium. The induction of BMP signaling acts as a brake on IL-13-induced tuft cell expansion, creating a negative feedback loop that limits further tuft cell expansion.

3. *Mmp17*-deficient mice exhibit heightened goblet cell effector expression in the colon and increased resistance to chronic *Trichuris muris* infection

The third paper in this thesis focuses on alterations in goblet cell expression within colon epithelium of *Mmp17* KO mice. We observed a significant upregulation in goblet cell effector genes, including *Ang4*, *Retnlb*, and *Cc1a1*, which are typically associated with immune responses to infections. We established that this

upregulation of goblet cell effectors is not a consequence of cytokines activity. *Mmp17* KO mice displayed no altered resistance to a bacterial *C. rodentium* infection. However, when these mice were challenged with a low dose of *T. muris*, we observed increased resistance. Our investigations did not identify an altered immune response as the cause for this improved clearance, suggesting that it might instead stem from changes in goblet cell effectors. Lastly, we detected elevated BMP signaling within colon crypts of *Mmp17* KO mice, which we propose to alter the goblet cell maturation state.

4 Discussion

In the introduction, I presented the remarkable and complex composition of the intestinal tract, including how various tissues and cell types, each with unique functions, collaborate to maintain the delicate balance of intestinal homeostasis. Studying intestinal homeostasis and its response to insults is vital for understanding and improving intestinal health, as it plays an essential role in maintaining barrier function, facilitating nutrient absorption, and coordinating immune responses. Disruptions to the intestinal epithelial layer can result in various gastrointestinal disorders such as IBD, infections, and cancer. Therefore, investigating the mechanisms and cell types that regulate the intestinal epithelium can assist in the development of targeted therapies.

In this thesis, I present the role of the smooth muscle as an integral component of the ISCs niche. I discuss the role of the smooth muscle-derived matrix metalloproteinase MMP17 as a regulator of intestinal homeostasis, impacting the ISCs niche and epithelial response to injury and infections. Goblet cell effectors, as an important part of innate immunity will also be a major discussion point. A spotlight will be put on the role of BMP signaling in regulating the composition and expression of the intestinal epithelium. Finally, I will put the results into context by considering the translatability of the findings.

4.1 Intestinal smooth muscle tissue: A novel source of niche factors in the ISC niche

Mesenchymal cells have only quite recently become recognized as an important component of the ISC niche. Particular attention has been given to mesenchymal stromal cell populations, including fibroblasts and telocytes, which supply niche factors like Wnts, BMPs and BMP antagonists.^{41,150} On the other hand, intestinal smooth muscle tissue has been predominantly regarded as a source of gut motility and producer of ECM molecules, and less as part of the ISC niche. This thesis introduces the intestinal smooth muscle as a source of niche factors such as the BMP antagonists *Grem1*, *Grem2* and *Chrdl1* (Paper 1, Figure 1b). Although these factors are expressed throughout the entire colon muscle, our primary focus was the expression of BMP antagonists in the muscularis mucosa, due to its location right beneath the epithelial layer (Paper 1, Figure 1c). BMP antagonists are essential at the bottom of the intestinal crypts to maintain ISCs, the close proximity of the BMP antagonist expressing smooth muscle tissue makes it likely to play a part in ISC niche regulation.

Organoid experiments further supported the role of the intestinal smooth muscle as BMP antagonist producers. Supernatant from intestinal smooth muscle explants demonstrated the potential to replace Noggin, a BMP antagonist, in SI organoid culture (Paper 1, Figure 1d,e). In these experiments, we also observed the induction of a reparative or fetal-like state by both WT and *Mmp17* KO intestinal smooth muscle explant supernatants, characterized by YAP signaling (Paper 1, Figure 7a-d). The organoids maintained a round (spheroid) morphology even after four days of culture, when control organoids had already formed crypts. Since BMP antagonists are presumably not mediating this phenotype, other factors produced by the intestinal smooth muscle must contribute to this phenotype (Paper 1, Figure 1d-g).

In this context, it is essential to address some limitations associated with the use of intestinal smooth muscle explant supernatant in organoid experiments. The muscle was separated from the mucosa by scraping it with a thin glass. Through IF staining, we verified that this technique effectively separates the colon tissue between the muscularis mucosae and the muscularis propria, leaving no epithelial cells attached to the muscularis propria (Paper 1, Figure S1). However, this method did not remove cells of the serosa or other non-smooth muscle cells that are interspersed in the within the smooth muscle tissue, such as enteric neurons, glial cells, immune cells, and various classes of interstitial cells.¹⁵¹ Consequently, the explants are not purely composed of smooth muscle cells. This issue could be addressed by isolating smooth muscle cells, and other interstitial cells based on marker expression separation, culturing them, and using the resulting culture supernatant in experiments. The extraction method might introduce an additional caveat, as the rough separation of the tissue could trigger an injury response that leads to the expression of factors that are not naturally present during homeostasis. In addition, the method used did not allow for potency control, due to the absence of an exact tissue-to-medium ratio. This results in significant batch-to-batch variations in potency, impacting the detection of subtle differences when using muscle from WT and KO animals. A normalization to muscle tissue weight could serve as a first starting point to approach this issue.

This research contributes to the rising research interest in mesenchymal populations and the role of the smooth muscle in intestinal niche in development, homeostasis and disease.^{31,36,42,152} For instance, McCarthy *et al.* highlight the importance of smooth muscle cells in the muscularis mucosa as a source of niche factors during maturation of the intestinal epithelium post-birth. It is becoming increasingly evident that niche cell populations show redundancy in expressing niche factors, and some may be dispensable during homeostasis. The presence of multiple sources of niche factors could enable more fine-tuned regulation, allowing the tissue to respond effectively to a variety of challenges.³⁶

4.2 MMP17: A key regulator of ISC niche and epithelial repair processes via ECM modulation

Aside from producing niche factors, the smooth muscle also functions as a source of ECM molecules and ECM regulators. The ECM helps form the physical and humoral niche of the intestinal crypt. One potential ECM regulator produced by the smooth muscle is Matrix metalloproteinase MMP17. In the intestine, *Mmp17* expression is almost exclusive to smooth muscle cells, with the expression pattern resembling that of BMP antagonists in the intestinal smooth muscle and enriched in the muscularis mucosae (Paper 1, Figure 2a-d). Low expression levels were also detected in PDGFR α + mesenchymal stromal cell populations located in the lamina propria near the crypt opening (Paper 3, Figure 7b). This data relies on the presence of a LacZ reporter gene in the *Mmp17* KO mouse model used in our studies, making it difficult to draw conclusions on the biological significance of these low expression levels of MMP17 in this cell population.

Examining changes in expression in the intestine of *Mmp17* KO mice, we discovered that the gene expression of intestinal smooth muscle tissue was only mildly affected by the loss of *Mmp17*, with a mere 42 genes differentially expressed. In contrast, the epithelial gene expression, where *Mmp17* is not expressed, was significantly different, with 191 genes dysregulated in the KO crypts compared to WT crypts (Paper 1, Figure 3a,b). This indicates that the loss of *Mmp17* expression heavily affects the epithelium. One notable difference in the KO epithelium is the upregulation of genes related to SMAD4 signaling. In the *Mmp17* KO mice, we observed elevated pSMAD4 and pSMAD1/5/9 levels, suggesting increased BMP signaling (Paper 1, Figure 3c-f). The rise in BMP signaling in the intestinal epithelium could account for some of the phenotypic changes detected in the KO intestine. The KO epithelium displayed reduced levels of the ISC markers *Lgr5* and *Olfm4*, and organoid formation efficiency was reduced in crypts isolated from KO mice. After splitting and culture, this difference disappeared, indicating that the loss of *Mmp17* *in vivo* alters the ISC niche (Paper 1, Figure 4a-d). As increased BMP signaling is detrimental for stem cell maintenance, the heightened BMP activity could explain the reduced number of ISCs.¹⁵³

Elevated levels of active BMP signaling can be caused by several factors, such as increased BMP (expression and/or bioavailability), reduced BMP antagonists (expression and/or bioavailability), or a change in available receptors on the cell surface. To determine the cause of increased BMP signaling, we looked for changes in BMPs, BMP inhibitors, and BMP receptors in the intestine (data not shown). Interestingly, no changes were found in any of the proteins assessed,

suggesting that the changes could be due to changes in bioavailability of those molecules. This could be due to binding, cleavage, or degradation.

MMP17 is a membrane-bound enzyme, suggesting it can only directly affect the pericellular space, the immediate area surrounding a cell. The pericellular space is filled with ECM molecules. Consequently, a direct effect of MMP17 on epithelial cells is unlikely. MMPs are known regulators of the ECM and ECM-associated molecules, such as growth factors. ECM molecules can bind growth factors or have growth factor-like sequences. Proteases like MMP17 can release those growth factors and thereby make them bioavailable. Although MMP17 has been found to exhibit low activity in cleaving classical ECM molecules, it is plausible that the changes in epithelial expression are due to MMP17's role as a modulator of ECM or ECM associated proteins. This is highlighted by decellularization experiments, wherein organoids were seeded on decellularized SI ECM from KO and WT mice. *De novo* crypt formation, referring to the implanting of the organoids onto the ECM, was significantly higher for WT ECM (Paper 2, Figure 4e-g). However, this could be rescued by adding smooth muscle supernatant from WT muscle or recombinant MMP17 to the culture medium, solidifying MMP17 as a regulator of the ECM and the intestinal niche (Paper 2, Figure 7 e).

De novo crypt formation plays an essential role in epithelial repair after injury and ISC loss.¹⁵⁴ Not only was the KO ECM not able to support *de novo* crypt formation *in vitro*, but *in vivo* intestinal repair was also impaired. In both an inflammatory (DSS-induced colitis) and a non-inflammatory (radiation) injury model, KO mice exhibited reparative epithelial defects, displaying more damage and weaker reparative responses (Paper 1, Figure 5a-l, Figure 6a-h). It is worth noting, that *C. rodentium* infection (a mouse infection model that causes mild colitis) does not show impaired regeneration (Paper 3, Figure 3), although this could be due to the mild level of damage caused during the infection. The increase in epithelial proliferation during infection was not affected by loss of MMP17 (Paper 3, Figure 3d,e). Additionally, *Mmp17* loss resulted in increased tumor risk. Combining the *Mmp17* KO with the *Apc*^{Min} tumor model led to the formation of a higher number of tumors compared to *Mmp17* WT *Apc*^{Min} mice (Paper 1, Figure 6i,j). Previous studies showed a correlation of MMP17 tumor expression with poor prognosis. In our case, the presence of MMP17 in the stroma seems to be protective.^{69,155-158} This indicates that the roles of MMP17 are diverse and context-dependent, as it seems to can either promote tumor progression or act preventative depending on which cell type it is expressed in.⁶⁸

As mentioned in the previous section, muscle supernatant was able to induce a reparative state in organoids. The muscle must, therefore, produce a factor that

induces this state. Mass spectrometry of muscle supernatant revealed that periostin (POSTN), a matricellular protein, is present in the muscle supernatant and is highly expressed in the intestinal smooth muscle (Paper 1, Figure 8a,b). POSTN has been reported to be a ligand for ITAGAV that activates AKT and YAP signaling.¹⁵⁹⁻¹⁶¹ Additionally, POSTN has been proposed to bind BMPs in the ECM.¹⁶² This makes POSTN a likely candidate to be involved in the ISC niche and repair processes. Indeed, POSTN was cleaved by MMP17 into several fragments *in vitro* (Paper 1, Figure 8c,e,f), and these fragments could be found *in vivo* in WT tissue while being significantly reduced in KO tissue (Paper 1, Figure 8d).

These results demonstrate that *Mmp17* loss alters the intestinal ECM in a way that impacts the intestinal niche, reducing stem cell numbers, impairing repair processes after injury and promoting tumorigenesis. We propose that MMP17's molecular mechanisms of action include influencing BMP signaling in homeostasis as well as during intestinal repair processes after damage, and cleaving POSTN.

4.3 Increased goblet cell-associated gene expression in *Mmp17* KO mice is not cytokine dependent

In addition to the observed increase in SMAD4 signaling-associated genes, we detected an upregulation of goblet cell-associated genes including *Ang4*, *Clca1*, *Retnlb*, and to a lesser extent *Muc2*, in the KO colon epithelium. These upregulated genes, primarily associated with mucus and anti-microbial functions, will be referred to as goblet cell effectors in this text. These goblet cell effectors are known to increase during intestinal infection, as they are induced by type 2 and/or type 3 cytokines, like IL-13 and IL-22, respectively.^{82,85,131}

In Paper 2, experiments using SI organoids treated with IL-13 or IL-22 revealed distinct goblet cell expression patterns (Paper 2, Figure 2b). For instance, *Clca1* and *Muc2* were only induced by IL-13, whereas *Retnlb* was induced by both, but more strongly by IL-22 (Paper 2, Figure c-g). Additionally, these organoid experiments demonstrated that IL-22 and IL-13 induce goblet cells through different mechanisms. While IL-13 appears to induce goblet cells classically via Notch signaling inhibition, relying on the transcription factors *Atoh1* and *Spdef*, IL-22 did not induce these transcription factors. In fact, although IL-22 altered the expression pattern of goblet cells, it did not lead to an increase in goblet cell numbers (Paper 2, Figure 2h), as previously shown in other organoid studies.¹⁶³

However, looking at the *Mmp17* KO mouse model, we did not observe increased levels of IL-13 or IL-22 in the intestinal tissue or altered immune cell polarization in lymphocytes from colon-draining mesenteric lymph nodes. Thus, the observed increase in goblet cell effectors in the KO mice cannot be explained by an increase in these cytokines. (Paper 3, Figure 2a). In this line, the epithelium showed no signs of elevated Signal Transducer and Activator of Transcription (STAT) 3 or STAT6 signaling (Paper 3, Figure 2b,c). STAT3 signaling would indicate the presence of IL-22 (type 3 cytokine) and STAT6 signaling would indicate the presence of IL-4/IL-13 (type 2 cytokines).¹⁶⁴ The lack of changes in IL-13 levels is supported by the absence of significant changes in the transcription *Atoh1* and *Spdef* (Paper 3, Figure 1e), both of which are induced by IL-13 (Paper 2, Figure 2h). Furthermore, the presence of IL-4/IL-13 has been shown to lead to goblet cell hyperplasia and IL-22 to cause increased epithelial proliferation in the intestinal epithelium (Paper 2, Figure 2d,f).^{163,165} In contrast, *Mmp17* KO mice exhibited normal crypt length and comparable goblet cell numbers to wild type mice, as confirmed by Alcian blue staining, suggesting that epithelial cell numbers and proliferation were not affected (Paper 3, Figure 1d).

In summary, due to absence of differences in homeostatic cytokine levels and immune cell populations in the colon mucosa (data not shown), MMP17 does not seem to possess an immune modulatory function. Consequently, other factors must be responsible for the observed change in goblet cell expression. A potential candidate will be discussed in the following section.

4.4 The multifaceted roles of BMP signaling in regulating epithelial differentiation and gene expression during homeostasis and inflammation

BMP is an essential factor in the ISC niche, promoting the maturation of progenitor cells into the differentiated cell types, such as enterocytes.³⁵ BMP signaling must be inhibited near the bottom of the crypt to maintain stem cells. This is regulated by gradients of BMPs and BMP antagonists that are majorly expressed by mesenchymal cells surrounding the crypt.

A recent study by Beumer *et al.*³⁵ proposes a role of BMP signaling in goblet cell states. This study demonstrates alternative goblet expression in SI organoids treated with BMPs. BMP also appeared to regulate antimicrobial gene expression, such as *Zg16* and *Tff1*, in goblet cells³⁵. We thus wondered if the increase in BMP signaling in the *Mmp17* KO crypt is the cause for the difference in goblet cell expression. However, the expression pattern in the study did not

show an increase in the same effector genes we observe in KO epithelium. This could be due to differences between SI and Colon, supported by the fact that, while we observed increased expression of RELM- β in the proximal colon, we did not in the small intestine (data not shown). Alternatively, additional signaling could be required to induce the observed expression pattern, for example small homeostatic levels of cytokines, other ECM components or growth factors, that are difficult to model *in vitro*. Still, we see indication of a factor gradient change in goblet cell expression along the crypt-colonic surface axis. Taking a closer look at cecum goblet cells we found significant differences in sizes of upper crypt goblet cells as well as altered expression of CLCA1 in lower crypt goblet cells in the KO (Paper 3, Figure 6c,e). This could point towards a more mature differentiation state in the lower crypt goblet cells, as well as higher mucus production by upper crypt goblet cells.

Recent single-cell RNA sequencing experiments have revealed different goblet cell subsets. Nyström *et al.*¹⁶ identified canonical goblet cells, primarily responsible for continuous mucus secretion during homeostasis and increased secretion upon stimulated as part of the innate immune defense. These cells are identified by high expression of *Atoh1*, *Muc2*, *Fcgbp*, and *Clca1*. In contrast, non-canonical goblet cells participate in metabolic processes, such as nutrient absorption and ion transport and express enterocyte-like genes like *Hes1*, *Dmbt1*, *Muc17*, and ion channels. Additionally, they described a population of inter-crypt goblet cells, located at the colonic epithelial surface between the crypts, which, along with upper crypt goblet cells, are the main mucus producers in the colon.^{16,17} The goblet cell morphology we observed in the cecum may indicate a predominance of canonical goblet cells and more upper crypt goblet cells, as we see strong upregulation of *Fcgbp* and *Clca1* expression, while *Hes1* is downregulated (Paper 3, Figure 1a, Supplementary Figure 1b, and un-published data).

Beyond goblet cells, BMP signaling also significantly influences tuft cell differentiation. While mesenchymal cells are the primary source of BMPs, we found that IL-13 can stimulate the expression of *Bmp2* and *Bmp8b* within the intestinal epithelium. This was demonstrated in SI organoid experiments, where mesenchymal cells can be excluded as BMP sources (Paper 2, Figure 3c). BMP2 protein levels in the organoid culture were verified by ELISA (Paper 2, Figure 3d). Furthermore, a rise in *Bmp2* expression was observed during *N. brasiliensis* infection (Paper 2, Figure 3e). Inhibiting BMP signaling in SI organoids induced tuft cell differentiation, confirming the role of BMP in regulating tuft cell expansion. This mechanism's biological relevance becomes evident during helminth infections when tuft cells detect the parasites, secrete IL-25, which induces IL-13 in ILC2s. Subsequently, IL-13 stimulates tuft cell differentiation in

the intestinal epithelium. The epithelium's BMP expression appears to create a negative feedback loop that limits tuft cell expansion during helminth infection. We confirmed this by blocking the BMP receptor ALK2 using DMH1, which resulted in an increase in tuft cells *in vitro* and during *N. brasiliensis* infection *in vivo* (Paper 2, Figure 6b,c).

In sum, BMP signaling plays numerous distinct roles in controlling the intestinal epithelium during homeostasis and disease. Various components contribute to establishing the BMP gradient in the intestinal niche. While, mesenchymal cells, including smooth muscle, are predominately responsible for BMP and BMP antagonist production, epithelial cells can also produce BMPs under specific circumstances. Given the multiple contributors to the BMP gradient and the presence of redundancies, deciphering these processes is a complex endeavor *in vivo*. Further investigations using *in vitro* organoid models, with the use of recombinant BMPs or co-culturing techniques with various BMP-producing cells, could provide valuable insights. Nevertheless, it is becoming increasingly evident that BMP signaling has multifaceted roles and that its manipulation can significantly alter the epithelial composition and expression.

4.5 Exploring the role of goblet cell effectors in the defense against intestinal pathogens

Goblet cells are the primary producers of mucus in the intestine, which protects against bacteria reaching and attaching to the intestinal epithelium. The mucus layer also contains AMPs that provide additional protection. Overcoming the mucus barrier is a critical step for pathogens when colonizing the intestines. While Paneth cells are considered as the main producers of AMPs during homeostasis, goblet cells also produce certain AMPs, which are typically upregulated upon cytokine stimulation. Various goblet cell effectors have been identified as beneficial or even essential during infections. In this section, I will discuss the goblet cell effector proteins observed to be elevated in the *Mmp17* KO epithelium (ANG4, CLCA1, RELM- β) and discuss their role during infections with *C. rodentium* and *T. muris*.¹⁷

RELM- β , expressed in the cecum and colon, is induced by both IL-22 and IL-13 (Paper 2, Figure 2c,e) and can kill Gram-negative bacteria through membrane damage.⁸³ It plays a crucial role in clearing bacterial infections like *C. rodentium* in mice.¹⁶⁶ ANG4 exhibits antibacterial activity by disrupting bacterial membranes.¹⁶⁷ In the *Mmp17* KO mouse epithelium, we observed an increase in RELM- β in the proximal colon and cecum during steady state, as well as increased expression of ANG4 in the colon epithelium (Paper 3, Figure 1a,b, Figure 6d).

However, these increased levels did not affect the course of *C. rodentium* infection, where WT and KO mice cleared the infection within a comparable timeframe (Paper 3, Figure 3a,b).

The role of RELM- β has also been explored during helminth infections. RELM- β was discovered to reduce helminth fitness by impairing their feeding ability and decreasing parasite motility.¹⁶⁸ ANG4 expression has been correlated with the expulsion of *T. muris*.^{85,169} Core mucus proteins like MUC2 and CLCA1 are upregulated during helminth infections, where mucus production is induced as part of the “weep and sweep” response leading to parasite clearance.^{169,170} In a high-dose *T. muris* infection model, which induces type 2 immunity and results in worm clearance after approximately 21 days in C57BL/6 mice, we did not observe any differences in worm clearance between WT and KO mice (Paper 3, Figure 4a). However, in a low dose infection model, which typically causes a chronic infection in male C57BL/6 mice and where polarization of the immune system towards a type 1 response prevents clearance mechanisms, we observed significant differences between WT and KO mice.¹²⁸ KO mice had overall lower worm burdens and almost half of the mice (46%) were able to completely clear the infection within 35 days (Paper 3, Figure 5a). Surprisingly, no elevated levels of type 2 cytokines, such as IL-4, IL-5, and IL-13 were measured in the infected KO mice, and while WT mice had increased levels of type 1 cytokines, the KO mice did not (Paper 3, Figure 5e,f). While the absence of Th2 cytokines could be a result of the sampling point, we observed low levels of total serum IgE (Paper 3, Figure 5h), which would normally accumulate after a type 2 response. These results call the current assumption into question that a type 2 immune response is necessary for the clearance of *T. muris*.¹²⁶ Interestingly, in both high dose and low dose infection, the number of RELM- β ⁺ cells were identical in WT and KO animals (Paper 3, Figure 4d and Figure 5d).

As we did not observe changes in immune polarization, proliferation or immune infiltration, that could explain the difference in clearance, we propose that the already activated state of the epithelium, including elevated *Muc2* and *Clca1* expression by goblet cell and additional AMP components, might be responsible for parasite clearance. Increased goblet cell effectors could prevent the worms from reaching and establishing themselves in the epithelial layer, acting like an early weep and sweep response and thereby preventing a chronic infection.⁸⁰ However, the state of the KO epithelium, did not lead to immediate expulsion of the larvae, as worms were found in the infected KO mice at day 14, albeit in slightly (not significantly) lower levels (Paper 3, Figure 4a). This indicates that the attachment of worms to the epithelium is not entirely prevented. The increased goblet cell effectors could also reduce the motility and viability of the worms,

making them more susceptible to other clearance mechanisms, such as increased epithelial proliferation and muscle contractions.

As *Mmp17* is expressed in the smooth muscle, we cannot discard the possibility that the loss of *Mmp17* might affect muscle contractions during *T. muris* infection. However, we did not observe any indicators of increased muscle activity at steady state and found no genes related to increased contractility in the muscle tissue. In addition to that, experiments done on aorta smooth muscle tissue from the same KO mouse strain did not reveal any significant changes in contractile strength in homeostasis.¹⁷¹ Additional experiments testing the gut motility such as measuring fecal pellet production or dye transit would give information on gut motility during homeostasis in *Mmp17* KO mice.¹⁷² Changes in contractions during infections could be measured in intestinal explants *in vitro*.¹⁷³

While this thesis was unable to conclusively determine the cause of clearance in the low-dose *T. muris* infection experiment, the results highlight that clearance mechanisms against helminths are not completely understood and introduce goblet cell effectors as an important factor.

4.6 Translatability of results from mouse and organoid to human and into medical applications

The results in this thesis were obtained using mouse and organoid studies, raising the important question of if these findings are transferrable to the human organism and if it could be relevant for medical applications. There are limited possibilities to study certain conditions and diseases, especially in an isolated and controlled environment in humans. Mouse studies are an alternative, as they are relatively fast to breed, cheap to house, and share over 90 % of genes with humans.¹⁷⁴ Physiological differences between the human and murine intestine were summarized in chapter 1.6.1 of the introduction. In short, the overall structure and cell types are the same between mouse and human, but differences diet, feeding patterns, body size and metabolic requirements can make some results obtained in mice difficult to extrapolate to humans. This is especially the case in studies regarding, nutrition and microbiota.¹¹¹ Additionally, differences in the immune system have been described between humans and mice, which required extra attention when studying immune responses. Part of those immunological differences can be attributed to the Specific Pathogen Free conditions most mice are kept in that restrict the exposure to pathogens.^{174,175}

We utilized a whole-body KO of *Mmp17* to study the role of MMP17 in the intestine. While *Mmp17* KO mice did not exhibit any severe symptoms, we cannot

rule out the possibility that the absence of *Mmp17* in other cell types or development stages, might influence our results. An inducible tissue-specific KO mouse would provide a more precise way to study the impact of intestinal smooth muscle derived MMP17. Ideally, we would use a “floxed” *Mmp17* gene under the control of the smooth muscle myosin heavy chain (*Myh11*) promoter, which could be selectively knocked out in smooth muscle cells upon administration of tamoxifen.¹⁷⁶

Due to the similarities between human and mouse MMP17, we can be confident that results concerning the *in vivo* cleavage of substrates are relevant. Furthermore, human recombinant MMP17 was used in our *in vitro* digestion experiments (Paper 1, Figure 8c). MMP17 has been mostly studied in the context of diseases, mainly cancers, but these studies have not elucidated MMP17’s mechanism of action.⁶⁶ We demonstrated MMP17’s ability to cleave POSTN as one potential link, however other, still unknown substrates of MMP17 could be responsible. Further investigations into potential MMP17 substrates and the nature of POSTN cleavage would be interesting, especially since POSTN has been heavily implicated in different steps of tumor biology.^{160,161}

Aside from mice, we utilized SI and colon organoids to study the intestinal epithelium in isolation, which made it possible to discover the expression of *Bmp2* and *Bmp8b* by the epithelium as a response to IL-13 treatment. Studying this mechanism *in vivo* would have been more difficult as BMP expression by the mesenchyme could have overshadowed these results, requiring higher resolution techniques like single cell RNA sequencing. Traditional cell culture, on the other hand, would not provide the combination of intestinal stem cells and differentiated epithelial cell types.

Organoids are a powerful tool to study isolated mechanisms; however, they are not without limitations. One significant limitation I want to highlight is the dependency on the matrix used for organoid culture. This matrix can either be synthetic or sourced from cells or tissue. The findings from our study, showing impact of *Mmp17* loss on the ECM and subsequently on the intestinal niche, underscores the influence the surrounding matrix can exert on organoid growth and differentiation. Complex matrixes like Matrigel™, where not all components are fully defined and composition varies from batch to batch, represent a challenge in the interpretation and reproducibility of results. Matrigel™, derived from mouse sarcoma cell secretions enriched in ECM proteins, does not optimally mimic the intestinal crypt environment. Alternative materials include decellularized tissue, bio-macromolecules such as collagen, synthetic polymers, recombinant proteins and combinations of them. Another aspect to consider is matrix stiffness, which is sensed by integrin receptor complexes and influences

epithelial cells through the Hippo signaling pathway. Coupled with the high costs and occasional shortages of MatrigelTM, these issues have prompted many research groups to start exploring other matrix options for intestinal organoids. Moreover, matrix components can bind molecules and thus impact the availability of factors that are added to organoid medium.^{54,177,178} While it is important to be cautious in the choice of matrix material when culturing organoids, this knowledge also opens up new opportunities to study the impact of the ECM on the intestinal niche. Particularly interesting could be to model different pathological ECM states, as the ECM is altered with age and after inflammations, infections, or injuries.^{178,179} An accurate replication of the intestinal ECM for intestinal organoid culture could also allow for a more detailed study of the impact of ECM-modifying proteins like MMP17 on the intestinal epithelium.

In summary, while the results presented here were derived from mouse and murine organoid studies, they provide valuable insights into epithelial regulation and pave the way for future lines of investigation.

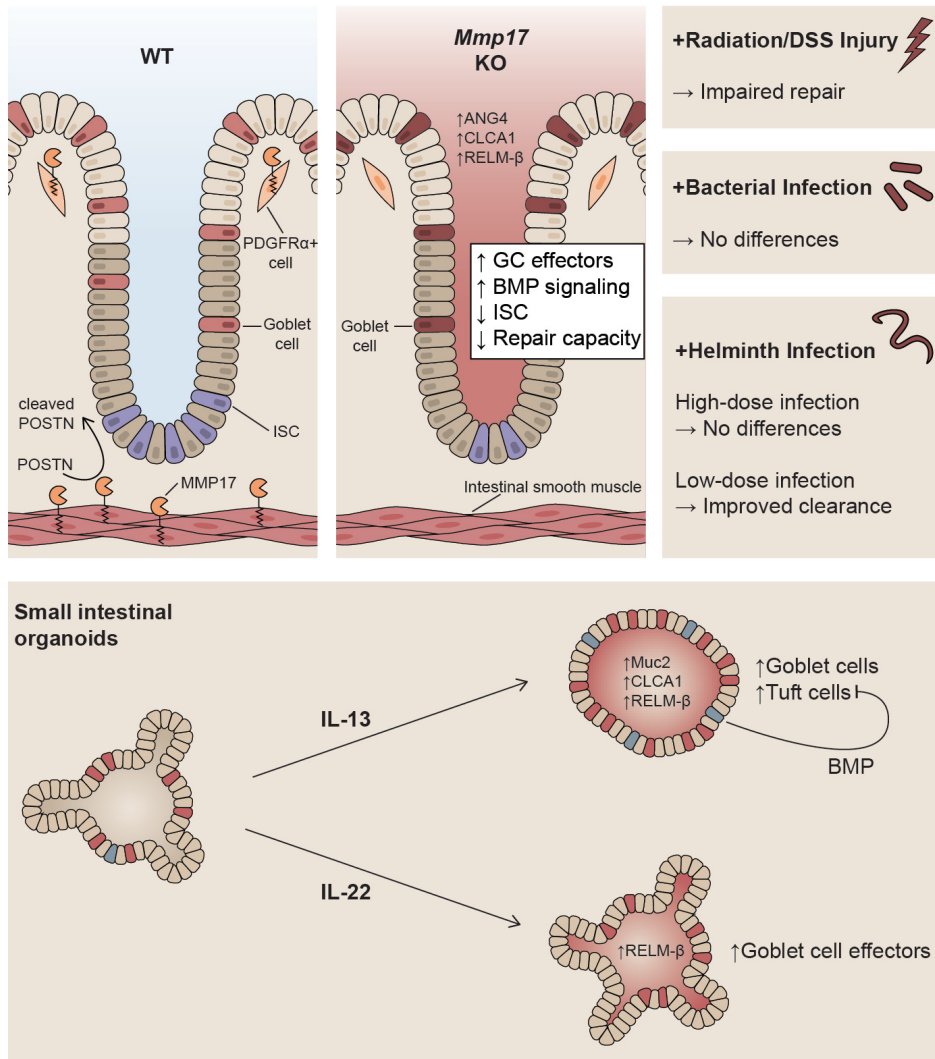


Figure 10: Summary of findings. Top. *Mmp17* is expressed in intestinal smooth muscle cells and PDGFR α + cells towards the top of colon crypts. *Mmp17* KO mice show several changes to the cell composition and expression of the colon epithelium. KO epithelium has reduced numbers of ISCs and shows increased BMP signaling and elevated expression levels of goblet cell effectors, such as ANG4, CLCA1, and RELM- β . This expression was not cytokine induced. MMP17 has been found to cleave periostin (POSTN). Challenging the *Mmp17* KO with injury and infection models, we found that *Mmp17* KO mice have an impaired repair response and show improved clearance of low-dose infection with the helminth *T. muris*. The loss of *Mmp17* appeared to make no difference during *C. rodentium* and high-dose *T. muris* infection. Bottom. Small intestinal organoids treated with IL-13 or IL-22. IL-13 induces the differentiation of both goblet cells and tuft cells. Goblet cells increased production of MUC2, CLCA1, and RELM- β upon IL-13 treatment. Expression of BMP was elevated by the intestinal epithelium, which limited tuft cell expansion in a negative feedback loop. IL-22 did not induce expansion of goblet cells, but did induce the expression of RELM- β .

5 Conclusion

This thesis explored the complex regulation of the ISC niche. The major findings are summarized in Figure 10. The research emphasized the role of the intestinal smooth muscle in supporting the ISC niche by providing factors such as BMP antagonists. A central focus of this work was on MMP17, predominantly expressed in smooth muscle cells and to a lesser extent in PDGFR α + mesenchymal stromal cells in the intestine. Our research underscores MMP17's significant role in modulating the intestinal epithelium, influencing ISC numbers, and altering goblet cell expression. Notably, the absence of MMP17 compromised the regenerative abilities of the intestinal epithelium following injury and promoted tumor formation in an Apc^{Min} mouse model.

Intriguingly, *Mmp17* KO mice also displayed enhanced clearance of the helminth *T. muris*, seemingly independent of a type 2 immune response. We proposed that this enhanced resistance may be linked to elevated homeostatic levels of goblet cell effectors in the proximal colon and cecum of *Mmp17* KO mice. We found increased levels of the goblet cell effector genes *Ang4*, *Ctca1* and *Retnlb*, which are typically associated with immune responses. In organoid models, we found that IL-13 and IL-22 induced distinct goblet cell effector signatures, with IL-13 also driving an increase in goblet cell numbers. However, the increase in goblet cell effectors in *Mmp17* KO mice was not caused by cytokines or other traditional modulators of goblet cells such as Notch signaling. Rather, we observed heightened BMP signaling within colon crypts of the KO mice, potentially altering the maturation state of goblet cells in the crypt. The presence of more mature goblet cells could explain the heightened amount of goblet cell effectors. These findings underscore the crucial role of goblet cells as part of innate immune responses and expose our gaps in our understanding of mechanisms regulating goblet cells.

We also identified another key role of BMP signaling in regulating tuft cell expansion. During helminth infections, IL-13 induces an increase in goblet cells and tuft cells in the intestinal epithelium. We demonstrated that the epithelium produces the BMPs in response to IL-13, which acts as a brake on IL-13-induced tuft cell expansion, creating a negative feedback loop. This regulatory mechanism is important during helminths infections.

In summary, this research provides valuable insights into MMP17's role within the intestine and the involvement of BMP signaling in regulating the intestinal epithelium during homeostasis, inflammation, and infection. It also uncovers, for the first time, the regulatory influence of the smooth muscle on epithelial behaviour during both homeostasis and following injury.

Future research should delve deeper into the role of the intestinal smooth muscle within the ISC niche, unravel the specific influences of MMP17 on the ISC niche, and explore the potential of goblet cell effectors during intestinal infections. This could further deepen our understanding and potentially open new therapeutic avenues in managing intestinal diseases.

6 List of Tables

Table 1: Overview of type 1, 2, and 3 immunity and immune tolerance.....	22
--	----

7 List of Figures

Figure 1: Mouse intestinal tract.....	2
Figure 2: Structure and composition of the SI and colon epithelial layer.....	4
Figure 3: Signaling pathways in the intestinal stem cell niche.	9
Figure 4: Signaling gradients and cell fate in the intestinal epithelial niche.....	11
Figure 5: Classification of MMPs and structure of MMP17.....	16
Figure 6: Human and mouse GI tract anatomy.	25
Figure 7: Immune responses to bacterial and parasitic infections.....	27
Figure 8: Epithelial injury models.....	30
Figure 9: Generation and growth of intestinal organoids.....	33
Figure 10: Summary of findings.	51

8 List of Abbreviations

Abbreviation	Explanation
AKT	Ak strain transforming, Protein kinase B
AMP	Antimicrobial peptide
ANG4	Angiogenin 4
APC	Adenomas polyposis coli
ATOH1	Protein atonal homolog 1
BMP	Bone morphogenic protein
CD-	Cluster of differentiation, nomenclature for cell surface molecules
Chrd1	Chordlin-like 1
CLCA1	Calcium-activated chloride channel regulator1
CSL	Suppressor of Hairless, Transcription factor
cSMAD	Common partner SMAD
DAMP	Damage-associated molecular pattern
DC	Dendritic cell
DLL1/4	Delta-like protein 1/4, Notch ligands
Dmbt1	Deleted in malignant brain tumors 1
DNA	Deoxyribonucleic acid
DPI	Days post infection
DSC	Deep crypt secretory cell
DSS	Dextran sodium sulfate
ECM	Extracellular matrix
EEC	Enteroendocrine cell
EGF	Epidermal growth factor
EGFR	Epidermal growth factor receptor
EHEC	Enterohaemorrhagic E. coli
EPEC	Enteropathogenic E. coli
FCGBP	Fc γ binding protein
FGF	Fibroblast growth factor
GAG	Glycosaminoglycan
GALT	Gut-associated lymphoid tissue
GFI1	Growth factor independent 1 transcriptional repressor
GI	Gastrointestinal tract
GPI	Glycosylphosphatidylinositol

GREM1/2	Gremlin 1/2
HES1	Hairy and enhancer of split-1, Transcription factor
IBD	Inflammatory bowel disease
IEL	Intraepithelial lymphocytes
IFN- γ	Interferon gamma
IgA	Immunoglobulin A
IL-	Interleukin
ILC	Innate lymphoid cell
ISC	Intestinal stem cell
JAK	Janus kinase
KO	Knock-out
LGR5	Leucine rich repeat containing G protein coupled receptor 5
LRP5/6	LDL receptor related protein 5/6
M cell	Microfold cell
MAMP	Microbial-associated molecular pattern
MAPK	Mitogen-activated protein kinase
MHC	Major histocompatibility complex
mLN	Mesenteric lymph node
mLNL	Mesenteric lymph node lymphocytes
MMP	Matrix metalloproteinase
mRNA	Messenger RNA
MUC2	Mucin-2
NICD	Notch intracellular domain
NLR	NOD-like receptor
PDGFR α	Platelet-derived growth factor receptor alpha
PG	Proteoglycan
PI3K	Phosphoinositide 3-kinase
POSTN	Periostin
PRR	Pattern recognition receptor
RankL	Receptor activator of nuclear factor κ -B ligand
RELM- β	Resistin-like molecule
RNA	Ribonucleic acid
RNAseq	RNA sequencing
rSMAD	receptor-regulated SMAD
RSPO	R-spondin
SI	Small intestine
SMAD	Suppressor of Mothers against Decapentaplegic

SMC	Smooth muscle cell
SPDEF	SAM Pointed Domain Containing ETS Transcription Factor
SPRR2A	Small proline-rich protein 2A
STAT	Signal transducer and activator of transcription
SAA	Serum amyloid A
TAZ	Transcriptional coactivator with PDZ-binding motif
TCF	T cell transcription factor
TCR	T cell receptor
TF	Transcription factor
TFF3	Trefoil factor 3
TGF- α	Transforming growth factor alpha
Th cell	T helper cell
TLR	Toll-like receptor
TNF- α	Tumor necrosis factor alpha
Treg	Regulatory T cell
TSLP	Thymic stromal lymphopoietin
Wnt	Wingless/Integrated
WT	Wild-type
YAP	Yes-associated protein
ZG16	Zymogen granule protein 16
α SMA	Alpha smooth muscle actin

9 Bibliography

- 1 Ovalle, W. K. & Nahirney, P. C. *Netter's essential histology: : with correlated histopathology*. 3rd. edn, (Elsevier, 2020).
- 2 Reed, K. K. & Wickham, R. Review of the Gastrointestinal Tract: From Macro to Micro. *Seminars in Oncology Nursing* **25**, 3-14, doi:<https://doi.org/10.1016/j.soncn.2008.10.002> (2009).
- 3 Greenwood-Van Meerveld, B., Johnson, A. C. & Grundy, D. in *Gastrointestinal Pharmacology* (ed Beverley Greenwood-Van Meerveld) 1-16 (Springer International Publishing, 2017).
- 4 Treuting, P. M., Valasek, M. A. & Dintzis, S. M. in *Comparative Anatomy and Histology* (eds Piper M. Treuting & Suzanne M. Dintzis) 155-175 (Academic Press, 2012).
- 5 Kenneth Murphy, C. W., Leslie Berg. in *Janeway's immunobiology* Ch. 12, (W.W. Norton and Company, 2022).
- 6 Barker, N. Adult intestinal stem cells: critical drivers of epithelial homeostasis and regeneration. *Nature Reviews Molecular Cell Biology* **15**, 19-33, doi:10.1038/nrm3721 (2014).
- 7 Gehart, H. & Clevers, H. Tales from the crypt: new insights into intestinal stem cells. *Nature Reviews Gastroenterology & Hepatology* **16**, 19-34, doi:10.1038/s41575-018-0081-y (2019).
- 8 Beumer, J. & Clevers, H. Cell fate specification and differentiation in the adult mammalian intestine. *Nature Reviews Molecular Cell Biology* **22**, 39-53, doi:10.1038/s41580-020-0278-0 (2021).
- 9 Cheng, H. & Leblond, C. P. Origin, differentiation and renewal of the four main epithelial cell types in the mouse small intestine. V. Unitarian Theory of the origin of the four epithelial cell types. *Am J Anat* **141**, 537-561, doi:10.1002/aja.1001410407 (1974).
- 10 Barker, N. *et al.* Identification of stem cells in small intestine and colon by marker gene Lgr5. *Nature* **449**, 1003-1007, doi:10.1038/nature06196 (2007).
- 11 Ramadan, R., van Driel, M. S., Vermeulen, L. & van Neerven, S. M. Intestinal stem cell dynamics in homeostasis and cancer. *Trends in Cancer* **8**, 416-425, doi:10.1016/j.trecan.2022.01.011 (2022).
- 12 Rees, W. D., Tandun, R., Yau, E., Zachos, N. C. & Steiner, T. S. Regenerative Intestinal Stem Cells Induced by Acute and Chronic Injury: The Saving Grace of the Epithelium? *Frontiers in Cell and Developmental Biology* **8**, doi:10.3389/fcell.2020.583919 (2020).
- 13 Zimmer, K.-P., de Laffolie, J., Barone, M. V. & Naim, H. Y. Endocytosis in enterocytes. *Wiener Medizinische Wochenschrift* **166**, 205-210, doi:10.1007/s10354-016-0448-z (2016).

- 14 Pelaseyed, T. *et al.* The mucus and mucins of the goblet cells and enterocytes provide the first defense line of the gastrointestinal tract and interact with the immune system. *Immunological Reviews* **260**, 8-20, doi:<https://doi.org/10.1111/imr.12182> (2014).
- 15 Burger-van Paassen, N. *et al.* Mucin Muc2 deficiency and weaning influences the expression of the innate defense genes Reg3 β , Reg3 γ and angiogenin-4. *PLoS One* **7**, e38798, doi:10.1371/journal.pone.0038798 (2012).
- 16 Nyström, E. E. L. *et al.* An intercrypt subpopulation of goblet cells is essential for colonic mucus barrier function. *Science* **372**, doi:10.1126/science.abb1590 (2021).
- 17 Gustafsson, J. K. & Johansson, M. E. V. The role of goblet cells and mucus in intestinal homeostasis. *Nature Reviews Gastroenterology & Hepatology* **19**, 785-803, doi:10.1038/s41575-022-00675-x (2022).
- 18 Sato, T. *et al.* Paneth cells constitute the niche for Lgr5 stem cells in intestinal crypts. *Nature* **469**, 415-418, doi:10.1038/nature09637 (2011).
- 19 Gerbe, F. *et al.* Intestinal epithelial tuft cells initiate type 2 mucosal immunity to helminth parasites. *Nature* **529**, 226-230, doi:10.1038/nature16527 (2016).
- 20 Hendel, S. K. *et al.* Tuft Cells and Their Role in Intestinal Diseases. *Front Immunol* **13**, 822867, doi:10.3389/fimmu.2022.822867 (2022).
- 21 Beumer, J. *et al.* High-Resolution mRNA and Secretome Atlas of Human Enteroendocrine Cells. *Cell* **181**, 1291-1306.e1219, doi:<https://doi.org/10.1016/j.cell.2020.04.036> (2020).
- 22 Muniz, L., Knosp, C. & Yeretssian, G. Intestinal antimicrobial peptides during homeostasis, infection, and disease. *Frontiers in Immunology* **3**, doi:10.3389/fimmu.2012.00310 (2012).
- 23 Johansson, Malin E. V. *et al.* Normalization of Host Intestinal Mucus Layers Requires Long-Term Microbial Colonization. *Cell Host & Microbe* **18**, 582-592, doi:<https://doi.org/10.1016/j.chom.2015.10.007> (2015).
- 24 Jones, D. L. & Fuller, M. T. in *Essentials of Stem Cell Biology (Second Edition)* (eds Robert Lanza *et al.*) 61-72 (Academic Press, 2009).
- 25 Beumer, J. & Clevers, H. Regulation and plasticity of intestinal stem cells during homeostasis and regeneration. *Development* **143**, 3639-3649, doi:10.1242/dev.133132 (2016).
- 26 Biton, M. *et al.* T Helper Cell Cytokines Modulate Intestinal Stem Cell Renewal and Differentiation. *Cell* **175**, 1307-1320.e1322, doi:<https://doi.org/10.1016/j.cell.2018.10.008> (2018).
- 27 Farin, H. F., Van Es, J. H. & Clevers, H. Redundant Sources of Wnt Regulate Intestinal Stem Cells and Promote Formation of Paneth Cells. *Gastroenterology* **143**, 1518-1529.e1517, doi:<https://doi.org/10.1053/j.gastro.2012.08.031> (2012).
- 28 Clevers, H. & Nusse, R. Wnt/ β -Catenin Signaling and Disease. *Cell* **149**, 1192-1205, doi:<https://doi.org/10.1016/j.cell.2012.05.012> (2012).

- 29 Meyer, A. R., Brown, M. E., McGrath, P. S. & Dempsey, P. J. Injury-Induced Cellular Plasticity Drives Intestinal Regeneration. *Cell Mol Gastroenterol Hepatol* **13**, 843-856, doi:10.1016/j.jcmgh.2021.12.005 (2022).
- 30 Yan, K. S. *et al.* Non-equivalence of Wnt and R-spondin ligands during Lgr5⁺ intestinal stem-cell self-renewal. *Nature* **545**, 238-242, doi:10.1038/nature22313 (2017).
- 31 Greicius, G. *et al.* PDGFR α ⁺ pericryptal stromal cells are the critical source of Wnts and RSPO3 for murine intestinal stem cells in vivo. *Proceedings of the National Academy of Sciences* **115**, E3173-E3181, doi:doi:10.1073/pnas.1713510115 (2018).
- 32 Abud, H. E., Chan, W. H. & Jardé, T. Source and Impact of the EGF Family of Ligands on Intestinal Stem Cells. *Frontiers in Cell and Developmental Biology* **9**, doi:10.3389/fcell.2021.685665 (2021).
- 33 Ueo, T. *et al.* The role of Hes genes in intestinal development, homeostasis and tumor formation. *Development* **139**, 1071-1082, doi:10.1242/dev.069070 (2012).
- 34 Shroyer, N. F. *et al.* Intestine-Specific Ablation of Mouse atonal homolog 1 (Math1) Reveals a Role in Cellular Homeostasis. *Gastroenterology* **132**, 2478-2488, doi:<https://doi.org/10.1053/j.gastro.2007.03.047> (2007).
- 35 Beumer, J. *et al.* BMP gradient along the intestinal villus axis controls zonated enterocyte and goblet cell states. *Cell Reports* **38**, 110438, doi:<https://doi.org/10.1016/j.celrep.2022.110438> (2022).
- 36 McCarthy, N. *et al.* Smooth muscle contributes to the development and function of a layered intestinal stem cell niche. *Developmental Cell* **58**, 550-564.e556, doi:<https://doi.org/10.1016/j.devcel.2023.02.012> (2023).
- 37 Hong, A. W., Meng, Z. & Guan, K.-L. The Hippo pathway in intestinal regeneration and disease. *Nature Reviews Gastroenterology & Hepatology* **13**, 324-337, doi:10.1038/nrgastro.2016.59 (2016).
- 38 Deng, F., Wu, Z., Zou, F., Wang, S. & Wang, X. The Hippo-YAP/TAZ Signaling Pathway in Intestinal Self-Renewal and Regeneration After Injury. *Front Cell Dev Biol* **10**, 894737, doi:10.3389/fcell.2022.894737 (2022).
- 39 Sasaki, N. *et al.* Reg4⁺ deep crypt secretory cells function as epithelial niche for Lgr5⁺ stem cells in colon. *Proc Natl Acad Sci U S A* **113**, E5399-5407, doi:10.1073/pnas.1607327113 (2016).
- 40 Degirmenci, B., Valenta, T., Dimitrieva, S., Hausmann, G. & Basler, K. GLI1-expressing mesenchymal cells form the essential Wnt-secreting niche for colon stem cells. *Nature* **558**, 449-453, doi:10.1038/s41586-018-0190-3 (2018).
- 41 Powell, D. W., Pinchuk, I. V., Saada, J. I., Chen, X. & Mifflin, R. C. Mesenchymal Cells of the Intestinal Lamina Propria. *Annual Review of Physiology* **73**, 213-237, doi:10.1146/annurev.physiol.70.113006.100646 (2011).

- 42 McCarthy, N. *et al.* Distinct Mesenchymal Cell Populations Generate the Essential Intestinal BMP Signaling Gradient. *Cell Stem Cell* **26**, 391-402.e395, doi:<https://doi.org/10.1016/j.stem.2020.01.008> (2020).
- 43 Sun, H., Tan, J., Chen, H., Wu, N. & Su, B. Immune niches orchestrated by intestinal mesenchymal stromal cells lining the crypt-villus. *Frontiers in Immunology* **13**, doi:10.3389/fimmu.2022.1057932 (2022).
- 44 Roulis, M. & Flavell, R. A. Fibroblasts and myofibroblasts of the intestinal lamina propria in physiology and disease. *Differentiation* **92**, 116-131, doi:<https://doi.org/10.1016/j.diff.2016.05.002> (2016).
- 45 Kosinski, C. *et al.* Gene expression patterns of human colon tops and basal crypts and BMP antagonists as intestinal stem cell niche factors. *Proceedings of the National Academy of Sciences* **104**, 15418-15423, doi:doi:10.1073/pnas.0707210104 (2007).
- 46 Stzpourginski, I. *et al.* CD34+ mesenchymal cells are a major component of the intestinal stem cells niche at homeostasis and after injury. *Proc Natl Acad Sci U S A* **114**, E506-e513, doi:10.1073/pnas.1620059114 (2017).
- 47 Shoshkes-Carmel, M. *et al.* Subepithelial telocytes are an important source of Wnts that supports intestinal crypts. *Nature* **557**, 242-246, doi:10.1038/s41586-018-0084-4 (2018).
- 48 Yu, S. *et al.* Paneth Cell Multipotency Induced by Notch Activation following Injury. *Cell Stem Cell* **23**, 46-59.e45, doi:<https://doi.org/10.1016/j.stem.2018.05.002> (2018).
- 49 Westphalen, C. B. *et al.* Long-lived intestinal tuft cells serve as colon cancer-initiating cells. *J Clin Invest* **124**, 1283-1295, doi:10.1172/jci73434 (2014).
- 50 Jadhav, U. *et al.* Dynamic Reorganization of Chromatin Accessibility Signatures during Dedifferentiation of Secretory Precursors into Lgr5+ Intestinal Stem Cells. *Cell Stem Cell* **21**, 65-77.e65, doi:10.1016/j.stem.2017.05.001 (2017).
- 51 Pompili, S., Latella, G., Gaudio, E., Sferra, R. & Vetuschi, A. The Charming World of the Extracellular Matrix: A Dynamic and Protective Network of the Intestinal Wall. *Frontiers in Medicine* **8**, doi:10.3389/fmed.2021.610189 (2021).
- 52 Gattazzo, F., Urciuolo, A. & Bonaldo, P. Extracellular matrix: A dynamic microenvironment for stem cell niche. *Biochimica et Biophysica Acta (BBA) - General Subjects* **1840**, 2506-2519, doi:<https://doi.org/10.1016/j.bbagen.2014.01.010> (2014).
- 53 Halder, G., Dupont, S. & Piccolo, S. Transduction of mechanical and cytoskeletal cues by YAP and TAZ. *Nature Reviews Molecular Cell Biology* **13**, 591-600, doi:10.1038/nrm3416 (2012).
- 54 Kozlowski, M. T., Crook, C. J. & Ku, H. T. Towards organoid culture without Matrigel. *Communications Biology* **4**, 1387, doi:10.1038/s42003-021-02910-8 (2021).

- 55 Jones , R. G. *et al.* Conditional deletion of $\beta 1$ integrins in the intestinal epithelium causes a loss of Hedgehog expression, intestinal hyperplasia, and early postnatal lethality. *Journal of Cell Biology* **175**, 505-514, doi:10.1083/jcb.200602160 (2006).
- 56 Ashton, G. H. *et al.* Focal adhesion kinase is required for intestinal regeneration and tumorigenesis downstream of Wnt/c-Myc signaling. *Dev Cell* **19**, 259-269, doi:10.1016/j.devcel.2010.07.015 (2010).
- 57 Schenk , S. *et al.* Binding to EGF receptor of a laminin-5 EGF-like fragment liberated during MMP-dependent mammary gland involution. *Journal of Cell Biology* **161**, 197-209, doi:10.1083/jcb.200208145 (2003).
- 58 Hynes, R. O. The Extracellular Matrix: Not Just Pretty Fibrils. *Science* **326**, 1216-1219, doi:doi:10.1126/science.1176009 (2009).
- 59 Nakayama, K. H., Batchelder, C. A., Lee, C. I. & Tarantal, A. F. Decellularized Rhesus Monkey Kidney as a Three-Dimensional Scaffold for Renal Tissue Engineering. *Tissue Engineering Part A* **16**, 2207-2216, doi:10.1089/ten.tea.2009.0602 (2010).
- 60 Gross, J. & Lapiere, C. M. Collagenolytic activity in amphibian tissues: a tissue culture assay. *Proc Natl Acad Sci U S A* **48**, 1014-1022, doi:10.1073/pnas.48.6.1014 (1962).
- 61 de Bruyn, M. *et al.* The molecular biology of matrix metalloproteinases and tissue inhibitors of metalloproteinases in inflammatory bowel diseases. *Critical Reviews in Biochemistry and Molecular Biology* **51**, 295-358, doi:10.1080/10409238.2016.1199535 (2016).
- 62 Jackson, B. C., Nebert, D. W. & Vasiliou, V. Update of human and mouse matrix metalloproteinase families. *Hum Genomics* **4**, 194-201, doi:10.1186/1479-7364-4-3-194 (2010).
- 63 Laronha, H. & Caldeira, J. Structure and Function of Human Matrix Metalloproteinases. *Cells* **9**, 1076 (2020).
- 64 Page-McCaw, A., Ewald, A. J. & Werb, Z. Matrix metalloproteinases and the regulation of tissue remodelling. *Nature Reviews Molecular Cell Biology* **8**, 221-233, doi:10.1038/nrm2125 (2007).
- 65 Sohail, A. *et al.* MT4-(MMP17) and MT6-MMP (MMP25), A unique set of membrane-anchored matrix metalloproteinases: properties and expression in cancer. *Cancer and Metastasis Reviews* **27**, 289-302, doi:10.1007/s10555-008-9129-8 (2008).
- 66 Yip, C., Foidart, P., Noël, A. & Sounni, N. E. MT4-MMP: The GPI-Anchored Membrane-Type Matrix Metalloprotease with Multiple Functions in Diseases. *International Journal of Molecular Sciences* **20**, 354 (2019).
- 67 Martín-Alonso, M. *et al.* Deficiency of MMP17/MT4-MMP Proteolytic Activity Predisposes to Aortic Aneurysm in Mice. *Circulation Research* **117**, e13-e26, doi:doi:10.1161/CIRCRESAHA.117.305108 (2015).

- 68 Host, L. *et al.* The proteolytic activity of MT4-MMP is required for its pro-angiogenic and pro-metastatic promoting effects. *International Journal of Cancer* **131**, 1537-1548, doi:<https://doi.org/10.1002/ijc.27436> (2012).
- 69 Paye, A. *et al.* EGFR Activation and Signaling in Cancer Cells Are Enhanced by the Membrane-Bound Metalloprotease MT4-MMP. *Cancer Research* **74**, 6758-6770, doi:10.1158/0008-5472.Can-13-2994 (2014).
- 70 Clemente, C. *et al.* MT4-MMP deficiency increases patrolling monocyte recruitment to early lesions and accelerates atherosclerosis. *Nature Communications* **9**, 910, doi:10.1038/s41467-018-03351-4 (2018).
- 71 Rikimaru, A. *et al.* Establishment of an MT4-MMP-deficient mouse strain representing an efficient tracking system for MT4-MMP/MMP-17 expression in vivo using β -galactosidase. *Genes to Cells* **12**, 1091-1100, doi:<https://doi.org/10.1111/j.1365-2443.2007.01110.x> (2007).
- 72 Perez-Lopez, A., Behnsen, J., Nuccio, S.-P. & Raffatellu, M. Mucosal immunity to pathogenic intestinal bacteria. *Nature Reviews Immunology* **16**, 135-148, doi:10.1038/nri.2015.17 (2016).
- 73 Turner, J. R. Intestinal mucosal barrier function in health and disease. *Nature Reviews Immunology* **9**, 799-809, doi:10.1038/nri2653 (2009).
- 74 Allaire, J. M. *et al.* The Intestinal Epithelium: Central Coordinator of Mucosal Immunity. *Trends in Immunology* **39**, 677-696, doi:10.1016/j.it.2018.04.002 (2018).
- 75 Burgueño, J. F. & Abreu, M. T. Epithelial Toll-like receptors and their role in gut homeostasis and disease. *Nature Reviews Gastroenterology & Hepatology* **17**, 263-278, doi:10.1038/s41575-019-0261-4 (2020).
- 76 Van der Sluis, M. *et al.* Muc2-Deficient Mice Spontaneously Develop Colitis, Indicating That MUC2 Is Critical for Colonic Protection. *Gastroenterology* **131**, 117-129, doi:<https://doi.org/10.1053/j.gastro.2006.04.020> (2006).
- 77 Johansson, M. E. V. & Hansson, G. C. Immunological aspects of intestinal mucus and mucins. *Nature Reviews Immunology* **16**, 639-649, doi:10.1038/nri.2016.88 (2016).
- 78 Farin, H. F. *et al.* Paneth cell extrusion and release of antimicrobial products is directly controlled by immune cell-derived IFN- γ . *J Exp Med* **211**, 1393-1405, doi:10.1084/jem.20130753 (2014).
- 79 Turner, J.-E., Stockinger, B. & Helmby, H. IL-22 Mediates Goblet Cell Hyperplasia and Worm Expulsion in Intestinal Helminth Infection. *PLOS Pathogens* **9**, e1003698, doi:10.1371/journal.ppat.1003698 (2013).
- 80 Sharpe, C., Thornton, D. J. & Grenicis, R. K. A sticky end for gastrointestinal helminths; the role of the mucus barrier. *Parasite Immunology* **40**, e12517, doi:<https://doi.org/10.1111/pim.12517> (2018).
- 81 Aamann, L., Vestergaard, E. M. & Grønbaek, H. Trefoil factors in inflammatory bowel disease. *World J Gastroenterol* **20**, 3223-3230, doi:10.3748/wjg.v20.i12.3223 (2014).

- 82 Horsnell, W. G. C. & Dewals, B. G. RELMs in the Realm of Helminths. *Trends in Parasitology* **32**, 512-514, doi:<https://doi.org/10.1016/j.pt.2016.04.011> (2016).
- 83 Propheter, D. C., Chara, A. L., Harris, T. A., Ruhn, K. A. & Hooper, L. V. Resistin-like molecule β is a bactericidal protein that promotes spatial segregation of the microbiota and the colonic epithelium. *Proceedings of the National Academy of Sciences* **114**, 11027-11033, doi:doi:10.1073/pnas.1711395114 (2017).
- 84 Bergström, J. H. *et al.* Gram-positive bacteria are held at a distance in the colon mucus by the lectin-like protein ZG16. *Proceedings of the National Academy of Sciences* **113**, 13833-13838, doi:doi:10.1073/pnas.1611400113 (2016).
- 85 Forman, R. A. *et al.* The Goblet Cell Is the Cellular Source of the Anti-Microbial Angiogenin 4 in the Large Intestine Post *Trichuris muris* Infection. *PLOS ONE* **7**, e42248, doi:10.1371/journal.pone.0042248 (2012).
- 86 Hu, Z. *et al.* Small proline-rich protein 2A is a gut bactericidal protein deployed during helminth infection. *Science* **374**, eabe6723, doi:doi:10.1126/science.abe6723 (2021).
- 87 Kulkarni, D. H. *et al.* Goblet cell associated antigen passages support the induction and maintenance of oral tolerance. *Mucosal Immunol* **13**, 271-282, doi:10.1038/s41385-019-0240-7 (2020).
- 88 Schneider, C., O'Leary, C. E. & Locksley, R. M. Regulation of immune responses by tuft cells. *Nature Reviews Immunology* **19**, 584-593, doi:10.1038/s41577-019-0176-x (2019).
- 89 Mörbe, U. M. *et al.* Human gut-associated lymphoid tissues (GALT); diversity, structure, and function. *Mucosal Immunology* **14**, 793-802, doi:<https://doi.org/10.1038/s41385-021-00389-4> (2021).
- 90 Chopp, L., Redmond, C., O'Shea, J. J. & Schwartz, D. M. From thymus to tissues and tumors: A review of T-cell biology. *Journal of Allergy and Clinical Immunology* **151**, 81-97, doi:<https://doi.org/10.1016/j.jaci.2022.10.011> (2023).
- 91 Ma, H., Tao, W. & Zhu, S. T lymphocytes in the intestinal mucosa: defense and tolerance. *Cellular & Molecular Immunology* **16**, 216-224, doi:10.1038/s41423-019-0208-2 (2019).
- 92 Maynard, C. L. & Weaver, C. T. in *Mucosal Immunology (Fourth Edition)* (eds Jiri Mestecky *et al.*) 721-732 (Academic Press, 2015).
- 93 Imam, T., Park, S., Kaplan, M. H. & Olson, M. R. Effector T Helper Cell Subsets in Inflammatory Bowel Diseases. *Frontiers in Immunology* **9**, doi:10.3389/fimmu.2018.01212 (2018).
- 94 Kenneth Murphy, C. W., Leslie Berg. in *Janeway's immunobiology* Ch. 9, (W.W. Norton and Company, 2022).
- 95 Kenneth Murphy, C. W., Leslie Berg. in *Janeway's immunobiology* Ch. 11, (W.W. Norton and Company, 2022).

- 96 Brucklacher-Waldert, V., Carr, E. J., Linterman, M. A. & Veldhoen, M. Cellular Plasticity of CD4⁺ T Cells in the Intestine. *Front Immunol* **5**, 488, doi:10.3389/fimmu.2014.00488 (2014).
- 97 Kiner, E. *et al.* Gut CD4⁺ T cell phenotypes are a continuum molded by microbes, not by TH archetypes. *Nature Immunology* **22**, 216-228, doi:10.1038/s41590-020-00836-7 (2021).
- 98 Cosovanu, C. & Neumann, C. The Many Functions of Foxp3⁺ Regulatory T Cells in the Intestine. *Frontiers in Immunology* **11**, doi:10.3389/fimmu.2020.600973 (2020).
- 99 Mowat, A. M. & Agace, W. W. Regional specialization within the intestinal immune system. *Nature Reviews Immunology* **14**, 667-685, doi:10.1038/nri3738 (2014).
- 100 Bunker, J. J. & Bendelac, A. IgA Responses to Microbiota. *Immunity* **49**, 211-224, doi:<https://doi.org/10.1016/j.immuni.2018.08.011> (2018).
- 101 Castro-Dopico, T. & Clatworthy, M. R. IgG and Fcγ Receptors in Intestinal Immunity and Inflammation. *Frontiers in Immunology* **10**, doi:10.3389/fimmu.2019.00805 (2019).
- 102 Spencer, J. & Bemark, M. Human intestinal B cells in inflammatory diseases. *Nature Reviews Gastroenterology & Hepatology* **20**, 254-265, doi:10.1038/s41575-023-00755-6 (2023).
- 103 Luciani, C., Hager, F. T., Cerovic, V. & Lelouard, H. Dendritic cell functions in the inductive and effector sites of intestinal immunity. *Mucosal Immunology* **15**, 40-50, doi:<https://doi.org/10.1038/s41385-021-00448-w> (2022).
- 104 Huang, Y., Mao, K. & Germain, R. N. Thinking differently about ILCs—Not just tissue resident and not just the same as CD4⁺ T-cell effectors. *Immunological Reviews* **286**, 160-171, doi:<https://doi.org/10.1111/imr.12704> (2018).
- 105 Haddad, E.-B. *et al.* Current and Emerging Strategies to Inhibit Type 2 Inflammation in Atopic Dermatitis. *Dermatology and Therapy* **12**, 1501-1533, doi:10.1007/s13555-022-00737-7 (2022).
- 106 Nausch, N. & Mutapi, F. Group 2 ILCs: A way of enhancing immune protection against human helminths? *Parasite Immunology* **40**, e12450, doi:<https://doi.org/10.1111/pim.12450> (2018).
- 107 Spits, H. *et al.* Innate lymphoid cells — a proposal for uniform nomenclature. *Nature Reviews Immunology* **13**, 145-149, doi:10.1038/nri3365 (2013).
- 108 Saez, A. *et al.* Innate Lymphoid Cells in Intestinal Homeostasis and Inflammatory Bowel Disease. *International Journal of Molecular Sciences* **22**, 7618 (2021).
- 109 Annunziato, F., Romagnani, C. & Romagnani, S. The 3 major types of innate and adaptive cell-mediated effector immunity. *Journal of Allergy and Clinical Immunology* **135**, 626-635, doi:<https://doi.org/10.1016/j.jaci.2014.11.001> (2015).

- 110 Nguyen, T. L. A., Vieira-Silva, S., Liston, A. & Raes, J. How informative is the mouse for human gut microbiota research? *Disease Models & Mechanisms* **8**, 1-16, doi:10.1242/dmm.017400 (2015).
- 111 Hugenholtz, F. & de Vos, W. M. Mouse models for human intestinal microbiota research: a critical evaluation. *Cellular and Molecular Life Sciences* **75**, 149-160, doi:10.1007/s00018-017-2693-8 (2018).
- 112 Nishiyama, K., Sugiyama, M. & Mukai, T. Adhesion Properties of Lactic Acid Bacteria on Intestinal Mucin. *Microorganisms* **4**, 34 (2016).
- 113 Girard-Madoux, M. J. H. *et al.* The immunological functions of the Appendix: An example of redundancy? *Seminars in Immunology* **36**, 31-44, doi:<https://doi.org/10.1016/j.smim.2018.02.005> (2018).
- 114 WHO. *Diarrhoeal disease*, <<https://www.who.int/news-room/fact-sheets/detail/diarrhoeal-disease>> (2017).
- 115 WHO. *E. coli*, <<https://www.who.int/news-room/fact-sheets/detail/e-coli>> (2018).
- 116 Collins, J. W. *et al.* *Citrobacter rodentium*: infection, inflammation and the microbiota. *Nature Reviews Microbiology* **12**, 612-623, doi:10.1038/nrmicro3315 (2014).
- 117 Mullineaux-Sanders, C. *et al.* *Citrobacter rodentium*–host–microbiota interactions: immunity, bioenergetics and metabolism. *Nature Reviews Microbiology* **17**, 701-715, doi:10.1038/s41579-019-0252-z (2019).
- 118 Silberger, D. J., Zindl, C. L. & Weaver, C. T. *Citrobacter rodentium*: a model enteropathogen for understanding the interplay of innate and adaptive components of type 3 immunity. *Mucosal Immunology* **10**, 1108-1117, doi:10.1038/mi.2017.47 (2017).
- 119 Cortés, A., Muñoz-Antoli, C., Esteban, J. G. & Toledo, R. Th2 and Th1 Responses: Clear and Hidden Sides of Immunity Against Intestinal Helminths. *Trends in Parasitology* **33**, 678-693, doi:<https://doi.org/10.1016/j.pt.2017.05.004> (2017).
- 120 Vacca, F. & Le Gros, G. Tissue-specific immunity in helminth infections. *Mucosal Immunology* **15**, 1212-1223, doi:10.1038/s41385-022-00531-w (2022).
- 121 Coakley, G. & Harris, N. L. The Intestinal Epithelium at the Forefront of Host–Helminth Interactions. *Trends in Parasitology* **36**, 761-772, doi:10.1016/j.pt.2020.07.002 (2020).
- 122 WHO. *Soil-transmitted helminth infections*, <<https://www.who.int/news-room/fact-sheets/detail/soil-transmitted-helminth-infections>> (2023).
- 123 Jourdan, P. M., Lamberton, P. H. L., Fenwick, A. & Addiss, D. G. Soil-transmitted helminth infections. *The Lancet* **391**, 252-265, doi:[https://doi.org/10.1016/S0140-6736\(17\)31930-X](https://doi.org/10.1016/S0140-6736(17)31930-X) (2018).
- 124 Chetty, A. *et al.* Il4ra-independent vaginal eosinophil accumulation following helminth infection exacerbates epithelial ulcerative pathology of HSV-2 infection. *Cell Host Microbe* **29**, 579-593.e575, doi:10.1016/j.chom.2021.02.004 (2021).

- 125 Montaña, K. J., Cuéllar, C. & Sotillo, J. Rodent Models for the Study of Soil-Transmitted Helminths: A Proteomics Approach. *Frontiers in Cellular and Infection Microbiology* **11**, doi:10.3389/fcimb.2021.639573 (2021).
- 126 Colombo, S. A. P. & Grecis, R. K. Immunity to Soil-Transmitted Helminths: Evidence From the Field and Laboratory Models. *Frontiers in Immunology* **11**, doi:10.3389/fimmu.2020.01286 (2020).
- 127 Klementowicz, J. E., Travis, M. A. & Grecis, R. K. *Trichuris muris*: a model of gastrointestinal parasite infection. *Seminars in Immunopathology* **34**, 815-828, doi:10.1007/s00281-012-0348-2 (2012).
- 128 Bancroft, A. J., Else, K. J., Humphreys, N. E. & Grecis, R. K. The effect of challenge and trickle *Trichuris muris* infections on the polarisation of the immune response. *International Journal for Parasitology* **31**, 1627-1637, doi:[https://doi.org/10.1016/S0020-7519\(01\)00281-8](https://doi.org/10.1016/S0020-7519(01)00281-8) (2001).
- 129 Bancroft, A. J., Else, K. J. & Grecis, R. K. Low-level infection with *Trichuris muris* significantly affects the polarization of the CD4 response. *European Journal of Immunology* **24**, 3113-3118, doi:<https://doi.org/10.1002/eji.1830241230> (1994).
- 130 Hurst, R. J. M. & Else, K. J. *Trichuris muris* research revisited: a journey through time. *Parasitology* **140**, 1325-1339, doi:10.1017/S0031182013001054 (2013).
- 131 Lindholm, H. T. *et al.* BMP signaling in the intestinal epithelium drives a critical feedback loop to restrain IL-13-driven tuft cell hyperplasia. *Sci Immunol* **7**, eab16543, doi:10.1126/sciimmunol.ab16543 (2022).
- 132 Filbey, K., Bouchery, T. & Le Gros, G. The role of ILC2 in hookworm infection. *Parasite Immunology* **40**, e12429, doi:<https://doi.org/10.1111/pim.12429> (2018).
- 133 Okayasu, I. *et al.* A novel method in the induction of reliable experimental acute and chronic ulcerative colitis in mice. *Gastroenterology* **98**, 694-702, doi:[https://doi.org/10.1016/0016-5085\(90\)90290-H](https://doi.org/10.1016/0016-5085(90)90290-H) (1990).
- 134 Laroui, H. *et al.* Dextran Sodium Sulfate (DSS) Induces Colitis in Mice by Forming Nano-Lipocomplexes with Medium-Chain-Length Fatty Acids in the Colon. *PLOS ONE* **7**, e32084, doi:10.1371/journal.pone.0032084 (2012).
- 135 Kiesler, P., Fuss, I. J. & Strober, W. Experimental Models of Inflammatory Bowel Diseases. *Cellular and Molecular Gastroenterology and Hepatology* **1**, 154-170, doi:<https://doi.org/10.1016/j.jcmgh.2015.01.006> (2015).
- 136 Kałużna, A., Olczyk, P. & Komosińska-Vassev, K. The Role of Innate and Adaptive Immune Cells in the Pathogenesis and Development of the Inflammatory Response in Ulcerative Colitis. *J Clin Med* **11**, doi:10.3390/jcm11020400 (2022).
- 137 Chassaing, B., Aitken, J. D., Malleshappa, M. & Vijay-Kumar, M. Dextran Sulfate Sodium (DSS)-Induced Colitis in Mice. *Current Protocols in Immunology* **104**, 15.25.11-15.25.14, doi:<https://doi.org/10.1002/0471142735.im1525s104> (2014).

- 138 Wirtz, S. *et al.* Chemically induced mouse models of acute and chronic intestinal inflammation. *Nat Protoc* **12**, 1295-1309, doi:10.1038/nprot.2017.044 (2017).
- 139 Kim, C. K., Yang, V. W. & Bialkowska, A. B. The Role of Intestinal Stem Cells in Epithelial Regeneration Following Radiation-Induced Gut Injury. *Curr Stem Cell Rep* **3**, 320-332, doi:10.1007/s40778-017-0103-7 (2017).
- 140 Moser, A. R., Pitot, H. C. & Dove, W. F. A dominant mutation that predisposes to multiple intestinal neoplasia in the mouse. *Science* **247**, 322-324, doi:10.1126/science.2296722 (1990).
- 141 Taketo, M. M. & Edelmann, W. Mouse Models of Colon Cancer. *Gastroenterology* **136**, 780-798, doi:10.1053/j.gastro.2008.12.049 (2009).
- 142 Clevers, H. Modeling Development and Disease with Organoids. *Cell* **165**, 1586-1597, doi:<https://doi.org/10.1016/j.cell.2016.05.082> (2016).
- 143 Kim, J., Koo, B.-K. & Knoblich, J. A. Human organoids: model systems for human biology and medicine. *Nature Reviews Molecular Cell Biology* **21**, 571-584, doi:10.1038/s41580-020-0259-3 (2020).
- 144 Rossi, G., Manfrin, A. & Lutolf, M. P. Progress and potential in organoid research. *Nat Rev Genet* **19**, 671-687, doi:10.1038/s41576-018-0051-9 (2018).
- 145 van de Wetering, M. *et al.* Prospective Derivation of a Living Organoid Biobank of Colorectal Cancer Patients. *Cell* **161**, 933-945, doi:<https://doi.org/10.1016/j.cell.2015.03.053> (2015).
- 146 Huang, Y. *et al.* Research Progress, Challenges, and Breakthroughs of Organoids as Disease Models. *Frontiers in Cell and Developmental Biology* **9**, doi:10.3389/fcell.2021.740574 (2021).
- 147 Sato, T. *et al.* Single Lgr5 stem cells build crypt-villus structures in vitro without a mesenchymal niche. *Nature* **459**, 262-265, doi:10.1038/nature07935 (2009).
- 148 Sato, T. *et al.* Long-term Expansion of Epithelial Organoids From Human Colon, Adenoma, Adenocarcinoma, and Barrett's Epithelium. *Gastroenterology* **141**, 1762-1772, doi:10.1053/j.gastro.2011.07.050 (2011).
- 149 Taelman, J., Diaz, M. & Guiu, J. Human Intestinal Organoids: Promise and Challenge. *Frontiers in Cell and Developmental Biology* **10**, doi:10.3389/fcell.2022.854740 (2022).
- 150 Kurashima, Y. *et al.* Mucosal Mesenchymal Cells: Secondary Barrier and Peripheral Educator for the Gut Immune System. *Frontiers in Immunology* **8**, doi:10.3389/fimmu.2017.01787 (2017).
- 151 Kurahashi, M. *et al.* A functional role for the 'fibroblast-like cells' in gastrointestinal smooth muscles. *J Physiol* **589**, 697-710, doi:10.1113/jphysiol.2010.201129 (2011).
- 152 Kraiczy, J. *et al.* Graded BMP signaling within intestinal crypt architecture directs self-organization of the Wnt-secreting stem cell niche. *Cell Stem*










- Cell* **30**, 433-449.e438, doi:<https://doi.org/10.1016/j.stem.2023.03.004> (2023).
- 153 Qi, Z. *et al.* BMP restricts stemness of intestinal Lgr5⁺ stem cells by directly suppressing their signature genes. *Nature Communications* **8**, 13824, doi:10.1038/ncomms13824 (2017).
- 154 Huang, X.-T. *et al.* Embryogenic stem cell-derived intestinal crypt fission directs de novo crypt genesis. *Cell Reports* **41**, 111796, doi:<https://doi.org/10.1016/j.celrep.2022.111796> (2022).
- 155 Xiao, C., Wang, Y., Cheng, Q. & Fan, Y. Increased expression of MMP17 predicts poor clinical outcomes in epithelial ovarian cancer patients. *Medicine (Baltimore)* **101**, e30279, doi:10.1097/md.00000000000030279 (2022).
- 156 Yip, C. *et al.* MT4-MMP and EGFR expression levels are key biomarkers for breast cancer patient response to chemotherapy and erlotinib. *British Journal of Cancer* **116**, 742-751, doi:10.1038/bjc.2017.23 (2017).
- 157 Hieronimus, B., Pfohl, J., Busch, C. & Graeve, L. Expression and Characterization of Membrane-Type 4 Matrix Metalloproteinase (MT4-MMP) and its Different Forms in Melanoma. *Cell Physiol Biochem* **42**, 198-210, doi:10.1159/000477311 (2017).
- 158 Cervantes-Garduño, A. *et al.* MT4-MMP Modulates the Expression of miRNAs in Breast Cancer Cells. *Arch Med Res* **49**, 471-478, doi:10.1016/j.arcmed.2019.02.001 (2018).
- 159 Khurana, S. *et al.* Outside-in integrin signalling regulates haematopoietic stem cell function via Periostin-Itgav axis. *Nat Commun* **7**, 13500, doi:10.1038/ncomms13500 (2016).
- 160 Bao, S. *et al.* Periostin potently promotes metastatic growth of colon cancer by augmenting cell survival via the Akt/PKB pathway. *Cancer Cell* **5**, 329-339, doi:[https://doi.org/10.1016/S1535-6108\(04\)00081-9](https://doi.org/10.1016/S1535-6108(04)00081-9) (2004).
- 161 Ma, H. *et al.* Periostin Promotes Colorectal Tumorigenesis through Integrin-FAK-Src Pathway-Mediated YAP/TAZ Activation. *Cell Rep* **30**, 793-806.e796, doi:10.1016/j.celrep.2019.12.075 (2020).
- 162 Maruhashi, T., Kii, I., Saito, M. & Kudo, A. Interaction between periostin and BMP-1 promotes proteolytic activation of lysyl oxidase. *J Biol Chem* **285**, 13294-13303, doi:10.1074/jbc.M109.088864 (2010).
- 163 Zha, J.-M. *et al.* Interleukin 22 Expands Transit-Amplifying Cells While Depleting Lgr5⁺ Stem Cells via Inhibition of Wnt and Notch Signaling. *Cellular and Molecular Gastroenterology and Hepatology* **7**, 255-274, doi:<https://doi.org/10.1016/j.jcmgh.2018.09.006> (2019).
- 164 Hu, X., li, J., Fu, M., Zhao, X. & Wang, W. The JAK/STAT signaling pathway: from bench to clinic. *Signal Transduction and Targeted Therapy* **6**, 402, doi:10.1038/s41392-021-00791-1 (2021).
- 165 Lindemans, C. A. *et al.* Interleukin-22 promotes intestinal-stem-cell-mediated epithelial regeneration. *Nature* **528**, 560-564, doi:10.1038/nature16460 (2015).

- 166 Bergstrom, K. S. B. *et al.* Goblet Cell Derived RELM- β Recruits CD4+ T Cells during Infectious Colitis to Promote Protective Intestinal Epithelial Cell Proliferation. *PLoS Pathogens* **11**, e1005108, doi:10.1371/journal.ppat.1005108 (2015).
- 167 Sultana, M. F. *et al.* Identification of Crucial Amino Acid Residues for Antimicrobial Activity of Angiogenin 4 and Its Modulation of Gut Microbiota in Mice. *Frontiers in Microbiology* **13**, doi:10.3389/fmicb.2022.900948 (2022).
- 168 Artis, D. *et al.* RELM β /FIZZ2 is a goblet cell-specific immune-effector molecule in the gastrointestinal tract. *Proceedings of the National Academy of Sciences* **101**, 13596-13600, doi:doi:10.1073/pnas.0404034101 (2004).
- 169 Datta, R. *et al.* Identification of novel genes in intestinal tissue that are regulated after infection with an intestinal nematode parasite. *Infect Immun* **73**, 4025-4033, doi:10.1128/iai.73.7.4025-4033.2005 (2005).
- 170 Hasnain, S. Z. *et al.* Mucin gene deficiency in mice impairs host resistance to an enteric parasitic infection. *Gastroenterology* **138**, 1763-1771, doi:10.1053/j.gastro.2010.01.045 (2010).
- 171 Martín-Alonso, M. *Role of the protease MT4-MMP in the arterial vasculature* PhD thesis, Universidad Autónoma de Madrid, (2016).
- 172 Kacmaz, H. *et al.* A simple automated approach to measure mouse whole gut transit. *Neurogastroenterol Motil* **33**, e13994, doi:10.1111/nmo.13994 (2021).
- 173 Zhao, A. *et al.* Dependence of IL-4, IL-13, and Nematode-Induced Alterations in Murine Small Intestinal Smooth Muscle Contractility on Stat6 and Enteric Nerves1. *The Journal of Immunology* **171**, 948-954, doi:10.4049/jimmunol.171.2.948 (2003).
- 174 Masopust, D., Sivula, C. P. & Jameson, S. C. Of Mice, Dirty Mice, and Men: Using Mice To Understand Human Immunology. *The Journal of Immunology* **199**, 383-388, doi:10.4049/jimmunol.1700453 (2017).
- 175 Tao, L. & Reese, T. A. Making Mouse Models That Reflect Human Immune Responses. *Trends in Immunology* **38**, 181-193, doi:10.1016/j.it.2016.12.007 (2017).
- 176 Daoud, F. *et al.* Inducible Deletion of YAP and TAZ in Adult Mouse Smooth Muscle Causes Rapid and Lethal Colonic Pseudo-Obstruction. *Cellular and Molecular Gastroenterology and Hepatology* **11**, 623-637, doi:<https://doi.org/10.1016/j.jcmgh.2020.09.014> (2021).
- 177 Heo, J. H., Kang, D., Seo, S. J. & Jin, Y. Engineering the Extracellular Matrix for Organoid Culture. *Int J Stem Cells* **15**, 60-69, doi:10.15283/ijsc21190 (2022).
- 178 Rezakhani, S., Gjorevski, N. & Lutolf, M. P. Extracellular matrix requirements for gastrointestinal organoid cultures. *Biomaterials* **276**, 121020, doi:<https://doi.org/10.1016/j.biomaterials.2021.121020> (2021).

- 179 Sutherland, T. E., Dyer, D. P. & Allen, J. E. The extracellular matrix and the immune system: A mutually dependent relationship. *Science* **379**, eabp8964, doi:doi:10.1126/science.abp8964 (2023).

Paper 1

Smooth muscle-specific MMP17 (MT4-MMP) regulates the intestinal stem cell niche and regeneration after damage

Mara Martín-Alonso ^{1✉}, Sharif Iqbal^{2,3}, Pia M. Vornewald ¹, Håvard T. Lindholm ¹, Mirjam J. Damen⁴, Fernando Martínez ^{5,6}, Sigrid Hoel¹, Alberto Díez-Sánchez ¹, Maarten Altelaar ⁴, Pekka Katajisto ^{2,3,7}, Alicia G. Arroyo ^{8,9} & Menno J. Oudhoff ^{1✉}

Smooth muscle is an essential component of the intestine, both to maintain its structure and produce peristaltic and segmentation movements. However, very little is known about other putative roles that smooth muscle cells may have. Here, we show that smooth muscle cells may be the dominant suppliers of BMP antagonists, which are niche factors essential for intestinal stem cell maintenance. Furthermore, muscle-derived factors render epithelium reparative and fetal-like, which includes heightened YAP activity. Mechanistically, we find that the membrane-bound matrix metalloproteinase MMP17, which is exclusively expressed by smooth muscle cells, is required for intestinal epithelial repair after inflammation- or irradiation-induced injury. Furthermore, we propose that MMP17 affects intestinal epithelial reprogramming after damage indirectly by cleaving diffusible factor(s) such as the matricellular protein PERIOSTIN. Together, we identify an important signaling axis that establishes a role for smooth muscle cells as modulators of intestinal epithelial regeneration and the intestinal stem cell niche.

¹Centre of Molecular Inflammation Research, and Department of Clinical and Molecular Medicine, Norwegian University of Science and Technology, Trondheim, Norway. ²Institute of Biotechnology, HiLIFE, University of Helsinki, Helsinki, Finland. ³Molecular and Integrative Bioscience Research Programme, Faculty of Biological and Environmental Sciences, University of Helsinki, Helsinki, Finland. ⁴Biomolecular Mass Spectrometry and Proteomics, Bijvoet Center for Biomolecular Research and Utrecht Institute for Pharmaceutical Sciences, Utrecht University, Utrecht, Netherlands. ⁵Bioinformatics Unit, Centro Nacional de Investigaciones Cardiovasculares (CNIC), Madrid, Spain. ⁶Centro de Investigación Biomédica en Red de Enfermedades Cardiovasculares (CIBERCV), Madrid, Spain. ⁷Department of Cell and Molecular Biology, Karolinska Institutet, Stockholm, Sweden. ⁸Department of Molecular Biomedicine, Centro de Investigaciones Biológicas Margarita Salas (CIB-CSIC), Madrid, Spain. ⁹Vascular Pathophysiology Area, Centro Nacional de Investigaciones Cardiovasculares (CNIC), Madrid, Spain. ✉email: maria.m.alonso@ntnu.no; menno.oudhoff@ntnu.no

The intestinal epithelium consists of a single layer of cells that is important for the uptake of nutrients as well as for providing a barrier to protect from pathogens. During homeostasis, intestinal epithelial cells are all derived from LGR5+ intestinal stem cells (ISCs) that reside at the bottom of crypts¹. Upon injury, however, or after depletion of LGR5+ cells, LGR5-cells can rapidly regain LGR5 expression and thus dedifferentiate to repopulate the crypt bottoms^{2,3}. In addition, within this dedifferentiation process, an epithelial reparative state exists, which is fetal-like, and depends on reprogramming by YAP^{4,5}, and is further characterized by markers such as SCA-1 and HOPX^{4,6,7}.

Adult intestinal epithelial (stem cell) maintenance relies on a variety of niche factors such as WNTs, R-spondins (RSPOs), Bone morphogenic proteins (BMPs), and prostaglandins, all of which are expressed by mesenchymal cell subtypes^{8–13}. These mesenchymal cells reside in the intestinal lamina propria between the epithelium and the muscularis mucosae. Here we find several cell types characterized by specific marker expression and ultra-structural features in electron microscopy such as different types of telocytes (FOXL1^{14,15}, PDGFRA high), trophocytes (PDGFRA low⁸), fibroblasts, myofibroblasts (SMA+, Desmin–), and mesenchymal stromal/stem cells^{16,17}. However, intestinal epithelial homeostasis does not solely rely on soluble niche factors. The mechanical or extracellular matrix (ECM) niche is an additional defining factor, for example, by modulating the mechanosensory HIPPO/YAP pathway^{4,18}. In addition, growth factors can interact with, or be embedded within the ECM to modulate their activity. Smooth muscle cells reside in the muscularis mucosae, as a layer underneath the lamina propria, as well as outside of the mucosa in the muscularis propria in two thick layers, circular and longitudinal, and can be distinguished by being SMA and Desmin positive^{16,17,19}. Smooth muscle cells are one of the most prevalent non-epithelial cell types throughout the intestine, yet, their role in providing niche factors or affecting the ECM niche is largely unknown. Nevertheless, smooth-muscle-specific deletion of tumor suppressor genes can result in defective epithelial growth²⁰. Furthermore, it was shown that cells that originated from the smooth-muscle can migrate into the mucosa to aid after injury²¹. Nevertheless, it is still largely undefined what role adult smooth muscle has in ISC maintenance or during repair after injury.

Matrix metalloproteinases (MMPs) are fundamental ECM regulators, both by modifying ECM components directly and by cleaving growth factors to control their ability to bind the ECM and to the cell^{22–24}. MMPs can play various roles in the injured intestine and many MMPs are upregulated in inflammatory bowel disease, likely by the increase in immune cell populations such as neutrophils with high proteolytic activity or in endothelial cells^{25,26}. Thus, inhibition of MMP activity may be an attractive therapeutic target for treating inflammatory bowel disease^{26,27}. Although the role of certain MMPs such as MMP2, MMP7, MMP9, and MT1-MMP are relatively well-studied, the role of other MMPs in intestinal biology is still largely unknown. Here, we show that MMP17, a membrane-bound MMP which is specifically expressed in smooth muscle, is important to maintain optimal ISC stemness during homeostasis, and preserve the regenerative capacity of intestinal epithelium.

Results

Intestinal smooth muscle is a rich source of BMP antagonists. Based on recent indications that fetal intestinal muscle is a provider of niche factors²⁸, we first isolated the smooth muscle tissue from the muscularis propria (circular and longitudinal muscle) and part of the muscularis mucosae of adult mouse colon and performed RNA-seq comparing it to isolated colonic crypts

(Figs. 1a, b, S1a, S1b). We found little evidence that intestinal smooth muscle expressed niche factors such as WNTs and RSPOs, or growth factors such as epidermal growth factor (EGF), however, we did find that smooth muscle expresses high levels of factors associated with BMP signaling including *Grem1*, *Grem2*, and *Chrdn1* (Figs. 1b, S1b). Fluorescent in situ hybridization (FISH) confirmed high levels of these factors in a muscle-specific manner, in particular, we found enrichment of these factors in the muscularis mucosa that resides in close proximity to the bottom of epithelial crypts (Fig. 1c).

Intestinal smooth muscle provides niche factors that render organoid growth independent of NOGGIN. Intestinal organoids (including small-intestinal organoids derived from the duodenum (SI organoids) and colon-derived organoids (colonoids)) are self-organizing in vitro epithelial structures that are widely used to model in vivo processes^{29–31}. To test for a functional role of smooth muscle cells in providing niche factors, we exposed SI organoids to supernatant from muscle explants (muscle-SN) that completely lacked the mucosa (Fig. S1a). We found that organoids exposed to muscle-SN grew 2–3 times larger than in standard conditions and had a predominantly spheroid morphology (Fig. 1d–g). SI organoids rely on the supplementation of 3 factors epithelium itself does not express sufficiently: EGF, NOGGIN, and RSPO1 (ENR). Thus, we next tested whether muscle-SN could replace these factors. We found that muscle-SN was unable to replace RSPO1, as SI organoids failed to grow in RSPO1-deficient medium irrespective of muscle-SN supplementation (Fig. 1d, e). In contrast, we found that muscle-SN was able to substitute for the BMP antagonist NOGGIN (Fig. 1d, e). This is in support of our RNA-seq data in which we observed low *Rspo1/2/3* levels, but ample expression of BMP antagonists such as *Grem1* in smooth muscle tissue (Figs. 1b, c, S1b). ENR medium supports self-renewal and differentiation of SI organoids that acquire a typical structure including proliferative budding crypts and non-proliferative villus regions (Fig. 1f, g). In contrast, muscle-SN exposed SI organoids lacked crypts and consisted of mainly proliferative cells that were equally distributed along the spheroid (Fig. 1f, g). Our findings are not unique for colonic smooth muscle explants as we obtained similar results with muscle-SN derived from the small intestine (Figs. S2a, S2b).

MMP17 is a smooth muscle-specific MMP that is enriched in the muscularis mucosa. We find that intestinal smooth muscle expresses and secretes soluble niche factors that can mediate epithelial organoid growth (Fig. 1). Next, we wished to determine whether smooth muscle may also affect the ECM. The ECM acts on ISCs by providing a ‘mechanical’ niche as well as by being a reservoir of ECM-bound niche factors^{23,32,33}. MMPs are known as important modulators of the ECM^{22,34}. By directly comparing epithelial crypt and smooth muscle we found several MMPs to be specifically expressed in smooth muscle tissue (Fig. 2a), including *Mmp17* (also known as MT4-MMP), a previously identified regulator of muscle growth factors and its surrounding ECM²⁴. Therefore, we analyzed *Mmp17* expression in intestinal tissue by using the KO/KI mouse strain *Mmp17^{LacZ/LacZ}* (referred to as KO mice from hereon)³⁵. We used LacZ staining (Fig. S3a) or a specific anti β -gal antibody to detect *Mmp17* promoter activity in the intestine from *Mmp17^{LacZ/+}* mice. As shown in Fig. 2b, MMP17+ cells are exclusively smooth muscle cells, SMA+ and DESMIN+ (Fig. 2b, Fig. S3b). Of these, we observed more smooth muscle MMP17+ cells in the muscularis mucosae compared to the muscularis propria (longitudinal and circular muscle layers) (Fig. 2c). The expression pattern is reminiscent of the expression of BMP antagonists (Fig. 1c), and indeed, using FISH,

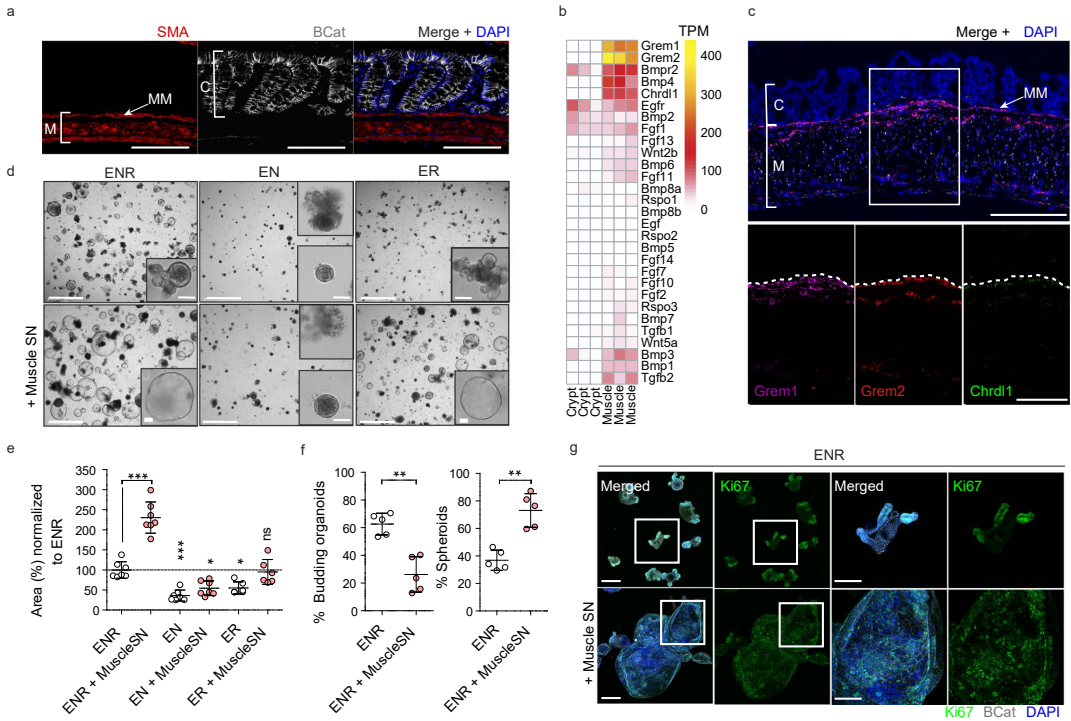


Fig. 1 Intestinal Smooth muscle expresses BMP antagonists that control epithelial behavior. **a** Representative confocal maximum intensity projection of a transverse colon cut showing specific staining for muscle (M), SMA (Red), and crypts (C), β Catenin (β cat, Gray). Clear distinction among muscularis mucosa (MM) close to the crypts and the muscularis propria (circular and longitudinal smooth muscle) can be observed. Scale bar 100 μ m. $n = 4$ mice. **b** Heatmap depicting gene expression levels in TPM (Transcripts per million) in crypts vs muscle intestinal samples. $n = 3$ biological replicates. **c** Representative confocal maximum intensity projections of fluorescence-coupled RNAscope showing BMP antagonists *Greml1* in magenta, *Greml2* in red, and *Chrdl1* in green, expressed in smooth muscle cells. Scale bar 100 μ m; 50 μ m in the magnified image. $n = 2$ mice. **d** Representative bright-field pictures showing SI organoids morphological changes when exposed to muscle-derived factors (Day4). Control media ENR (EGF, NOGGIN, RSP01) or ER (no NOGGIN) were used to assess SI organoids reliance on external growth factors. Scale 1250 μ m; 100 μ m in magnified image. **e** Graph shows SI organoids area in response to different media. Depicted average values normalized to ENR condition. $n = 6$ (for ER and ER + MuscleSN) to 7 (the rest) independently performed experiments. Each dot corresponds to the average of 2-3 wells/experiment. **f** Graphs represent the percentage of budding organoids or spheroids in response to ENR or ENR+ muscle supernatant (Muscle-SN). $n = 5$ independently performed experiments with 2-3 wells/experiment. **g** Representative maximum projection confocal images showing proliferative active cells (Ki67) in green and cell shape (β cat, gray) staining. Scale 200 μ m, 100 μ m in magnified image. $n = 3$ independent experiments. Numerical data are means \pm SD. Data were analyzed by one-way ANOVA ($F = 57.06$, $p < 0.0001$) followed by Bonferroni's multiple comparison test (ENR vs ENR + Muscle SN $***p < 0.001$; ENR vs EN $***p < 0.001$; ENR vs EN + Muscle SN $*p < 0.05$; ENR vs ER $*p < 0.05$; ENR vs ER + Muscle SN, ns, not significant.) **(e)** or by Mann-Whitney-test, two-tailed ($**p = 0.0079$ in both) **(f)**. Source data are provided as a Source Data file.

we find that *Mmp17* has an overlapping expression pattern with these BMP antagonists including enrichment in the muscularis mucosa (Fig. 2d).

Muscle-specific MMP17 controls BMP signaling in crypts. Since MMP17 is enriched in the muscularis mucosa smooth muscle cells where its expression correlates with BMP antagonists, we asked about the possible impact of MMP17 loss in crypts. To unbiasedly gain mechanistic insight, we performed RNA-seq comparing WT and KO colonic smooth muscle and crypts. *Mmp17* is expressed in smooth muscle cells but not in the epithelium (Fig. 2), and we were surprised to find that only 42 genes were dysregulated in the KO smooth muscle whereas 191 genes were dysregulated in KO crypts compared to their WT counterparts (Fig. 3a). In support, principal component analysis (PCA) was unable to distinguish WT from KO smooth muscle, whereas KO crypts had a different distribution

compared to WT crypts (Fig. 3b). Furthermore, *Mmp17* absence in intestinal smooth muscle cells did not result in any structural alteration at the smooth muscle level (Fig. S4a). Upon closer examination, using the online gene enrichment tool Enrichr^{36,37}, we found SMAD4 as the top TF associated with upregulated genes in KO crypts (Figs. 3c, S4c). To test whether increased SMAD4 target genes in KO crypts were a direct result of SMAD4 protein levels, we performed immunostaining and western blot for SMAD4. Corroborating our unbiased transcriptome analysis, we found heightened nuclear localization of SMAD4 in the bottom of KO crypts compared to WT crypts, and increased levels of total SMAD4 in KO mucosa (Fig. 3d, e). The nuclear translocation or overall accumulation of SMAD4 is the result of cellular activation by TGF β family members, including BMPs that specifically induce SMAD1/5/9 phosphorylation³⁸. Indeed, we found pSMAD1/5/9 to be particularly enriched in the bottom of KO crypts compared to WT

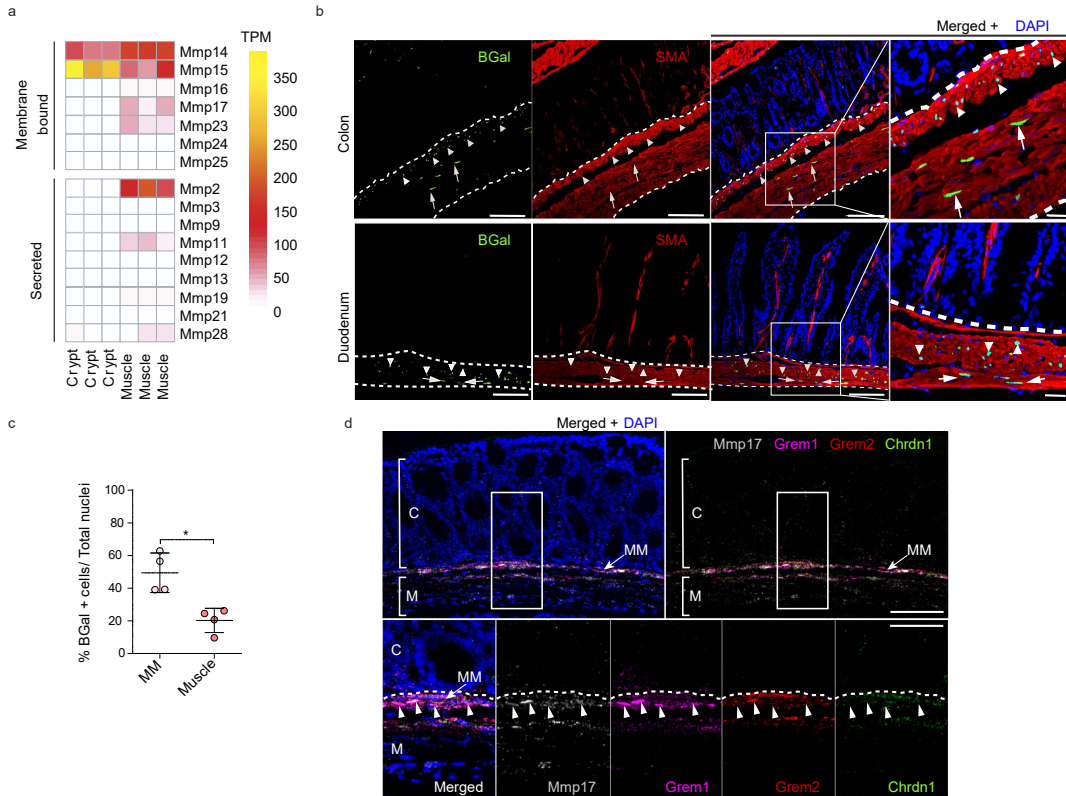


Fig. 2 Muscle-specific matrix metalloproteinase Mmp17 is enriched in the muscularis mucosa together with BMP antagonists expressing cells.

a Heatmap shows TPM levels of Matrix Metalloproteinases (MMPs) in the crypts vs muscle. **b** Representative confocal microscopy images showing active Mmp17 promoter (β Gal staining, green) in positive SMA (red) muscle (white dashed line) stained in transverse intestinal sections of *Mmp17* \pm mice. Scale bar 100 μ m; 20 μ m in the magnified image. **c** Graph shows quantification of the % number of β Gal positive cells in muscularis mucosa (MM) vs circular and longitudinal muscle (Muscle) in colon samples. **d** Representative confocal maximal projections of fluorescence-coupled RNAscope showing *Mmp17* (gray), and BMP antagonists (*Grem1*, magenta, *Grem2*, red and *Chrdn1*, green) co-expression in muscular cells (arrowheads). C, crypts, M, Muscle and MM, muscularis mucosa. Scale bar 100 μ m; 50 μ m in the magnified image. $n = 2$ independent experiments with 1–2 samples/genotype. Numerical data in (**c**) are means \pm SD and was analyzed by Mann-Whitney test (two-sided, $*p = 0.0286$). Source data are provided as a Source Data file.

crypts (Fig. 3f), which suggests altered BMP signaling in KO intestinal epithelium.

MMP17 regulates the ECM-ISC niche necessary for epithelial de novo crypt formation. SMAD signaling is essential to maintain ISCs, which is exemplified by the requirement of the BMP antagonist NOGGIN in intestinal organoid maintenance²⁹. To test if MMP17 affects ISCs, we quantified levels of the ISC markers *Lgr5* and *Olfm4* by ISH. We found that KO intestinal tissue had lower *Lgr5* and *Olfm4* levels compared to WT tissue in both the small and large intestines (Fig. 4a, b). In addition, decreased ISC marker gene expression was echoed by reduced colonoid and SI organoid formation efficiency comparing KO with WT crypts (Figs. 4c and S5, respectively). Importantly, colonoids splitting, or culturing with excessive niche factors (WNR medium), resulted in equal organoid efficiency between WT and KO cultures (Fig. 4d). These data indicate that the reduced capacity of KO crypts to form organoids relied on the in vivo niche rather than a consequence of an intrinsic epithelial defect. To formally test whether MMP17 controls the ‘ECM niche’, we utilized a recently

developed regeneration assay³⁹ in which small intestinal epithelium was cultured on decellularized small intestinal extracellular matrix (iECM). Unlike Matrigel-based closed format organoids, here, organoids engraft on the iECM by first generating an epithelial monolayer³⁹. After initial attachment in a monolayer, de novo crypt formation occurs on former crypt pits, and thus is surrounded by the tissue native ECM. Since the reparative growth of the epithelium does not rely on Matrigel during the culture on iECM—this system was used to investigate the role of the extracellular niche on ISC function ex vivo³⁹. When we cultured wild-type epithelium on WT and KO iECM, we observed a robust reduction of the de novo crypt formation on KO iECM (Fig. 4e–g). This suggests a poor regeneration supporting capacity of KO iECM.

MMP17 is required for intestinal repair after inflammation or radiation-induced injury. De novo crypt formation is important during epithelial repair which is needed upon injury, for example after the damage inflicted by inflammation or due to irradiation. To test if smooth muscle, and in particular MMP17, could play a

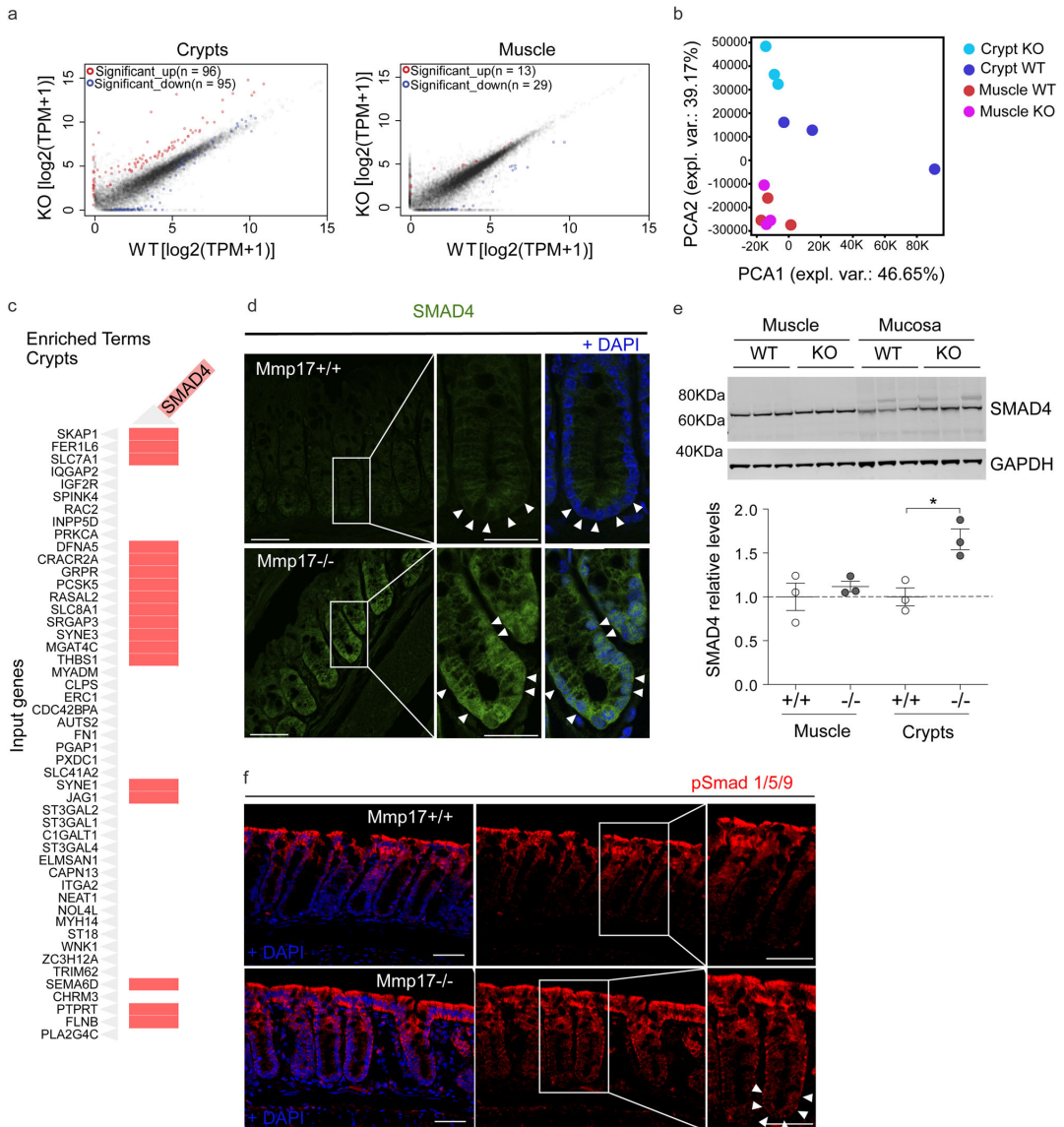
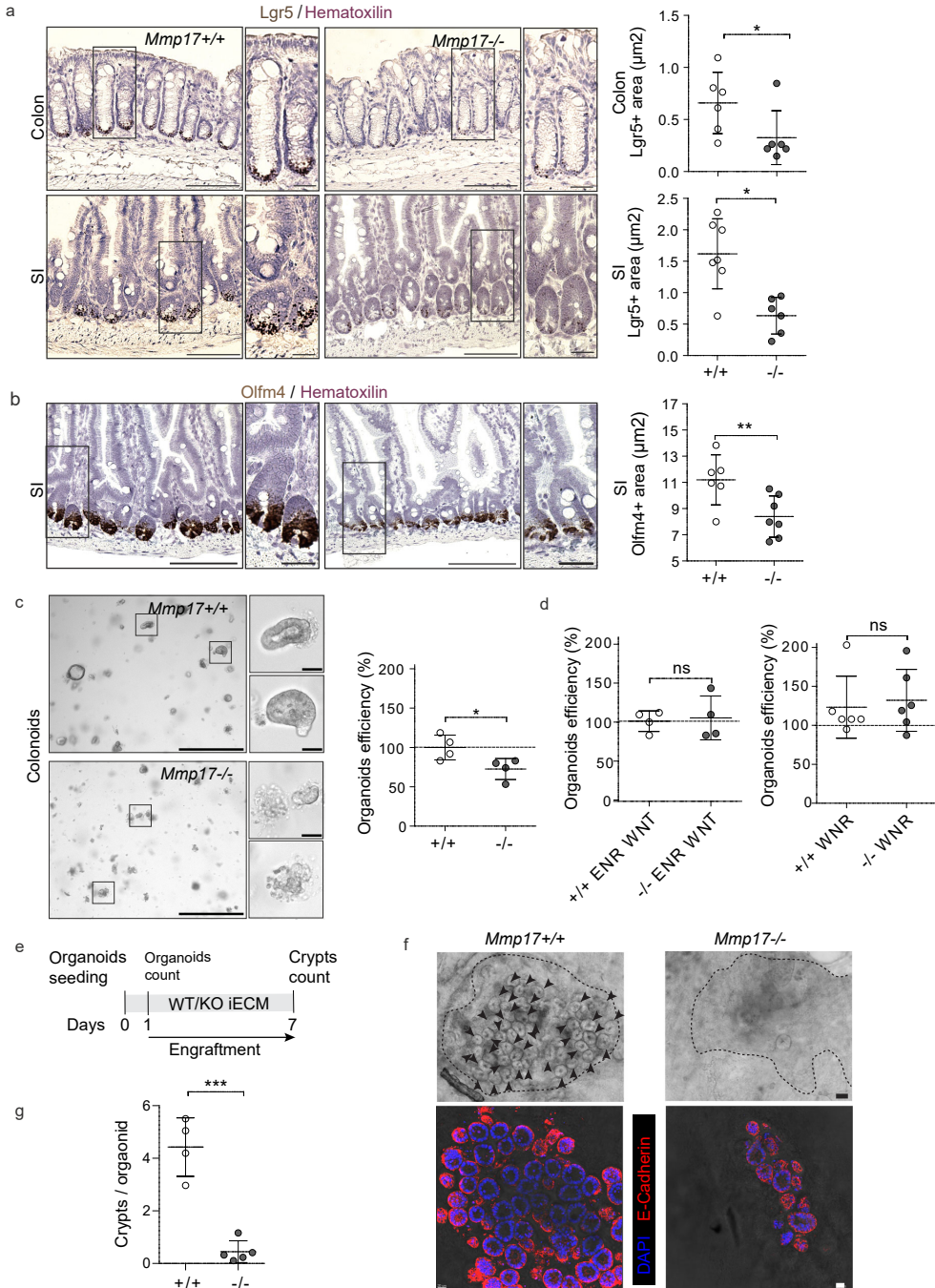


Fig. 3 Muscle *Mmp17* regulates crypts BMP signaling. **a, b** RNA seq assay comparing WT and *Mmp17* KO crypts, we showed that loss of MMP17 in the muscle strongly affects epithelial gene expression to a greater extent than muscle gene expression. $n = 3$ biological replicates. **c** Graph shows the presence of genes related to SMAD4 signaling among the upregulated genes in WT vs KO crypts. **d, e** We observed higher SMAD4 signaling that was further confirmed by immunofluorescence in **(d)** (arrowheads indicate nuclear location in *Mmp17* KO) and western blot **(e)**. $n = 3$ mice/genotype. Scale bar 50 μ m, 25 μ m in magnified views to the right. **f** Representative confocal images showing pSmad 1/5/9 staining in intestinal crypts of WT vs KO mice. Arrowheads highlight crypt base pSmad 1/5/9 staining. Scale 50 μ m. $n = 3$ independent experiments with 2–4 samples/genotype. Numerical data in **(e)** are means \pm SD and were tested by one-way ANOVA ($F = 7.43$, $p = 0.0106$) followed by Tukey's test (WT vs KO Crypts * $p < 0.05$). Source data are provided as a Source Data file.

role in intestinal injury responses, we used dextran sulfate sodium (DSS) to induce experimental colitis and compare WT to KO littermates (Fig. 5a). On day 5, we found that both WT and KO mice had indistinguishable features of disease indicating that damage was induced equally (Fig. S6a–e). Of note, during DSS, MMP17 (BGal) expression remained limited to smooth muscle

cells as CD45⁺ infiltrating cells were BGal negative (Fig. S6f). After 5 days, DSS was replaced by regular drinking water to allow for intestinal repair, which is initiated rapidly and requires reprogramming of the intestinal epithelium^{4,9}. Two days after DSS, KO mice had shorter colons and sustained hemorrhage, including an increased presence of blood in stool compared to



WT mice (Fig. 5b, c). Furthermore, other disease features were also exacerbated in KO mice compared to WT mice. We found that KO mice had a higher injury score than WT mice, as was determined using a genotype-blind injury classification based on H&E images (Fig. 5d, e). H&E analysis further revealed a larger area of ulcerated mucosa and lower presence of epithelial crypts

in KO mice compared to WT mice (Fig. 5e, f). In addition, we found a significant reduction in the proliferative epithelium in KO mice (Fig. 5g, h), suggesting that epithelial reprogramming towards a reparative state relies on MMP17. This reprogramming it is known to rely on the activation of YAP signaling, which is characterized by an induction of (nuclear) YAP^{4,5}. Indeed, we

Fig. 4 Muscular Mmp17 regulates crypt formation. **a, b** *Lgr5/Olfm4* RNAscope representative images of WT vs KO intestines and their quantification. Scale bar 100 μm ; 25 μm in inset. $n = 6$ mice per genotype in Colon Lgr5 and WT Olfm4 and 7 mice per genotype in the rest. **c** Representative bright-field images of colonoids from WT vs KO crypts 48 h after crypt isolation (left). Scale 650 μm ; 50 μm in cropped image. Graph shows relative colonoids number as percentage normalized to WT. $n = 5$ experiments performed. One representative experiment is shown in which each dot represents a well. **d** Graphs represent the percentage of colonoids after the first split (left) and the percentage of colonoids derived from colon crypts after 72 h in response to the enriched medium WNR (right). $n =$ pooled 4 wells per condition in ENR WNT experiments and 6 wells per condition in WNR experiment performed in two independent experiments. **e** Schematic of crypt formation assay on iECM; SI organoids were seeded on the iECM, counted on day 1 for attachment and survival and left to engraft into the scaffold until Day7. de novo crypts per seeded organoid (as assessed at day 1) were counted at day 7 post plating. The number of de novo crypts was counted by brightfield imaging as shown in **(f)**. **f** Representative brightfield (top) and fluorescent (bottom, E-Cadherin (red), DAPI (blue), images showing epithelial crypt formation in WT and KO iECM. Arrows demonstrate the de novo formed crypts. Scale bar 50 μm (brightfield) and 20 μm (fluorescent). $n = 2$ (fluorescent) to 5 (brightfield) mice per genotype. **g** Quantification of number of crypts in WT and KO iECM. $n = 4$ WT and 5 KO mice pooled from two independent experiments (based on brightfield imaging). Numerical data are means \pm SD and were tested by Mann-Whitney test (two-sided, with the following p values; $p = 0.0411$ (colon) and $p = 0.0140$ (SI) in **(a)**; $p = 0.0082$ in **(b)** and $p = 0.0378$ in **(c)**) and Student's unpaired t -test (two-tailed, $p < 0.0001$) in **(g)**. Source data are provided as a Source Data file.

observe YAP-high reparative epithelium in WT tissues, however, this was nearly absent in KO tissue (Fig. 5i). This suggest that KO epithelium is unable to properly make the transition from normal to a reparative state.

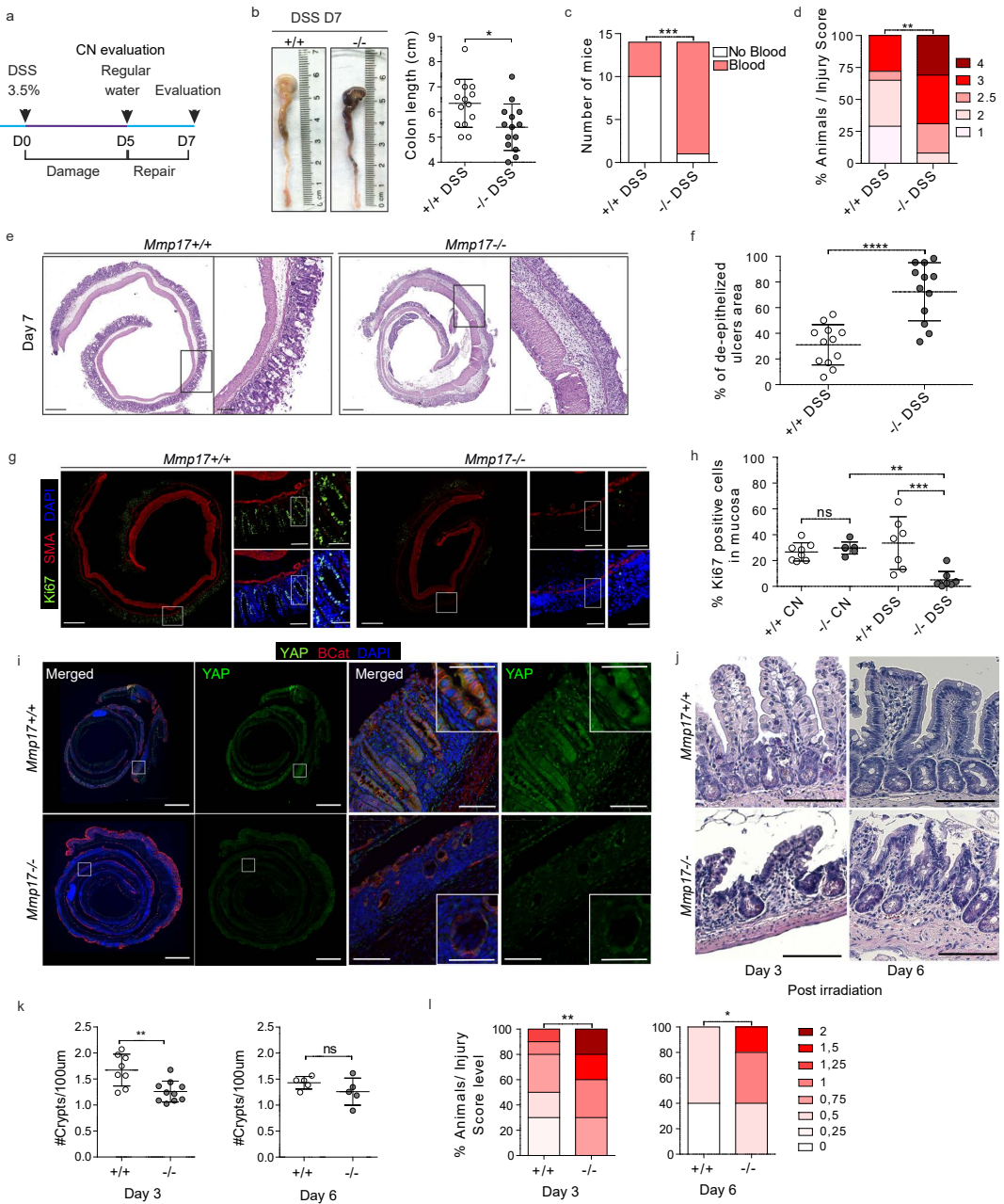
Next, we performed an alternative non-inflammatory injury model based on whole-body irradiation. Indeed, a single dose of ionizing radiation (10 Gy) induces equal apoptosis in WT and KO intestines (Fig. S6g). As custom in this model, WT animals regained crypt structures 3 days after irradiation, which was delayed in KO animals and was only observed by day 6 (Fig. 5j, k). A genotype-blinded evaluation of damage features in H&E images showed increased signs of damage in small intestines of KO mice compared to WT mice 3 and 6 days after irradiation (Figs. 5l and S6h). Together, these data suggest that muscle-specific MMP17 plays a role in intestinal repair processes after damage.

Mmp17 loss results in long-term reparative epithelial defects and increased tumor risk. We wondered whether the intestines of KO mice would eventually heal, and thus we evaluated weight gain for a prolonged time after DSS administration (Fig. 6a, b). WT mice rapidly returned to their original weight; however, KO mice never fully regained their starting weight (Fig. 6b for females, Fig. S7a for males). In support, while WT mice largely returned to homeostatic conditions at end point, KO mice retained shorter colons, experienced sustained blood in stool, still had areas of unhealed ulcers in the epithelial surface and had higher injury scores compared to WT mice (Fig. 6c–h). In addition, we detected the presence of crypt distortions named reactive atypia, and these morphological changes were predominantly found in KO mice (Figs. 6f, g, S7b). These morphological changes resemble those found in intestinal neoplastic lesions, so we next decided to evaluate the impact of *Mmp17* loss in the initiation and progression of intestinal tumors using the *Apc*^{Min} mouse model. *Apc*^{Min} mice develop tumors primarily in the small intestinal epithelium⁴⁰. We found that loss of *Mmp17* predispose mice to the formation of a higher number of tumors both quantified macroscopically (Fig. 6i), and microscopically using H&E-stained sections (Fig. 6j). We did not observe differences in tumor diameter (Fig. S7c) suggesting that MMP17 mediates tumor initiation but not tumor progression. In support, WT and KO tumors were indistinguishable in terms of β -CATENIN and OLFM4 distribution (Fig. S7d). Of note, *Mmp17* expression was restricted to muscle cells also in tumor areas (Fig. S7e). In sum, our data indicate that MMP17 is required for short and long-term intestinal epithelial repair and its loss predisposes to intestinal neoplastic alterations.

Muscle-SN induces a reparative epithelial state in organoids via activation of YAP, and is sufficient to rescue regenerative growth of WT epithelium on KO iECM.

Since we observed that smooth muscle MMP17 is essential for intestinal repair we wondered whether muscle indeed could promote epithelial reprogramming towards a reparative state. We found that muscle-SN can replace NOGGIN in the culture media, and muscle-SN treated organoids grow as large spheroids (Fig. 1). Organoid spheroid growth can either be characterized as reparative that is associated with fetal-like gene programs, such as organoids derived from SCA-1+ cells⁷, or it can be the result of increased WNT signaling such as upon treatment with the GSK3 inhibitor CHIR⁴¹. These two different organoid spheroid states are on opposite ends when it concerns ISCs; a reparative state is characterized by a loss of LGR5+ ISCs whereas ISCs expand upon CHIR treatment⁴⁷. To determine what type of spheroids are induced by muscle-SN, we performed RNA-seq comparing normal organoids to muscle-SN treated SI organoids (Fig. 7a). Using gene set enrichment analysis, we found a distinct enrichment of gene sets associated with fetal and reparative programs in muscle-SN treated SI organoids^{4,7} (Fig. 7b). Intestinal epithelial repair programs are coupled with YAP signaling and, indeed, an intestinal epithelial YAP signature gene set was also enriched in muscle-SN treated SI organoids⁵ (Fig. 7b). In contrast, genes associated with LGR5+ cells⁴², as well as genes upregulated in SI organoids treated with CHIR⁴¹, were downregulated in muscle-SN treated organoids (Fig. 7b, Supplementary Data 1 includes all gene sets). In support, we found that YAP was localized nuclear throughout muscle-SN induced spheroids, whereas it was cytoplasmic in the center of budding SI organoids (Fig. 7c). In addition, in a side-by-side comparison we find that muscle-SN induces larger spheroids than treatment with CHIR, and that treatment with the YAP inhibitor Verteporfin completely abolished muscle-SN driven growth (Fig. 7d). Together, we conclude that muscle-SN induces spheroid growth that is associated with reparative/fetal-like reprogramming that may be mediated by YAP.

Next, we examined whether muscle-SN or recombinant MMP17 (rMMP17) could rescue the impaired regenerative growth of epithelium on KO iECM (Fig. 4e, f). We tested the regenerative growth on WT and KO iECM by supplementing it with muscle-SN derived from WT and KO mice or rMMP17 (Fig. 7e). We found that WT, but not KO, muscle-SN increased the crypt formation on KO iECM (Fig. 7e). Similarly, rMMP17 incubation led to increased crypt formation on KO iECM (Fig. 7e). In contrast, the different treatments of WT iECM did not affect de novo crypt formation (Fig. 7e). Taken together, these findings highlight that the enzymatic activity of MMP17 is necessary for the reparative growth of intestinal epithelium.



PERIOSTIN is a muscle-derived factor cleaved by MMP17 and that can activate YAP and induce organoid growth. MMP17 is expressed by intestinal smooth muscle cells and is required to allow for epithelial repair in vivo (Figs. 5, 6). Furthermore, muscle-SN is able to reprogram epithelium towards a reparative state in vitro and can stimulate de novo crypt formation (Fig. 7). We, therefore, hypothesize that MMP17 cleaves a smooth muscle-derived factor that facilitates epithelial reprogramming that is needed for repair. To identify said factor, we examined smooth

muscle-derived proteins by performing mass-spectrometry on muscle-SN, and we detected 550 proteins (Supplementary Data 2). We next curated this list to only display proteins known to be growth/niche factors and/or extracellular proteins (Fig. 8a). Among these was PERIOSTIN (POSTN), which is a matricellular protein that is highly expressed in smooth muscle (Fig. 8b). We previously identified a different matricellular protein, OSTEO-PONTIN (OPN), as an MMP17 substrate²⁴ (Fig. S8a). Of note, POSTN can serve as a ligand for ITGAV to activate AKT and

Fig. 5 Muscle-specific Mmp17 is required for intestinal repair after injury. **a** Timeline of DSS treatment. **b** Representative colonic images from DSS-treated animals. Graph shows colon length, and blood in stool and/or colonic cavity at D7 in **(c)**. $n = 14$ from five independent experiments. **d** Histology-based blind scoring of DSS-derived injury in the colon. $n = 14$. **e** Images of H&E staining of the distal colon. Scale 500 μm ; 100 μm in magnified. **f** Graph represents damaged mucosa as % of total length. $n = 12$. **g** Images of DSS-treated distal colon stained for Ki67 (Green), SMA (Red) and DAPI (Blue). Scale 500 μm ; 100 (left) and 50 (right) μm . **h** Graph shows % of Ki67+ cells in mucosa, normalized to total mucosal cell number. $n = 7$ mice in KO CN and WT DSS and eight mice per genotype in the rest. **i** Representative images of DSS-treated distal colon stained for YAP (green), β -Cat (red), and DAPI (blue). Scale = 1 mm (tile scan), 100 and 50 μm (insets). $n = 3$. **j** Representative images of H&E sections of small intestine 3 and 6 days after 10 Gy irradiation. Scale 100 μm . $n = 7$ WT, 8 KO analyzed from two independent experiments at Day 3 and $n = 5$ from Day 6. **k** Graph shows quantification of crypts/100 μm on Day3 and Day6 post irradiation. $n = 8$ WT, 10 KO at Day 3, and $n = 5$ at Day 6. **l** Blind scored injury level in irradiated mice. $n = 8$ WT, 10 KO (Day3) and $n = 5$ (Day 6). Numerical data in **(b)**, **(f)**, **(h)**, and **(k)** are represented as means \pm SD. Data in **(b)**, **(f)** and **(k)** were tested by unpaired *t*-test (two-tailed) with $p = 0.0127$ in **(b)**, $p < 0.0001$ in **(f)** and $p = 0.0033$ in **(k)**. Data in **(c)** was analyzed by Fisher's exact test (One-tailed, $p = 0.0007$) and **d** and **l** were analyzed by Mann-Whitney test (two-sided) ($p = 0.0030$ in **(d)**, $p = 0.0078$ and $p = 0.0434$ in day 3 and 6 in **(l)**, respectively). One-way ANOVA ($F = 10.01$; $p = 0.0009$), was applied in **(h)**, followed by Tukey's Multiple Comparison test ($-/-\text{CN vs } -/-\text{DSS}$ $^{**}p < 0.01$; $+/+ \text{DSS vs } -/-\text{DSS}$ $^{***}p < 0.001$). Source data are provided as a Source Data file.

YAP signaling^{43–45}. Further, POSTN has been proposed to capture BMP members in the ECM⁴⁶. These features may be relevant for biological processes we identified to be affected by MMP17. Co-incubation of human POSTN with MMP17 led to several POSTN fragments indicating MMP17 is able to cleave POSTN (Fig. 8c). In addition, we examined POSTN in MMP17-WT and KO smooth muscle and we found a decrease in POSTN fragments in KO muscle samples, suggesting that cleavage of POSTN also occurs in vivo and it is impaired in KO intestines (Fig. 8d). Next, we used mass spectrometry (MS) to identify putative cleavage sites in POSTN after incubation with MMP17. After tryptic digestion we found at least nine cleavage sites that had five or more peptide-spectrum matches and were not caused by tryptic digestion (Figs. 8e, S8b,c). Several of these could explain the presence of the ~25 kDa fragment we found in vivo as all identified cleavage sites are conserved in both mice and human. In order to define which of these cleavage sites could be targeted in vivo, we modeled in silico the interaction between MMP17 active form (membrane-bound MMP17 dimer) and POSTN. As shown in the 3D model of Fig. 8f (and Fig S8c) cleavage site 664 between I and P amino acids was the best-suited candidate, located at MMP17 active site. In addition, three other cleavage sites in the POSTN molecule, 157VN, 291MG, and 793GG, would be accessible for cleavage according to in silico docking. Of note, cleavage of 291MG would expose the Integrin alpha-5 binding motif of POSTN which is located within amino acids 300–314 in the FAS2 domain⁴⁷. Finally, we found that POSTN itself modestly induces SI organoid growth that is associated with the induction of Ki67 and nuclear YAP (Fig. 8g–j).

Discussion

The role of smooth muscle cells in the intestine, other than in peristalsis, has been largely undefined. However, in a recent preprint, it was found that in early human gut development ACTA2+ muscularis mucosa cells are the major source of WNT, RSPO, and GREM niche factors⁴⁸. In contrast, in adult mice, there have been various mucosa-resident mesenchymal cell populations described that express *Rspo* and *Wnt* genes^{10,12,13}. We here find that smooth muscle cells, and in particular, the ones residing in the muscularis mucosa, are the primary source of BMP antagonists such as *Grem1/2* (Fig. 1). The importance of GREMLIN1 as an ICS niche factor was recently determined by an experiment in which *Grem1*-expressing cells were depleted using the diphtheria-toxin system, which also led to the rapid loss of LGR5+ ISCs⁸. Based on our results, this experiment would thus have led to the death of practically all muscularis-mucosa smooth muscle cells. Our work here highlights the importance of smooth muscle for providing niche factors important for ISC homeostasis. Thus, future studies are warranted in which niche factors

are deleted in a cell-type specific manner to determine the relative importance of each cell type as a niche factor provider.

We find an important role for MMP17 in vivo. We show that KO mice have a reduction of ISC-associated genes in homeostasis (Fig. 4), which may be caused by increased levels of SMAD4 at the bottom of KO crypts (Fig. 3). Indeed, BMP signaling can impair ISC-signature genes by direct repression via SMAD1/4 recruitment of HDAC1⁴⁹. We further identify that MMP17 is required for intestinal epithelial repair after injury, which we potentially link to the ability of MMP17 to cleave POSTN. We hypothesize that MMP17 cleavage of POSTN is necessary upon injury to reprogram epithelial cells in a YAP-dependent manner. Thus, cleavage of POSTN by MMP17 is an activation step in our model. However, there may be other smooth-muscle cell-derived factors in play as POSTN was only able to induce organoid area by 25% compared to double or triple the size by Muscle-SN, even though we observed YAP activation in both (Figs. 7c and 8j). Recently, Ma *et al.* described a role for POSTN in activating YAP/TAZ through an integrin-FAK-Src pathway using colon cancer cell lines⁴⁵. In addition, it was found that POSTN can act through Integrin alpha-5 in various cell types^{43,44}. We here extend these findings and show that POSTN can also affect primary non-tumor intestinal epithelial cells (Fig. 8). In addition to this direct role affecting the epithelium, others have shown that POSTN can alter the ECM by binding to a variety of ECM-associated proteins including BMP1, FIBRONECTIN, and TENASCIN-C⁵⁰. We speculate that through this link with the ECM, cleaved POSTN may broadly affect intestinal homeostasis in vivo, which would be impaired in MMP17-deficient mice such as we observe. In addition, others have also shown that POSTN is cleaved for example by CATHEPSIN K which results in a 35–40 kDa product during bone remodeling⁵¹. Finally, *Postn*-deficient mice have general issues with repair in various tissues^{52,53}. Thus, although the importance of cleavage of POSTN remains not fully comprehended⁵⁴, it is clear that POSTN plays an important role in reparative processes and the identification of MMP17 as an enzyme that can cleave POSTN can be used in future studies.

MMP17, unlike other MMP members, exert minimal activity against classical ECM components⁵⁵. So far, only a few bona fide substrates have been described in other tissue environments, such as ADAMTS-4⁵⁶, alphaM integrin⁵⁷, and two matricellular proteins; OPN²⁴ and POSTN described in this work. We cannot discard the possibility that these or other unidentified MMP17 substrates play a role in ISCs niche regulation or the intestinal response to injury, particularly OPN which expression is increased in patients with inflammatory bowel disease⁵⁸. Furthermore, in a tumor environment, both ADAMTS4 and OPN are overexpressed in colon cancers^{59–61}. Finally, also non-

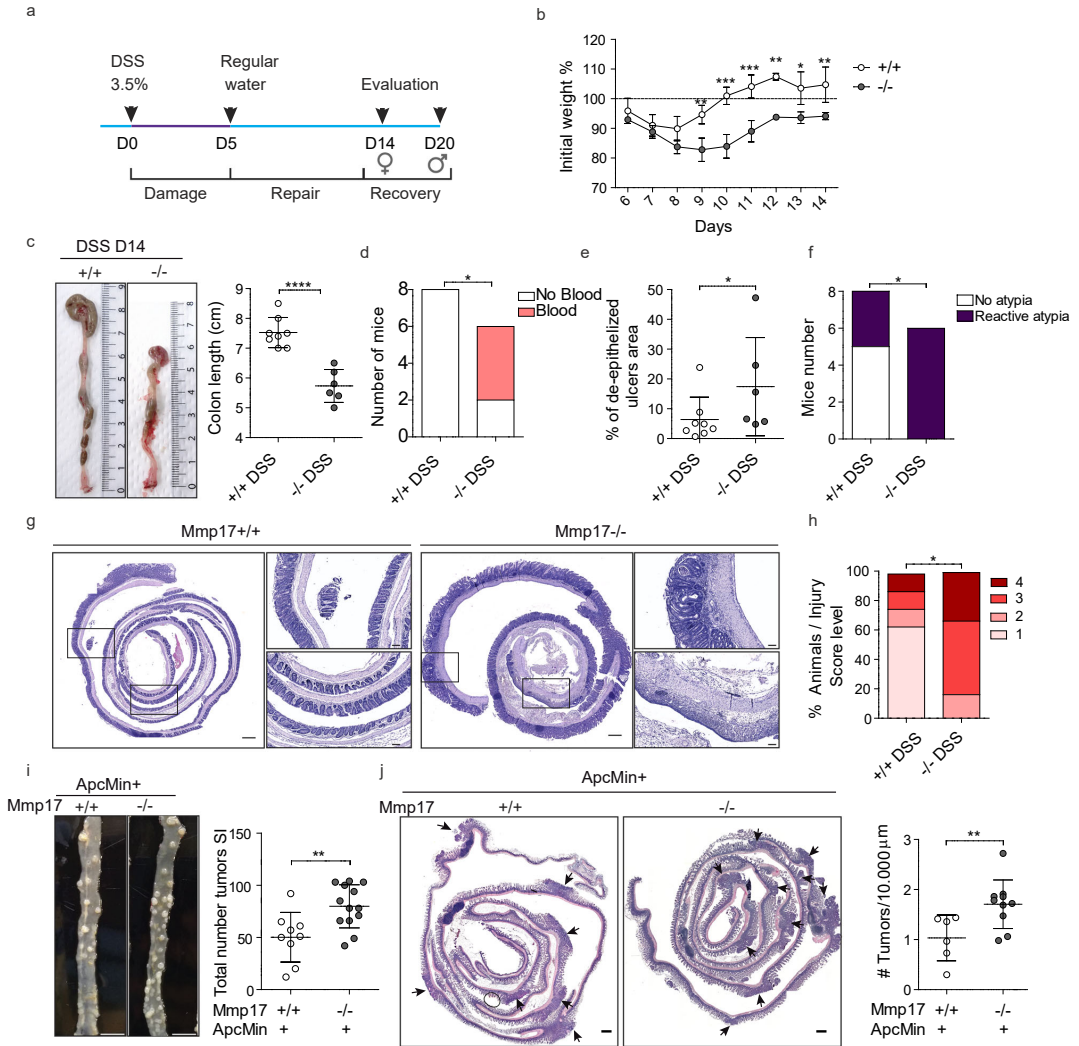


Fig. 6 MMP17 absence hinders long-term repair in mouse intestinal epithelia and leads to increased tumorigenesis. **a** Timeline of DSS-long treatment. Mice were exposed to 3.5% DSS for 5 days followed by 14 (females) or 19 days (males) days of regular water to allow epithelial restoration. **b** Weight loss relative to % to initial weight. $n = 3$ KO and 4 WT mice per genotype. Represented one experiment with females. **c** Representative images showing colon length at end point and its quantification. **d** Graph shows the presence of blood in stool/colon lumen at end point. **e** Graph represents the percentage of unhealed areas (ulcers) in WT and KO colonic mucosa at end point. **f** Graph shows the incidence of reactive atypia (or reactive epithelial changes after DSS). **g** Representative H&E pictures of colon swiss rolls showing healed crypts in WT vs ulcered areas and reactive atypia in KO. Scale 500 μm . **h** Injury score representation of damaged colon evaluation. $n = 6$ KO and 8 WT mice per genotype in (c–h). **i** Representative pictures showing tumor incidence in a portion of the small intestine of *ApcMin* + *Mmp17* WT and KO mice (Jejunum). Scale bar 1 cm. Graph shows total number of tumors counted in fresh tissue (small intestine complete length). $n = 9$ WT and 13 KO mice per genotype. **j** H&E representative images of small intestine swiss rolls in transverse cut. Arrows highlight visible tumors. Scale bar 500 μm . Graph shows tumor quantification normalized to tissue length. $n = 6$ WT and 10 KO mice per genotype. Numerical data in (b) was analyzed by two-way ANOVA ($F = 11.56$, $***p < 0.001$), followed by Bonferroni post-test, asterisks correspond to comparison between WT and KO in each time point ($*p < 0.05$, $**p < 0.01$, $***p < 0.001$). Fisher’s exact test, one tailed was used in (b) and (f) ($p = 0.0150$ in (d) and $p = 0.0280$ in (f)). Numerical data in e and h were analyzed by Mann–Whitney *t*-test (two-sided) with $p = 0.0296$ in (e) and $p = 0.0230$ in (h). Data in (c), (i), (j) were analyzed by unpaired *t*-test (two-tailed, $p < 0.0001$ in (c), $p = 0.0055$ in (i) and $p = 0.0075$ in (j)). Source data are provided as a Source Data file.

catalytic activities for MMP17 have been described related to tumors⁶².

To summarize, we discover a previously unappreciated role for intestinal smooth muscle tissue. We find that smooth muscle cells

are likely the major contributors of BMP antagonists, which are essential niche factors for the maintenance of ISCs. In addition, we describe an important role for smooth-muscle restricted expression of MMP17, which *in vivo* is required for epithelial

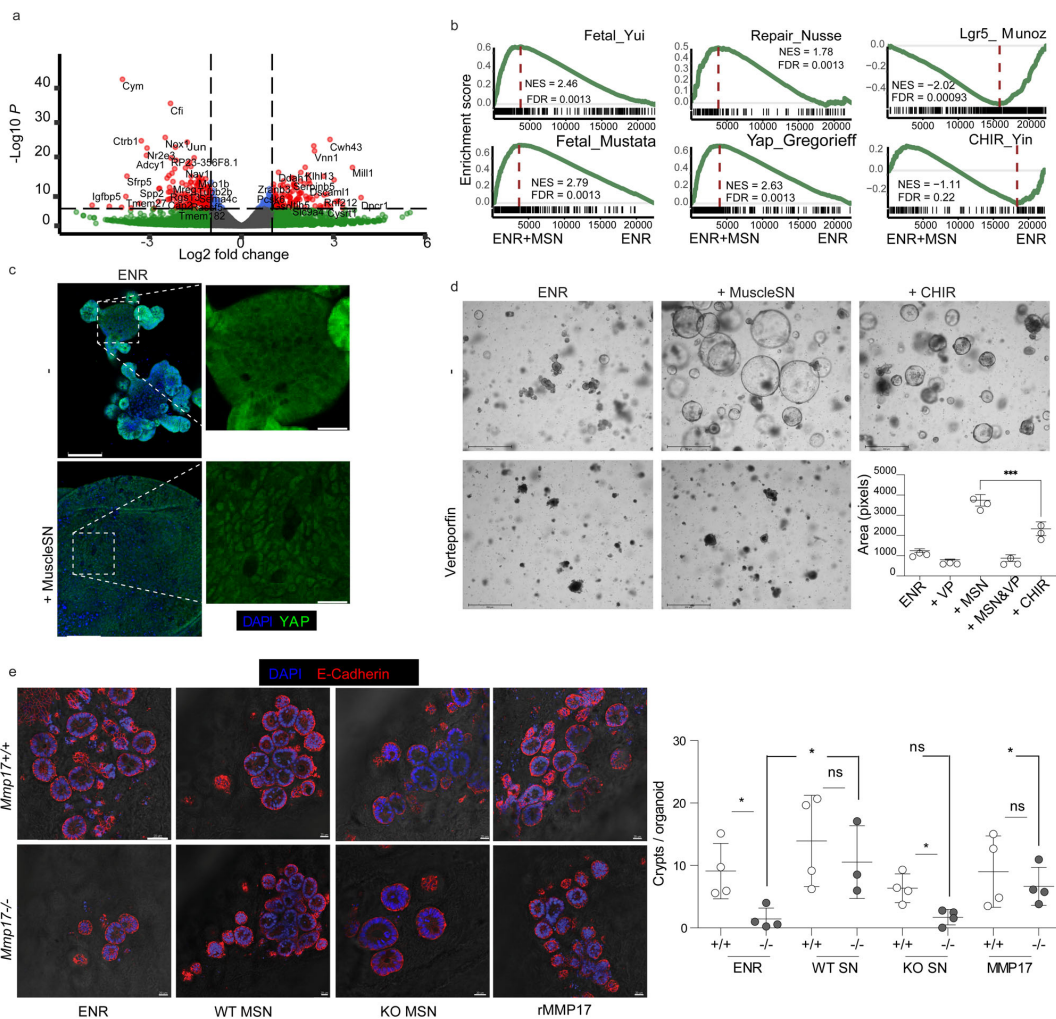


Fig. 7 Muscle-SN induces a reparative epithelial state in organoids and rescues the reparative growth on KO iECM. a Volcano plot showing significantly up and downregulated genes in SI organoids exposed to muscle-SN vs ENR. **b** GSEA of indicated gene sets comparing ENR with Muscle-SN (MSN) treated SI organoids. NES (normalized enrichment score) and FDR (false discovery rate) are depicted. **c** Representative maximal projection confocal images showing cytoplasmic vs nuclear YAP staining (green) in ENR vs Muscle-SN treated SI organoids. Scale 100 μm; insert is 25 μm. *n* = 2 independent experiments. **d** Representative images of WT SI organoids 3 days after splitting (scale is 650 μm), grown in the presence of indicated factors. Average area per organoid was quantified for three independent wells. **e** Representative immunofluorescent images of de novo crypt formation on WT and KO iECM with different treatment conditions. Matrigel-cultured 3-day old SI organoids were plated on WT and KO iECM. Adhered organoids were quantified at day 1 post-planting and de novo crypt formation per organoid was analyzed at day 7. Culture media was supplemented with either WT MSN, KO MSN, or rMMP17. Scale bar 40 μm. *n* = 4 samples per condition analyzed in two independent experiments. Numerical data are means ± SD and were tested by one-way ANOVA (*F* = 98.8; *p* < 0.0001) followed by Bonferoni post-test (MSN vs CHIR *p* < 0.001) in **(d)**. Numerical data in **(e)** is average of crypts per iECM pooled from two independent experiments (*n* = 4 mice). One-way ANOVA (*F* = 3.714; *p* = 0.0079) and unpaired *t*-test to compare groups (**p* < 0.05). Source data are provided as a Source Data file.

repair. Finally, we provide evidence that MMP17 may act via cleavage of the matricellular protein POSTN, which in itself can induce repair-like features in the intestinal epithelium.

Methods

Mice. *Mmp17*^{-/-} mice in the C57BL/6 background have been described previously³⁵. Mice were handled under pathogen-free conditions in accordance with CoMed NTNU institutional guidelines. Experiments were performed

following Norwegian legislation on animal protection and were approved by the local governmental animal care committee. Particularly, experimental designs for DSS, irradiation procedures, and ApcMin mice colony handling and tumor evaluation, were approved in advance by Norwegian authorities as stated in FOTS protocols (11842, 15888, and 17072). Mice included in these protocols were carefully monitored daily or weekly to avoid situations of moderate to high pain and comply with ethical procedures established prior to experiment development in agreement with CoMed facility at NTNU. End point protocols were applied when needed. All mice were genotyped by PCR of earclip samples using the following primers: Mt4-mmp SK1 5'-TCAGACACAGCCAGATCAGG-3' SK2

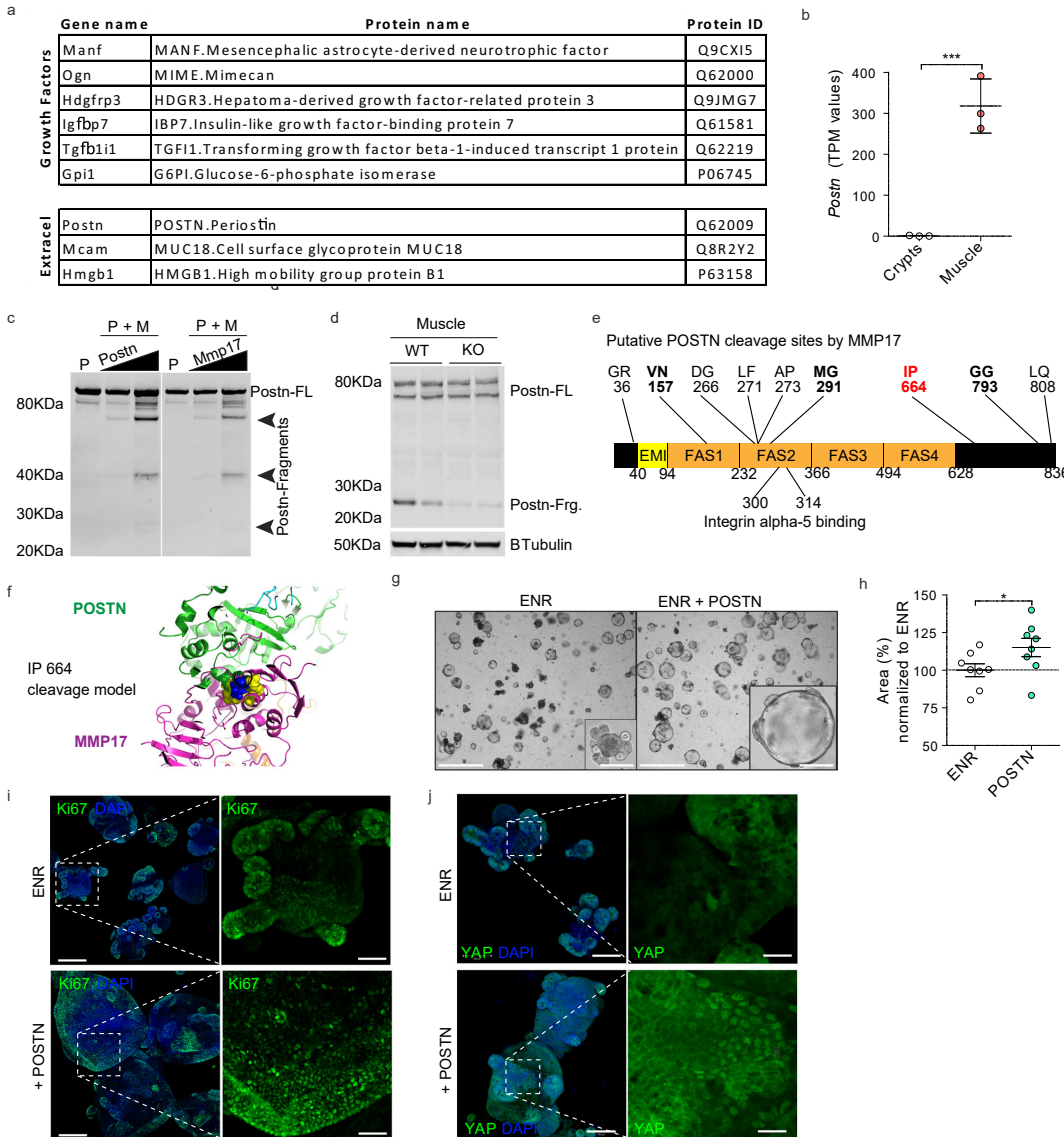


Fig. 8 Identification of smooth muscle-derived factor PERIOSTIN as an *in vivo* and *in vitro* substrate for MMP17. **a** List of growth factors and extracellular proteins found in muscle-SN. $n = 3$ biological replicates. **b** TPM values for *Postn* comparing crypts with smooth muscle tissue. $n = 3$ biological replicates. **c** *In vitro* digestion experiment with human recombinant proteins showing POSTN fragments when in contact with MMP17 catalytic domain. P, POSTN, M, MMP17, FL, full length. $n = 2$ experiments with increasing concentrations of POSTN or MMP17. **d** WB of mouse intestinal muscle showing decreased POSTN fragments in the absence of MMP17. $n = 2$ biological replicates. **e** Scheme of POSTN molecule showing putative sites of MMP17 cleavage based on digestion assays followed by MS. Sites that are noted all had 5 or more peptide-spectrum matches (PSMs). In blue and red are available sites after *in silico* modeling (see Fig. 8f for a model of the best fitted (red) site). **f** *In silico* model of MMP17 (magenta)-POSTN (green) docking showing close proximity of 664-665 POSTN cleavage site (cyan) to MMP17 catalytic site (yellow). **g, h** Representative brightfield images showing SI organoids morphology in the presence of POSTN and area quantification in **(h)** (Day 3). Scale 1250 and 200 μm in inset. $n = 8$ wells/genotype pooled from three independently performed experiments with 2-3 wells/experiment. **i, j** Representative confocal maximum intensity projection images showing YAP or Ki67 (green) staining in POSTN-treated SI organoids. Scale 100 μm ; 25 μm in inset (YAP pictures) and 200 μm and 100 μm in Ki67 pictures. Numerical data are means \pm SD. Data in **(b)** represents p -adjusted value from RNAseq analysis (padj value of $1.02\text{e}-06$), and data in **(h)** was analyzed by Mann-Whitney test (two-sided, $p = 0.0260$). Source data are provided as a Source Data file.

5'-AGCAACACGGCATCCACTAC-3' and SK3 5'-AATATGCGAAGTG-GACCTGG-3' and ApcMin: 1. 5'-TTCCACTTTGGCATAAGGC-3' 2. 5'-GCCATCCCTTCACGTTAG-3' 3. 5'-TTCTGAGAAAACAGAGAAGTTA-3'. Experiments were conducted on mice from 8 weeks to 20 weeks of age.

Small intestine and colon crypt isolation. Small intestinal crypts were isolated and cultured following previously published protocol to generate SI organoids⁶³. Colonoids were cultured according to a published method³¹. Briefly, 10 first cm of the duodenum or the entire colon, were excised, flushed with cold PBS, and opened longitudinally. The internal surface of the duodenum was scrapped carefully with a coverslip to remove most of the mucus and part of the intestinal villus. Small pieces of duodenum or colon (2–4 mm in length) were cut with scissors and further washed with ice-cold PBS until the supernatant was clear. Next, tissue fragments were incubated in cold 2 mmol/L EDTA chelation buffer, for 30 min (small intestine) to 1 h (colon) at 4 °C. After removal of the EDTA buffer, tissue fragments were vigorously resuspended in cold PBS (small intestine) or cold chelation buffer (colon) using a 10-mL pipette-BSA coated to isolate intestinal crypts. The tissue fragments were allowed to settle down under normal gravity for 1 min, and the supernatant was removed for inspection by inverted microscopy. The resuspension/sedimentation procedure was repeated typically 8 times and the supernatants containing crypts (from wash 1 to 8) were collected in 50-mL Falcon tubes coated with BSA, through a 70 μ m cells strainer to remove villi in case of the SI. Isolated crypts were pelleted, washed in PBS, and centrifuged at 200 \times g for 3 min at 4 °C to separate crypts from single cells. Crypts were resuspended in 10 ml basal crypt medium (BCM, advanced Dulbecco's modified Eagle medium -F12 supplemented with penicillin/streptomycin, 10 mM HEPES, 2 mM Glutamax) to quantify its number. After centrifugation and supernatant removal, crypts were resuspended in matrigel (Corning, 734-1101) and plated in P24 well plates (150 to 250 crypts/well) or 8-well ibidi imaging μ slides (80821, Ibidi). Crypts were cultured in ENR (BCM+ factors, explained below).

Intestinal organoid culture. SI organoids were cultured in ENR medium consisting of BCM (advanced Dulbecco's modified Eagle medium -F12 supplemented with penicillin/streptomycin, 10 mM HEPES, 2 mM Glutamax) + 1 \times N2 [ThermoFisher Scientific 100 \times , 17502048], 1 \times B-27 [ThermoFisher Scientific 50X, 17504044], and 1 \times N-acetyl-L-cysteine [Sigma, A7250] and overlaid with ENR factors containing 50 ng/ml of murine EGF [Thermo Fisher Scientific, PMG8041], 20% R-Spondin-CM (conditioned medium, a kind gift from Calvin Kuo, Stanford University School of Medicine, Stanford, CA, USA), 10% Noggin-CM. For colonoids, same medium and reagents were used, plus 65% Wnt-CM (kind gifts from Hans Clevers, Hubrecht Institute, Utrecht, The Netherlands). We also made use of L-WRN (ATCC 3276) cell line conditioned media, which is considered as enriched media due to higher levels of Wnt, R-spondin, and Noggin than in the described ENR. Medium was renewed every other day. For passaging, organoids cultures were washed, and matrigel and organoids were disrupted mechanically by strong pipetting, centrifuged at 300 \times g, 5 min at 4 °C and resuspended in matrigel to plate in P24 wells or eight-well ibidi chambers (80821, Ibidi). In different experiments SI organoids and/or colonoids were exposed to ENR, ER, EN mediums, muscle-SN, obtained as explained below, human recombinant Periostin (50–500 ng) (3548-F2-050, R&D), CHIR99021 (3 μ M, Sigma-Aldrich), or Verteporfin (3 μ M, Sigma-Aldrich) for 3–5 days.

Intestinal smooth muscle isolation and muscle-SN collection. Smooth muscle samples were obtained as followed: after flushing with cold PBS, whole mice colon or 10 first cm of mice duodenum were open in longitudinal to expose the epithelial part and dissected under a bench scope. Using a coverslip, the epithelium and most of the mucosa (except the muscularis mucosae) were carefully removed under the dissection scope. The remaining tissue was further inspected under the microscope for residual crypts or fat and further cleaned. Samples were then fixed in PFA4% and stained as described below to ensure the presence of exclusively muscularis propria (circular and longitudinal layers) and some portions of muscularis mucosae and for the absence of epithelium. Smooth muscle samples were deep frozen in N2 (for RNA seq or WB analysis), rolled into swiss rolls for immunostaining, or cut in small pieces of muscle strips (around 2–4 mm long) used to obtain muscle-SN. To obtain this supernatant, the samples were then washed with sterile PBS twice, spin down, and collected in P24 well plates. One piece of muscle (2–4 mm) was included in each P24 well and cultured in 1 ml of DMEM-F12 for 24 h. Muscle-SN from different wells were then pooled and filtered (0.20 μ m) and used directly + ENR factors in organoid cultures (right after splitting), sent for MS evaluation or frozen at –80 °C. Organoids were exposed to muscle-SN for 4–5 days. Muscle samples were obtained from the colon and used to obtain Muscle-SN, in RNA seq, WB or MS experiments. Small intestinal tissue was used for smooth muscle isolation for data in Fig. S2.

Quantification and imaging of organoids. P24 well plates were imaged using automatized Z-stack in EVOS2 microscope with CO₂, temperature, and humidity-controlled incubation chamber (Thermo-Fisher Scientific). SI organoid area and classification were evaluated using a custom analysis program written in python based on opencv2 (Lindholm et al., 2020). Images were autoscaled, and a canny

edge detection algorithm was run on each individual z-plane using the cv2.canny function. Small pixel groups were removed and a minimal projection of the edges was generated. The contour of objects was defined based on this image. A watershed algorithm was used to split somewhat overlapping objects from each other and the object center was defined as the pixel furthest from the edge of the object. Each object was extracted in a 120 \times 120 image on a white background and classified as either "Junk", "Budding" or "Spheroid" in a neural network implemented and trained using Tensorflow and Keras. A custom visual classification editor was then used to correct the locations of organoid centers and the classification group. The order of images was randomized, and treatment information hidden during the classification correction. The images then went through a second segmentation step where the segmentation was re-done as described above. The objects of contours with multiple centers were then split apart with a watershed algorithm that used the corrected organoid centers to split overlapping organoids. Organoids formation efficiency in SI organoids and in colonoids was calculated by manually counting the number of successful organoids 24, 48, and 72 h after crypt isolation in EVOS2 bright field pictures. SI organoids size was evaluated from day 1 to 5. For muscle-SN experiments quantification was performed at day 4 and at day 3 in POSTN treatments.

Immunofluorescence staining in organoids and imaging. For immunofluorescent labeling and imaging, SI organoids were grown in 70% Matrigel-30% ENR on eight-chamber ibidi μ slides (80821, Ibidi). SI organoids were fixed in PBS containing 4% paraformaldehyde (pH 7.4) and 2% sucrose for 30–45 min, permeabilized, and blocked in PBS-Triton X-100 0.2%, 2% normal goat serum (NGS), 1% BSA Glycine 100 μ M for 1 h at RT. Next, SI organoids were incubated with primary antibodies against the following antigens diluted in PBS-TX100 0.2% + BSA 0.5% + NGS 1%: Ki67 (1:200, rabbit monoclonal antibody (mAb), Invitrogen, MA5-14520), β -catenin (1:200, mouse mAb, BD Biosciences, 610154), and YAP (1:100, rabbit mAb, Cell Signaling, 14074) overnight at 4 °C with slow agitation. Organoids were washed in PBS containing 0.1% Tween20 and incubated overnight in the same buffer at 4 °C with the appropriate Alexa Fluor secondary antibody (1:500) along with Hoechst 33342 (1:10,000). SI organoids were washed with PBS buffer with 0.1% Tween 20 and mounted using Fluoromount G (ThermoFisher Scientific, 00-4958-02). SI organoids were imaged in a Zeiss Airyscan confocal microscope, using a 10x and 20x objective lens. Images were analyzed using Zen black edition software (Zeiss) and maximal projections are shown. For immunofluorescent staining on re-epithelialized iECM—samples were fixed with 4% PFA for 20 min, and blocked with blocking buffer (5% Horse serum, 0.2% BSA, and 0.3% Triton X-100 in PBS) for 30 min at room temperature. Samples were then incubated with Anti-E-Cadherin antibody (DECM-1 clone, Sigma, MABT26) and DAPI (1 μ g/ml, Sigma) for 48 h at +4 °C on a shaker. Following the washes (3 \times) with the blocking buffer, samples were incubated with Alexa Fluor secondary antibody overnight at +4 °C. Samples were incubated with 80% glycerol in PBS overnight before imaging with Leica TCS SP8 STED confocal microscope.

RNA seq of organoids and tissue. Pieces of clean colon muscle, colon crypts (obtained using colon crypt isolation protocol previously described), or pooled SI organoids were used for RNA isolation. Tissues were first placed in lysis buffer (RLT, provided in RNeasy[®] Mini Qiagen Kit, 74104) and disrupted with sterile ceramic beads (Magna Lyser green beads tubes 03358941001) using a Tissue Lyser (FastPrep-24[®], SKU 116004500), with two rounds of 6500 rpm for 30 s each, with care taken to maintain the sample cold. SI organoid wells were first disrupted by strong pipetting and pelleted before lysis. RNA isolation was performed following manufacturer instructions (RNeasy[®] Mini Kit, Qiagen, 74104, for tissue and Direct-zol[™] RNA MiniPrep, BioSite R-2052, for organoids). RNA was quantified by spectrophotometry (ND1000 Spectrophotometer, NanoDrop, Thermo Scientific) and 25 μ l at a 50 ng/ μ l concentration of RNA were used for RNA seq. Library preparation and sequencing for tissue RNA seq was performed by NTNU Genomic Core facility. Lexogen SENSE mRNA library preparation kit was used to generate the library and samples were sequenced at 2 \times 75 bp paired end using Illumina NS500 flow cells. Library preparation and sequencing for organoid RNA seq was performed by Novogene (UK) Co. NEB Next[™] Ultra[™] RNA Library Prep Kit was used to generate the library and samples were sequenced at 150 \times 2 bp paired end using a Novaseq 6000 (Illumina). The STAR aligner was used to align reads to the Mus musculus genome build mm10^{64,65}. featureCounts was used to count the number of reads that uniquely aligned to the exon region of each gene in GENCODE annotation M18 of the mouse genome⁶⁶. Genes that had a total count of <10 were filtered out. DESeq2 with default settings was used to do a differential expression analysis⁶⁷. Heatmaps were generated using the R-package heatmap⁶⁸. PCA analysis was done with the scikit-learn package using the function sklearn.decomposition.PCA⁶⁹. Gene set enrichment analysis (GSEA) was performed on the full list of genes from differential expression sorted by log₂ fold change and with log₂ fold change as weights. GSEA was run with the R package clusterProfiler using 10,000 permutations and otherwise default settings⁷⁰. A list of the top 250 genes upregulated in crypts was used for Enrichr analysis^{36,37}.

All raw sequencing data are available online through ArrayExpress: WT and KO smooth muscle and crypt RNA seq: E-MTAB-9180; ENR vs MuscleSN treated SI organoids RNA seq: E-MTAB9181.

Mass spectrometry of muscle-SN. Muscle supernatants were collected as stated above. For each sample, 100 ml of soluble protein was taken and proteins were reduced with 4 mM DTT at room temperature for 1 h, and alkylated with 8 mM iodoacetamide at room temperature for 30 min in the dark, after which additional 4 mM DTT was added. A first digestion was carried out with 40 ng Lys-C at 37 °C for 4 h. The samples were diluted four times and further digested with 40 ng trypsin at 37 °C overnight. Digested protein were desalted using Sep-Pak C18 cartridges (Waters), dried by vacuumcentrifuge and stored at -20 °C for further use.

For MS analysis the peptides were dissolved in 2% formic acid and 5 μ l of each digested sample was injected on an UHPLC 1290 system (Agilent) connected to an Orbitrap Q Exactive HF spectrometer (Thermo Scientific). Reconstituted peptides were trapped on an in-house packed, double-fritted (Dr Maisch Reprosil C18, 3 μ m, 2 cm \times 100 μ m) precolumn for 5 min in solvent A (0.1% formic acid in water) at 5 μ l/min before being separated on an analytical column (Agilent Poroshell, EC-C18, 2.7 μ m, 50 cm \times 75 μ m). Solvent A consisted of 0.1% formic acid, solvent B of 0.1% formic acid in 80% acetonitrile. Separation was performed at a column flow rate of ~300 nl/min (split flow from 0.2 ml/min) using a 95 min gradient of 13–44% buffer B followed by 44–100% B in 3 min and 100% B for 1 min was applied. MS data were obtained in data-dependent acquisition mode. Full scan MS spectra from m/z 375–1600 were acquired at a resolution of 60,000 to a target value of 3×10^6 or a maximum injection time of 20 ms. The top 15 most intense precursors with a charge state of 2+ to 5+ were chosen for fragmentation. HCD fragmentation was performed at 27 normalized collision energy on selected precursors with 16 s dynamic exclusion at a 1.4 m/z isolation window after accumulation to 1×10^5 ions or a maximum injection time of 50 ms. Tandem mass spectrometry (MS/MS) spectra were acquired at a resolution of 30,000.

Proteins IDs and intensity values (abundance) are represented in Supplementary Data 1.

MS data analysis. All raw MS files were searched using MaxQuant software (version 1.6.10.43). MS/MS spectra were searched by Andromeda against a reviewed Uniprot Mus Musculus (17,068 entries, 2020) using the following parameters: trypsin digestion; maximum of three missed cleavages; cysteine carbamidomethylation as fixed modification; oxidized methionine and protein N-terminal acetylation as variable modifications. Mass tolerance was set to 20 ppm for MS1 and MS2. The protein and PSM False Discovery Rate (FDR) were set to 1%.

Recombinant MMP17-Periostin cleavage site discovery. Recombinant Human periostin (3548-F2-050 R&D systems) and MMP17 (human) recombinant (P4928 Abnova) were dissolved in 50 mM Tris-HCL, 10 mM CaCl₂, 80 mM NaCl pH7.4 to reach a concentration of 250 ng/ μ l. 18 μ l MMP17 and 72 μ l Periostin were mixed and incubated for 2 h at 37 °C. After incubation 22.5 μ l of sample buffer with DTT (XT sample buffer 4x Bio-Rad) was added. Samples were heated for 5 min 95 °C, before loading on a 12% gel (Criterion, Bio-Rad). The gel was run for ~3 cm, then stopped and stained with Imperial safe stain (Pierce, Thermo). The gel lane was cut in 3 pieces and the excised gel pieces were reduced with DTT, alkylated with iodoacetamide, and in-gel digested with trypsin⁷¹.

Samples were analyzed with LC-MS performed on an UltiMate 3000 RSLCnano System (Thermo Scientific) coupled to a Orbitrap Exploris (Thermo Scientific). Peptides were first trapped onto an in-house packed precolumn (3 μ m C18 Dr. Maisch Reprosil, 2 cm \times 100 μ m) and eluted for separation onto an analytical column (Agilent Poroshell, EC-C18, 2.7 μ m, 50 cm \times 75 μ m). Solvent A consisted of 0.1% formic acid, solvent B of 0.1% formic acid in 80% acetonitrile. Trapping was performed for 5 min at 5 μ l/min flowrate in solvent A. Peptides were separated at a column flowrate of 300 nl/min by a 95 min gradient of 12–44% buffer B, followed by 30–100% B in 3 min, 100% B for 1 min.

The mass spectrometer was operated in data-dependent acquisition (DDA) mode. Full scan MS was acquired from 375–1600 m/z with a 60,000 resolution at 400 m/z and an accumulation target value of 3e6 ions. Up to 15 most intense precursor ions were selected for HCD fragmentation performed at normalized collision energy (NCE) 27, after accumulation to target value of 1E5. MS/MS acquisition was performed at a resolution of 30,000.

Proteome data (RAW files) were analyzed by Proteome Discoverer (version 2.4.1.15, Thermo Scientific) using Percolator and standard settings. MS/MS data were searched against the Swissprot database (564277 entries, 01-2021) with Mascot. The maximum allowed precursor mass tolerance was 10 ppm and 0.05 Da for fragment ion masses. False discovery rates for peptide and protein identification were set to 5%. Trypsin was chosen as cleavage specificity allowing two missed cleavages. Carbamidomethylation (C) was set as a fixed modification, while oxidation (M) and acetyl (Protein N-term) were used as variable modifications.

Tissue immunostaining and immunohistochemistry. Intestines were open in longitudinal, flushed, and rolled into “Swiss rolls” as previously described⁷². Tissues were then fixed in PFA 4% 16 h and, in the case of frozen samples, included in sucrose 2% from 3 h to overnight. Swiss rolls were then included in paraffin or in OCT compound for frozen sectioning. Transversal cuts of swiss rolls were used in all experiments. For immunohistochemistry and H&E staining, paraffin sections of 4 μ m were subjected to normal deparaffination and hydration. Antigen retrieval protocol (citrate buffer or pH9 EDTA buffer) was used for immunohistochemistry.

After blocking unspecific binding on BSA 2%, NGS 5% PBS-TritonX100 0.3%, samples were incubated overnight with one of the following primary antibodies: anti-Muc2 (1:200, Santa Cruz, rabbit mAb, sc-515032) or anti-Lysozyme (1:500, rabbit polyclonal antibody (pAb), Dako, A0099) in same blocking buffer. Specific secondary antibody and DAB (Vector technology) protocol were used. For LacZ staining, frozen sections were stained following β -gal staining kit indications (K1465-01, Fisher Scientific). Tissue sections were imaged using brightfield microscope EVOS2 with 10 or 20 \times objective lens and tile scan for the visualization of the complete swiss roll was performed when needed. For immunofluorescence, sections of 4–7 μ m were incubated in blocking buffer for 1 h (PBS-Tx100 0.3%, NGS 5%, BSA 2%, Glycine 100 μ M), followed by primary antibody incubation overnight. The following antibodies were used for immunofluorescence: anti- β -Galactosidase (β Gal, Frozen sections, Dil 1:100, Rabbit polyclonal antibody, Abcam, ab4761), anti-Ki67 (Paraffin, 1:200, rabbit monoclonal antibody, Invitrogen, MA5-14520) anti-SMAD4 (Frozen sections, methanol 10 min –20C, Dil 1:400, Cell signaling, 46535), anti- β -catenin (Paraffin, 1:200, Mouse mAb, BD Biosciences, 610154), anti-Olfm4 (Paraffin, 1:200, Rabbit mAb, Cell signaling, 39141), anti-cleaved caspase 3 (Paraffin, Dil 1:200, Rb pAb, Cell signaling, 9661), anti-pSMAD1/5/9 (Frozen sections, 10 μ m, Dil 1:800, 13820, Cell Signaling, following TSA amplification, NEL744001KT, Perkin Elmer, following previous specifications⁷³), anti-YAP (Paraffin, 1:100, rabbit mAb, Cell Signaling, 14074), anti-Desmin and anti-CD31 (Frozen sections, Dil 1:200 for both antibodies, Mouse mAb, Thermo Fisher Scientific, MA5-13259 and Hamster mAb, Millipore, MAB1398z, respectively) and anti-CD45 (Frozen sections, 1:200, rat mAb, Abcam, 25386), and anti E-Cadherin (Rabbit mAb, Cell signaling 3195). After washing the slides in PBS-Tween 20 0.2%, tissues were incubated with the appropriate Alexa Fluor secondary antibody, Anti-SMA-Cy3 directly labeled antibody (1:500, mouse mAb, Sigma-Aldrich C6198) and Hoechst 33342 (1:10,000). Tissue sections were imaged with a Zeiss Airyscan confocal microscope, using a 10 \times and 20 \times objective lens. Images were analyzed using Zen black edition software (Zeiss) and maximal projections are shown except for SMAD4 staining (single plane). Tile scans of swiss rolls were performed when required. The percentage of β Gal positive cells in the muscle was calculated manually in Zen software by counting the total number of nuclei in muscularis mucosa or circular/longitudinal muscle vs β Gal positive nuclei in these tissues.

DSS colon injury. Experimental epithelial colon injury was induced in 8–10 weeks mice by supplying 3.5% DSS (MP Biomedicals, 0216011010) in drinking water ad libitum during 5 days. Before (Day 0) and during experimental development (up to day 7 in short protocol or up to 19 days in long-term protocol), mice were monitored daily for signs of stress, pain, body weight loss, and presence of blood in stool (detected by hemoFEC, Cobas, 10243744). At day 5, DSS was replaced by regular water to allow epithelial recovery. Control mice to evaluate DSS damage level were euthanized at Day5. For the long-term protocol, weight recovery determined end point (14 days for females and 19 days for males). Colon tissue was then harvested, measured, imaged, fluxed with cold PBS, open in longitudinal, and processed for paraffin or OCT, as indicated above. Paraffin sections were stained for H&E, or Ki67 and SMA. H&E sections were imaged on EVOS2 (tile scan of complete swiss rolls) and genotype-blind analyzed for signs of injury. Crypt loss, presence of ulcerated tissue in the mucosa, signs of immune infiltrate in mucosa and edema were evaluated to create an injury level profile for each sample (Injury Score). The % of de-epithelialized mucosa was calculated using Fiji (Image J) as the total length of intestinal surface devoid of epithelium vs total length of swiss roll. The % of Ki67+ cells were obtained by quantifying Ki67 positive nuclei in mucosa vs total nuclei in mucosa using Cell Profiler. Long-term DSS samples were evaluated by a pathologist to determine the presence of reactive atypia.

Irradiation. Eight-week-old male mice were subjected to whole body 10 Gy irradiation under anesthesia. Weight loss was evaluated at Day 0 and during the length of the experiment (3 or 6 days). Animals were carefully checked daily for signs of pain or stress. At end point, mice were euthanized and small intestine and colon were harvested, flushed with cold PBS, and processed in swiss rolls for paraffin. H&E sections were imaged and evaluated blindly for signs of impaired recovery of the mucosal tissue. Parameters as crypt loss, immune infiltrate, crypt length and villus length and width were evaluated to rate the injury score. Villus length and width were measured using Fiji (Image J). We evaluated caspase 3 levels through staining at Day 1 as a positive control for irradiation. Microcolony assay was performed on swiss rolls H&E images of Day3 and Day6 irradiated intestines and represented as #Crypts/100 μ m of tissue. On average, crypts number was evaluated in 0.6–1 cm of ileum swiss roll extension in transversal cut, and more than 100 crypts counted/sample. Image quantification was performed using Fiji (Image J).

Mmp17-ApcMin tumor evaluation. The presence and number of intestinal tumors were evaluated in 18–20 weeks old *ApcMin* + *Mmp17*^{+/+}, *Mmp17*^{-/-} or *Mmp17*[±] (females and males) mice. Mice were weekly monitored for weight loss and signs of pain, to avoid situations of moderate to high pain. At end point, mice were euthanized and small intestinal tumors were visualized and counted. Brightfield pictures were taken to double check tumor number and quantify tumor size (Fiji, Image J). Tissues were fixed as swiss rolls overnight and processed in

paraffin or for OCT as described above 5 µm microtome cuts were stained for H&E and/or for immunostaining. Immunostaining was performed as previously described in paraffin for β-Catenin and Olfm4 staining. For the evaluation of *Mmp17* expression in tumors, *Mmp17*^{-/-} tissues were processed in OCT and stained for β-Gal as stated above.

Protein extraction and western blot analysis. Intestinal tissue (muscle or mucosa tissue isolated as previously described) was disrupted using a tissue lyzer and ceramic beads (Magna Lyser green beads tubes 03358941001) in cold regular RIPA buffer (+ protease and phosphatase inhibitors). Proteins (20–100 µg) were resolved by 7–12% SDS-PAGE in reducing conditions and transferred onto nitrocellulose membranes using iBlot2™ dry blotting technology (Thermo Fisher Scientific). Antibodies against SMAD4 (rabbit mAb, Cell signaling, 46535), POSTN (mouse mAb, SAB4200197, MERK, Sigma-Aldrich), β-tubulin (ab6160, Abcam), and GAPDH (mouse mAb, Abcam, ab125247) were used at 1:1000 dilution (4 °C overnight). Immunoreactive proteins were visualized with corresponding fluorochrome-conjugated secondary antibodies (680 or 800 ODYSSEY IRDye®) and recorded by Licor Odyssey technology. Quantification of western blot bands was performed using ODYSSEY software (LI-COR Biosciences) and normalized to GAPDH or β-tubulin levels.

In vitro digestion and western blot. Human recombinant POSTN (250 ng to 1 µg; hrPOSTN, 3548-F2-050, R&D) or human recombinant OPN as control (1 and 2 µg; hrOPN, 1433-OP, R&D) were incubated in digestion buffer (50 mM Tris-HCl, 10 mM CaCl₂, 80 mM NaCl, [pH7.4]) with or without human recombinant MMP17 (250 ng) (hrMMP17, P4928, Abnova) catalytic domain for 2 h at 37 °C. Samples were separated by 12% SDS-PAGE and transferred to nitrocellulose membranes. Full-length hrPOSTN and fragments were detected with an anti-POSTN monoclonal mouse antibody (SAB4200197, MERK, Sigma-Aldrich). Full length and Ct fragments of OPN were detected using 1H3F7 mouse monoclonal antibody as previously described²⁴. An anti-mouse secondary antibody was used to visualize the different protein sizes.

In situ hybridization (ISH) of intestinal tissues. ISH using RNAscope technology (ACD, Bio-Techne) was performed using freshly cut paraffin sections of intestinal swirl rolls of *Mmp17*^{+/+} and *Mmp17*^{-/-} mice. Chromogenic RNA-scope of *Lgr5* (Mm-Lgr5, 312171) and *Olfm4* (Mm-Olfm4, 311831) in colon and small intestine was performed following manufacturer indications (RNAscope® 2.5 HD Assay-BROWN). Sections were imaged using bright field automated microscope EVOSE2 (tile scan). Quantification of positive *Lgr5* cells was performed using Fiji (Image J); total area of positive *Lgr5* crypts was normalized to tissue length. Immunofluorescence RNAscope (FISH) was performed following manufacturer protocol (RNAscope® Multiplex Fluorescent v2) and the following probes were used: *Mmp17* (Mm-Mmp17-C4 ACD design of NM_011846.5), *Grem1* (Mm-Grem1-C3, 314741), *Grem2* (473981-C2), *Chrdl1* (Mm-Chrdl1, 442811). Zeiss Airyscan scope images are maximal projections of the different channels taken with 10× and 20× objectives.

iECM-based crypt regeneration assay. iECM was prepared as previously described³⁹. To obtain a decellularized small iECM from the intestine, 10 cm of MMP17 WT or KO ileum was flushed with cold PBS and incubated overnight in MQ water. Dead cells were cleared by flushing the intestinal lumen with cold MQ water. Next, the intestine was cut into 1 cm pieces, followed by 3 h incubation with 1% Sodium Deoxy Cholate (Sigma) on a shaker (10 rpm) at RT. Tissue pieces were washed with MQ water for 10 min., followed by 2 h RT incubation with 1 M Sodium Chloride and DNaseI (1 U/10 µl, on a shaker). Tissue pieces were then cut open longitudinally and placed on 35 mm glassbottom dishes (MatTek) keeping the luminal side upward. Luminal orientation of the iECM was confirmed with the bright field microscope. The iECM was then used to assess crypts formation from organoids laying on top of this decellularized tissue. 3-day old Matrigel-cultured organoid were washed with cold PBS (3×) and plated onto iECM. The number of adhered organoids on iECM was quantified under light microscope after 24 h, and further cultured for 7 days in standard ENR media or in supplementation with WT/KO MSN or hrMMP17. At day 7, re-epithelialized iECM were imaged and number of crypts attached to the iECM were quantified (ratio Crypts/organoids). iECM was then fixed in 4% PFA for further IF analysis.

In silico modeling of MMP17-POSTN docking and cleavage. Fasta sequences of mature human POSTN protein (Q15063 with the signal-peptide removed) was aligned to Unidust-30 (release 08-2018) and pdb70 (release 09-2019) databases using the hhhblits/hhsearch tools of the HH-suite3⁷⁴ to obtain a multisequence alignment (MSA) and pdb templates for comparative modeling.

For docking the full dimer a comparative modeling was made using de RosettaCM⁷⁵ tool of the Rosetta suite v3.12 (www.rosettacommons.org) with the fasta sequence, the alignment and templates obtained before.

The model with best structural alignment to the template (5yjj) and minimal energy was selected as final candidate. A final cycle of refinement for minimize clashes and energy was made with the relax tool⁷⁶ of Rosetta suite v3.12 (www.rosettacommons.org). This tool recomputes the side-chain coordinates of

the protein residues with account of the composition of the protein. As before, the models with the best energy and correct folding were selected as the final model.

Previous results for in vitro experiments show the putative cleavage sites in POSTN by MMP17 protein. The 2711LF and 273AP sites are buried in the dimeric model. To evaluate the accessibility of the exposed residues, the model of POSTN was manually located close to the active-site of MMP17 modeled before²⁴ using the pymol 2.4 software (www.pymol.org) for each exposed position. The positions at 36GR and 266DG have strong steric impediment that makes access impossible.

In each case, the complex was modeled using the docking protocol of the Rosetta software suite v3.12 (www.rosettacommons.org)⁷⁷. Models were clustered and manually analyzed in pymol to select the best candidate in each case. No model with the 808LQ position near to the active site of MT4-MMP was obtained.

Models for position 157VN, 291MG, and 793GG are near to the active site of MMP17 and, probably, are accessible. The 664IP position is in the active-site of MMP17 and is the best candidate.

Statistical analysis. The statistical analysis performed in each case is explained in detail in the corresponding figure legend, together with the n and the times the experiment was performed. Data were analyzed by two-tailed Student's *t*-test or by one- or two-way ANOVA followed by Bonferroni post-test for data with Gaussian normal distribution. Non-normal distributions were analyzed by Mann-Whitney test. The one-tailed Fisher's exact test was used to analyze the incidence of blood in stool or the presence of reactive atypia. Statistical tests were conducted with Prism 5 software (GraphPad Software, Inc.). Data are presented as mean ± S.D. and differences were considered statistically significant at *p* < 0.05: **p* value < 0.05, ***p* value < 0.01, ****p* value < 0.001 and *p* value < 0.0001.

Reporting summary. Further information on research design is available in the Nature Research Reporting Summary linked to this article.

Data availability

All raw sequencing data are available through ArrayExpress: WT and KO smooth muscle and crypt RNA seq; The WT and KO smooth muscle and crypt RNA seq data generated in this study have been deposited in the ArrayExpress database under accession code "E-MTAB-9180". The ENR vs MuscleSN treated organoids RNA seq data generated in this study has been deposited in the ArrayExpress database under accession code "E-MTAB-9181". The mass spectrometry proteomics data have been deposited to the ProteomeXchange Consortium via the PRIDE⁷⁸ partner repository with the dataset identifiers "PXD020561 (MSN supernatant)" and "PXD025770 (POSTN cleavage)". Supplementary Data 2 with proteomic data generated in this study is provided in the Supplementary Information. All other relevant data supporting the key findings of this study are available within the article and its Supplementary Information files or from the corresponding author upon reasonable request. All source data are available as a Source Data file. Source data are provided with this paper.

Received: 10 July 2020; Accepted: 28 October 2021;

Published online: 18 November 2021

References

- Barker, N. et al. Identification of stem cells in small intestine and colon by marker gene *Lgr5*. *Nature* <https://doi.org/10.1038/nature06196> (2007).
- Tian, H. et al. A reserve stem cell population in small intestine renders *Lgr5*-positive cells dispensable. *Nature* <https://doi.org/10.1038/nature10408> (2011).
- Murata, K. et al. Ascl2-dependent cell dedifferentiation drives regeneration of ablated intestinal stem cells. *Cell Stem Cell* <https://doi.org/10.1016/j.stem.2019.12.011> (2020).
- Yui, S. et al. YAP/TAZ-dependent reprogramming of colonic epithelium links ECM remodeling to tissue regeneration. *Cell Stem Cell* **22**, 35–49.e7 (2018).
- Gregorieff, A., Liu, Y., Inanlou, M. R., Khomchuk, Y. & Wrana, J. L. Yap-dependent reprogramming of *Lgr5*+ stem cells drives intestinal regeneration and cancer. *Nature* <https://doi.org/10.1038/nature15382> (2015).
- Wang, Y. et al. Long-term culture captures injury-repair cycles of colonic stem cells. *Cell* <https://doi.org/10.1016/j.cell.2019.10.015> (2019).
- Nusse, Y. M. et al. Parasitic helminths induce fetal-like reversion in the intestinal stem cell niche. *Nature* **559**, 109–113 (2018).
- McCarthy, N. et al. Distinct mesenchymal cell populations generate the essential intestinal BMP signaling gradient. *Cell Stem Cell* <https://doi.org/10.1016/j.stem.2020.01.008> (2020).
- Miyoshi, H. et al. Prostaglandin E2 promotes intestinal repair through an adaptive cellular response of the epithelium. *EMBO J.* <https://doi.org/10.15252/embj.201694660> (2017).
- Shoshkes-Carmel, M. et al. Subepithelial telocytes are an important source of Wnts that supports intestinal crypts. *Nature* **557**, 242–246 (2018).

11. Roulis, M. et al. Paracrine orchestration of intestinal tumorigenesis by a mesenchymal niche. *Nature* <https://doi.org/10.1038/s41586-020-2166-3> (2020).
12. Degirmenci, B., Valenta, T., Dimitrieva, S., Hausmann, G. & Basler, K. GLI1-expressing mesenchymal cells form the essential Wnt-secreting niche for colon stem cells. *Nature* **558**, 449–453 (2018).
13. Greicius, G. et al. PDGFR α + pericryptal stromal cells are the critical source of Wnts and RSPO3 for murine intestinal stem cells in vivo. *Proc. Natl Acad. Sci. USA* <https://doi.org/10.1073/pnas.1713510115> (2018).
14. Shoshkes-Carmel, M. et al. Subepithelial telocytes are an important source of Wnts that supports intestinal crypts. *Nature* <https://doi.org/10.1038/s41586-018-0084-4> (2018).
15. Halpern, K. B. et al. Lgr5 + telocytes are a signaling hub at the intestinal villus tip. (2019).
16. Roulis, M. & Flavell, R. A. Fibroblasts and myofibroblasts of the intestinal lamina propria in physiology and disease. *Differentiation* <https://doi.org/10.1016/j.diff.2016.05.002> (2016).
17. Powell, D. W., Pinchuk, I. V., Saada, J. I., Chen, X. & Mifflin, R. C. Mesenchymal cells of the intestinal lamina propria. *Annu. Rev. Physiol.* **73**, 213–237 (2011).
18. Gjorevski, N. et al. Designer matrices for intestinal stem cell and organoid culture. *Nature* <https://doi.org/10.1038/nature20168> (2016).
19. Pinchuk, I. V., Mifflin, R. C., Saada, J. I. & Powell, D. W. Intestinal mesenchymal cells. *Curr. Gastroenterol. Rep.* <https://doi.org/10.1007/s11894-010-0135-y> (2010).
20. Katajisto, P. et al. LKB1 signaling in mesenchymal cells required for suppression of gastrointestinal polyposis. *Nat. Genet.* <https://doi.org/10.1038/ng.98> (2008).
21. Chivukula, R. R. et al. An essential mesenchymal function for miR-143/145 in intestinal epithelial regeneration. *Cell* <https://doi.org/10.1016/j.cell.2014.03.055> (2014).
22. Page-McCaw, A., Ewald, A. J. & Werb, Z. Matrix metalloproteinases and the regulation of tissue remodelling. *Nat. Rev. Mol. Cell Biol.* <https://doi.org/10.1038/nrm2125> (2007).
23. Kessenbrock, K., Wang, C. Y. & Werb, Z. Matrix metalloproteinases in stem cell regulation and cancer. *Matrix Biol.* <https://doi.org/10.1016/j.matbio.2015.01.022> (2015).
24. Martín-Alonso, M. et al. Deficiency of MMP17/MT4-MMP proteolytic activity predisposes to aortic aneurysm in mice. *Circ. Res.* <https://doi.org/10.1161/CIRCRESAHA.117.305108> (2015).
25. O'Sullivan, S., Gilmer, J. F. & Medina, C. Matrix metalloproteinases in inflammatory bowel disease: an update. *Mediators Inflamm.* **2015**, 964131 (2015).
26. Esteban, S. et al. Endothelial MT1-MMP targeting limits intussusceptive angiogenesis and colitis via TSP1/nitric oxide axis. *EMBO Mol. Med.* <https://doi.org/10.15252/emmm.201910862> (2020).
27. Jakubowska, K. et al. Expressions of matrix metalloproteinases (MMP-2, MMP-7, and MMP-9) and their inhibitors (TIMP-1, TIMP-2) in inflammatory bowel diseases. *Gastroenterol. Res. Pract.* <https://doi.org/10.1155/2016/2456179> (2016).
28. Holloway, E. M. et al. Mapping development of the human intestinal niche at single-cell resolution. *Cell Stem Cell* <https://doi.org/10.1016/j.stem.2020.11.008> (2021).
29. Sato, T. et al. Single Lgr5 stem cells build crypt-villus structures in vitro without a mesenchymal niche. *Nature* <https://doi.org/10.1038/nature07935> (2009).
30. Serra, D. et al. Self-organization and symmetry breaking in intestinal organoid development. *Nature* (2019) <https://doi.org/10.1038/s41586-019-1146-y>.
31. Sato, T. et al. Long-term expansion of epithelial organoids from human colon, adenoma, adenocarcinoma, and Barrett's epithelium. *Gastroenterology* **141**, 1762–1772 (2011).
32. Meran, L., Baules, A. & Li, V. S. W. Intestinal stem cell niche: the extracellular matrix and cellular components. *Stem Cells Int.* **2017**, 7970385 (2017).
33. Gattazzo, F., Urciuolo, A. & Bonaldo, P. Extracellular matrix: a dynamic microenvironment for stem cell niche. *Biochim. Biophys. Acta - General Subjects* <https://doi.org/10.1016/j.bbagen.2014.01.010> (2014).
34. Rodríguez, D., Morrison, C. J. & Overall, C. M. Matrix metalloproteinases: what do they not do? New substrates and biological roles identified by murine models and proteomics. *Biochim. Biophys. Acta - Mol. Cell Res.* <https://doi.org/10.1016/j.bbamcr.2009.09.015> (2010).
35. Rikimaru, A. et al. Establishment of an MT4-MMP-deficient mouse strain representing an efficient tracking system for MT4-MMP/MMP-17 expression in vivo using β -galactosidase. *Genes Cells* <https://doi.org/10.1111/j.1365-2443.2007.01110.x> (2007).
36. Chen, E. Y. et al. Enrichr: Interactive and collaborative HTML5 gene list enrichment analysis tool. *BMC Bioinformatics* <https://doi.org/10.1186/1471-2105-14-128> (2013).
37. Kuleshov, M. V. et al. Enrichr: a comprehensive gene set enrichment analysis web server 2016 update. *Nucleic Acids Res.* <https://doi.org/10.1093/nar/gkw377> (2016).
38. Massagué, J. TGF β signalling in context. *Nat. Rev. Mol. Cell Biol.* <https://doi.org/10.1038/nrm3434> (2012).
39. Iqbal, S. Fetal-like reversion in the regenerating intestine is regulated by mesenchymal Asporin. Preprint at *bioRxiv* <https://doi.org/10.1101/2021.06.24.449590> (2021).
40. McCart, A. E., Vickaryous, N. K. & Silver, A. Apc mice: models, modifiers and mutants. *Pathol. Res. Pract.* **204**, 479–490 (2008).
41. Yin, X. et al. Niche-independent high-purity cultures of Lgr5 + intestinal stem cells and their progeny. *Nat. Methods* **11**, 106–112 (2014).
42. Muñoz, J. et al. The Lgr5 intestinal stem cell signature: robust expression of proposed quiescent ' +4' cell markers. *EMBO J.* **31**, 3079–3091 (2012).
43. Khurana, S. et al. Outside-in integrin signalling regulates haematopoietic stem cell function via Periostin-Itgav axis. *Nat. Commun.* <https://doi.org/10.1038/ncomms13500> (2016).
44. Bao, S. et al. Periostin potently promotes metastatic growth of colon cancer by augmenting cell survival via the Akt/PKB pathway. *Cancer Cell* [https://doi.org/10.1016/S1535-6108\(04\)00081-9](https://doi.org/10.1016/S1535-6108(04)00081-9) (2004).
45. Ma, H. et al. Periostin promotes colorectal tumorigenesis through integrin-FAK-Src pathway-mediated YAP/TAZ activation. *Cell Rep.* <https://doi.org/10.1016/j.celrep.2019.12.075> (2020).
46. Maruhashi, T., Kii, I., Saito, M. & Kudo, A. Interaction between periostin and BMP-1 promotes proteolytic activation of lysyl oxidase. *J. Biol. Chem.* <https://doi.org/10.1074/jbc.M109.088864> (2010).
47. Orecchia, P. et al. Identification of a novel cell binding site of periostin involved in tumour growth. *Eur. J. Cancer* <https://doi.org/10.1016/j.ejca.2011.04.026> (2011).
48. Czerwinski, M. et al. In vitro and in vivo development of the human intestinal niche at single cell resolution. Preprint at *bioRxiv* <https://doi.org/10.1101/2020.01.31.928788> (2020).
49. Qi, Z. et al. BMP restricts stemness of intestinal Lgr5 + stem cells by directly suppressing their signature genes. *Nat. Commun.* **8**, 1–14 (2017).
50. Kudo, A. & Kii, I. Periostin function in communication with extracellular matrices. *J. Cell Commun. Signal.* <https://doi.org/10.1007/s12079-017-0422-6> (2018).
51. Bonnet, N., Brun, J., Rousseau, J. C., Duong, L. T. & Ferrari, S. L. Cathepsin K controls cortical bone formation by degrading periostin. *J. Bone Miner. Res.* <https://doi.org/10.1002/jbmr.3136> (2017).
52. Shimazaki, M. et al. Periostin is essential for cardiac healing after acute myocardial infarction. *J. Exp. Med.* **205**, 295–303 (2008).
53. Nishiyama, T. et al. Delayed re-epithelialization in periostin-deficient mice during cutaneous wound healing. *PLoS ONE* **6**, e18410 (2011).
54. Kudo, A. Periostin in fibrolysis for tissue regeneration: Periostin actions inside and outside the cell. *Cell. Mol. Life Sci.* **68**, 3201–3207 (2011).
55. Kolkenbrock, H., Essers, L., Ulbrich, N. & Will, H. Biochemical characterization of the catalytic domain of membrane-type 4 matrix metalloproteinase. *Biol. Chem.* <https://doi.org/10.1515/BC.1999.137> (1999).
56. Clements, K. M. et al. Matrix metalloproteinase 17 is necessary for cartilage aggrecan degradation in an inflammatory environment. *Ann. Rheum. Dis.* <https://doi.org/10.1136/ard.2010.130757> (2011).
57. Clemente, C. et al. MT4-MMP deficiency increases patrolling monocyte recruitment to early lesions and accelerates atherosclerosis. *Nat. Commun.* **9**, 4–6 (2018).
58. Neuman, M. G. Osteopontin biomarker in inflammatory bowel disease, animal models and target for drug discovery. *Digestive Dis. Sci.* <https://doi.org/10.1007/s10620-012-2120-9> (2012).
59. Zhao, M., Liang, F., Zhang, B., Yan, W. & Zhang, J. The impact of osteopontin on prognosis and clinicopathology of colorectal cancer patients: a systematic meta-analysis. *Sci. Rep.* <https://doi.org/10.1038/srep12713> (2015).
60. Zhao, H. et al. The role of osteopontin in the progression of solid organ tumour. *Cell Death Dis.* <https://doi.org/10.1038/s41419-018-0391-6> (2018).
61. Chen, J. et al. Promotion of tumor growth by ADAMTS4 in colorectal cancer: focused on macrophages. *Cell. Physiol. Biochem.* <https://doi.org/10.1159/000489245> (2018).
62. Paye, A. et al. EGFR activation and signaling in cancer cells are enhanced by the membrane-bound metalloprotease MT4-MMP. *Cancer Res.* <https://doi.org/10.1158/0008-5472.CAN-13-2994> (2014).
63. Sato, T. & Clevers, H. Primary mouse small intestinal epithelial cell cultures. *Methods Mol. Biol.* https://doi.org/10.1007/978-1-62703-125-7_19 (2013).
64. Dobin, A. et al. STAR: ultrafast universal RNA-seq aligner. *Bioinformatics* <https://doi.org/10.1093/bioinformatics/bts635> (2013).
65. Frankish, A. et al. GENCODE reference annotation for the human and mouse genomes. *Nucleic Acids Res.* <https://doi.org/10.1093/nar/gky955> (2019).
66. Liao, Y., Smyth, G. K. & Shi, W. FeatureCounts: an efficient general purpose program for assigning sequence reads to genomic features. *Bioinformatics* <https://doi.org/10.1093/bioinformatics/btt656> (2014).

67. Love, M. I., Huber, W. & Anders, S. Moderated estimation of fold change and dispersion for RNA-seq data with DESeq2. *Genome Biol.* <https://doi.org/10.1186/s13059-014-0550-8> (2014).
68. Kolde, R. pheatmap: Pretty Heatmaps. *R package version 1.0.8* (2015).
69. Pedregosa, F. et al. Scikit-learn: Machine Learning. *J. Mach. Learn. Res.* **12**, 2825–2830 (2011).
70. Yu, G., Wang, L. G., Han, Y. & He, Q. Y. ClusterProfiler: an R package for comparing biological themes among gene clusters. *Omi. A J. Integr. Biol.* <https://doi.org/10.1089/omi.2011.0118> (2012).
71. Shevchenko, A., Tomas, H., Havliš, J., Olsen, J. V. & Mann, M. In-gel digestion for mass spectrometric characterization of proteins and proteomes. *Nat. Protoc.* <https://doi.org/10.1038/nprot.2006.468> (2007).
72. Moelenbeek, C. & Ruitenberg, E. J. The 'Swiss roll': a simple technique for histological studies of the rodent intestine. *Lab. Anim.* **15**, 57–59 (1981).
73. Huycke, T. R. et al. Genetic and mechanical regulation of intestinal smooth muscle development. *Cell* <https://doi.org/10.1016/j.cell.2019.08.041> (2019).
74. Steinegger, M. et al. HH-suite3 for fast remote homology detection and deep protein annotation. *BMC Bioinforma.* <https://doi.org/10.1186/s12859-019-3019-7> (2019).
75. Song, Y. et al. High-resolution comparative modeling with RosettaCM. *Structure* <https://doi.org/10.1016/j.str.2013.08.005> (2013).
76. Fleishman, S. J. et al. RosettaScripts: a scripting language interface to the Rosetta Macromolecular modeling suite. *PLoS One* <https://doi.org/10.1371/journal.pone.0020161> (2011).
77. Marze, N. A., Roy Burman, S. S., Sheffler, W. & Gray, J. J. Efficient flexible backbone protein-protein docking for challenging targets. *Bioinformatics* <https://doi.org/10.1093/bioinformatics/bty355> (2018).
78. Perez-Riverol, Y. et al. The PRIDE database and related tools and resources in 2019: improving support for quantification data. *Nucleic Acids Res.* <https://doi.org/10.1093/nar/gky1106> (2019).

Acknowledgements

We would like to thank Dr. Motoharu Seiki for kindly sharing the *Mmp17^{KO/KI}* mouse line and Dr. Kaisa Lehti for first inspiring this study. We would like to thank to Anne Beate L. Marthinsen for performing the irradiation, and the Department of Radiology and Nuclear Medicine (St. Olav's Hospital) for allowing the use of their instruments. We also thank Arne Wibe and Elin Ronne for their evaluation of colon crypt reactive atypia. We thank Shreya Gopalakrishnan for sharing reagents and input on organoids growth, Yashwanth Subbannayya and Time Veth for input on MS analysis, and Rosalie Zwiggelaar for assisting in mouse experiments. We thank the imaging (CMIC) and animal care (CoMed) core facilities (NTNU), as well as the histology and animal facilities at CNIC for assisting in this work. The WT KO crypt-muscle RNA-seq was done by the Genomics Core Facility at NTNU, which receives funding from the Faculty of Medicine and Health Sciences and Central Norway Regional Health Authority. This research was part of the Netherlands X-omics Initiative and partially funded by NWO (project

184.034.019). This work was further financially supported by the Norwegian Research Council (Centre of Excellence grant 223255/F50, and 'Young Research Talent' 274760 to M.J.O.) and the Norwegian Cancer Society (182767 to M.J.O.). MMA is the recipient of a Marie Skłodowska-Curie IF (DLV-794391).

Author contributions

M.M.A. and M.J.O. designed the research project with help from F.M., M.A., P.K., and A.G.A. for specific experiments. M.M.A., S.I., P.M.V., H.T.L., M.J.D., F.M., S.H., A.D.S., M.A., P.K., A.G.A., and MJO planned and performed experiments and/or analyzed data. M.M.A. and M.J.O. drafted the manuscript and all authors provided input.

Competing interests

The authors declare no competing interests.

Additional information

Supplementary information The online version contains supplementary material available at <https://doi.org/10.1038/s41467-021-26904-6>.

Correspondence and requests for materials should be addressed to Mara Martin-Alonso or Menno J. Oudhoff.

Peer review information *Nature Communications* thanks Kari Basso, Michael Blennerhassett and the other anonymous reviewer(s) for their contribution to the peer review this work. Peer reviewer reports are available.

Reprints and permission information is available at <http://www.nature.com/reprints>

Publisher's note Springer Nature remains neutral with regard to jurisdictional claims in published maps and institutional affiliations.



Open Access This article is licensed under a Creative Commons Attribution 4.0 International License, which permits use, sharing, adaptation, distribution and reproduction in any medium or format, as long as you give appropriate credit to the original author(s) and the source, provide a link to the Creative Commons license, and indicate if changes were made. The images or other third party material in this article are included in the article's Creative Commons license, unless indicated otherwise in a credit line to the material. If material is not included in the article's Creative Commons license and your intended use is not permitted by statutory regulation or exceeds the permitted use, you will need to obtain permission directly from the copyright holder. To view a copy of this license, visit <http://creativecommons.org/licenses/by/4.0/>.

© The Author(s) 2021

Smooth muscle-specific MMP17 (MT4-MMP) regulates the intestinal stem cell niche and regeneration after damage

Mara Martín-Alonso¹, Sharif Iqbal^{2,3}, Pia M. Vornewald¹, Håvard T. Lindholm¹, Mirjam J. Damen⁴, Fernando Martínez^{5,6}, Sigrid Hoel¹, Alberto Díez-Sánchez¹, Maarten Altelaar⁴, Pekka Katajisto^{2,3,7}, Alicia G. Arroyo^{8,9}, Menno J. Oudhoff¹

¹Centre of Molecular Inflammation Research, and Department of Clinical and Molecular Medicine, Norwegian University of Science and Technology, Trondheim, Norway

²Institute of Biotechnology, HiLIFE, University of Helsinki, Finland

³Molecular and Integrative Bioscience Research Programme, Faculty of Biological and Environmental Sciences, University of Helsinki, Helsinki, Finland

⁴Biomolecular Mass Spectrometry and Proteomics, Bijvoet Center for Biomolecular Research and Utrecht Institute for Pharmaceutical Sciences, Utrecht University, Utrecht, Netherlands.

⁵Bioinformatics Unit. Centro Nacional de Investigaciones Cardiovasculares (CNIC), Madrid, Spain. CNIC, Madrid, Spain

⁶Centro de Investigación Biomédica en Red de Enfermedades Cardiovasculares (CIBERCV), Madrid, Spain

⁷Department of Biosciences and Nutrition, Karolinska Institutet, Stockholm, Sweden

⁸Department of Molecular Biomedicine, Centro de Investigaciones Biológicas Margarita Salas (CIB-CSIC), Madrid, Spain

⁹Vascular Pathophysiology Area, Centro Nacional de Investigaciones Cardiovasculares (CNIC), Madrid, Spain.

Correspondence should be addressed to MMA (e-mail: mara.m.alonso@ntnu.no) and MJO (email: menno.oudhoff@ntnu.no).

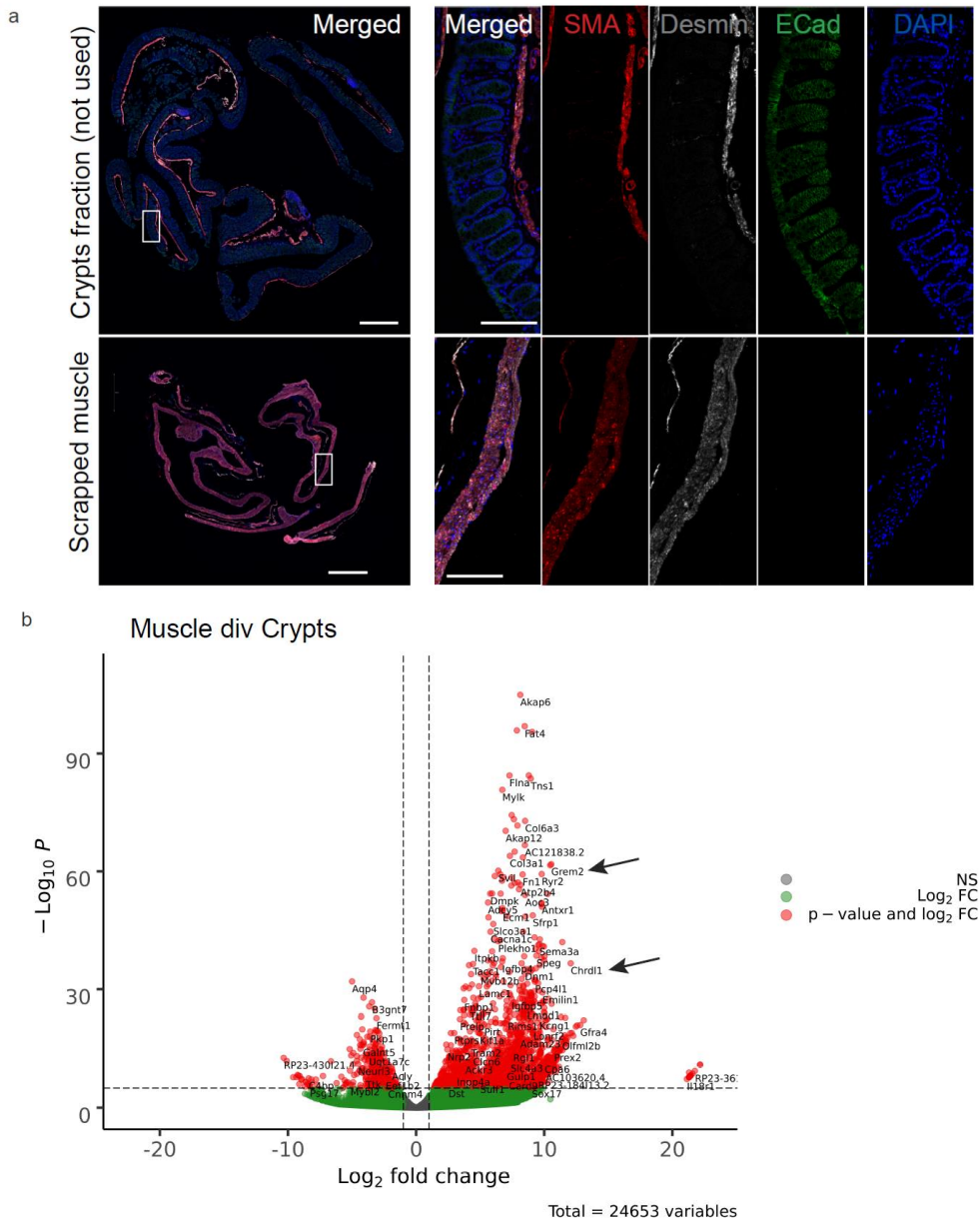


Figure S1. Purity of smooth muscle explants and RNAseq of intestinal crypts. **a**, Representative confocal image of mucosa fraction (top) and muscle fraction (bottom), showing only Desmin/SMA double positive cells in the muscle fraction (smooth muscle cells) and absence of myofibroblasts (SMA+Desmin- cells). Tissue was stained for SMC markers SMA (red), Desmin (grey), and epithelial marker E-Cadherin (green). Nuclei were stained with DAPI (blue). Only scrapped clean muscle was used for RNAseq or to obtain muscle-SN. Crypts fraction obtained by this method was discarded. Scale in tile scan is 500 μm and 100 μm in insets. $n=3$ biological replicates **b**, Volcano plot showing differential

expression of genes between muscle and crypts as Gremlins and Chordin like1 (arrows), BMP signaling antagonists. n= 3 biological replicates.

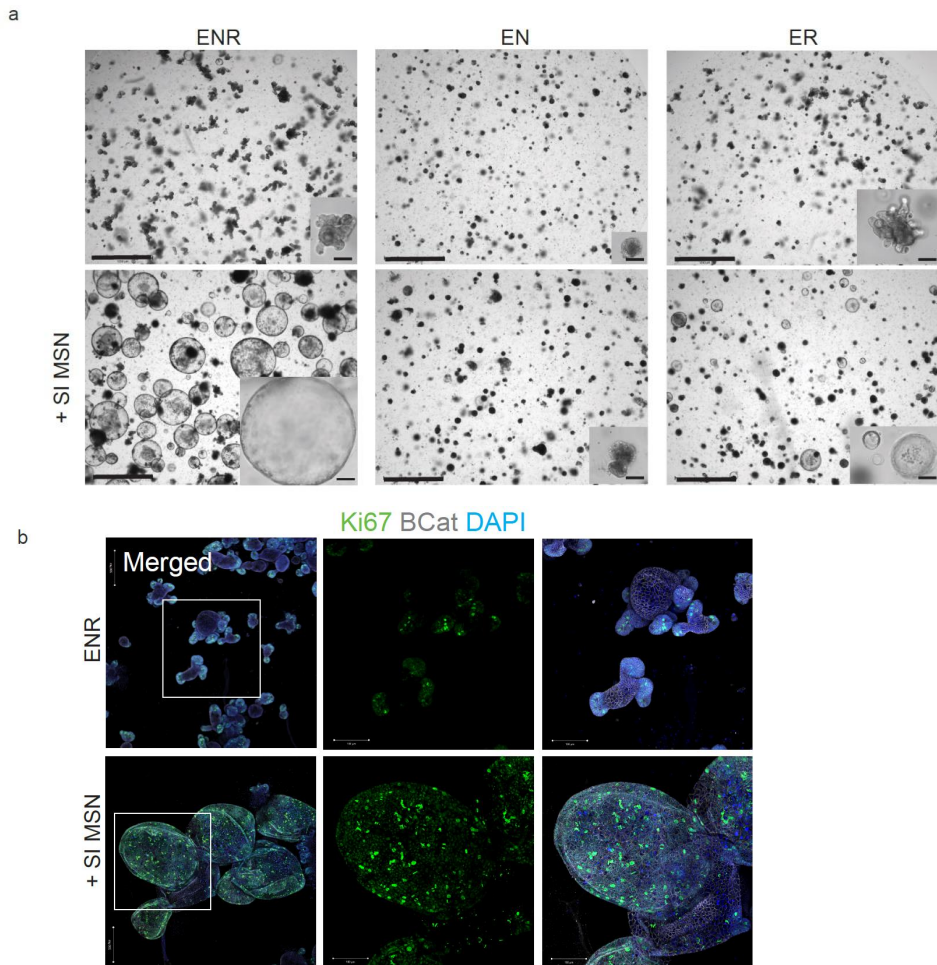
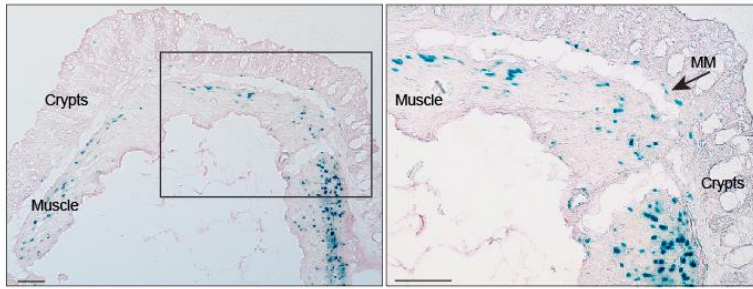


Figure S2. Small intestinal derived muscle also induces large spheroids. **a.** Small intestinal muscle supernatant (SI MSN) induces large spheroid organoids, similar to colonic muscle supernatant that was used throughout the main manuscript. SI MSN cannot replace RSPO1, but can replace NOGGIN in the culture medium. Scale is 1250 μm and 100 μm on inset. n= 3 wells per condition. 2 independent experiments performed. **b.** Ki67 (green) has crypt-specific staining in ENR organoids, but in SI MSN-mediated large spheroids Ki67 is positive throughout organoid. Scale 200 μm and 100 μm on inset. n= 3 wells per condition. 2 independent experiments performed.

a



b

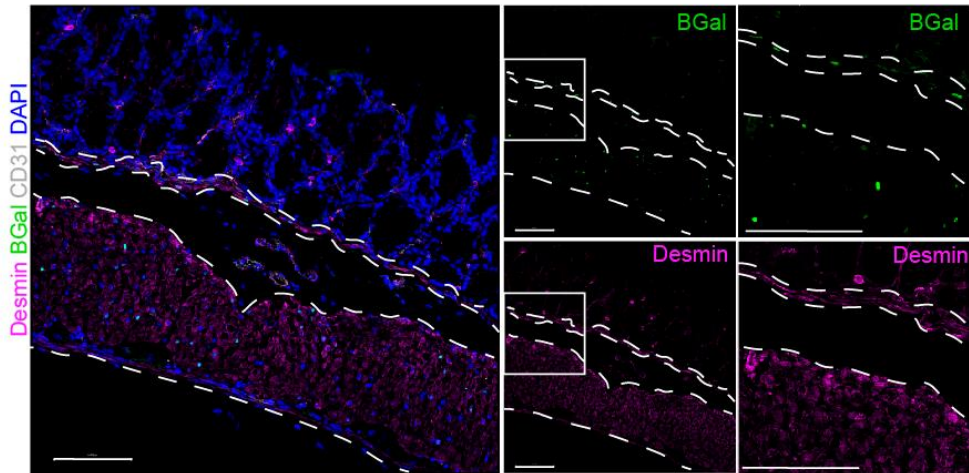
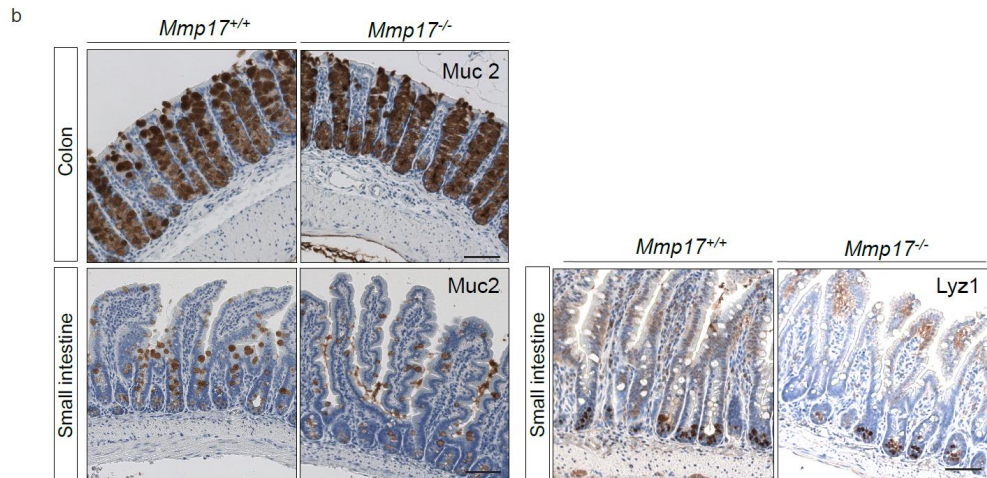
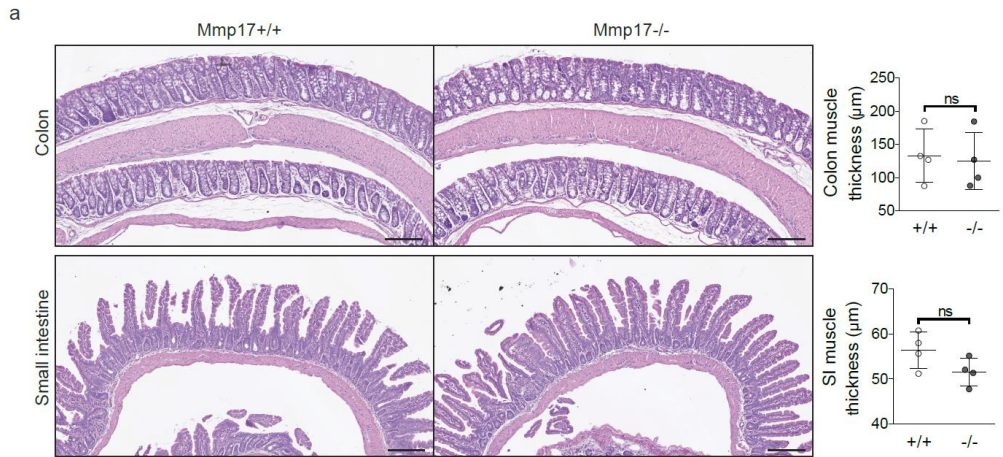


Figure S3. Mmp17 promoter is active in muscle cells from muscularis mucosa and circular and longitudinal muscle. a. Representative image of a transverse colon cut stained for β -Galactosidase activity (blue). Scale bar 100 μ m. n= 3 Mmp17^{+/-} mice. **b.** Representative images of Desmin (smooth muscle), anti-BGal, CD31 (endothelium) and DAPI stained sections showing that MMP17-BGal positive cells (nuclear staining) are Desmin positive (cytoplasmic) in the smooth muscle. Muscle is highlighted by a dashed white line. Scale bar 100 μ m. n= 3 Mmp17^{+/-} mice.



c

Enrichr
 ENCODE and ChEA Consensus TFs from ChIP-X
 Sorted by p-value ranking

Name	P-value	Adjusted p-value
SMAD4	0.0004016	0.04177
STAT3	0.07080	1.000
SALL4	0.1558	1.000
KAT2A	0.03088	1.000
GATA1	0.2078	1.000
EGR1	0.3556	1.000
REST	0.3307	1.000
GATA2	0.3671	1.000
NFE2L2	0.3956	1.000
BCL3	0.4425	1.000

Figure S4. No structural differences in KO smooth muscle and ENRICH results on transcription factors differences between WT and KO crypts a. Representative H&E images of transverse colon and small intestine (SI) tissues. Scale 150 μm . n = 4 mice per genotype. Graphs represent average

values for muscularis propria thickness along the swiss roll. b. Representative images of goblet cells (Muc2) and Paneth cells (Lysozyme (Lyz1), only present in small intestine) stainings. Scale bar 100um. n= 3 animals per genotype. c.List of transcription factors altered when comparing WT and KO epithelium (Enrichr), Padj value=0.04177, two-tailed. Data in a are means \pm SD and were analyzed using Mann-Whitney test. Source data are provided as a Source Data file.

a

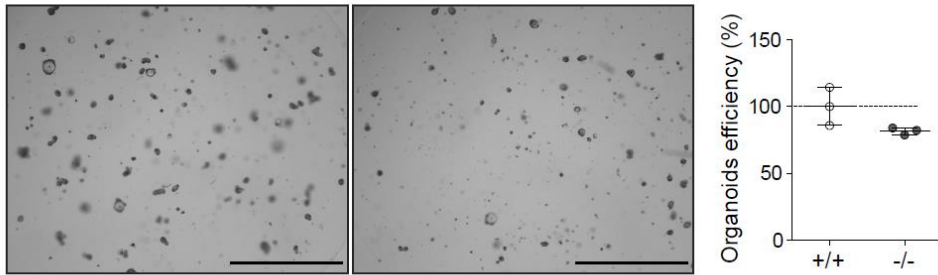


Figure S5. Organoids efficiency formation in *Mmp17*^{-/-} small intestine cultured in ENR medium.

a. Bright field representative images of small intestine organoids 72h after crypt isolation. Graph represents organoids efficiency after 72h of WT or KO crypt culture. n= 3 wells analyzed. Scale 650 μm. Data in a are means ± SD and were analyzed using Mann-Whitney test (two-sided). Source data are provided as a Source Data file.

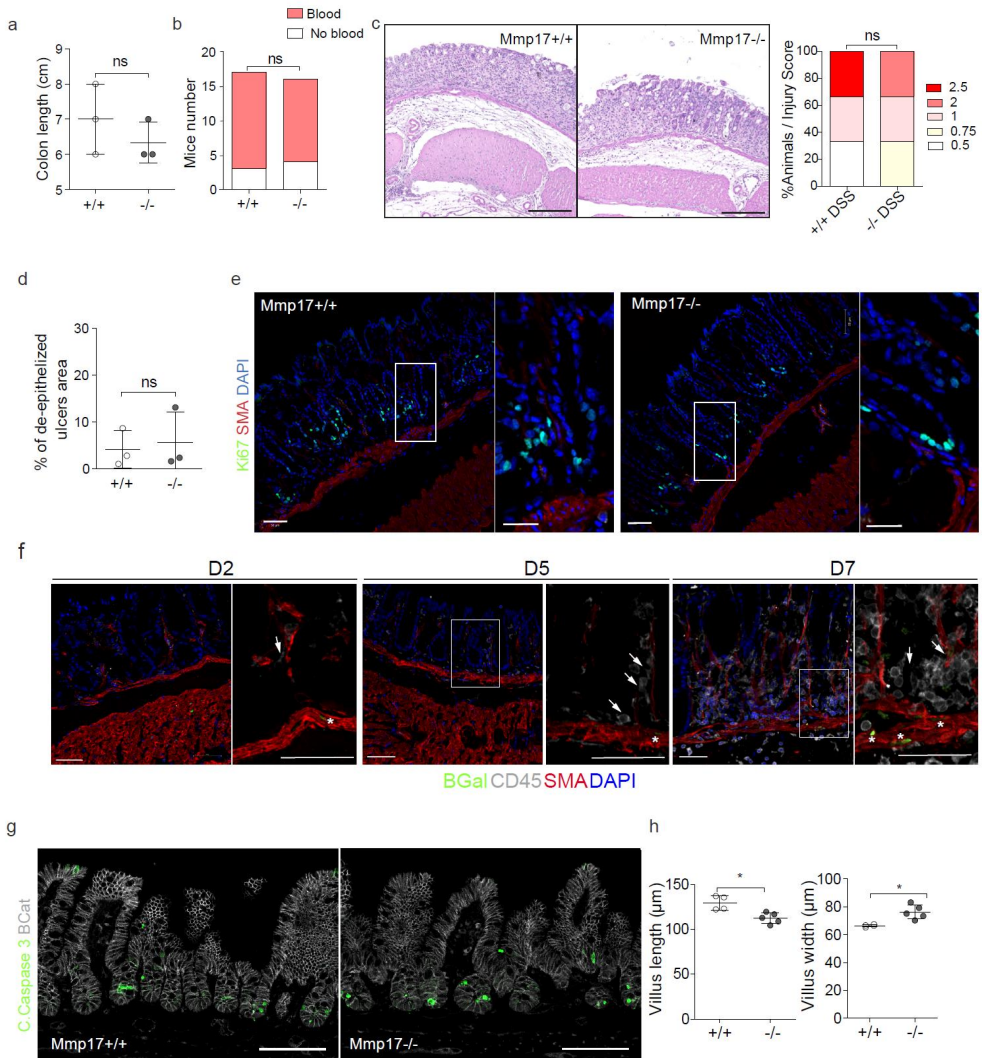


Figure S6. Intestinal damage models produce same injury level in WT and KO mice. a-d. Graphs represent colon length and presence of blood in stool at D5 of DSS treatment. $n = 3$ mice per genotype in a and d (1 experiment) and 17 and 16 mice in b. c. Representative H&E picture of a transverse colon cut from mice treated with DSS 3.5% for 5 days (left), and injury score evaluation of such pictures (right). Scale $200 \mu\text{m}$. $n = 3$ mice per genotype, 1 experiment. d. Graph represents the presence of ulcers in the mucosa as a percentage of the total swiss roll length at D5. $n = 3$ mice per genotype (1 experiment). e. Representative confocal images stained for Ki67 (green), SMA (red) and nuclei (blue), showing the equivalent reduction in proliferative cells at D5 of DSS treatment in WT and KO. Scale $50 \mu\text{m}$; $25 \mu\text{m}$ in magnified view to the right. $n = 3$ mice per genotype. f. Representative confocal images showing BGal positive cells (green) during DSS timepoints treatment (Day 2, 5 and 7). BGal positive cells are SMA

(red) positive. Immune cells stained with CD45 (grey) are negative for BGal. Asterisks point to muscle BGal positive signal, arrows to immune component. Scale 50 μm . n= 2- 3 Mmp17 \pm mice per time point. g. Representative confocal image showing Cleaved Caspase 3 staining (green) predominantly at the bottom of the crypts in ileum (24h after irradiation). β Cat staining was performed to highlight epithelial cells. Scale bar 100 μm . n= 4 mice per genotype. h. Graph represents villi length and width in small intestinal tissue 3 days after irradiation. n= 4 WT and 5 KO mice analyzed per genotype in two independent experiments, 30 to 40 crypts/villi per mouse were quantified. Numerical data in a, d and h are means \pm SD. Data were analyzed by Mann-Whitney test (a, d and h, two-sided) and one-tailed Fisher exact test in b. p=0.0159 in h, for both villus length and villus width. Source data are provided as a Source Data file.

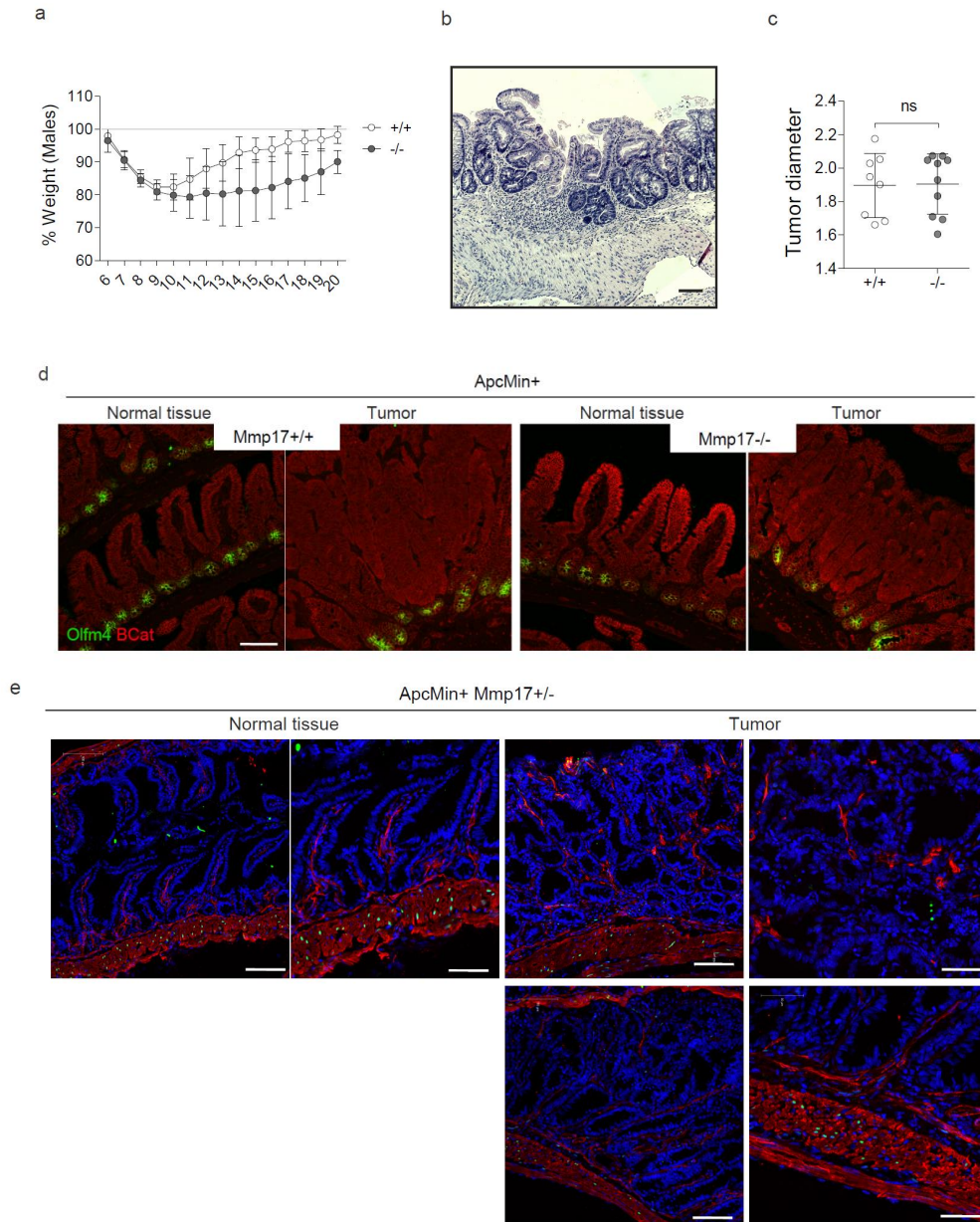


Figure S7. Mmp17 loss in ApcMin background predispose to tumors with no structural differences between WT and KO. **a.** Graph shows weight evolution in males after 5 days of DSS treatment. $n = 3$ KO and 4 WT mice per genotype. **b.** Representative H&E image of crypt reactive atypia in a KO mouse treated with DSS (long-term experiment). Scale bar 100 μm . $n = 6-8$ mice per genotype. **c.** Graph represents average tumor diameter (mm) in small intestines of *ApcMin+* *Mmp17* WT or KO. $n = 8$ WT and 10 KO mice analyzed per genotype. **d.** Confocal maximum projection images of normal vs tumor area stained for SC marker Olfm4 (Green) and βCat (Red). Scale bar 100 μm . $n = 3-5$ mice

per genotype. e. Representative confocal maximum projection images showing β -Gal staining (Green) in normal tissue vs tumor areas. B-Gal signal was only found in muscle cells (SMA+, Red). Scale bar 100 μ m. n= 3 mice. Data are means \pm SD, numerical data in a was analyzed by two way ANOVA followed by Bonferroni post-test and t-test was applied in c. Source data are provided as a Source Data file.

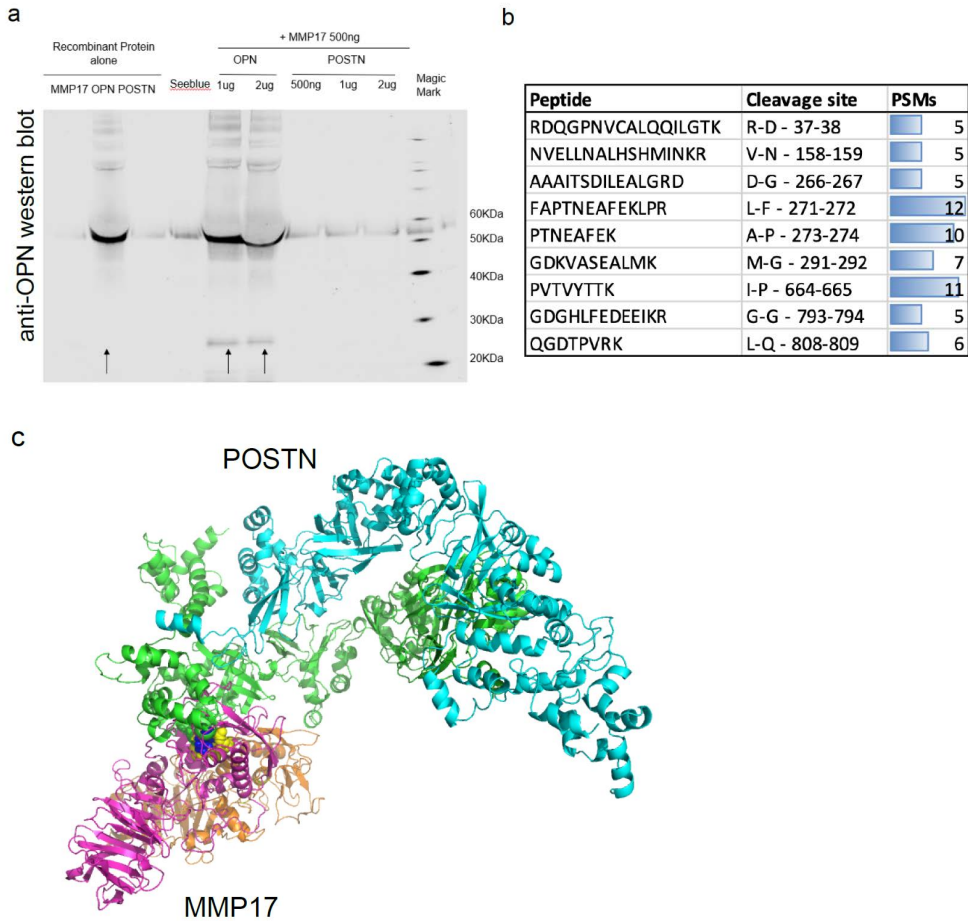


Fig. S8. MMP17 catalytic activity control. **a.** WB showing bands corresponding to a known MMP17 substrate named OPN (Osteopontin). Only smaller bands consistent with a cleavage product are observed when incubating the OPN together with MMP17, using the same method as for POSTN (Periostin) digestion. Full length OPN bands are observed (55KDa aprox) and cleavage products around 25KDa. An specific antibody against OPN C-terminus was used (1H3F7, Martín-Alonso et al. Cir Res. 2015). n=1 WB performed for control. **b.** Overview of POSTN cleavage sites with more than 5 PSMs. **c.** In silico model of MMP17-Periostin interaction. Model shows MMP17 dimer (magenta-orange) catalytic site in yellow in close proximity to POSTN (green-blue) cleavage site 664IP depicted in blue. Complete molecules are shown.

Paper 2

MUCOSAL IMMUNOLOGY

BMP signaling in the intestinal epithelium drives a critical feedback loop to restrain IL-13–driven tuft cell hyperplasia

Håvard T. Lindholm^{1*†}, Naveen Parmar^{1†}, Claire Drurey², Marta Campillo Poveda², Pia M. Vornewald¹, Jenny Ostrop¹, Alberto Díez-Sánchez¹, Rick M. Maizels², Menno J. Oudhoff^{1*}

The intestinal tract is a common site for various types of infections including viruses, bacteria, and helminths, each requiring specific modes of immune defense. The intestinal epithelium has a pivotal role in both immune initiation and effector stages, which are coordinated by lymphocyte cytokines such as IFN γ , IL-13, and IL-22. Here, we studied intestinal epithelial immune responses using organoid image analysis based on a convolutional neural network, transcriptomic analysis, and in vivo infection models. We found that IL-13 and IL-22 both induce genes associated with goblet cells, but the resulting goblet cell phenotypes are dichotomous. Moreover, only IL-13–driven goblet cells are associated with classical NOTCH signaling. We further showed that IL-13 induces the bone morphogenetic protein (BMP) pathway, which acts in a negative feedback loop on immune type 2–driven tuft cell hyperplasia. This is associated with inhibiting *Sox4* expression to putatively limit the tuft cell progenitor population. Blocking ALK2, a BMP receptor, with the inhibitor dorsomorphin homolog 1 (DMH1) interrupted the feedback loop, resulting in greater tuft cell numbers both in vitro and in vivo after infection with *Nippostrongylus brasiliensis*. Together, this investigation of cytokine effector responses revealed an unexpected and critical role for the BMP pathway in regulating type 2 immunity, which can be exploited to tailor epithelial immune responses.

INTRODUCTION

Gut infections remain a common threat for patients and are an immense burden on health systems worldwide (1). Resistance to intestinal pathogens relies on the capacity of the immune system to mount an appropriate response. For example, one requires a different type of response to intracellular viruses compared with extracellular pathogens including bacteria or parasites. Cytokines are key participants in polarizing the immune response by altering the cellular composition and state. Innate lymphoid cells (ILCs) are tissue-resident immune cells that are early responders to infections and create a local cytokine environment. ILCs are classically divided into three groups and secrete interferon- γ (IFN γ ; group 1), interleukin-13 (IL-13; group 2), and IL-22 (group 3). Which ILC subtype is dominant depends on the nature of the pathogenic challenge (2).

In addition to defining the immune landscape, cytokines directly affect intestinal epithelial cells (IECs) to drive immune type-specific responses (3). The intestinal epithelium consists of a single layer of cells and is responsible for both taking up nutrients and providing a protective barrier. One of the hallmarks of IECs is their rapid turnover (3 to 5 days), which allows for prompt cellular responses, for example, expansion of goblet cells that can produce protective mucus. This plasticity of IECs makes them particularly well suited to defend against pathogens (4).

In addition to responding to immune cues, the epithelium can also be involved in tailoring immune responses. For example, tuft

cells, which are important for defending against parasitic helminths, are the main source of IL-25 to control ILC2 populations both in homeostasis and upon helminth infection (5–7). As tuft cells rapidly expand upon exposure to type 2 cytokines, they exemplify both how the intestinal epithelium changes upon an immune response and how it can also partake in shaping it. Of note, tuft cells are not only important in immunity to helminth infections; activation of tuft cells by succinate is protective in a murine model of colitis, and reduced tuft cell numbers are found in patients with Crohn's disease that have more severe inflammation (8). Thus, tuft cells have been gaining interest as important regulators of intestinal diseases (9), and the discovery of regulatory mechanisms used by tuft cells could have clinical ramifications.

Intestinal organoids are self-organizing structures that are useful to study epithelial stem cell biology (10). They are particularly instructive to identify epithelial-intrinsic responses as they lack any other cell type normally present in vivo, such as fibroblasts. This also means that their culture medium requires addition of growth factors normally supplied by fibroblasts, such as those that target pathways such as WNT and bone morphogenetic protein (BMP). In addition, organoid cultures come with challenges as most metrics cannot capture the complexity of these large multicellular structures. To capture this complexity, a previous study used single-cell RNA sequencing (scRNA-seq) to systematically compare single-cell responses with cytokines of the three immune environments (3). However, there are still many unclear aspects to how cytokines induce epithelial responses, especially mechanistically. Here, we combine quantitative imaging with bulk RNA-seq to define how cytokines intersect with developmental pathways to instruct epithelial differentiation and maturation. Most prominently, we identify a feedback loop by which IL-13–induced tuft cell hyperplasia is self-limiting in a BMP-dependent manner and confirm this in a murine helminth infection model using *Nippostrongylus brasiliensis*.

¹CEMIR—Centre of Molecular Inflammation Research, Department of Clinical and Molecular Medicine, NTNU—Norwegian University of Science and Technology, 7491 Trondheim, Norway. ²Wellcome Centre for Integrative Parasitology, Institute of Infection, Immunology and Inflammation, University of Glasgow, G12 8TA Glasgow, UK.

*Corresponding author. Email: havard.t.lindholm@ntnu.no (H.T.L.); menno.oudhoff@ntnu.no (M.J.O.)

†These authors contributed equally to this work.

RESULTS

IFN γ , IL-13, and IL-22 differentially affect intestinal organoid growth and morphology

Intestinal organoids grow as a morphologically heterogeneous population, with a fraction of organoids growing as immature “spheroids” and the rest forming mature “budding” organoids. *Lgr5*⁺ stem cells and Paneth cells are found in the buds in budding organoids (mimicking crypts), while spheroids consist of less differentiated, proliferating cells (11). Building on our recent work on organoid segmentation (12), we developed an automated image analysis pipeline that segments organoid objects from the background and subsequently classifies them into spheroid or budding categories based on a convolutional neural network (Fig. 1A). This includes an optional manual correction step for organoids that were difficult to automatically segment or classify (fig. S1A). Comparing manually verified with automatically classified and segmented images had a good correlation in analysis of >20,000 organoids (fig. S1B). As expected, we found that over time the number of spheroids decreases and they appear darker, confirming that our systematic approach captured what is observed visually (fig. S1, C to E).

To mimic three major types of immune responses, we treated organoids with the signature cytokines IFN γ , IL-13, or IL-22. As was previously found (13, 14), long-term IL-22 or IFN γ treatment ultimately led to organoid disintegration (fig. S1F). At an earlier time point (day 2), this was characterized by a darker appearance, a reduced percentage of spheroids, and an increased percentage of budding organoids (Fig. 1, B and C, and fig. S1G). In contrast, a population of IL-13-treated organoids formed large spheroids at day 2 (Fig. 1C and fig. S1G).

Tuft cells are a specific epithelial cell type involved in type 2 immunity and are induced by IL-13 (6, 7). Tuft cells in organoids share the characteristic shape and F-actin brush with their in vivo counterparts (fig. S2A) (15). We next combined our classification setup with confocal imaging to automatically quantify tuft cells in organoid subtypes. This configuration allows for classification and counting of tuft cells in hundreds of organoids and supports both automatic estimates of tuft cell number and a more accurate manually curated count (fig. S2B). We found that tuft cells primarily appear in budding organoids in both control and IL-13-treated conditions (fig. S2, C to E). Together, these data show that classification of organoids

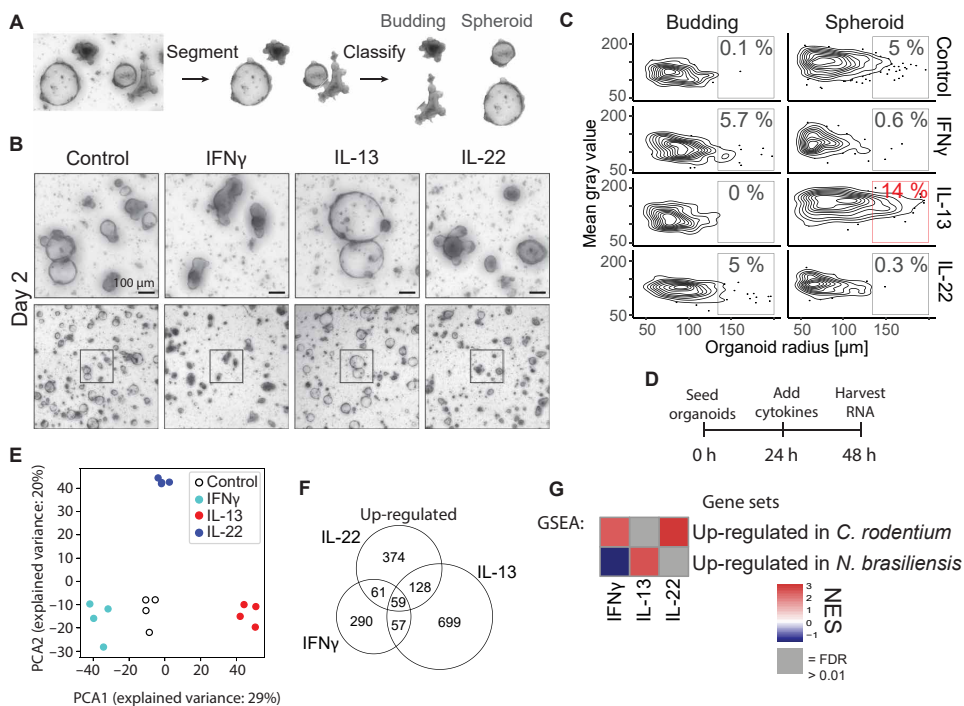


Fig. 1. Cytokines modify development of small intestinal epithelium in a cytokine-specific manner and correspond to in vivo infection models. (A) Image segmentation and classification of organoid images. (B) Representative bright-field images of small intestinal organoids treated with cytokine (10 ng/ml) since the day of splitting. Images are projection of z-stack. (C) Distribution of gray value (higher value is lighter) and area of all organoids in the same experiment as (B). Percentages are relative to total number of organoids in that treatment. Plot shows distribution of total 2310 organoids (representative result of five mice). (D) Time points for experiment from small intestinal organoids treated with cytokine (10 ng/ml). (E) PCA plot of $\log_2(\text{TPM} + 1)$ values determined as shown in (D). Each circle is one biological replicate. (F) Number of up-regulated significant genes from the same experiment as in (D) ($P < 0.05$ and $\log_2fc > 1$). (G) GSEA using gene sets consisting of the 300 most significantly up-regulated genes from intestinal epithelium from mice infected with *N. brasiliensis* or *C. rodentium*. These gene sets are compared with intestinal organoids stimulated with indicated cytokine compared with control. See data file S1 for gene sets. NES, normalized enrichment score.

combined with confocal imaging provides a tractable measure of epithelial cellular responses.

IFN γ , IL-13, and IL-22 differentially affect RNA expression in organoids in a manner aligned to in vivo infection profiles

To assess in detail how IFN γ , IL-13, and IL-22 affect IECs, we performed bulk RNA-seq on organoids treated with indicated cytokines for 24 hours compared with untreated controls (Fig. 1D). The different cytokines showed up-regulation of unique genes that grouped separately in a principal components analysis (PCA) plot, and each cytokine induced different gene ontology (GO) terms, highlighting the different effector responses associated with each type of immune response (Fig. 1, E and F, and fig. S3, A to D).

To investigate to what degree cytokines control the epithelial response in vivo, we performed RNA-seq on intestinal epithelium from mice infected with *N. brasiliensis* or *Citrobacter rodentium*, which are classical intestinal infection models for a parasitic and extracellular bacterial infection, respectively (fig. S4, A and B). Intestinal epithelium infected with *N. brasiliensis* showed the expected induction of tuft cells (fig. S4, C to E) and had enrichment of GO terms associated with wound healing (fig. S4F). Intestinal epithelium infected with *C. rodentium* had up-regulation of GO terms associated with inflammatory response (fig. S4G). We found that duodenal epithelium isolated from *N. brasiliensis*-infected mice was similar to IL-13-treated organoids (Fig. 1G). In contrast, colonic epithelium isolated from *C. rodentium*-infected mice aligned with IL-22- and IFN γ -treated organoids using gene set enrichment analysis (GSEA) (Fig. 1G). A caveat to the *C. rodentium* analysis is that this epithelium was isolated from colon and not small intestine. The correlation with IL-13-induced genes in *N. brasiliensis*-infected epithelium and IL-22-induced genes in *C. rodentium*-infected intestinal epithelium aligns with the standard model of the involvement of these cytokines in specific immune responses and indicates that treating intestinal organoids with cytokines provides a relevant model to, in part, mimic in vivo epithelial responses.

IL-13 and IL-22 induce different gene signatures in goblet cells

To test the effects of IFN γ , IL-13, and IL-22 on cell lineage differentiation, we used cell type-specific gene signatures acquired through scRNA-seq (16). GSEA revealed that these cytokines broadly affect intestinal cell lineage differentiation

in an expected manner (Fig. 2A). For example, giving IL-13 to organoids induced a tuft cell signature, supported by tuft cell staining in vitro (fig. S2C) and in vivo upon *N. brasiliensis* infection (fig. S4, C to E). In addition, both IL-13 and IL-22 induced a goblet cell-associated gene signature (Fig. 2A). However, close examination showed that each cytokine induced a different set of goblet cell genes with relatively little overlap after both 24 and 72 hours of cytokine stimulation (Fig. 2B and fig. S5A); see data file S2 for complete gene lists. This is exemplified by goblet cell markers *Muc2* and *Cla1* being specifically induced by IL-13, whereas another goblet cell marker, RELM β (*Retnlb*), was induced more strongly by IL-22 (Fig. 2C and fig. S5B). Although not all mucins are goblet cell specific (17), we

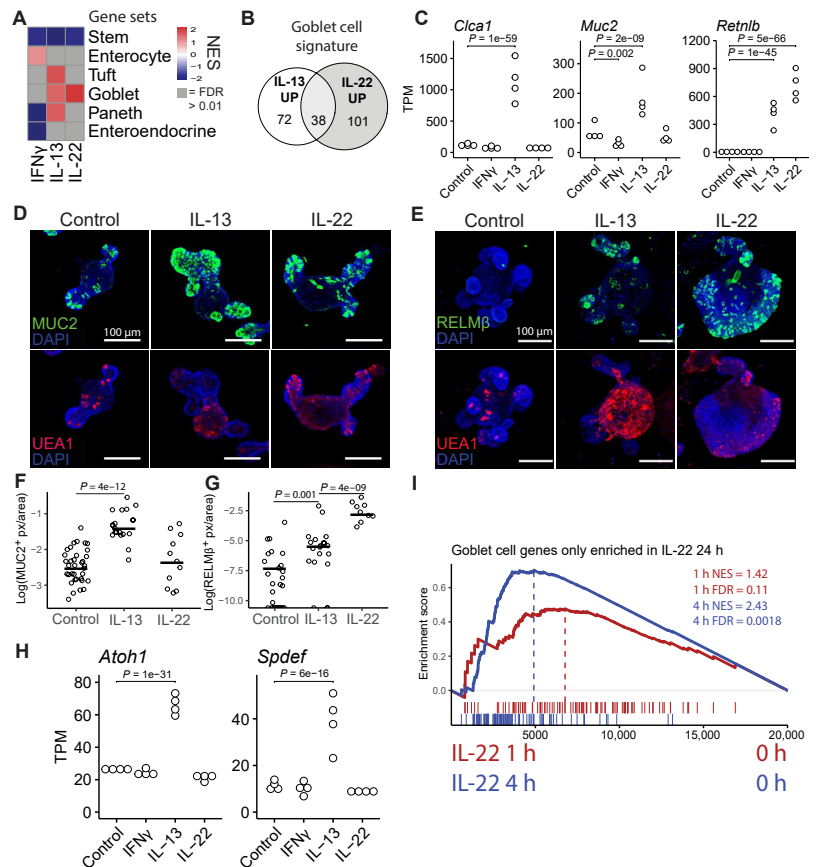


Fig. 2. IL-13 and IL-22 induce different subsets of goblet cell genes. (A) Heatmap of NES values from GSEA analysis of gene sets representing different cell types compared with data from organoids treated for 24 hours with cytokines; see data file S1 for gene sets. (B) Distribution of how the goblet cell gene set from plate-based scRNA-seq from Haber *et al.* (16) is changed upon 24-hour IL-13 and IL-22 treatment in organoids. UP is defined as $\log_2fc > 0.5$ and $P_{adj} < 0.05$. (C) Gene expression from intestinal organoids was treated for 24 hours with indicated cytokine. Statistics calculated with DESeq2. (D and E) Confocal staining of MUC2 and UEA1 2 days after splitting (D) and RELM β and UEA1 at 3 days after splitting (E) in small intestinal organoids. Representative images of three mice. IL-22 (5 ng/ml) and IL-13 (10 ng/ml) were used. (F and G) Quantification of images acquired as in (D) and (E). Pixels are defined as positive above a set threshold. Each circle represents one organoid, and statistics are calculated with unpaired two-tailed t test. (H) See (C). (I) GSEA of IL-22-specific goblet cell genes from (B) compared with data from organoids stimulated with IL-22 for 1 and 4 hours. All images are projections of z-stacks.

found mucin genes to have different expression patterns between IL-13 and IL-22 treatment (fig. S5C). In accordance with our previous work (18), confocal staining confirmed that MUC2 was induced by IL-13 (Fig. 2, D and F), and that RELM β was more strongly induced by IL-22 (Fig. 2, E and G). As a control, we also include staining of the lectin *Ulex europaeus* agglutinin I (UEA I) that binds a multitude of glycoproteins (Fig. 2, D and E). We noted that IL-22-induced (RELM β ⁺) goblet cells also looked different from those induced by IL-13 and often lacked large granule-like structures (Fig. 2E). To determine whether these cells were positive for *Muc2* by mRNA, we combined staining of *Muc2* by RNAscope with MUC2 protein staining (fig. S5D). We found that IL-22 led to the expansion of *Muc2*-high cells with patterns mimicking (RELM β ⁺) staining (fig. S5D). These cells also had low MUC2 protein levels. Canonical differentiation of goblet cells occurs through inhibition of NOTCH and relies on transcription factors ATOH1 and SPDEF (19). IL-13 induced *Atoh1* and *Spdef*; however, IL-22 did not, indicating that IL-22 induces goblet cell genes in an atypical manner (Fig. 2H and fig. S5E). It is not clear from these results what mechanism leads to IL-22-dependent induction of goblet cells, but RNA-seq at early time points after IL-22 stimulation shows that *Retnlb* is induced after just a few hours and GSEA of goblet cell-specific IL-22 response genes shows significant enrichment after just 4 hours (fig. S5F and Fig. 2I). These results indicate that IL-22-specific goblet cell genes are direct targets of IL-22. Furthermore, GO term analysis of the goblet cell genes uniquely induced by IL-13 and IL-22 revealed different terms. For example, “response to endoplasmic reticulum (ER) stress” was the top GO term associated with goblet cell genes induced by IL-22 (fig. S5, G and H). Together, we propose that cytokine-driven goblet cell responses are linked to their function. IL-13 primarily induces mucus to aid in parasite clearance, whereas IL-22 responses are characterized by induction of antimicrobials to kill extracellular pathogens. More specifically, IL-13 leads to a quantitative increase in relative goblet cell numbers, whereas IL-22 treatment leads to a change in qualitative goblet cellular state including the induction of high levels of RELM β .

The BMP pathway is associated with IL-13 and limits tuft cell differentiation in vitro

We were interested in how cytokines control mechanisms that define cell fate in the intestinal epithelium such as the changes in tuft and goblet cells (Fig. 3A). Intestinal epithelium relies on NOTCH,

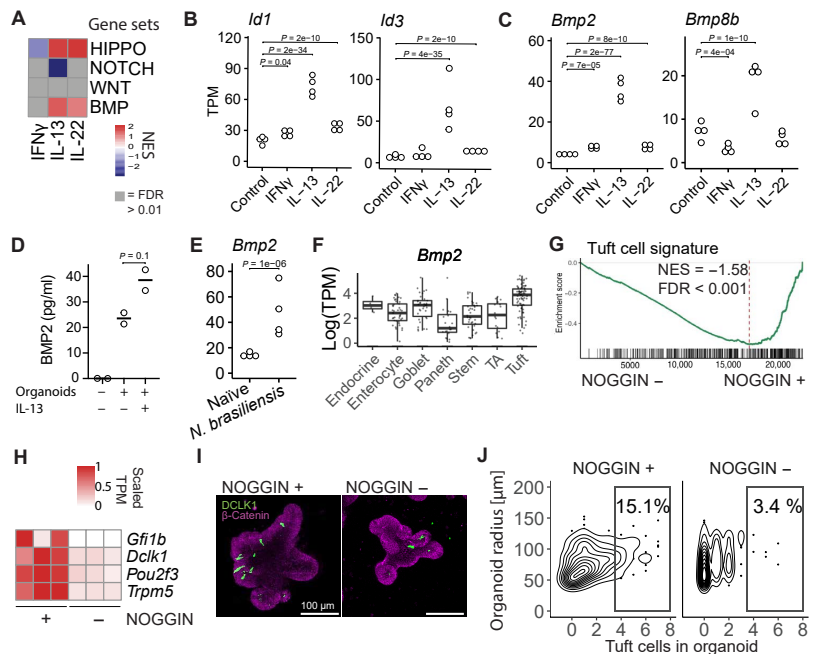


Fig. 3. IL-13 induces BMP2 in intestinal epithelium. (A) GSEA analysis of gene sets representing developmental pathways important in IEC development of bulk data from organoids treated with cytokine (10 ng/ml) for 24 hours. Gene set sources: HIPPO, genes up in artificial YAP induction and down-regulated in YAP-KO; WNT, genes up in organoids treated with the GSK3 inhibitor CHIR; NOTCH, genes up in organoids from ATOH1 KO epithelium compared with wild type (WT); BMP, genes up in organoid treated with BMP4 compared with control. Gene sets and references in data file S1. (B and C) Gene expression in small intestinal organoids treated with cytokines for 24 hours determined with RNA-seq. Each dot is one biological replicate. (D) Concentration of BMP2 in supernatant + Matrigel after spinning down organoids stimulated with IL-13 determined with enzyme-linked immunosorbent assay (ELISA). A control of Matrigel and supernatant but no organoids was included. Each dot is one biological replicate. Representative of two experiments. (E) Gene expression in epithelium from duodenum extracted from mice infected with *N. brasiliensis* determined with RNA-seq. Each dot is one biological replicate. (F) Plate-based scRNA-seq expression data from Haber *et al.* (16) in small intestinal epithelium. TA, transit amplifying. (G) GSEA of tuft cell gene set on small intestinal organoids grown in the presence of NOGGIN or not for 5 days since splitting. (H) Tuft cell marker genes from the same data as (G). (I) DCLK1 confocal staining of small intestinal organoids grown in the presence of NOGGIN or not for 72 hours since splitting. Images are projections of z-stacks. (J) Quantitation of experiment in (I). Representative of two experiments. Plot shows a total of 462 organoids. TPM, transcripts per million.

WNT, BMP, and HIPPO signaling to maintain homeostatic differentiation of cell lineages. We hypothesized that cytokines may use these developmental pathways in directing epithelial cell differentiation. We generated gene sets for these different pathways from published transcriptome datasets (20–23). GSEA analysis revealed that cytokines, and in particular IL-13 and IL-22, alter transcription of genes normally associated with HIPPO, NOTCH, and BMP pathways (Fig. 3A).

We were somewhat surprised to find a strong enrichment of the BMP pathway upon IL-13 treatment. BMP family members are traditionally expressed by mesenchymal cells, so it is unclear how IL-13 may induce the BMP pathway. Nonetheless, established BMP target genes *Id1* and *Id3* (21) are up-regulated specifically after IL-13 treatment (Fig. 3B). Next, we assessed the expression pattern of the transforming growth factor- β (TGF- β) family members and unexpectedly found that IL-13 robustly induced *Bmp2* and *Bmp8b*, but

not any other members (Fig. 3C and fig. S6A). The change in *Bmp2* gene expression was also reflected with an increase of BMP2 protein secreted by organoids stimulated with IL-13 (Fig. 3D). In support, there was also an increase of *Bmp2* during an *N. brasiliensis* infection (Fig. 3E). Haber *et al.* (16) list *Bmp2* as a bona fide tuft cell marker in their gene sets from plate-based scRNA-seq of small intestinal epithelium (Fig. 3F). The connection between tuft cells and IL-13 signaling is further highlighted by the fact that tuft cells specifically expressed high levels of *IL13ra1* as noted by Haber *et al.* (16), whereas *IL4ra* or other cytokine receptors did not have such skewed cell type-specific receptor expression (fig. S6, B to D). In addition, tuft cells have increased phosphorylated signal transducer and activator of transcription 6 (pSTAT6) levels compared with other lineages (24). To test whether BMP pathway activation affects tuft cell differentiation, we compared organoids grown in normal epidermal growth factor (EGF), NOGGIN, and RSPO (ENR) media with organoids grown without the presence of the BMP antagonist NOGGIN (ER media), thus removing the obstructing factor for BMP activation. Organoids grown with NOGGIN in the media showed enrichment for a tuft cell signature and had higher expression of established tuft cell markers (Fig. 3, G and H). Furthermore, antibody staining of the tuft cell marker DCLK1 revealed higher levels of tuft cells in organoids grown in the presence of NOGGIN (Fig. 3, I and J).

The BMP pathway acts as a feedback loop to limit tuft cell expansion

Tuft cells are crucial mediators of parasitic immunity. In a feed-forward loop, tuft cells amplify ILC2s by expressing IL-25, and ILC2s, in turn, express IL-13 to expand tuft cells (5–7). Our findings so far may suggest that IL-13 treatment induces an epithelial-intrinsic feedback loop mediated by BMP pathway activation. To further investigate this, we tested the ALK2 (BMP type I receptor) inhibitor dorsomorphin homolog 1 (DMH1) in combination with IL-13 (Fig. 4A) (25). We found that DMH1 completely blocked the induction of canonical BMP target genes *Id1* and *Id3* (Fig. 4B) but did not affect IL-13-induced *Bmp2* expression (Fig. 4C). Furthermore, the overall enrichment of BMP pathway target genes by IL-13 is blocked by DMH1, without modulating the effect of IL-13 on HIPPO or NOTCH target genes (Fig. 4D). Although DMH1 by itself did not change expression of tuft cell-associated genes such as *Dclk1*, *Pou2f3*, *Trpm5*, and *Alox5*, it did increase the expression of these genes when combined with IL-13 (Fig. 4E). The tuft cell marker gene *Il25* could not be detected in our RNA-seq data, but we did see an increase in *Il25* after IL-13 + DMH1 treatment compared with DMH1 alone when we tested this separately by quantitative polymerase chain reaction (qPCR) (fig. S7A). In support, the tuft cell gene signature was enriched in IL-13 + DMH1 compared with IL-13 by GSEA analysis, whereas no other cell type gene signature was altered (Fig. 4F). Confocal staining confirmed the specific enrichment of tuft cells upon combination treatment of IL-13 and DMH1 (Fig. 4, G to I). In addition, we noted that IL-13 also induced expression of the TGF- β -induced gene *Tgfb1*, independently of ALK2 (Fig. 4J), and this also occurred after *N. brasiliensis* infection (Fig. 4K). BMP signaling is complex and is mediated by multiple receptors. For example, BMP2 can activate both SMAD1/5/8 (BMP) and SMAD2/3 (TGF- β) (26). Therefore, we decided to also test SB525334, an inhibitor for the TGF- β type I receptor ALK5. Just as seen with DMH1, we see an increase in IL-13-induced tuft cells in

organoids treated with SB525334 in a dose-dependent manner (Fig. 4L and fig. S7, B and C). Together, this supports a model in which activation of the BMP and/or TGF- β pathways limits IL-13-induced tuft cell differentiation, thus providing a feedback loop to limit tuft cell expansion during immune responses.

IL-13 activates the BMP pathway in stem cells

To gain further insight into what role the BMP pathway plays in the effect of IL-13 on the intestinal epithelium, we stimulated small intestinal organoids with IL-13 for 1, 4, 8, and 24 hours with and without DMH1 (Fig. 5A). We found that IL-13 itself rapidly affects the transcriptome with 91 significantly changed genes after 1 hour compared with untreated, and 770 genes after 8 hours ($P < 0.01$). In contrast, comparing DMH1 + IL-13 versus IL-13, we found a slower response with only 13 significantly changed genes after 8 hours, but 188 genes after 24 hours ($P < 0.01$) (Fig. 5B). This suggests that BMP target genes are not early response genes upon IL-13 treatment. In accordance, we found that *Bmp2* and *Bmp8b* were rapidly induced after 1 hour (Fig. 5C and fig. S8A), whereas maximal up-regulation of canonical BMP target genes *Id1* and *Id3* and TGF- β target gene *Tgfb1* occurs only after 24 hours (Fig. 5D and fig. S8B). Together, we propose that IL-13-mediated activation of the BMP pathway is mediated by rapid induction of BMP family members such as *Bmp2* and *Bmp8b* to subsequently activate BMP receptors.

We have found that activation of the BMP pathway limits IL-13-mediated tuft cell expansion (Figs. 4 and 5). To determine the cellular sequence of events, we downloaded and reanalyzed an scRNA-seq dataset from small intestinal organoids that were treated with IL-13 (Fig. 5E) (3). We split the tuft cell population in two, and by RNA velocity analysis, we found that there is a tuft cell progenitor (with closer proximity to the stem cell population) and a mature tuft cell population (Fig. 5F). The mature tuft cells have a high expression of *Dclk1*, *Pou2f3* is expressed in both populations, and *Sox4* is specific for tuft cell progenitors (Fig. 5G). The transcription factor *Sox4* has previously been found to be important in tuft cell development (27). Although *Sox4* has been associated with the intestinal stem cell signature (28), in this dataset, it is more highly correlated with progenitor tuft cells (Fig. 5G). Qi *et al.* (21) found that mice with an inducible epithelial specific knockout of *Bmpr1a* (ALK3) had up-regulation of *Sox4* expression in *Lgr5*⁺ stem cells and that *Sox4* is down-regulated in *Lgr5*⁺ stem cells from intestinal organoids stimulated with BMP4, indicating that the BMP pathway might actively regulate the amount of *Sox4*-positive tuft cell progenitors. To investigate where the BMP pathway affected tuft cell development, we plotted *Id1* and *Id3* expression and found them to be specifically induced in stem cells by IL-13 (Fig. 5H). Furthermore, *Sox4* was rapidly induced by IL-13 before it returned to homeostasis levels after 24 hours, and this down-regulation was not seen in 24 hours of IL-13 stimulation with DMH1 (Fig. 5I). This result is supported by our 72-hour stimulation data where we see an up-regulation of *Sox4* in IL-13 + DMH1 compared with IL-13 (Fig. 5J). We were not able to associate ALK2 receptor (*Acvr1*) expression to stem cells specifically (fig. S8C), so how stem cell-enriched responses occur is still unclear. In summary, these data indicate a model where IL-13 induces differentiation of stem cells into tuft cell progenitors positive for *Sox4*. At the same time, IL-13 induces production of molecules activating the BMP pathway, which acts on stem cells and inhibits them from developing into *Sox4*-positive tuft cell progenitors.

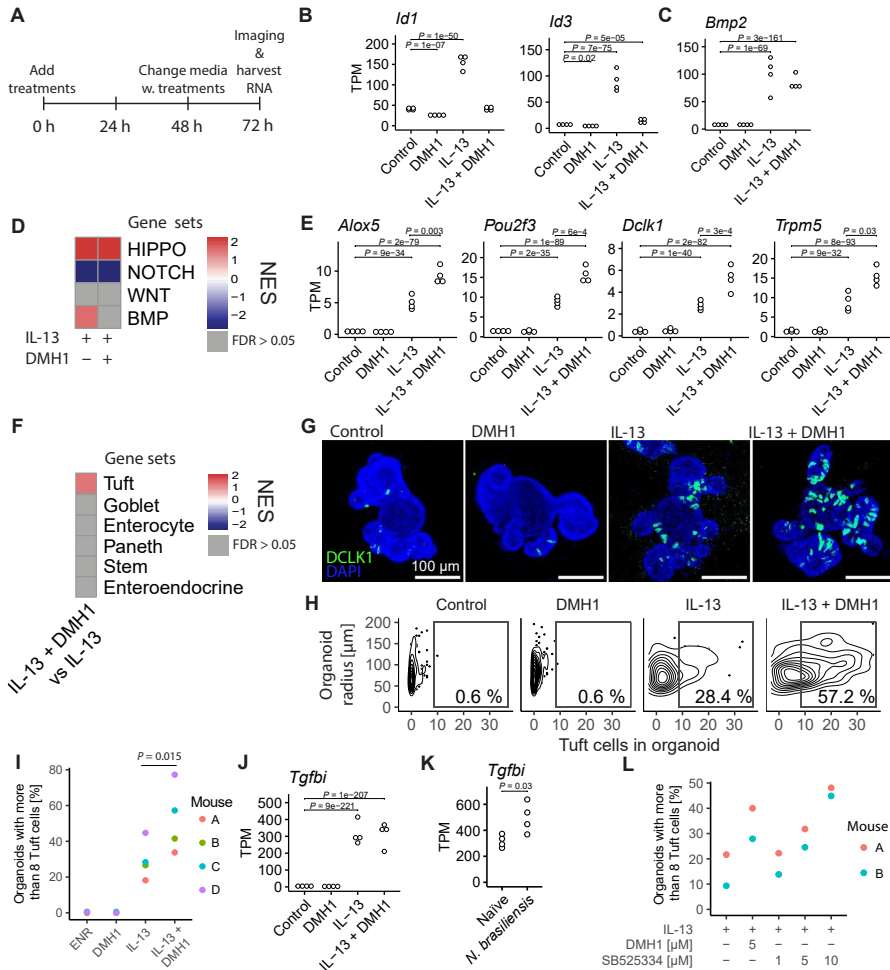


Fig. 4. Activation of the BMP pathway restricts IL-13-induced tuft cell expansion. (A) Time points since seeding for experiment from small intestinal organoids treated with cytokine (10 ng/ml) and 5 μ M DMH1 for 72 hours. (B and C) Gene expression determined as described in (A). Each circle is one biological replicate, and statistics were calculated with DESeq2. (D) Heatmap of NES values from GSEA of gene sets representing signaling pathways in indicated treatments versus control condition. See data file S1 for exact gene sets. (E) See (B). (F) Heatmap of NES values from GSEA of gene sets representing cell types from Haber *et al.* (16) in IL-13 + DMH1-treated organoids versus IL-13 organoids. See data file S1 for exact gene sets. (G) Confocal staining of DCLK1 in small intestinal organoids treated with indicated treatments for 72 hours. Images are projections of z-stacks. (H) Manual quantification of the same experiment as (G); plot represents a total of 566 organoids. (I) Percentage determined as in (H), where each circle is a biological replicate from independent experiments. *P* value determined with a paired *t* test. (J) See (B). (K) Gene expression in intestinal epithelium extracted from mice infected with *N. brasiliensis* determined with RNA-seq. Each circle is one biological replicate, and statistics are calculated with DESeq2 (see Materials and Methods). (L) Percentage of organoids with more than eight tuft cells. Determined in similar fashion as in previous figures [see (G) to (I)] except that this is automatic tuft cell counts. Each circle is one biological replicate. Representative of two experiments. DMH1 inhibits ALK2, and SB525334 inhibits ALK5.

BMP signaling restricts *N. brasiliensis*-induced tuft cell expansion in vivo

Organoid work allows us to study intestinal epithelial mechanisms in isolation. However, in vivo, there are many additional cell types that together orchestrate immunity to infection. To investigate the role of ALK2 signaling in *N. brasiliensis*-induced tuft cell hyperplasia, we injected mice with either DMH1 or its solvent [dimethyl sulfoxide (DMSO)] intraperitoneally every other day

starting 1 day before infection (Fig. 6A). Confocal staining of DCLK1 revealed an increase in the number of tuft cells at both day 6 and day 8 after infection when comparing DMH1-treated with DMSO-treated animals (Fig. 6, B and C). The increase in tuft cells was also associated with a nonsignificant increase in *Il25*, but not *Il13* (fig. S9A). No difference was found in RELM β - or UEA I (goblet)-positive cells, indicating that the difference is specific to tuft cells (Fig. 6, D to F).

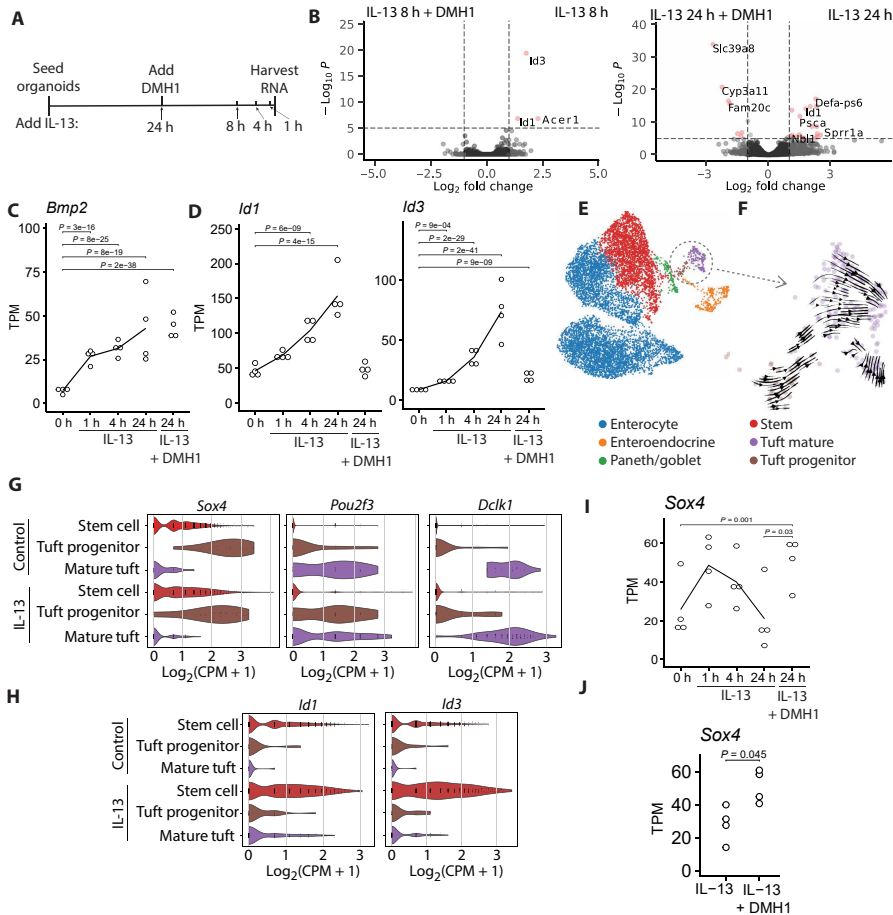


Fig. 5. IL-13 activates the BMP pathway in stem cells, skewing them away from tuft cell progenitors. (A) Time points for experiment from small intestinal organoids treated with cytokine (10 ng/ml) at indicated time points and with and without 5 μ M DMH1 for 24 hours. (B) Volcano plots comparing indicated treatments from experiment described in (A). (C and D) Gene expression of experiment described in (A). Each circle is one biological replicate, and statistics are calculated with DESeq2. (E) scRNA-seq data of small intestinal organoids were treated with IL-13 and untreated from Biton *et al.* (3). (F) RNA velocity analysis of tuft cell populations from scRNA-seq data presented in (E). (G and H) Violin plots of gene expression in tuft cells from scRNA-seq data presented in (E). (I) See (C). (J) Gene expression of small intestinal organoids treated with indicated treatment for 72 hours. Each circle is one biological replicate, and statistics are calculated with DESeq2; see Materials and Methods. CPM, counts per million.

To test whether BMP/TGF- β signaling is altered during infection, we performed pSMAD2 staining (Fig. 7, A and B). We found that there was a significant induction of nuclear pSMAD2 levels in crypt cells of infected mice compared with uninfected mice, and that this induction required ALK2 signaling as it did not occur in DMH1-treated mice (Fig. 7, A and B). On the basis of our organoid work, we proposed that activation of the BMP/TGF- β pathway leads to repression of *Sox4* (Fig. 5, G to J). We found a reduction of crypt base-located *Sox4* levels after infection, and this repression did not occur in DMH1-treated animals (Fig. 7, C and D). As reported by others, we found *Sox4* enriched at the stem cell zone (27, 28); however, the reduction of *Sox4* did not lead to a reduction of numbers of intestinal stem cells, as measured by counting

OLFM4⁺ cells in crypts (Fig. 7, E and F), nor did it affect crypt proliferation as assessed by Ki67 staining (fig. S9, B and C) or apoptosis as assessed with cleaved caspase 3 staining (fig. S9, D and E). Last, we investigated the association between *Bmp2* and tuft cells *in vivo* by using RNAscope probes for *Bmp2* and *Dclk1*. We found *Bmp2* to be associated with tuft cells in the crypt (Fig. 7, G and H). This association is not exclusive to tuft cells, as we detect *Bmp2* in nontuft cells, especially at the villus tip, a conclusion that is supported by the association of *Bmp2* with both enterocytes and tuft cells in organoids stimulated with IL-13 in scRNA-seq data from Biton *et al.* (3) (Fig. 7I). Together, these results suggest that BMP/TGF- β signaling restricts *N. brasiliensis*-dependent tuft cell expansion *in vivo* by controlling *Sox4* expression.

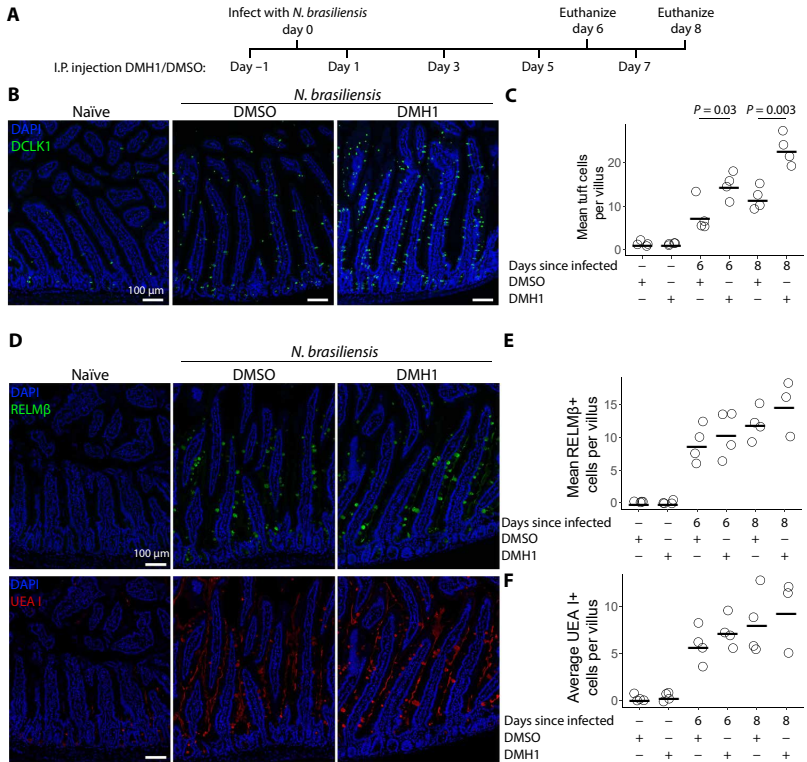


Fig. 6. BMP signaling restricts *N. brasiliensis*-induced tuft cell expansion in vivo. (A) Timeline of *N. brasiliensis* infection and intraperitoneal injection of 5 μM DMH1 dissolved in DMSO or solvent alone. (B) DCLK1 antibody staining of duodenum from mice 8 days after infection with *N. brasiliensis* and injected with DMH1 according to the timeline shown in (A). (C) Quantification of images shown in (B) and additional images. Each dot represents one mouse. Statistics were calculated with unpaired two-tailed t test. (D) RELMβ antibody and UEA I staining of duodenum from mice 8 days after infection with *N. brasiliensis* and injected with DMH1 according to the timeline shown in (A). (E and F) Quantification of images shown in (D) and additional images. Each dot represents one mouse.

DISCUSSION

The intestinal epithelium is capable of rapidly altering its cellular composition to defend against pathogens. Here, we provide a comprehensive comparison of how different types of immune responses mechanistically drive changes in the intestinal epithelium. Specifically, we find that key cytokines associated with different modes of immunity influence developmental pathways to guide changes in epithelial composition.

In recent years, tuft cells have been identified as regulators of intestinal health in general (9), and have taken center stage in the defense against helminth infections specifically (29). They express receptors that help them detect helminths, which together with type 2 cytokines result in their expansion (30, 31). This culminates in a feed-forward loop where tuft cell-derived IL-25 activates ILC2s and ILC2-derived IL-13 induces tuft cell differentiation (5–7). There are factors that can limit this feed-forward loop. For example, the putative epithelial-intrinsic PGD₂-CRTH2 axis counteracts the IL-13-induced epithelial response (32), and ILC2-expressed cytokine-inducible SH2-containing protein (CISH) blocks ILC2 activation, which in turn limits tuft cell

expansion (33). Other competing cytokines can also affect this loop, as IL-22 inhibits IL-13-induced tuft cell responses (34). Last, pathogens may also take part. Two studies recently showed that *Heligmosomoides polygyrus*-secreted products can inhibit tuft cell expansion, likely by directly reprogramming epithelium toward a fetal-like state (35, 36).

Here, we identify that intestinal epithelial-intrinsic BMP signaling can act as a brake on IL-13-induced tuft cell expansion (Fig. 4). We attribute this feedback mechanism to BMP/TGF-β signaling in general rather than a single BMP protein, as we found both *Bmp2* and *Bmp8b* to be induced by IL-13 in organoids. The ALK5 inhibitor SB525334 showed a similar ability to the ALK2 inhibitor DMH1 to increase tuft cell numbers upon IL-13 treatment (Fig. 4L and fig. S7). Previous scRNA-seq experiments listed *Bmp2* as a putative tuft cell marker (16), and we confirm that there is enrichment in tuft cells (Fig. 7, G to I). However, and especially upon IL-13 treatment, we also observe that enterocytes express *Bmp2* (Fig. 7, G and I). As enterocytes are the most prevalent cell type, the relative contribution of tuft cell-derived BMP2 should be further examined to assess its importance relative to enterocyte-derived BMP2.

Our data indicate that the IL-13-mediated tuft cell hyperplasia is limited by BMP/TGF-β-dependent inhibition of *Sox4*. *Sox4*⁺ tuft cell progenitors are thus initially expanded by IL-13 and then repressed by the BMP pathway. It is paradoxical that inhibition of the BMP pathway can affect intestinal epithelial stem

cells because the crypt is surrounded by BMP antagonists (37), and it is thought that most BMP signaling takes place in the villus (38). However, these BMP antagonists incompletely block BMP signaling because some pSMAD1/5/8 activation is still found in LGR5⁺ stem cells (21), and we observed a distinct increase of pSMAD2 in intestinal crypts upon infection with *N. brasiliensis* (Fig. 7). Furthermore, our experiments comparing IL-13 and IL-13 + DMH1 were done in the presence of NOGGIN, a BMP inhibitor, indicating that these crypt-localized inhibitors only partly inhibit BMP signaling. There is a strong and rather specific induction of canonical BMP target genes *Id1* and *Id3* in intestinal stem cells upon IL-13 treatment (Fig. 5H), and IL-13-induced *Id1* and *Id3* were abrogated by DMH1 treatment (Fig. 5D). In support, a recent study showed that there was specific accumulation of *Id1* in intestinal stem cells in vivo upon ablation of GREMLIN⁺ cells (39). These data suggest that intestinal stem cells express the relevant BMP receptor(s). Unfortunately, the ALK2 (*Acvr1*) expression levels in the scRNA-seq dataset were rather low overall and did not provide conclusive evidence [fig. S8C; based on data from (3)]. Thus, to determine whether the differential activation

Downloaded from https://www.science.org at Norwegian University of Science & Technology - University of Trondheim on May 31, 2023

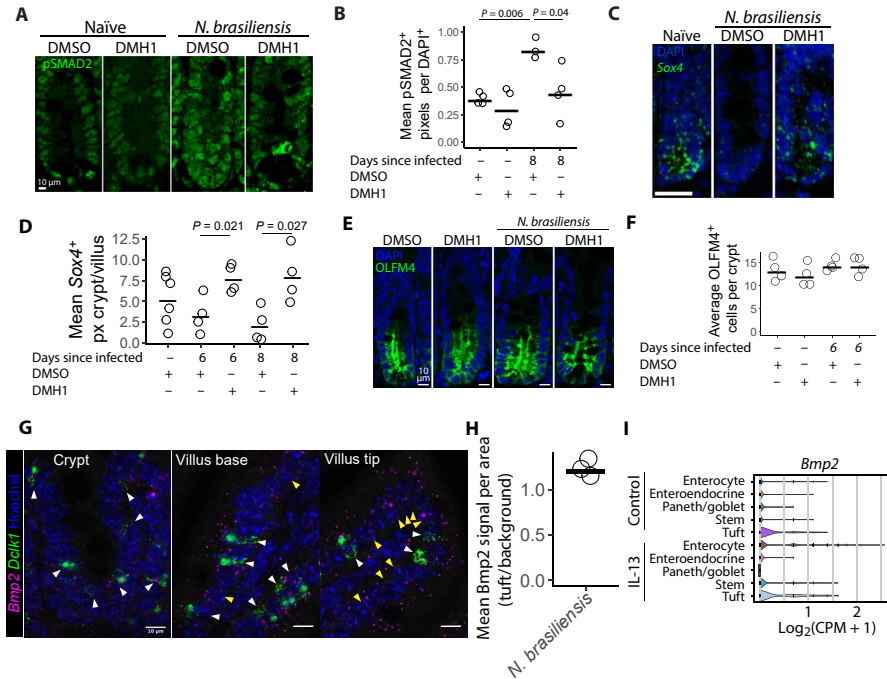


Fig. 7. DMH1 restricts *N. brasiliensis*–induced BMP signaling. (A) pSMAD2 antibody staining in crypts from duodenum from mice 8 days after infection with *N. brasiliensis*. DMSO or DMH1 was injected every other day starting 2 days before infection. (B) Quantification of images shown in (A). Each circle represents the mean of at least five crypts in one mouse measuring pSMAD2⁺ pixels divided by DAPI⁺ pixels. Statistics were calculated with unpaired two-tailed t test. (C) RNAscope probe for *Sox4* in crypts from duodenum 8 days after infection. Scale bar, 25 μ m. (D) Quantification of images shown in (C) and additional images. Each circle represents the mean of at least five crypts in one mouse measuring *Sox4*⁺ pixels in the crypt divided by *Sox4*⁺ pixels in the villus. Statistics calculated with unpaired two-tailed t test. (E) Confocal images of OLFM4 staining in crypts from duodenum 6 days after infection. (F) Quantification of images shown in (E). Each dot represents the average of at least five crypts from one mouse. (G) RNAscope probe for *Bmp2* in indicated tissue from duodenum 6 days after infection. (H) Quantification of crypts from images shown in (G). *Bmp2* signal per area was measured in the immediate vicinity of *Dclk1* signal divided by cells not positive for *Dclk1* (defined as background). Both tuft cell area and background area were manually defined, and each circle represents one mouse. (I) Violin plots of gene expression of small intestinal organoids treated with IL-13 or untreated based on scRNA-seq data from Biton *et al.* (3).

of the BMP pathway in intestinal stem cells compared with other cell types, as measured by *Id1* and *Id3* expression, is regulated by receptor abundance, additional tools are warranted. Overall, it seems like intestinal stem cells are protected from BMP pathway activation by antagonists like GREMLIN 1, but this can be overcome under specific conditions such as those induced by IL-13 treatment or infection.

In addition to our findings regarding cytokine-driven tuft cell expansion, we also provide data suggesting that both IL-13 and IL-22 induce goblet cell gene signatures, but these are different (Fig. 2). There have been conflicting reports on whether IL-22 influences goblet cell levels in intestinal epithelium. Some studies find that the number of MUC2⁺ cells are unchanged or reduced upon IL-22 treatment (40, 41); however, a study that overexpressed the IL-22 inhibitor IL-22BP in the gut found a reduction in goblet cells (42), and IL-22 knockout mice infected with *N. brasiliensis* have reduced goblet cell induction as measured by periodic acid–Schiff (PAS) staining (43). In addition, the goblet cell effector RELM β is critical for resistance against both bacterial and helminth infections (44–46). We hypothesize that the difference between IL-13– and IL-22–induced goblet cells is related to the type of immune response.

Immunity to parasites requires a “weep and sweep” response, in which goblet cells play an essential role by secreting mucus (weeping) to facilitate the expulsion of helminths (47), whereas other responses may rely less on the induction of mucus and expansion of goblet cell numbers. Instead, we find that IL-22 rapidly induces goblet cell–specific ER stress response genes, which corroborates recent work that identified a pathologically relevant role for IL-22 in colitis (48).

Overall, our approach of stimulating intestinal organoids with cytokines has revealed that developmental pathways underlie the cellular composition changes that occur as part of immune responses taking place in the intestine. In support, a recent study showed that IL-17RA signaling in intestinal stem cells induces ATOH1, thereby inducing secretory cells through NOTCH signaling (49). These changes have been confirmed using relevant *in vivo* models of infection or inflammation. It is important to balance both active immunity/inflammation with resolution of inflammation, and many immunopathologies reflect the importance of maintaining this balance. The discovery of an innate BMP-driven brake on IL-13–induced immune changes suggest that targeting this pathway may

therefore be a useful tool to aid resolution of inflammation in clinically relevant diseases.

MATERIALS AND METHODS

Study design

The aim of this study was to identify how immune cues such as cytokines markedly change the intestinal epithelial composition, which is needed as an effector response during immunity to infection. We used organoid cultures treated with cytokines and developed image analysis tools to assess them in combination with transcriptomic analyses. We also used transcriptomic analysis to compare in vitro epithelial organoid responses with epithelial responses occurring in vivo in mice upon infection with *C. rodentium* (bacterium) or *N. brasiliensis* (helminth). Upon identification of the link between tuft cells and the BMP pathway in vitro in organoids, we verified this in vivo by treating mice infected with *N. brasiliensis* with DMH1, an ALK2 inhibitor. Last, we relied on tissue antibody and RNAscope staining to assess whether signaling molecules such as pSMAD2 and key transcription factor *Sox4* were changed in intestinal crypts, which is where IEC fate is decided.

Animal experiments

All mouse work done in Norway was performed in accordance with CoMed NTNU (Norwegian University of Science and Technology) institutional guidelines and Norwegian legislation on animal experiments. These experiments used C57BL/6 mice bred in house using mice originally obtained from Janvier Labs.

The experiments with *C. rodentium* were approved by Norwegian Food Safety Authority (FOTS ID: 11842). *C. rodentium* was grown at 37°C in LB medium supplemented with chloramphenicol (30 µg/ml) overnight. Nine- to 11-week-old mice were orally gavage with a culture of 10⁸ to 10⁹ colony-forming units per mouse delivered in a volume of 100 µl of sterile phosphate-buffered saline (PBS). To determine infection level, fecal samples were collected on day 5, homogenized in sterile PBS with a FastPrep homogenizer, and plated on chloramphenicol-resistant agar plates in serial dilutions. The plates were counted after 24 hours of growth at 37°C. After 6 days of infection, mice were euthanized by CO₂ inhalation, and parts of distal colon tissue were harvested for isolation of crypts as described below. RNA was isolated, and samples were further used for analysis.

Mouse experiments with *N. brasiliensis* used C57BL/6 mice (obtained from Envigo UK) aged 8 to 12 weeks maintained in individually ventilated cages according to UK Home Office guidelines. *N. brasiliensis* was maintained as previously described (50). Mice were infected with larva of *N. brasiliensis* subcutaneously. In total, 200 L3 larvae were used for sequencing experiments, and 400 L3 larvae were used for experiments with DMH1. For experiments with DMH1, DMH1 (4 mg/kg) dissolved in 20 µl of DMSO, or control of DMSO alone, was administered every other day, starting 1 day before infection. Mice were euthanized via cervical dislocation, and duodenal tissue was harvested for use in imaging and for isolation of crypts as described below.

Small intestine and colon crypt isolation

Crypts from small intestine and colon were isolated according to a published protocol (51). In summary, the duodenal small intestine or distal colon was washed in ice-cold PBS and opened

longitudinally. A microscopy coverslip was used to gently scrape off excess mucus and villus before the intestine was cut into 2- to 4-mm pieces. The fragments were resuspended in 30 ml of ice-cold PBS and pipetted up and down with a 10-ml pipette. Supernatant was discarded, and this step was repeated 5 to 10 times until the supernatant was clear. The fragments were incubated in 2 mM EDTA in PBS for small intestine, and 10 mM EDTA in PBS for colon, at 4°C for 30 min with gentle rocking. The supernatant was removed, 20 ml of ice-cold PBS was added, and the fragments were pipetted up and down. This washing step was repeated until the crypt fraction appeared. The one to three consecutive crypt fractions were passed through a 70-µm cell strainer and collected into a fetal calf serum-coated 50-ml tube. The crypts were spun down at 300g for 5 min and washed once in 10 ml of ice-cold PBS at 200g for 5 min.

Small intestinal organoid culture

About 200 to 500 crypts were resuspended in 50 µl of Matrigel (Corning, 734-1101) and kept at 4°C. A total of 50 µl of the Matrigel solution was added to the center of a prewarmed 24-well plate or 8-well microscopy slide (Ibidi, 80821) and transferred to an incubator at 37° with 5% CO₂. After 5 min, the pellet had solidified and 500 µl of basal culture medium [advanced Dulbecco's modified Eagle's medium/F12 supplemented with penicillin/streptomycin, 10 mM Hepes, 2 mM Glutamax, 1× N₂ (Thermo Fisher Scientific 100X, 17502048), 1× B27 (Thermo Fisher Scientific 50X, 17504044), and 1× *N*-acetyl-L-cysteine (Sigma-Aldrich, A7250)] overlaid with ENR factors containing murine EGF (50 ng/ml; Thermo Fisher Scientific, PMG8041), 20% conditioned medium (CM) from a cell line producing R-spondin (gift from C. Kuo, Stanford University School of Medicine, Stanford, CA, USA), and 10% Noggin-CM (a gift from H. Clevers, Hubrecht Institute, Utrecht, The Netherlands) was added. The culture medium was replaced every 2 to 3 days. Organoids were passaged by disrupting them with strong mechanical pipetting, letting the solution cool on ice before centrifuging at 200g, 5 min at 4°C, and resuspending in Matrigel. Organoid lines were maintained, and normal budding morphology was observed throughout passaging. All experiments were done within the range of 4 to 50 passaging events.

Compounds or cytokines were diluted in culture medium and added to culture medium: IL-13 (10 ng/ml; PeproTech, 210-13), IL-22 (5 or 10 ng/ml; PeproTech, 210-22), IFNγ (10 ng/ml; BioLegend, 575306), 5 µM DMH1 (STEMCELL Technologies, 73632), and 1, 5, and 10 µM SB525334 (Selleckchem, S1476).

Enzyme-linked immunosorbent assay

Small intestinal organoids were cultured for 72 hours with or without IL-13 (10 ng/ml). A total of 200 µl of medium per well was used to disrupt the Matrigel. The solution was centrifuged, and the resulting supernatant was used undiluted in the BMP2 Mouse ELISA Kit (Abcam, ab119582). The manufacturer's protocol was followed, with PBS being used as washing buffer.

Quantitative polymerase chain reaction

Duodenum tissue was harvested and stored in RNAlater at -80°C. Four beads and 300 µl of RNA-Solv Reagent (Omega Bio-Tek, R6830-02) were added to tissue samples and homogenized using a FastPrep homogenizer with 20-s pulses. The samples were lysed for 10 min and centrifuged (12,000g, 30 s). RNA was isolated from the supernatant using the Quick-RNA Miniprep Kit (R1055, Zymo Research) with deoxyribonuclease I treatment according to

the manufacturer's protocol. Complementary DNA (cDNA) was synthesized using the Maxima First Strand cDNA Synthesis Kit for reverse transcription qPCR (K1641, Thermo Fisher Scientific) using 1 µg of RNA. cDNA was diluted 1:5, and qPCR was performed using Perfecta Ta SYBR Green FastMix on the StepOnePlus Real-Time PCR System. qPCR from organoids was performed similarly from the lysis buffer addition step except for using 500 ng of RNA for cDNA synthesis. See table S1 for primer sequences.

Bright-field imaging and quantification of intestinal organoids

Z-stacks covering the entire Matrigel droplet were captured using an EVOS2 microscope. Two-dimensional morphological properties of organoid objects and their classification were gathered using a custom analysis program written in Python based on `opencv2` (see above for link to code). The brightness of images was autoscaled to max brightness, and a canny edge detection algorithm was run on each individual z-plane using the `opencv2.canny` function. Groups of pixels below a certain size were removed, and a minimal projection of the edges was generated. This image was used to define the contour of objects. `opencv2s` watershed algorithm was used to split objects from each other, and the center of the object was defined as the pixel furthest from the edge of the object. Each defined object contour was used to extract a 120 × 120 pixel picture of the object on a white background from a minimal projection of the original z-stack. These images were used to classify the organoid as either "junk," budding, or spheroid with a convolutional neural network implemented using TensorFlow and Keras. The network was trained on 25,656 manually classified 120 × 120 images prepared as just described. For initial analysis, these data were plotted, but for plots used in this publication, the pictures were reviewed manually in a graphical user interface (GUI) written in Python. This GUI displayed the center of each object and its classification and enabled addition of new object centers or editing of automatically found object centers. The manually verified annotations were used to rerun the segmentation as described above, but this time, the classification of the objects was not changed and a watershed algorithm was used to segment object contours based on the manually curated object centers. Last, objects with a size less than 300 pixels were filtered out. To highlight differences between treatments, thresholds for percentage calculations were chosen to be set around the upper bound of the treatment with the lowest organoid radius.

Immunofluorescence staining of organoids

Organoids grown for immunofluorescent imaging were cultured in Matrigel mixed with 25% basal culture medium (described above) in eight-well slides (Ibidi, 80821). Organoids were fixed in 300 µl of 4% paraformaldehyde with 2% sucrose for 30 min and washed with PBS two times (5 min). Cells were permeabilized in 0.2% Triton X-100 in PBS for 30 min and then washed with PBS three times (5 min). Free aldehydes were blocked in 100 mM glycine for 1 hour, and wells were incubated in 300 µl of blocking buffer [2% normal goat serum, 1% bovine serum albumin (BSA), and 0.2% Triton X-100 in PBS] for 1 hour. Primary antibodies, β -catenin [1:200, mouse monoclonal antibody (mAb); Santa Cruz Biotechnology, sc-7963, RRID:AB_626807], DCLK1 [1:250, rabbit pAb; Abcam, ab31704, RRID:AB_873537], MUC2 [1:200, rabbit polyclonal antibody (pAb); Santa Cruz Biotechnology, sc-15334, RRID:AB_2146667], and RELM β [1:200, rabbit pAb; PeproTech, 500-P215, RRID:AB_1268845] were diluted in

150 µl of blocking buffer and incubated overnight at 4°C. Samples were washed in PBS with agitation three times (10 min). The appropriate Alexa Fluor secondary antibody (1:500), 4',6-diamidino-2-phenylindole (DAPI) (1:10,000), and UEA 1 (rhodamine-labeled diluted 1:500; Vector Laboratories, RL1062) were added in blocking buffer (1% normal goat serum, 0.5% BSA, and 0.2% Triton X-100 in PBS) and incubated at 4°C with agitation overnight. For samples where F-actin was stained, rhodamine phalloidin (1:100, Invitrogen, R415) was added together with the secondary antibodies overnight. Samples were washed in PBS, three times (5 min), and 250 µl of Fluoromount-G medium (Thermo Fisher Scientific, 00-4958-02) was added to the well. Images were acquired with a Zeiss Airyscan confocal microscope.

Immunofluorescence staining of tissue sections

The harvested intestinal tissue was fixed with 10% formalin for 48 hours at room temperature. Tissue was subsequently dehydrated through a series of graded ethanol and embedded in paraffin wax blocks. Five-micrometer-thick sections were cut using a microtome. The tissue sections were heated in an oven at 60°C for 30 min and deparaffinized in two changes of Neo-Clear (Sigma-Aldrich, 109843) for 5 min, followed by graded ethanol [100% ethanol two times (3 min) and once through 95, 80, and 70% ethanol and water (3 min)]. Heat-mediated antigen retrieval was performed using citrate buffer except for pSMAD2 (phospho-S255) and cleaved CASP3 for which tris-EDTA buffer pH 9 was used. For antigen retrieval, slides were boiled for 15 min, left to cool in the buffer for 20 min for all stainings except for cleaved CASP3, which was done for 2 hours, and then briefly washed with H₂O. Tissue sections on glass slides were marked with a hydrophobic pen (PAP pen, ab2601). Staining with primary and secondary antibodies was added as described above except that a humidified chamber was used for incubations. Primary antibodies used for tissue were Ki67 (1:100, rabbit mAb; Invitrogen, MA5-14520, RRID:AB_10979488), pSMAD2 (phospho-S255) (1:100, rabbit mAb; Abcam, ab188334, RRID:AB_2732791), OLFM4 (1:100, rabbit mAb; Cell Signaling Technology, 39141S, RRID:AB_2650511), and anti-cleaved caspase 3 (1:200, rabbit pAb; Cell Signaling Technology, 9661, RRID:AB_2341188).

RNAscope in situ hybridization of tissue sections and organoids

RNAscope was done using the kit RNAscope Multiplex Fluorescent V2 Assay (Advanced Cell Diagnostics) according to the manufacturer's protocol for formalin-fixed paraffin-embedded (FFPE) samples. The following probes were used: Sox4-C2 (1:50; 471381-C2), Mm-Bmp2 (1:50; 406661-C4), Mm-Dclk1 (1:50; 1476631), and Mm-Muc2 (1:100; 315451-C3). When staining organoids, 8 Well Chamber, removable (Ibidi, catalog no. 80841) was used, and after the RNAscope protocol, slides were blocked and stained with antibodies for RELM β and MUC2 as described above.

Quantification of immunofluorescence images

The same code base was used as described for bright-field images of organoids except that the first step was to add the center position of all intestinal organoids and their class manually. Furthermore, tuft cells were manually annotated in the DCLK1 channel using the custom GUI. The number of tuft cells inside each organoid could therefore be counted. To highlight differences between treatments, thresholds for percentage calculations were set around the upper

bound of the treatment with the lowest induction in tuft cells. The analysis was done blindly by randomizing the order of images and hiding image identity when manually annotating images.

The same code base was used to analyze confocal images of tissues stained for pSMAD2, *Sox4*, and OLFM4 with some changes. A binary mask defining the tissue area to quantify, for example, crypts, villus, or both was manually made for each tissue section. Both the mean intensity of each channel and the number of pixels above a channel-individual threshold were measured for each channel inside each marked region in the tissue mask. The analysis was done blindly by randomizing the order of images and hiding image identity when manually creating masks for tissue area to quantify.

A similar approach to what is described in the previous paragraph was used to quantify *Bmp2* RNAscope signal in tuft cells compared with background. A mask was manually drawn around each *Dclk1*-positive area approximately encompassing a single tuft cell. Another mask (called background) was drawn around the rest of the cells in the crypt without *Dclk1* signal.

The number of DCLK1⁺, RELM β ⁺, UEA I⁺, and cleaved CASP3⁺ cells per villus was manually counted. The analysis was done blindly by randomizing the order of images and hiding image identity when manually creating masks for tissue area to quantify.

RNA isolation and sequencing

RNA was extracted with the Quick-RNA Microprep Kit according to the manufacturer's instructions (Zymo, R1050). Library preparation and sequencing for 24-hour cytokine samples were performed by NTNU Genomic Core facility. Library preparation was done with Lexogen SENSE mRNA kit, and the library was sequenced on two Illumina NS500 HO flow cells using 75–base pair (bp) single-stranded reads. All other library preparation and sequencing were performed by Novogene UK using the NEB Next Ultra RNA Library Prep Kit. Samples were sequenced using 150-bp paired-end reads using NovaSeq 6000 (Illumina).

Batch RNA-seq analysis

Reads were aligned to the *Mus musculus* genome build mm10 using the STAR aligner. The count of reads that aligned to each exon region of a gene in GENCODE annotation M18 of the mouse genome was counted using featureCounts. Genes with a total count less than 10 across all samples were filtered out. Differential expression analysis was done with the R package DESeq2, and volcano plots were plotted with the R package EnhancedVolcano. PCA analysis was performed with the scikit-learn package with the function sklearn.decomposition.PCA. GSEA analysis was run with the log₂(fold change) calculated by DESeq2 as weights, 10,000 permutations, and otherwise default settings using the R package clusterProfiler. GO term analysis was run using the function enrichGO in clusterProfiler. The R packages pheatmap and eulerr were used to make heatmaps and venn diagrams, respectively. RNA-seq of organoids grown in the absence and presence of Noggin can be found from the ArrayExpress accession E-MTAB-9181 and analyzed as described in (52).

scRNA-seq analysis

Barcodes, genes, and matrix files for control and IL-13–treated samples were downloaded from Gene Expression Omnibus (GEO) accession GSE106510 (3). In addition, BAM files from GSE106510 were downloaded from sequencing read archive, and velocity was run on these data using mouse genome mm10 with repeatmask for

mm10. Matrix data and velocity output were loaded into one adata object in scanpy. Quality control filtering was already performed on the matrix files, and therefore, only cells with less than 500 genes detected and genes found in less than 20 cells were filtered out. Counts were normalized to log(count + 1) using the natural logarithm. A uniform manifold approximation and projection (UMAP) was created with 50 PCA dimensions. Cell clusters were named on the basis of comparison with the gene sets for cell types defined by Haber *et al.* (16). Tuft cells were then selected and subgrouped into two clusters using the Leiden algorithm with a resolution of 0.09. RNA velocity was calculated and plotted with scVelo.

Statistical analysis

Statistical tests were performed using the R programming language. An unpaired two-tailed Student's *t* test was used for all statistical tests except for RNA-seq and GSEA, where statistics were calculated using the R packages DESeq2 and clusterProfiler, respectively. Adjusted *P* values are reported from DESeq2, and false discovery rate is reported from clusterProfiler.

SUPPLEMENTARY MATERIALS

www.science.org/doi/10.1126/sciimmunol.abl6543

Figs. S1 to S9

Table S1

Data files S1 to S3

MDAR Reproducibility Checklist

[View/request a protocol for this paper from Bio-protocol.](#)

REFERENCES AND NOTES

- M. D. Kirk, S. M. Pires, R. E. Black, M. Caipo, J. A. Crump, B. Devleesschauwer, D. Döpfer, A. Fazil, C. L. Fischer-Walker, T. Hald, A. J. Hall, K. H. Keddy, R. J. Lake, C. F. Lanata, P. R. Torgerson, A. H. Havelaar, F. J. Angulo, World Health Organization estimates of the global and regional disease burden of 22 foodborne bacterial, protozoal, and viral diseases, 2010: A data synthesis. *PLOS Med.* **12**, e1001921 (2015).
- H. Spits, D. Artis, M. Colonna, A. Diefenbach, J. P. di Santo, G. Eberl, S. Koyasu, R. M. Locksley, A. N. McKenzie, R. E. Mebius, F. Powrie, E. Vivier, Innate lymphoid cells—A proposal for uniform nomenclature. *Nat. Rev. Immunol.* **13**, 145–149 (2013).
- M. Biton, A. L. Haber, N. Rogel, G. Burgin, S. Beyaz, A. Schnell, O. Ashenberg, C.-W. Su, C. Smillie, K. Shekhar, Z. Chen, C. Wu, J. Ordovas-Montanes, D. Alvarez, R. H. Herbst, M. Zhang, J. Tirosh, D. Dionne, L. T. Nguyen, M. E. Xifaras, A. K. Shalek, U. H. von Andrian, D. B. Graham, O. Rozenblatt-Rosen, H. N. Shi, V. Kuchroo, O. H. Yilmaz, A. Regev, R. J. Xavier, T helper cell cytokines modulate intestinal stem cell renewal and differentiation. *Cell* **175**, 1307–1320.e22 (2018).
- P. W. Tetteh, H. F. Farin, H. Clevers, Plasticity within stem cell hierarchies in mammalian epithelia. *Trends Cell Biol.* **25**, 100–108 (2015).
- M. R. Howitt, S. Lavoie, M. Michaud, A. M. Blum, S. V. Tran, J. V. Weinstock, C. A. Gallini, K. Redding, R. F. Margolskee, L. C. Osborne, D. Artis, W. S. Garrett, Tuft cells, taste-chemosensory cells, orchestrate parasite type 2 immunity in the gut. *Science* **351**, 1329–1333 (2016).
- F. Gerbe, E. Sidot, D. J. Smyth, M. Ohmoto, I. Matsumoto, V. Dardalhon, P. Cesses, L. Garnier, M. Pouzolle, B. Brulin, M. Bruschi, Y. Harcus, V. S. Zimmermann, N. Taylor, R. M. Maizels, P. Jay, Intestinal epithelial tuft cells initiate type 2 mucosal immunity to helminth parasites. *Nature* **529**, 226–230 (2016).
- J. von Moltke, M. Ji, H.-E. Liang, R. M. Locksley, Tuft-cell-derived IL-25 regulates an intestinal ILc2–epithelial response circuit. *Nature* **529**, 221–225 (2016).
- A. Banerjee, C. A. Herring, B. Chen, H. Kim, A. J. Simmons, A. N. Southard-Smith, M. M. Allaman, J. R. White, M. C. Macedonia, E. T. McKinley, M. A. Ramirez-Solano, E. A. Scoville, Q. Liu, K. T. Wilson, R. J. Coffey, M. K. Washington, J. A. Goettl, K. S. Lau, Succinate produced by intestinal microbes promotes specification of tuft cells to suppress ileal inflammation. *Gastroenterology* **159**, 2101–2115.e5 (2020).
- S. K. Hendel, L. Kellermann, A. Hausmann, N. Bindsliev, K. B. Jensen, O. H. Nielsen, Tuft cells and their role in intestinal diseases. *Front. Immunol.* **13**, 822867 (2022).
- P. H. Dedhia, N. Bertaux-Skeirik, Y. Zavros, J. R. Spence, Organoid models of human gastrointestinal development and disease. *Gastroenterology* **150**, 1098–1112 (2016).
- D. Serra, U. Mayr, A. Boni, I. Lukonin, M. Rempfler, L. C. Meylan, M. B. Stadler, P. Strnad, P. Papasaikas, D. Vischi, A. Waldt, G. Roma, P. Liberali, Self-organization and symmetry breaking in intestinal organoid development. *Nature* **569**, 66–72 (2019).

12. J. Ostrop, R. T. Zwiggelaar, M. Terndrup Pedersen, F. Gerbe, K. Bösl, H. T. Lindholm, A. Díez-Sánchez, N. Parmar, S. Radetzki, J. P. von Kries, P. Jay, K. B. Jensen, C. Arrowsmith, M. J. Oudhoff, A semi-automated organoid screening method demonstrates epigenetic control of intestinal epithelial differentiation. *Front. Cell Dev. Biol.* **8**, 618552 (2021).
13. C. A. Lindemans, M. Calafiore, A. M. Mertelsmann, M. H. O'Connor, J. A. Dudakov, R. R. Jenq, E. Velardi, L. F. Young, O. M. Smith, G. Lawrence, J. A. Ivanov, Y.-Y. Fu, S. Takahima, G. Hua, M. L. Martin, K. P. O'Rourke, Y.-H. Lo, M. Mokry, M. Romera-Hernandez, T. Cupedo, L. E. Dow, E. E. Nieuwenhuis, N. F. Shroyer, C. Liu, R. Kolesnick, M. R. M. van den Brink, A. M. Hanash, Interleukin-22 promotes intestinal-stem-cell-mediated epithelial regeneration. *Nature* **528**, 560–564 (2015).
14. H. F. Farin, W. R. Karthaus, P. Kujala, M. Rakhshandehroo, G. Schwank, R. G. J. Vries, E. Kalkhoven, E. E. S. Nieuwenhuis, H. Clevers, Paneth cell extrusion and release of antimicrobial products is directly controlled by immune cell-derived IFN- γ . *J. Exp. Med.* **211**, 1393–1405 (2014).
15. F. Gerbe, J. H. van Es, L. Makrini, B. Brulin, G. Mellitzer, S. Robine, B. Romagnolo, N. F. Shroyer, J.-F. Bourgaux, C. Pignodel, H. Clevers, P. Jay, Distinct ATOH1 and Neurog3 requirements define tuft cells as a new secretory cell type in the intestinal epithelium. *J. Cell Biol.* **192**, 767–780 (2011).
16. A. L. Haber, M. Biton, N. Rogel, R. H. Herbst, K. Shekhar, C. Smillie, G. Burgin, T. M. Delorey, M. R. Howitt, Y. Katz, I. Tirosh, S. Beyaz, D. Dionne, M. Zhang, R. Raychowdhury, W. S. Garrett, O. Rozenblatt-Rosen, H. N. Shi, O. Yilmaz, R. J. Xavier, A. Regev, A single-cell survey of the small intestinal epithelium. *Nature* **551**, 333–339 (2017).
17. T. Pelaseyed, J. H. Bergström, J. K. Gustafsson, A. Ermund, G. M. H. Birchenough, A. Schütte, S. van der Post, F. Svensson, A. M. Rodriguez-Piñeiro, E. E. L. Nyström, C. Wising, M. E. V. Johansson, G. C. Hansson, The mucus and mucins of the goblet cells and enterocytes provide the first defense line of the gastrointestinal tract and interact with the immune system. *Immunity* **260**, 8–20 (2014).
18. N. Parmar, K. Burrows, P. M. Vornwald, H. T. Lindholm, R. T. Zwiggelaar, A. Díez-Sánchez, M. Martín-Alonso, M. Fossile, B. A. Vallance, J. A. Dahl, C. Zaph, M. J. Oudhoff, Intestinal-epithelial LSD1 controls goblet cell maturation and effector responses required for gut immunity to bacterial and helminth infection. *PLOS Pathog.* **17**, e1009476 (2021).
19. T. K. Noah, A. Kazanjian, J. Whittsett, N. F. Shroyer, SAM pointed domain ETS factor (SPDEF) regulates terminal differentiation and maturation of intestinal goblet cells. *Exp. Cell Res.* **316**, 452–465 (2010).
20. A. Gregorieff, Y. Liu, M. R. Inanlou, Y. Khomchuk, J. L. Wrana, Yap-dependent reprogramming of Lgr5⁺ stem cells drives intestinal regeneration and cancer. *Nature* **526**, 715–718 (2015).
21. Z. Qi, Y. Li, B. Zhao, C. Xu, Y. Liu, H. Li, B. Zhang, X. Wang, X. Yang, W. Xie, B. Li, J.-D. J. Han, Y.-G. Chen, BMP restricts stemness of intestinal Lgr5⁺ stem cells by directly suppressing their signature genes. *Nat. Commun.* **8**, 13824 (2017).
22. X. Yin, H. F. Farin, J. H. van Es, H. Clevers, R. Langer, J. M. Karp, Niche-independent high-purity cultures of Lgr5⁺ intestinal stem cells and their progeny. *Nat. Methods* **11**, 106–112 (2014).
23. T.-H. Kim, F. Li, I. Ferreiro-Neira, L.-L. Ho, A. Luyten, K. Nalapareddy, H. Long, M. Verzi, R. A. Shivdasani, Broadly permissive intestinal chromatin underlies lateral inhibition and cell plasticity. *Nature* **506**, 511–515 (2014).
24. C. A. Herring, A. Banerjee, E. T. M. Kinley, A. J. Simmons, J. Ping, J. T. Roland, J. L. Franklin, Q. Liu, M. J. Gerdes, R. J. Coffey, K. S. Lau, Unsupervised trajectory analysis of single-cell RNA-seq and imaging data reveals alternative tuft cell origins in the gut. *Cell Syst.* **6**, 37–51.e9 (2018).
25. A. H. Mohamed, X. Xing, K. A. Armstrong, A. N. Bullock, G. D. Cunny, P. B. Yu, Development of an ALK2-biased BMP type I receptor kinase inhibitor. *ACS Chem. Biol.* **8**, 1291–1302 (2013).
26. A. Holtzhausen, C. Golzio, T. How, Y.-H. Lee, W. P. Schieman, N. Katsanis, G. C. Blobel, Novel bone morphogenetic protein signaling through Smad2 and Smad3 to regulate cancer progression and development. *FASEB J.* **28**, 1248–1267 (2014).
27. A. D. Gracz, L. A. Samsa, M. J. Fordham, D. C. Trotter, B. Zwarzyk, Y.-H. Lo, K. Bao, J. Stamer, J. R. Raab, N. F. Shroyer, R. L. Reinhardt, S. T. Magness, Sox4 promotes Atoh1-independent intestinal secretory differentiation toward tuft and enteroendocrine fates. *Gastroenterology* **155**, 1508–1523.e10 (2018).
28. J. Muñoz, D. E. Stange, A. G. Schepers, M. van de Wetering, B.-K. Koo, S. Itzkovitz, R. Volckmann, K. S. Kung, J. Koster, S. Radulescu, K. Myant, R. Versteeg, O. J. Sansom, J. H. van Es, N. Barker, A. van Oudenaarden, S. Mohammed, A. J. R. Heck, H. Clevers, The Lgr5 intestinal stem cell signature: Robust expression of proposed quiescent '44' cell markers. *EMBO J.* **31**, 3079–3091 (2012).
29. C. Schneider, C. E. O'Leary, R. M. Locksley, Regulation of immune responses by tuft cells. *Nat. Rev. Immunol.* **19**, 584–593 (2019).
30. C. Schneider, C. E. O'Leary, J. von Moltke, H.-E. Liang, Q. Y. Ang, P. J. Turnbaugh, S. Radhakrishnan, M. Pellizzon, A. Ma, R. M. Locksley, A metabolite-triggered tuft cell-ILC2 circuit drives small intestinal remodeling. *Cell* **174**, 271–284.e14 (2018).
31. M. S. Nadjisombati, J. W. McGinty, M. R. Lyons-Cohen, J. B. Jaffe, L. D. Peso, C. Schneider, C. N. Miller, J. L. Pollack, G. A. Nagana Gowda, M. F. Fontana, D. J. Erle, M. S. Anderson, R. M. Locksley, D. Raftery, J. von Moltke, Detection of succinate by intestinal tuft cells triggers a type 2 innate immune circuit. *Immunity* **49**, 33–41.e7 (2018).
32. O. O. Oyelola, M. T. Shanahan, M. Kanke, B. M. Mooney, L. M. Webb, S. Smita, M. K. Matheson, P. Campioli, D. Pham, S. P. Früh, J. W. McGinty, M. J. Churchill, J. L. Cahoon, P. Sundaravaradan, B. A. Flitter, K. Mouli, M. S. Nadjisombati, E. Kamynina, S. A. Peng, R. L. Cubitt, K. Gronert, J. D. Lord, I. Rauch, J. von Moltke, P. Sethupathy, E. D. Tait Wojno, PGD2 and CRTH2 counteract type 2 cytokine-elicited intestinal epithelial responses during helminth infection. *J. Exp. Med.* **218**, e20202178 (2021).
33. M. E. Kotas, N. M. Mroz, S. Koga, H.-E. Liang, A. W. Schroeder, R. R. Ricardo-Gonzalez, C. Schneider, R. M. Locksley, c15H constrains the tuft-ILC2 circuit to set epithelial and immune tone. *Mucosal Immunol.* **14**, 1295–1305 (2021).
34. Z. Fu, J. W. Dean, L. Xiong, M. W. Dougherty, K. N. Oliff, Z.-m. E. Chen, C. Jobin, T. J. Garrett, L. Zhou, Mitochondrial transcription factor A in ROR γ ⁺ lymphocytes regulate small intestine homeostasis and metabolism. *Nat. Commun.* **12**, 4462 (2021).
35. C. Drury, H. T. Lindholm, G. Coakley, M. C. Poveda, S. Löser, R. Doolan, F. Gerbe, P. Jay, N. Harris, M. J. Oudhoff, R. M. Maizels, Intestinal epithelial tuft cell induction is negated by a murine helminth and its secreted products. *J. Exp. Med.* **219**, e20211140 (2022).
36. D. Karo-Atar, S. Ouladan, T. Javkar, L. Joumier, M. K. Matheson, S. Merritt, S. Westfall, A. Rochette, M. E. Gentile, G. Fontes, G. J. Fonseca, M. Parisien, L. Diatchenko, J. von Moltke, M. Malleshaiah, A. Gregorieff, I. L. King, Direct reprogramming of the intestinal epithelium by parasitic helminths subverts type 2 immunity. *bioRxiv* 2021.09.25.461778 [Preprint], 25 September 2021. <https://doi.org/10.1101/2021.09.25.461778>.
37. C. Kosinski, V. S. W. Li, A. S. Y. Chan, J. Zhang, C. Ho, W. Y. Tsui, T. L. Chan, R. C. Mifflin, D. W. Powell, S. T. Yuen, S. Y. Leung, X. Chen, Gene expression patterns of human colon tops and basal crypts and BMP antagonists as intestinal stem cell niche factors. *Proc. Natl. Acad. Sci. U.S.A.* **104**, 15418–15423 (2007).
38. A.-P. G. Haramis, H. Begthel, M. van den Born, J. van Es, S. Jonkheer, G. J. A. Offerhaus, H. Clevers, De novo crypt formation and juvenile polyposis on BMP inhibition in mouse intestine. *Science* **303**, 1684–1686 (2004).
39. N. McCarthy, E. Manieri, E. E. Storm, A. Saadatpour, A. M. Luoma, V. N. Kapoor, S. Madha, L. T. Gaynor, C. Cox, S. Keerthivasan, K. Wucherpfennig, G.-C. Yuan, F. J. de Sauvage, S. J. Turley, R. A. Shivdasani, Distinct mesenchymal cell populations generate the essential intestinal BMP signaling gradient. *Cell Stem Cell* **26**, 391–402.e5 (2020).
40. X. Zhang, S. Liu, Y. Wang, H. Hu, L. Li, Y. Wu, D. Cao, Y. Cai, J. Zhang, X. Zhang, Interleukin-22 regulates the homeostasis of the intestinal epithelium during inflammation. *Int. J. Mol. Med.* **43**, 1657–1668 (2019).
41. J.-M. Zha, H.-S. Li, Q. Lin, W.-T. Kuo, Z.-H. Jiang, P.-Y. Tsai, N. Ding, J. Wu, S.-F. Xu, Y.-T. Wang, J. Pan, X.-M. Zhou, K. Chen, M. Tao, M. A. Odenwald, A. Tamura, S. Tsukita, J. R. Turner, W.-Q. He, Interleukin 22 expands transit-amplifying cells while depleting Lgr5⁺ stem cells via inhibition of Wnt and notch signaling. *Cell. Mol. Gastroenterol. Hepatol.* **7**, 255–274 (2019).
42. K. Sugimoto, A. Ogawa, E. Mizoguchi, Y. Shimomura, A. Andoh, A. K. Bhan, R. S. Blumberg, J. R. Xavier, A. Mizoguchi, IL-22 ameliorates intestinal inflammation in a mouse model of ulcerative colitis. *J. Clin. Invest.* **118**, 534–544 (2008).
43. J.-E. Turner, B. Stockinger, H. Helmbj, IL-22 mediates goblet cell hyperplasia and worm expulsion in intestinal helminth infection. *PLOS Pathog.* **9**, e1003698 (2013).
44. D. Artis, M. L. Wang, S. A. Keilbaugh, W. He, M. Brenes, G. P. Swain, P. A. Knight, D. D. Donaldson, M. A. Lazar, H. R. P. Miller, G. A. Schad, P. Scott, G. D. Wu, RELM β /FIZZ2 is a goblet cell-specific immune-effector molecule in the gastrointestinal tract. *Proc. Natl. Acad. Sci. U.S.A.* **101**, 13596–13600 (2004).
45. D. C. Propheter, A. L. Chara, T. A. Harris, K. A. Ruhn, L. V. Hooper, Resistin-like molecule β is a bactericidal protein that promotes spatial segregation of the microbiota and the colonic epithelium. *Proc. Natl. Acad. Sci. U.S.A.* **114**, 11027–11033 (2017).
46. K. S. B. Bergstrom, V. Morampudi, J. M. Chan, G. Bhinder, J. Lau, H. Yang, C. Ma, T. Huang, N. Ryz, H. P. Sham, M. Zarepour, C. Zaph, D. Artis, M. Nair, B. A. Vallance, Goblet cell derived RELM- β recruits CD4⁺ T cells during infectious colitis to promote protective intestinal epithelial cell proliferation. *PLOS Pathog.* **11**, e1005108 (2015).
47. W. C. Gause, C. Rothlin, P. Locke, Heterogeneity in the initiation, development and function of type 2 immunity. *Nat. Rev. Immunol.* **20**, 603–614 (2020).
48. N. Powell, E. Pantazi, P. Pavlidis, A. Tsakmaki, K. Li, F. Yang, A. Parker, C. Pin, D. Cozzetto, D. Minns, E. Stolarczyk, S. Saveljeva, R. Mohamed, P. Lavender, B. Afzali, J. Digby-Bell, T. Tjir-Li, A. Kaser, J. Friedman, T. J. MacDonald, G. A. Bewick, G. M. Lord, Interleukin-22 orchestrates a pathological endoplasmic reticulum stress response transcriptional programme in colonic epithelial cells. *Gut* **69**, 578–590 (2020).
49. X. Lin, S. J. Gaudino, K. K. Jang, T. Bahadur, A. Singh, A. Banerjee, M. Beaupre, T. Chu, H. T. Wong, C.-K. Kim, C. Kempen, J. Axelrad, H. Huang, S. Khalid, V. Shah, O. Esakiocak, O. B. Parks, A. Berisha, J. P. McAleer, M. Good, M. Hoshino, R. Blumberg, A. B. Bialkowska, S. L. Gaffen, J. K. Kolls, V. W. Yang, S. Beyaz, K. Cadwell, P. Kumar, IL-17RA-signaling in Lgr5⁺ intestinal stem cells induces expression of transcription factor ATOH1 to promote secretory cell lineage commitment. *Immunity* **55**, 237–253.e8 (2022).

50. M. Camberis, G. Le Gros, J. Urban, Animal model of *Nippostrongylus brasiliensis* and *Heligmosomoides polygyrus*. *Curr. Protoc. Immunol.* **Chapter 19**, Unit 19.12 (2003).
51. T. Sato, H. Clevers, Primary mouse small intestinal epithelial cell cultures, in *Epithelial Cell Culture Protocols*, S. H. Randell, M. L. Fulcher, Eds. (Humana Press, ed. 2, 2013), pp. 319–328.
52. M. Martín-Alonso, S. Iqbal, P. M. Vornewald, H. T. Lindholm, M. J. Damen, F. Martínez, S. Hoel, A. Díez-Sánchez, M. Altelaar, P. Katajisto, A. G. Arroyo, M. J. Oudhoff, Smooth muscle-specific MMP17 (MT4-MMP) regulates the intestinal stem cell niche and regeneration after damage. *Nat. Commun.* **12**, 6741 (2021).

Acknowledgments: We thank the animal care (CoMed) and imaging (CMIC) core facilities that assisted in this work (NTNU). Part of the RNA-seq was done by the Genomics Core Facility at NTNU, which receives funding from the Faculty of Medicine and Health Sciences and Central Norway Regional Health Authority. **Funding:** This work was financially supported by the Norwegian Research Council (Centre of Excellence grant 223255/F50 and 'Young Research Talent' 274760 to M.J.O.) and the Norwegian Cancer Society (182767 to M.J.O.). This work was

supported by the Wellcome Trust through Investigator Awards to R.M.M. (Ref. 106122 and 219530) and the Wellcome Trust core-funded Wellcome Centre for Integrative Parasitology (Ref. 104111). **Author contributions:** H.T.L., N.P., C.D., M.C.P., P.M.V., J.O., and A.D.-S. performed experiments. R.M.M. and M.J.O. supervised and provided conceptual insights. H.T.L. made the figures. H.T.L. and M.J.O. wrote the first draft with subsequent input from all authors. **Competing interests:** The authors declare that they have no competing interests. **Data and materials availability:** The RNA-sequencing data have been deposited in the ArrayExpress database at EMBL-EBI (www.ebi.ac.uk/arrayexpress) under the following accession numbers: E-MTAB-9182, E-MTAB-9183, E-MTAB-9184, E-MTAB-9185, E-MTAB-10455, and E-MTAB-11273. Code used for bright-field and confocal analysis can be found at: <https://github.com/havardtl/coco>.

Submitted 27 July 2021
Resubmitted 26 February 2022
Accepted 21 April 2022
Published 13 May 2022
10.1126/sciimmunol.abl6543

BMP signaling in the intestinal epithelium drives a critical feedback loop to restrain IL-13–driven tuft cell hyperplasia

Hvard T. Lindholm, Naveen Parmar, Claire Drurey, Marta Campillo Poveda, Pia M. Vornewald, Jenny Ostrop, Alberto Dezsanchez, Rick M. Maizels, and Menno J. Oudhoff

Sci. Immunol., 7 (71), eabl6543.
DOI: 10.1126/sciimmunol.abl6543

BMP puts the brakes on tuft cells

Intestinal parasite infections or allergic reactions promote IL-13–induced differentiation of tuft cells as one manifestation of type 2 immunity in the gut. Using organoid cultures of intestinal epithelial cells, Lindholm *et al.* investigated how the lymphocyte cytokines IL-13, IL-22, and IFN γ regulate the signaling pathways that influence epithelial differentiation. While tuft cell IL-25 promoted expansion of IL-13–producing ILC2s in a feed-forward loop, the resulting IL-13 also induced ligands of the bone morphogenetic protein (BMP) signaling pathway. BMP agonists acted on stem cells to prevent runaway tuft cell expansion by limiting expression of Sox4, a transcription factor required for tuft cell differentiation. These findings provide new molecular insights into how intestinal epithelial differentiation is carefully choreographed in response to a diverse array of cytokine signals.

View the article online

<https://www.science.org/doi/10.1126/sciimmunol.abl6543>

Permissions

<https://www.science.org/help/reprints-and-permissions>

Use of this article is subject to the [Terms of service](#)

Science Immunology (ISSN) is published by the American Association for the Advancement of Science, 1200 New York Avenue NW, Washington, DC 20005. The title *Science Immunology* is a registered trademark of AAAS.
Copyright © 2022 The Authors, some rights reserved; exclusive licensee American Association for the Advancement of Science. No claim to original U.S. Government Works

Supplementary Materials for

**BMP signaling in the intestinal epithelium drives a critical feedback loop to
restrain IL-13–driven tuft cell hyperplasia**

Håvard T. Lindholm *et al.*

Corresponding author: Håvard T. Lindholm, havard.t.lindholm@ntnu.no; Menno J. Oudhoff,
menno.oudhoff@ntnu.no

Sci. Immunol. 7, eabl6543 (2022)
DOI: 10.1126/sciimmunol.abl6543

The PDF file includes:

Figs. S1 to S9
Table S1
Legends for data file S1 to S3

Other Supplementary Material for this manuscript includes the following:

Data file S1 to S3
MDAR Reproducibility Checklist

Supplementary materials

Figure S1: Image analysis pipeline.

Figure S2: Quantification of number of tuft cells in organoids.

Figure S3: Details of RNA sequencing data of cytokines.

Figure S4: Details of RNA sequencing data of epithelial cells infected with *N. brasiliensis* and *C. rodentium*.

Figure S5: IL-13 and IL-22 gives different goblet cells also after 72 hours of cytokine stimulation.

Figure S6: *Bmp2* is the main TGF- β superfamily member induced by IL-13.

Figure S7: The effect of SB525334 on IL-13 dependent tuft cell hyperplasia.

Figure S8: Time course of *BMP8b* and *Tgfb1* expression.

Figure S9: Further characterization of mice treated with DMH1 and DMSO and infected with *N. brasiliensis*.

Table S1: Primers used for qPCR.

Data file S1 - GSEA gene sets

Data file S2 - Goblet cell gene signatures

Data file S3 - Raw data file

MDAR Reproducibility Checklist

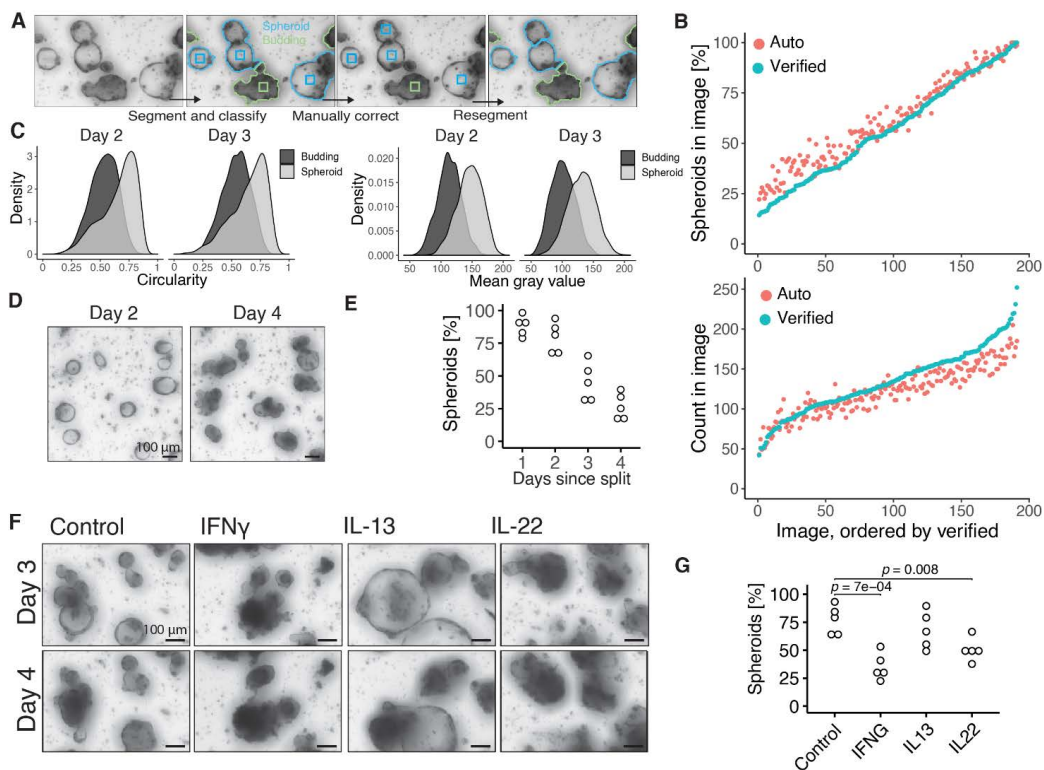


Figure S1: Image analysis pipeline. **A**, A segmentation algorithm is used to find the outline and center of an organoid and the segmented organoid is classified by a neural network. An optional manual correction of organoid centers and classification can be performed. The organoids can then be segmented again which gives an updated segmentation following the manual correction. **B**, Comparison of automatic segmentation and automatic classification of organoids compared to manually verified segmentation and manually verified classification. Each circle represents one image with approximately 100 organoids each. **C**, Distribution of circularity and mean gray value (higher value is lighter) of untreated small intestinal organoids. **D**, Representative images of untreated organoids. Media changed at day 2. **E**, Average fraction of spheroids in each image in same experiment as D. Each circle is one biological replicate and is the average of at least 3 images and in total this plot represents 16,462 organoids. **F**, Minimal projections of small intestinal organoids treated with cytokines. Days since seeding. **G**, Average fraction of spheroids at day 2 since splitting. Each circle is one biological replicate and is the average of at least 3 images and in total represents 10,462 organoids. P-values calculated with unpaired two-tailed T-test.

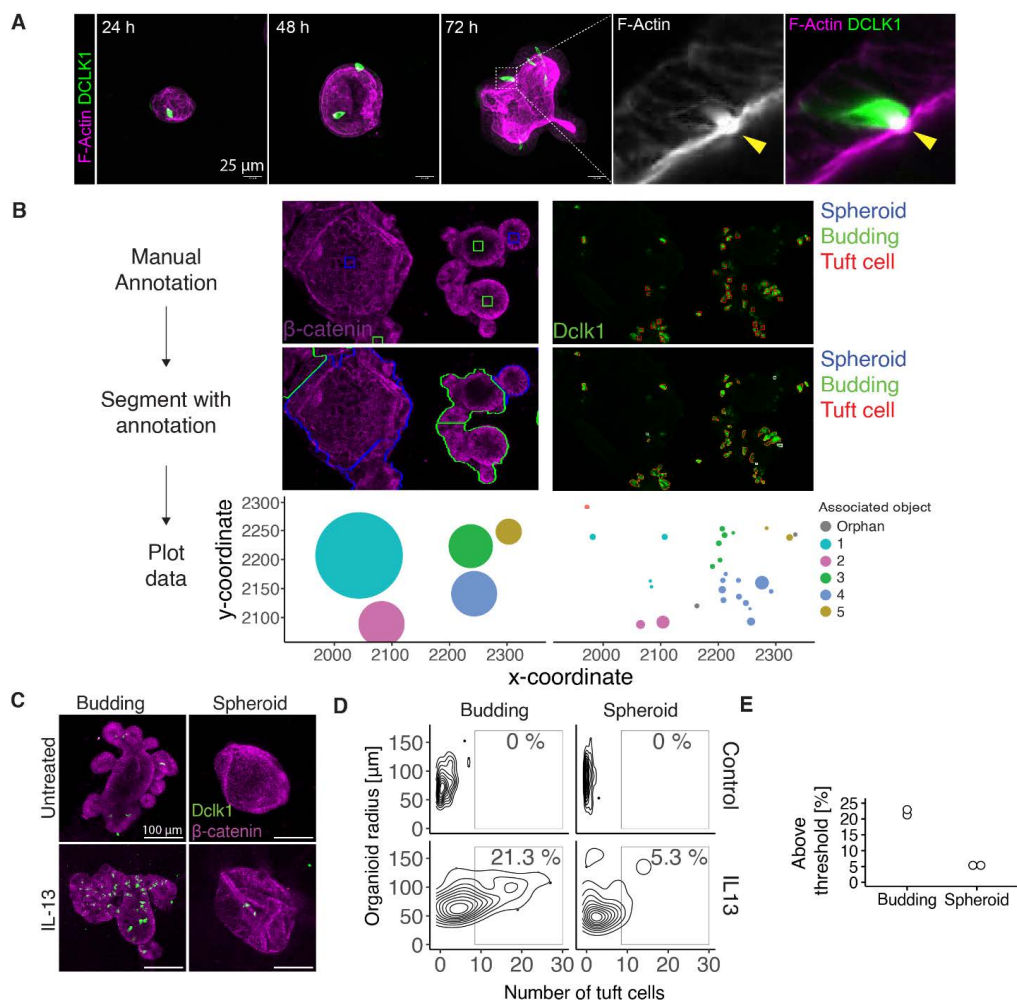


Figure S2: Quantification of number of tuft cells in organoids. **A**, Time course of tuft cell development in organoids. Times are hours since seeding. **B**, Image output from each step in the confocal image analysis pipeline. The center of each object of interest is marked with a square in a custom graphical user interface, and this information is used to separate overlapping objects. Furthermore, objects in other channels, like tuft cells, are analyzed to map which organoid they are inside. This information is summarized and used to plot number of tuft cells per organoid. **C**, Representative confocal images of small intestinal organoids at day 3 since splitting. **D**, Quantification of images shown in C. Percentages are relative to total number of organoids in that treatment. Plot shows the distribution of 192 organoids. **E**, Percentages for IL-13 treated organoids calculated as shown in D. Each circle is one biological replicate. All images in this figure are projections of Z-stacks.

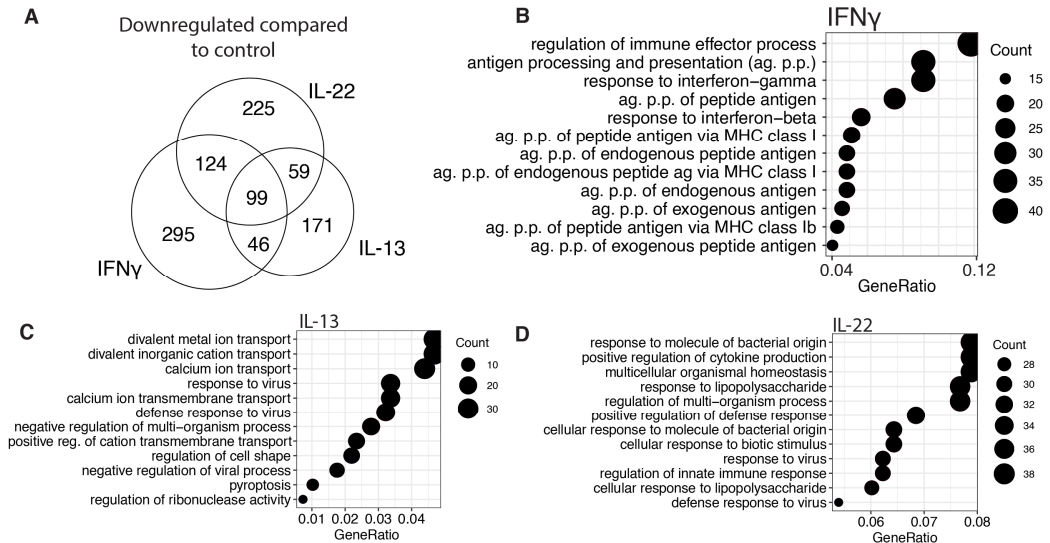


Figure S3: Details of RNA sequencing data of cytokines. **A**, Number of down-regulated significant genes from small intestinal organoids treated with indicated cytokine for 24 hours compared to control ($p < 0.05$ and $\log_2 f_c < -1$). **B-D**, Top hits from GO-term analysis of "biological process" in RNA-seq data from intestinal organoids treated with indicated cytokine for 24 hours compared to control.

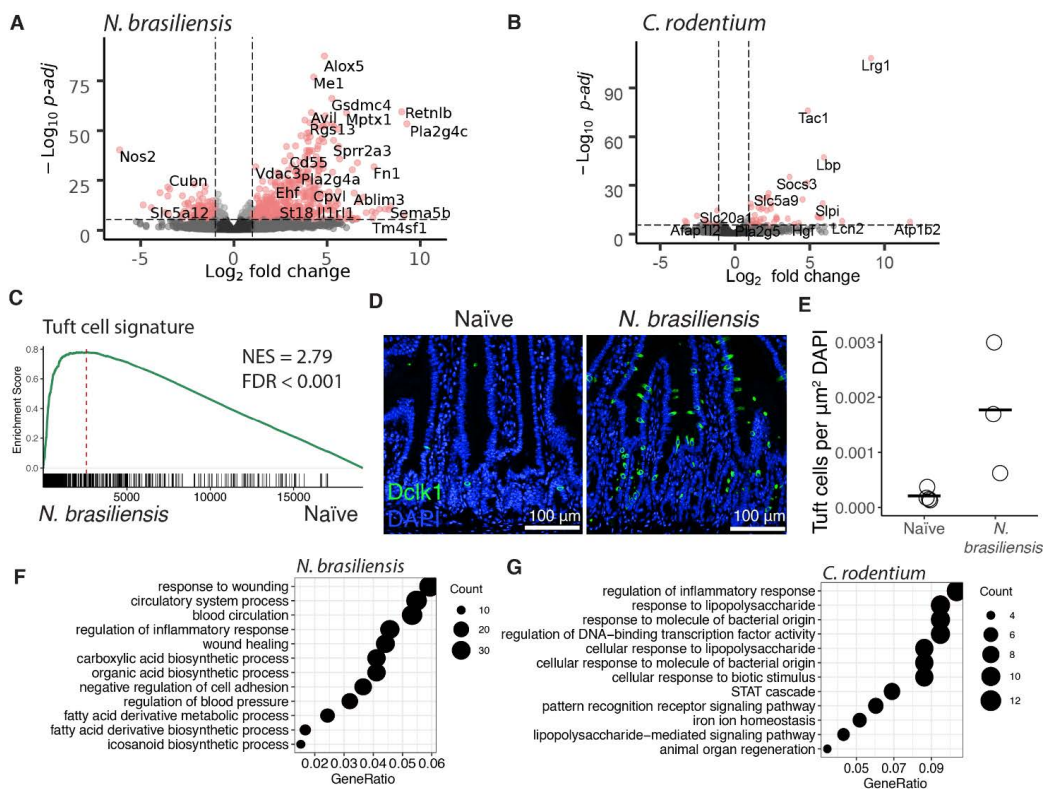


Figure S4: Details of RNA sequencing data of epithelial cells infected with *N. brasiliensis* and *C. rodentium*. **A**, Volcano plot of RNA-seq from intestinal epithelial tissue extracted from duodenum from mice seven days after infection with *N. brasiliensis*. **B**, Volcano plot of RNA-seq from intestinal epithelial tissue extracted from colon from mice six days after infection with *C. rodentium*. **C**, GSEA analysis of a tuft cell signature on mRNA data from intestinal epithelium from *N. brasiliensis* infected mice. **D**, Confocal microscopy of cross section of mouse intestine seven days after infection with *N. brasiliensis* and naïve. **E**, Automatic tuft cell count from same experiment as D. Each circle represents quantitation from one full cross section from one mouse. **F**, **G**, Top hits from GO term analysis of "biological process" in RNA-seq data from mouse intestine infected with indicated pathogen.

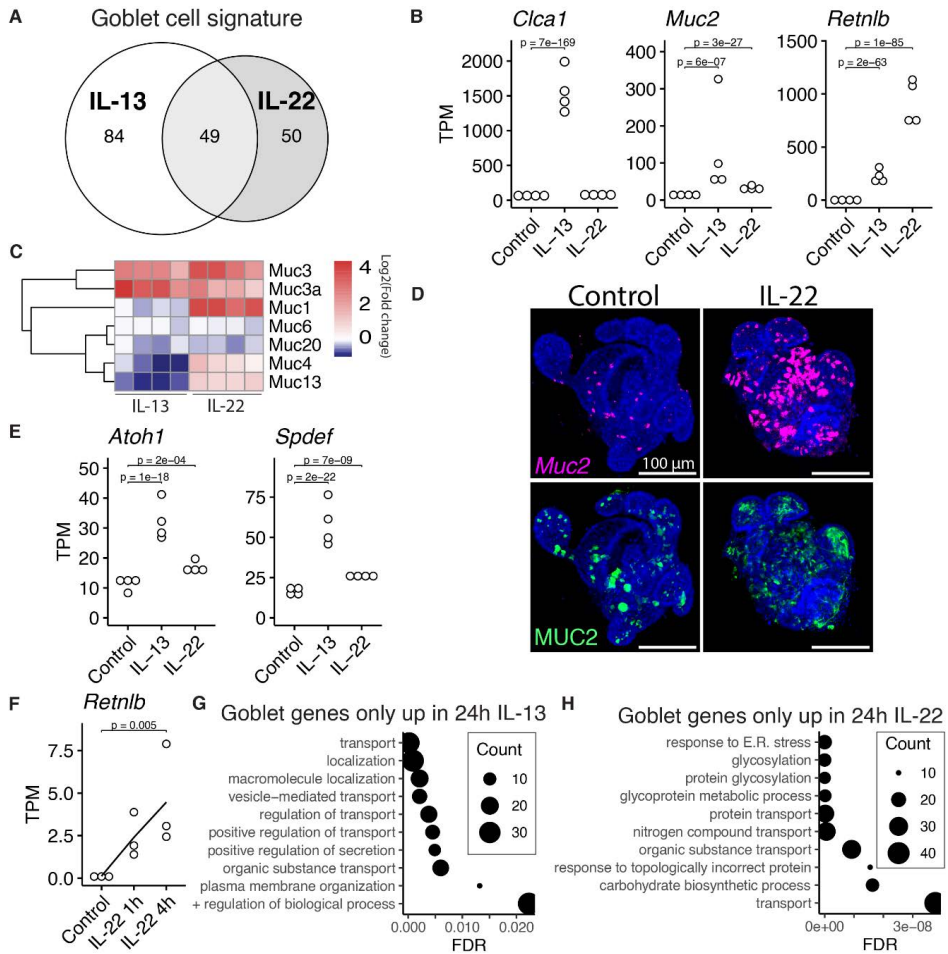


Figure S5: IL-13 and IL-22 gives different goblet cells also after 72 hours of cytokine stimulation. **A**, Distribution of how the plate based scRNA-seq goblet cell gene set from Haber et al is changed upon 72 hours of IL-13 and IL-22 treatment. Up is defined as $\lg_2fc > 0.5$ and $p\text{-adj} < 0.05$. **B**, Gene expression from intestinal organoids treated for 72 hours with indicated cytokine. Each circle is one biological replicate. Statistics calculated with DESeq2, see methods. **C**, Expression of mucins in intestinal organoids stimulated IL-13 or IL-22 for 24 hours compared to control. **D**, Confocal imaging of organoids stained with an antibody staining for MUC2 in green and RNAscope probe for *Muc2* in purple. Organoids were imaged 3 days after seeding and 5 ng/mL of IL-22 was used since day of seeding. **E**, See B. **F**, Gene expression from intestinal organoids treated for 1 and 4 hours with IL-22. Each circle is one biological replicate. Statistics calculated with DESeq2, see methods. **G,H**, GO terms associated with gene sets seen in the Venn diagram in figure 2B. FDR = False discovery rate.

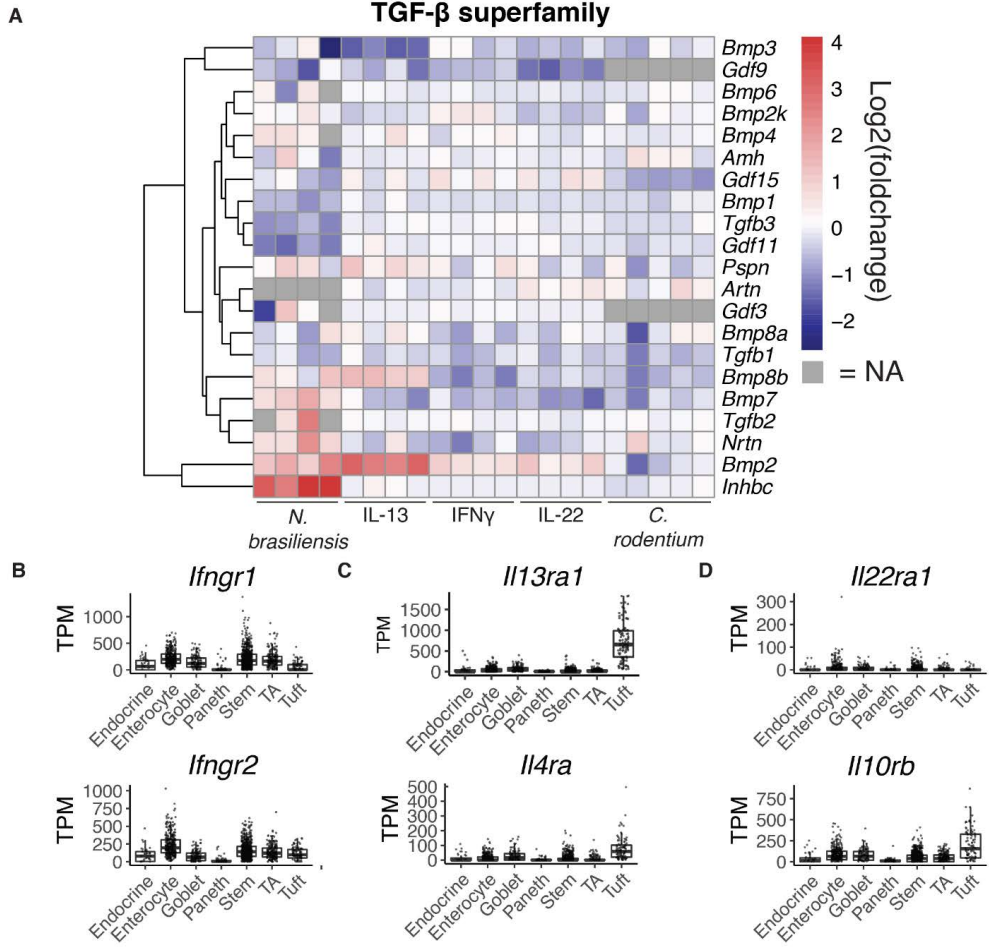


Figure S6: Bmp2 is the main TGF- β superfamily member induced by IL-13. **A**, Heatmap of log₂ fold change for TGF- β superfamily members from RNA-seq data from intestinal epithelium from mice infected with *N. brasiliensis* or *C. rodentium* and organoids treated for 24 hours with indicated cytokine. **B-D**, Expression of cytokine receptors, for IFN γ (B), IL-13 (C) and IL-22 (D), from plate based scRNA-seq from Haber et al (16). TA = Transit amplifying.

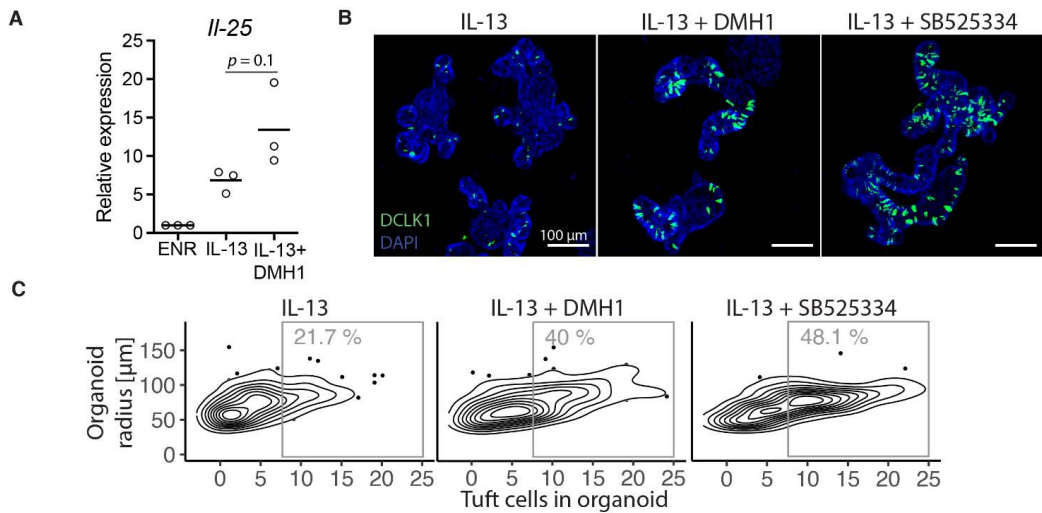


Figure S7: The effect of SB525334 on IL-13 dependent tuft cell hyperplasia. **A**, Relative expression of *I/25* in intestinal organoids treated with indicated treatment for 72 hours determined with qPCR. p-value is calculated with unpaired two tailed T-test. **B**, Confocal staining of DCLK1 in small intestinal organoids treated with indicated treatments for 72 hours. **C**, Automatic quantification of same experiment as B. Each dot is one organoid.

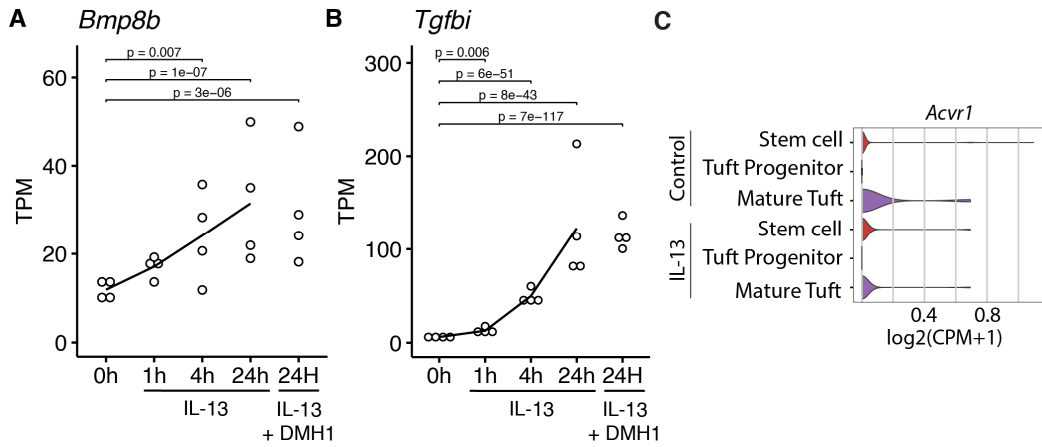


Figure S8: Time course of *BMP8b* and *Tgfb1* expression. **A,B**, Time points for RNA-seq experiment from small intestinal organoids treated with 10 ng/mL IL-13 at indicated timepoints and with and without 5 μ M DMH1 for 24 hours. Each circle is one biological replicate, statistics calculated with DESeq2, see methods. **C**, Violin plots of gene expression from scRNA-seq data of small intestinal organoids treated with IL-13 and untreated from Biton et al (3).

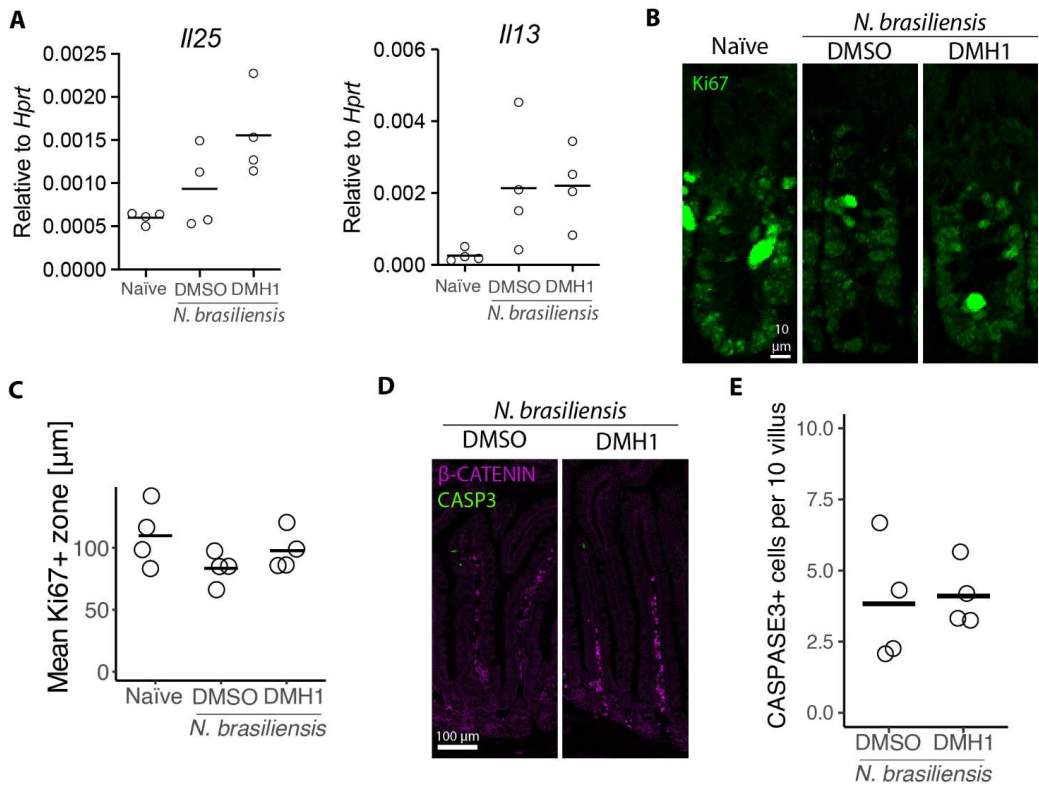


Figure S9: Further characterization of mice treated with DMH1 and DMSO and infected with *N. brasiliensis*. **A**, qPCR of indicated gene in duodenal intestinal tissue after 8 days of infection with *N. brasiliensis*. **B**, Ki67 staining in duodenal crypts from mice after 8 days of infection with *N. brasiliensis*. **C**, Quantification of height of Ki67+ zone in images shown in B. Each dot is the average of at least 5 crypts in one mouse. **D**, Staining of cleaved Caspase3 in duodenal crypt and villus from mice after 8 days of infection with *N. brasiliensis*. **E**, Manual quantification of images shown in D. Each circle is the average of at least 20 villus in one mouse.

Table S1: Primers used for qPCR.

Gene	Forward primer	Reverse primer
<i>Ii13</i>	CCTGGCTCTTGCTTGCTT	GGTCTGTGTGATGTTGCTCA
<i>Ii25</i>	TGGCTGAAGTGGAGCTCTGCAT	CCCGATTCAAGTCCCTGTCCAA
<i>Hprt</i>	CCTCCTCAGACCGCTTTTT	AACCTGGTTCATCATCGCTAA

Paper 3

***Mmp17*-deficient mice exhibit heightened goblet cell effector expression in the colon and increased resistance to chronic *Trichuris muris* infection**

Pia M. Vornewald¹, Ruth Forman², Rouan Yao¹, Naveen Pamar¹, Håvard T. Lindholm³, Mara Martín-Alonso¹, Kathryn J. Else², Menno J. Oudhoff^{1,4,*}

¹ CEMIR – Center of Molecular Inflammation Research, Department of Clinical and Molecular Medicine, NTNU – Norwegian University of Science and Technology, 7491 Trondheim, Norway

² Lydia Becker Institute of Immunology & Inflammation, School of Biological Sciences, The University of Manchester, Manchester, United Kingdom

³ Princess Margaret Cancer Centre, University Health Network, Toronto, Canada

⁴ Department of Health Sciences, Carleton University, Ottawa, Ontario, Canada

*Corresponding authors, e-mail: mennooudhoff@cunet.carleton.ca

ABSTRACT

Intestinal epithelial homeostasis is maintained by intrinsic and extrinsic signals. The extrinsic signals include those provided by mesenchymal cell populations that surround intestinal crypts and is further facilitated by the extracellular matrix (ECM) that is modulated by proteases such as matrix metalloproteinases (MMPs). Extrinsic signals ensure an appropriate balance between intestinal epithelial proliferation and differentiation. This study explores the role of MMP17, which is expressed by mesenchymal cells, in intestinal homeostasis and during immunity to infection. Mice lacking MMP17 expressed high levels of goblet-cell associated genes, such as CLCA1 and RELM- β , which are normally associated with immune responses to infection. Nevertheless, *Mmp17* KO mice did not have altered resistance during a bacterial *Citrobacter rodentium* infection. However, when challenged with a low dose of the helminth *Trichuris muris*, *Mmp17* KO mice had increased resistance, without a clear role for an altered immune response during infection. Mechanistically, we did not find changes in traditional modulators of goblet cell effectors such as the NOTCH pathway or specific cytokines. Instead, we found elevated BMP signaling in *Mmp17* KO mouse colon crypts that we propose to alter the goblet cell maturation state. Together, our data suggests that MMP17 extrinsically alters the goblet cell maturation state *via* a BMP signaling axis, which is sufficient to alter clearance in a helminth infection model.

INTRODUCTION

The intestinal tract is lined by a single layer of intestinal epithelial cells. This intestinal epithelium comprises multiple cell types, each with distinct functions, that work together to provide a barrier against harmful microorganisms, while at the same time allowing for nutrient and water absorption.(1) To fulfill those functions the intestinal epithelium is constantly replenished by a pool of LGR5+ stem cells located at the base of epithelial invaginations known as intestinal crypts, with a turnover rate of 3-5 days.(2, 3) This remarkable regenerative capacity enables the intestinal epithelium to rapidly respond to injury or infection.

Goblet cells play a critical role in maintaining the intestinal homeostasis by producing key components of the mucus layer, such as MUC2, CLCA1, and FCGBP.(4-7) The mucus serves as a physical barrier, preventing the attachment and penetration of bacteria(8) and other pathogens, including helminths.(9) Additionally, the mucus contains proteins with antimicrobial properties like RELM- β and ANG4, which further bolsters the gut's innate immune defense.(10-14) In response to infections both the amount of mucus and its composition can be altered, with goblet cell specific antimicrobial proteins (AMPs) increasing due to immune-cell derived cytokines that directly induce signaling in intestinal epithelium.(15) In fact, an increase in goblet cell numbers is crucial in the defense against pathogenic helminths.(9)

Epithelial homeostasis depends on a niche created by gradients of factors to preserve stemness at the base of crypts while enabling the differentiation of mature and functionally diverse cell types towards the lumen. The most critical niche factors include WNTs, R-spondins, Bone morphogenic proteins (BMPs), and prostaglandins, which are expressed by

mesenchymal cell subtypes and immune cells such as macrophages that are present in the lamina propria between the epithelium and the smooth muscle layers.(16-22)

In addition to secreted factors, the structure and composition of the extracellular matrix (ECM) within the lamina propria also regulates the intestinal niche.(23) Matrix metalloproteinases (MMPs) are a key group of ECM regulators, modifying the structure and function of the ECM both through direct action on ECM components and by cleaving ECM associated-molecules, such as growth factors.(24) MMPs have been implicated in wound healing, (chronic) inflammations, and cancer.(25-27) We recently demonstrated that the membrane-bound MMP, MMP17 (also called MT4-MMP) is important in maintaining epithelial homeostasis and its ability to respond to injury. Furthermore, we identified the intestinal smooth muscle as a source of niche factors.(28)

In the present work, we show that the loss of *Mmp17* induces goblet cell effector genes in the colon and cecum epithelium. We propose that these are caused by elevated BMP signaling in the epithelium and that these changes to the epithelium result in improved clearance of low-dose *Trichuris muris* infection.

RESULTS

Mmp17 KO mice show increased expression of goblet cell-effectors in proximal colon goblet cells

We recently demonstrated that mice lacking the membrane-bound matrix metalloproteinase MMP17 display impaired intestinal regenerative capacities in both a chemically-induced colitis and whole-body irradiation injury models. In our previous study, we conducted a transcriptomic analysis of colon crypts isolated from naïve *Mmp17*^{+/+} (WT) and *Mmp17*^{-/-} (KO) mice using bulk RNA sequencing (RNA-seq).(28) We re-examined this dataset and identified several goblet cell-associated genes among the most upregulated genes in crypts derived from KO animals, particularly *Ang4*, *Clca1*, *Retnlb*, and *Muc2* (Figure 1a). *Retnlb*, *Clca1*, and *Ang4* can be classified as AMPs, which are typically upregulated in the intestine during infections. Immunofluorescence (IF) staining of RELM- β , the protein encoded by the *Retnlb* gene, confirmed increased protein levels and revealed a distinct pattern of RELM- β positive cells in the proximal region of the colon (Figure 1b). Similarly, we observed a higher fluorescent intensity in KO tissue compared to WT tissue in the proximal colon when stained for CLCA1 (Figure 1c). Examination of other AMP genes, including *Spr2a1*, *Spr2a2*, and *Spr2a3*, showed slightly increased levels, albeit not significant (Supplementary Figure 1a).(29) RNA levels of the core mucus protein *Fcgbp* were also significantly elevated in KO epithelium (Supplementary Figure 1b). The upregulation in goblet cell-associated genes in KO animals did not correlate with an increased number of this cell type, as demonstrated by the quantification of total goblet cell numbers per crypt in WT and KO mouse colon using alcian blue staining (Figure 1d). Accordingly, we detected no changes in the expression of the transcription factors *Atoh1* and *Spdef* (Figure 1e), which are involved in NOTCH signaling to regulate goblet cell differentiation. Since our previous data indicated that MMP17 is not expressed in the intestinal epithelium, we sought to determine whether the increase in

epithelial goblet cell genes was intrinsic to the epithelium or due to changes in the surrounding niche *in vivo*. We isolated colonic crypts from WT and KO mice to cultivate colon organoids (colonoids), measured *Retnlb* expression via qPCR (Figure 1f) and assessed RELM- β protein expression using IF staining (Figure 1g). We observed no differences in RELM- β protein and *Retnlb* mRNA expression, suggesting that the increased expression of goblet cell-associated genes in KO mouse crypts is not intrinsic to the intestinal epithelium but rather a consequence of the environment in the surrounding niche. In summary, we find that animals lacking MMP17 exhibit elevated levels of goblet cell effector proteins without an increase in goblet cell numbers, that are presumably induced by extrinsic factors in the proximal colon.

Goblet cell effector upregulation is not caused by a change in cytokine levels

Ang4, *Clca1*, and *Retnlb* are goblet-cell associated genes that are induced during immune responses, such as bacterial and helminth infections, and are typically stimulated by type 2 and 3 immune cytokines such as IL-4/IL-13 (type 2) and IL-22 (type 3). (10, 11, 14, 15, 30) To investigate whether naïve KO animals inherently exhibit elevated cytokine levels, we measured levels of IL-13, IL-22, and IFN- γ in re-stimulated mesenteric lymph node lymphocytes (mLNL) *in vitro* and homogenized colon tissue using ELISA (Figure 2a first and second row). We also isolated mRNA from whole proximal colon tissue and measured gene expression of the same cytokines (Figure 2a last row). Our analysis revealed no significant differences in the levels of IL-13 and IL-22 protein (mLNL, colon) or gene expression (colon) between wild-type (WT) and knockout (KO) mice. Of note, in all cases, we did observe a subtle increase in the levels of IFN- γ /*Ifng*, but only with a significant elevation in colon tissue (Figure 2a). While IFN- γ is not known to induce goblet cell effectors

or their differentiation in intestinal epithelium (15), it has been reported that RELM- β can stimulate IFN- γ production in T-cells. (31) Therefore, we propose that the modest increase in IFN- γ levels may be a result of RELM- β upregulation rather than the inverse. To further rule out the possibility that the observed increase in goblet cell effector proteins was due to IL-4/IL-13 or IL-22 signaling, which are known to induce such effectors, we also analyzed the levels of phosphorylated (p)STAT6 and pSTAT3, which are downstream signaling molecules of IL-4/IL-13 signaling and IL-22 signaling respectively. We observed no significant difference in protein levels of pSTAT6 (Figure 2b) or pSTAT3 (Figure 2c) between WT and KO colon crypts, thus excluding IL-4/IL-13 and IL-22 signaling as the cause for the altered epithelial expression. In conclusion, the heightened levels of goblet cell effectors in Mmp17 KO mice are not the result of a heightened level of cytokines during homeostasis.

Increased expression of goblet cell effector proteins does not influence the course of *Citrobacter rodentium* infection

Goblet cell effector proteins, which are secreted into the intestinal lumen as part of the mucus layer, form a crucial line of defense against pathogens in the intestine. We hypothesized that the elevated levels of these effectors might offer an advantage in clearing intestinal infections, as both ANG4 and RELM- β have been described to have anti-bacterial properties.(11, 32) Consequently, we infected WT and KO mice with *Citrobacter rodentium*, a gram-negative bacterial pathogen that primarily infects the colon, causing mild colitis and diarrhea. Generally, mice with a C57BL/6 background exhibit resistance to *C. rodentium* and can clear the pathogen in 2 to 4 weeks, depending on the infectious dose.(33, 34) Both WT and KO-infected mice cleared the infection between 11-20 days. Although the average duration for clearance was shorter in KO mice (14.7 dpi) compared to WT mice (16.7 dpi),

these differences were not significant (Figure 3a). Furthermore, we observed equal peak bacterial burdens at day 12 post-infection, averaging at 10^8 colony-forming units (CFU) per gram (g) of fecal matter for all mice (Figure 3b). The immune response to *C. rodentium* is characterized by the induction of IL-22 and IL-17A which contribute to the clearance.(35) We noted similar levels of IL-22 and IL-17A in both WT and KO animals at day 12 indicating there was no difference in mounting a type 3 response (Figure 3c). Crypt hyperplasia, resulting from increased epithelial proliferation is a hallmark of *C. rodentium* infection. As we previously discovered that epithelial proliferation was nearly absent in KO animals after chemical-induced colitis-type injury in the colon(28), we measured the crypt length and Ki67 staining to assess proliferation. We observed no changes in either crypt length or Ki67+ staining (Figure 3d and 3e). In conclusion, despite KO animals displaying heightened homeostatic levels of goblet cell effectors, including bacteria-targeting AMPs like RELM- β (11, 29), this does not impact immunity to *C. rodentium* infection.

Increased expression of goblet cell effector proteins does not influence the course of a high dose *Trichuris muris* infection

Clearance of parasitic worms (helminths) in the gut relies on a “weep and sweep” response induced by type 2 cytokines (IL-4, IL-5, IL-13), which includes increased epithelial turnover, upregulated mucus production by goblet cells, and enhanced muscle contraction, collectively working to expel the parasites.(36) Goblet cell effectors CLCA1, ANG4, and RELM- β are induced during infection with the helminth *Trichuris muris*.(9, 30, 37, 38) CLCA1 plays a role in the formation of the two distinct mucus layers in the colon and is upregulated upon *T. muris* infection(39), while RELM- β can reduce the viability of *T. muris*(10) and ANG4 expression has been correlated with the expulsion of *T. muris*.(14, 40) Given heightened

levels of these effector proteins during homeostasis, we hypothesized that KO animals would be better equipped to combat *T. muris* infection compared to WT animals.

Male mice on a C57BL/6 background exhibit a dose-dependent immune response to *T. muris*. Depending on the infective dose of *T. muris*, the immune system is polarized towards a susceptibility-associated type 1 immune response (low dose) or a resistance-associated type 2 immune response (high dose)(36). Initially, we infected both WT and KO male mice with a high dose of *T. muris* eggs. After 14 days all mice developed an infection, which was mostly cleared after 21 days (Figure 4a). During *T. muris* infection, increased epithelial proliferation leads to crypt hyperplasia. Histological analysis showed comparable crypt length at both day 14 and day 21 (Figure 4b), and Ki67 staining indicated equivalent increased proliferation at d21 (Figure 4c) in both WT and KO animals. As observed during *C. rodentium* infection, the previously described lack of regenerative ability of the KO epithelium does not impair increased epithelial proliferation during infection. Counts of RELM- β ⁺ cells were not significantly different d21 days post infection (Figure 4d). To assess the immune response, we stimulated mLN with E/S antigen and measured the cytokine levels for IFN γ , IL-6, IL-10, IL-4, IL-5, and IL-13 (Figure 4e). Increased levels of IL-13 and IL-5 in re-stimulated mLN cells as well as serum IgE indicated a typical and equal type 2 immune response in both WT and KO animals (Figure 4e and 4f). Mice with a type 2 cytokine profile produce high levels of IgG1, while mice with increased levels of type 1 cytokines exhibit elevated levels of IgG2. Although there was no difference in IgG1 levels, *Mmp17* KO mice showed significantly higher, through variable, levels of IgG2 despite having comparable type 1 cytokine levels to WT animals (Fig 4g). In conclusion, while the expression of AMPs and mucus proteins during *T. muris* infection has been shown to be essential(29), the higher baseline levels in *Mmp17* KO mice do not influence the course of high dose *T. muris* infection.

***Mmp17* KO mice are resistant to low-dose *T. muris* infection without inducing a type 2 immune response**

Low-dose *T. muris* infection in C57BL/6 mice leads to a chronic infection due to the induction of a non-protective type 1 immune response.(41) We found that *T. muris*-infected *Mmp17* KO mice are resistant to chronic infection. Compared to WT mice, KO mice exhibited significantly reduced worm burdens (Figure 5a) with 46% (6 out of 13 mice) completely clearing the worms after 35 days, while all WT mice remained infected. At the endpoint (d35), we observed no morphological differences. Measurement of crypt length and Ki67 positive percentage of the crypt revealed no changes in epithelial proliferation (Figure 5b,c). Although we observed increased levels of RELM- β in the proximal colon in the naïve state (Fig 1a,b), we do not see any differences in RELM- β + cells in the proximal colon of infected mice when comparing WT and KO (Figure 5d). Interestingly, this appears to be the case for all infection models we tested. While we observed significant differences in goblet cell effector expression in healthy KO animals, these differences disappeared during infections (Figure 4d, Figure 5d).

Infected WT mice exhibited a type 1 cytokine profile consistent with a chronic infection, showing significantly increased levels of IFN- γ , in addition to IL-6 and IL-10, while cytokine levels in KO animals remained low (Figure 5e). It is generally assumed that a type 2 immune response is essential for clearing *T. muris*; however, we did not observe increased levels of type 2 cytokines like IL-4, IL-5 or IL-13 in the KO (Figure 5e) at the time of sampling. To confirm the lack of a local type 2 response in the KO colon, infected colon tissue samples were analyzed for *Ifng*, *Il10*, *Il13*, and *Il4* mRNA levels (Figure 5f). Furthermore, tissue mRNA levels of *Tgfb1* and *Foxp3* suggested no involvement of regulatory T-cells in the downregulation of type 1 cytokines in the KO (Figure 5g). Whilst the lack of a detectable Th2 immune response in the KO may reflect the sampling point, and thus a consequence of

lower worm burdens at the end point, the significantly lower total serum IgE compared to WT (Figure 5h) suggests that the enhanced resistance to infection seen in the KO mouse is not accompanied by an elevated Th2 immunity. Alcian blue/PAS staining of paraffin sections from infected colon tissue revealed no difference in mucus pH, hinting towards similar mucus quality between WT and KO mice (Supplemental Figure 2a,b). This data collectively demonstrates that *Mmp17* KO mice can clear low-dose *T. muris* infection without mounting a type 2 immune response which is typically seen as requisite for parasite clearance. Thus, we propose that the changes in the naïve state contribute to the enhanced ability of the KO to clear the infection.

***Mmp17* KO mice show increased goblet cell maturation in cecum crypts**

T. muris primarily colonizes the cecum and proximal colon(36, 42), therefore, we analyzed if there were also changes in goblet cell effectors in the cecum at steady state. Consequently, we examined the cecum of KO mice, assessing RELM- β and CLCA1 levels and analyzing goblet cell numbers and morphology. Consistent with our findings in the proximal colon (Figure 1d), we detected no differences in goblet cell numbers when comparing WT and KO cecum (Figure 6a,b). However, we observed an increase in goblet cell size in the upper part of the crypt (Figure 6c), suggesting enhanced goblet cell maturation. Upon evaluating goblet cell effectors, both RELM- β and CLCA1 levels were markedly increased in the KO cecum, as demonstrated by IF staining (Figure 6d,e). Moreover, while RELM- β ⁺ cells were predominantly located towards the base of the cecum crypts, CLCA1 signal was mainly present in the upper crypt in WT animals, suggesting that CLCA1 is produced by mature goblet cells.(7) In contrast, in KO mouse cecum, we observed significantly more CLCA1 positive cells toward the lower half of the crypts (Figure 6e).

In accordance with Figure 1, our results suggest an increased goblet cell maturation state in KO mice, which did not correlate with elevated cytokines levels (Figure 1). The change in the zonation of goblet cell effector expression could imply that an altered gradient controlling goblet cell maturation might be the cause for our observations, as it has been demonstrated that BMP signaling is in part responsible for goblet cell maturation along the crypt villus axis.(43)

***Mmp17* is expressed in putative BMP-niche providing cells, and *Mmp17* KO mice have heightened epithelial SMAD4 levels**

We have previously reported that the primary cell type expressing *Mmp17* in the colon at steady state are smooth muscle cells, particularly those in the muscularis mucosa, a thin layer of muscle located right beneath the epithelium, which exhibit high levels of *Mmp17* expression.(28) Using the reporter gene β -Galactosidase in the *Mmp17* KO mouse model, we observed lower, yet distinct expression also in non-epithelial cells located in the upper part of the crypt, that do not express the smooth muscle marker alpha-smooth muscle actin (Figure 7a,b). Others have shown that *Mmp17* can also be expressed by monocytes and macrophages in the vasculature. (44) To investigate whether gut macrophages express *Mmp17*, we co-stained with the macrophage marker CD68; however, we did not find co-localization of β -Galactosidase and CD68 (Figure 7a). Instead, we discovered that cells with low β -Galactosidase expression were positive for the mesenchymal marker PDGFR α (Figure 7b). These mesenchymal cells in the intestine play a crucial role in forming the intestinal niche, for instance, by maintaining the BMP gradient through the expression of BMP agonists and antagonists.(16) In a recent paper, Beumer et al. described how the BMP gradient along the crypt-villus-axis influences goblet cell gene expression in the small intestine using both a

KO-mouse model and small intestinal organoids.(43) As KO mice have increased goblet cell maturation (Figure 6), but no changes in NOTCH signaling (Figure 1), we were prompted to see if there was altered BMP signaling in the epithelium. Indeed, in KO mice we found an increase in SMAD4 signal in the colon epithelium as an indicator for increased BMP signaling (Figure 7c). Together, we propose that increased BMP signaling is resulting in enhanced goblet cell maturation in *Mmp17* KO mice.

DISCUSSION

In the *Mmp17* KO mouse model, we observed an elevated expression of goblet cell effector genes, such as *Ang4*, *Clca1*, and *Retnlb*, in cecum and proximal colon (Figures 1 and 5).

While previous studies have shown that mice lacking RELM- β are highly susceptible to *C. rodentium* infection, to our knowledge there have been no investigations into the effect of increased RELM- β levels. Our study did not find any evidence that suggest that the elevated homeostatic levels of MUC2, ANG4, CLCA1, and RELM- β are beneficial during *C. rodentium* infection, as WT and KO mice cleared the infection at the same time, and peak infection numbers were comparable. In a previous study, we reported that *Mmp17* KO mice were highly susceptible to DSS-induced colitis.(28) However, in the case of *C. rodentium* infection, which induces only mild colitis in C57BL/6 mice, we observed no elevated tissue damage in KO mice. This may be due to less overall damage caused by *C. rodentium*-induced colitis, and thus the deficiencies in repair might not be significant in this model. Moreover, both WT and KO mice showed crypt hyperplasia with a comparable average crypt length, indicating a similar proliferation rate.

Resistance to intestinal helminths has been mainly attributed to the type of immune response elicited, with a type 2 response typically leading to clearance, while a type 1 response results in chronic infection.(36) However, our findings suggest that the ability to clear the infection may also be influenced by other factors. *Mmp17* KO mice, infected with a low dose of *T. muris* eggs, were able to clear the infection, while WT C57BL/6 mice developed a chronic infection. Thus, in the KO mouse, worm counts were significantly lower, and almost half of the mice completely cleared the worms by day 35 post infection. Additionally, the KO mice did not show the typical increase in cytokines of a chronic (type 1) infection (IFN γ , IL-6, IL-10), nor did they have increased levels of IL-4, IL-13, or IL-5, which would be indicative of a

type 2 immune response. Whilst the relative absence of Th2 cytokines, yet enhanced resistance seen in the KO might reflect the sampling point, low cytokine levels were accompanied by subdued total IgE levels in serum which would normally accumulate over time post infection. Further, no differences in epithelial or immune responses were observed in the infected mice. Thus, enhanced resistance is not accompanied by an elevated Th2 immune response. Interestingly a similar disconnect between resistance and Th2 immunity has been reported before in the context of goblet cell derived mucins, with the MUC5ac deficient mice failing to expel *T. muris* despite mounting a strong Th2 response.(45) This could indicate that the changes in the epithelium of KO mice at steady-state may be responsible for the improved clearance of *T. muris* infection in KO mice.

Notably, altered expression of genes involved in mucus production and processing, as well as AMPs were observed in the cecum and proximal colon of KO mice, which are the areas of the intestine that are colonized by *T. muris*. Specifically, there was an increase in goblet cell effectors such as RELM- β and ANG4, both upregulated during helminth infection and RELM- β being able to directly affect the viability of *T. muris* and other parasitic helminths.(14, 46) Additionally, CLCA1, which plays an important role in mucus processing and helps form the two distinct inner and outer mucus layers of the colon by processing mucin 2 (MUC2), is also described to be upregulated during *T. muris* infection.(39) While CLCA1 is not essential in the steady state to form a functional mucus barrier, it is crucial during nematode infections.(47)

One possible mechanism for the improved clearance of *T. muris* infection in KO mice is a thicker mucus layer, which could prevent some larvae invading the epithelium. However, worm burdens at day 14 post infection were equivalent in WT and KO evidencing equivalent establishment. Thus the significantly lower worms burdens seen at day 35 implicate mucus

as an aid in flushing worms out in concert with other clearance mechanisms like increased epithelial proliferation and muscle contractions.(48) The increase in goblet cell effectors could also contribute to the enhanced clearance of *T. muris* in KO mice by exerting direct effects on the worms themselves, lowering their viability and hindering their movement. It is of note that while we observe differences in goblet cell effectors in the steady-state, those differences disappear after infection.

Mucus and goblet cell effector genes, such as *Ang4*, *Clca1*, *Retnlb*, and *Muc2* are typically induced during infections by cytokines, especially IL-4, IL-13 and IL-22. However, we see no indication of increased cytokine levels in the naïve colon or re-stimulated mesenteric lymph node cells that could cause this change (Figure 1g). Furthermore, we did not observe any signs of goblet cell hyperplasia, which is often associated with cytokine-mediated activation (Figures 1c and 5). However, mature goblet cells in the upper part of the crypt appear to be larger in KO animals compared to WT animals, indicating an increase in total mucus production. This finding is consistent with the increased expression of *Muc2* mRNA in KO crypts (Figure 1a). We did not detect any changes in the pH of the mucus, indicating no significant differences in mucus quality (Supplementary Figure 2a,b).

As we could not find detectable differences in cytokine levels in the *Mmp17*^{-/-} colon to explain this changed goblet cell expression pattern there must be another mode of induction. The colon epithelium is regulated by growth factor gradients that help preserve the stem cells at the bottom of intestinal crypts while allowing for mature cells with different functions in the upper part of the crypt. One of those gradients is BMP signaling, kept low by BMP-antagonists at the bottom of the crypt and increasing towards the top. In the *Mmp17* KO mouse colon epithelium we find an increase in BMP-signaling. Beumer *et al.* show that BMP signaling can induce changes in goblet cell expression in the small intestine and while there

appears to be no induction in AMPs in their BMP treated small intestinal organoids, we do find a number of genes that are upregulated in both data sets. This could be caused by differences between colon and small intestine as well as other factors that are present *in vivo* and not *in vitro*, such as base levels of cytokines. Another indication of an altered gradient is the fact that we find more CLCA1+ cells in the lower cecum crypts. CLCA1 is a marker for upper crypt goblet cells that are among the main mucus producers in the colon. The presence of CLCA1 towards the bottom of the crypt may indicate a more mature goblet cell state.

Overall, our findings suggest that the altered steady-state with increased expression of goblet cell effectors in the *Mmp17* KO mouse epithelium could be responsible for its ability to clear low dose *T. muris* infection. We find evidence of increased BMP signaling in the intestinal niche that we suspect to be responsible for a more mature and activated goblet cell state. This study contributes to highlighting the importance of mesenchymal cells as important regulators of the intestinal niche.

METHODS

Mmp17^{-/-} mice

Mmp17^{-/-} mice in the C57BL/6 background have been described previously.(49) Mice were handled under pathogen-free conditions in accordance with CoMed NTNU institutional guidelines. Experiments were performed following Norwegian legislation on animal protection and were approved by the local governmental animal care committee.

Citrobacter rodentium infection studies were approved by Norwegian Food Safety Authority (FOTS ID: 11842) and were performed in accordance with the guidelines and recommendations for the care and use of animals in research.

Trichuris muris infections were performed at the University of Manchester and were approved by the University of Manchester Animal Welfare and Ethical Review Board and performed within the guidelines of the Animals (Scientific Procedures) Act, 1986. Mice were maintained at a temperature of 20-22°C in a 12h light, 12h dark lighting schedule, in sterile, individually ventilated cages with food and water *ad lib*. Mice were culled via exposure to increasing carbon dioxide levels, an approved schedule 1 method as specified within the guidelines of the Animals (Scientific Procedures) Act.

***Citrobacter rodentium* infection**

C. rodentium infection was performed following established protocols.(50) In brief, a GFP-expressing *C. rodentium* strain was cultured in Luria- Bertani (LB) medium supplemented with 30 µg/ml chloramphenicol at 37°C. Male and female mice, aged 6–10 weeks, were infected with a dose of 10⁸-10⁹ CFU via oral gavage in a total volume of 0.1ml sterile PBS. The mice were monitored daily after the oral administration of *C. rodentium* for weight loss and pain associated behaviors such as hunched posture, piloerection, and rectal prolapse.

Fresh fecal pellets were collected, weighed and homogenized in sterile PBS using a FastPrep homogenizer from MP Biomedicals. Dilutions of the homogenate were plated on agar plates supplemented with 30 µg/ml chloramphenicol. The plates were incubated at 37°C overnight and the number of colonies was assessed. At the end of each experiment (12 days post infection or until clearance), mice were euthanized and organ samples were collected for histology, RNA isolation and CFU analysis.

***T. muris* infection**

The parasite was maintained, E/S products generated, and eggs prepared as previously described.⁽⁵¹⁾ Mice were infected with 150 infective *T. muris* eggs in 200ul by oral gavage.

At necropsy the caecum and proximal colon were collected, blinded and stored at -20°C. For worm counts, caecum and colon were defrosted, opened longitudinally and washed in water to remove gut contents. The gut mucosa was scraped off using curved forceps to remove epithelia and worms from the gut tissue. Both the gut contents and removed gut mucosa were then examined and *T. muris* worms counted using a dissecting microscope (Leica S8 APO).

Mesenteric lymph node (mLN) cells re-stimulation and cytokine bead array

mLN were brought to cell suspension and 5×10^6 cells/ml were cultured for 48h at 37°C 5% CO₂ in RPMI 1640 with 4 hr E/S antigen (50µg/ml). Supernatants were harvested and stored at -20°C until they were assayed for cytokines.

Cytokines were analyzed using the Cytometric Bead Array (CBA) Mouse/Rat soluble protein flex set system (BD Bioscience) in accordance with the manufacturer's instructions. Cell acquisition was performed on a FACS Verse (BD Biosciences) and analyzed utilizing FCAP Array v3.0.1 software (BD Cytometric Bead Array) was used.

Mesenteric lymph node lymphocyte restimulation and cytokine ELISA

The mesenteric lymph nodes were dissected from naïve or *C. rodentium* infected mice and kept in sterile PBS. The lymph nodes were passed through 70 µm cell strainer to form a single cell suspension. The cell viability was assessed using Trypan blue and a Countess automated cell counter (Invitrogen). A 96 well plate was pre-incubated with a 5 µg/ml solution of anti-mouse CD3e (100314, Biolegend) in sterile PBS at 37°C for 2 h. The antibody solution was then removed and the isolated lymph node cells were added at 2×10^5 cells per well together with soluble anti-mouse CD28 (102112, Biolegend) at a final concentration of 2 µg/ml. After incubating the cells for 4 days at 37°C, 5% CO₂, the cell-supernatant was collected for cytokine analysis by ELISA.

Supernatants from restimulated mesenteric lymph node lymphocytes and tissue homogenates were assessed for IL-13(88-7137, Invitrogen), IL-17A (88-7371, Invitrogen), IL-22 88-7422, Invitrogen) and IFN γ (88-7422, Invitrogen) cytokine levels by ELISA. The kits were used following the manufacturers protocol.

Total IgE ELISA

Serum was assayed for IgE antibody production. 96 well plates were coated with purified anti-mouse IgE (2µg/ml, Biolegend, Clone: RME-1) in 0.05M carbonate/ bicarbonate buffer and incubated overnight at 4°C. Following incubation, plates were washed in PBS-Tw and non-specific binding blocked with 3% BSA (Sigma-Aldrich) in PBS for 1 hour at room temperature. Block was removed and diluted serum (1:10) added to the plate and incubated for 2hrs at 37°C. After washing HRP conjugated goat anti-mouse IgE (1µg/ml; Bio-rad) was added to the plates for 1 hour. Finally, plates were washed and developed with TMB substrate kit (BD Biosciences, Oxford, UK). The reaction was stopped using 0.18M H₂SO₄, when sufficient colour had developed. The plates were read by a Versa max microplate

reader (Molecular Devices) through SoftMax Pro 6.4.2. software at 450 nm, with reference of 570 nm subtracted.

IgG ELISA

Serum was analyzed for parasite specific IgG1 and IgG2c antibody production. 96 well plates were coated with 5µg/ml *T. muris* overnight E/S antigen overnight, plates were washed, and non-specific binding blocked with 3% BSA (Sigma-Aldrich) in PBS. Following washing, plates were incubated with serum (2 fold dilutions, 1:20-1:2560) and parasite specific antibody was measured using biotinylated IgG1 (BD Biosciences) or IgG2c (BD Biosciences) antibodies which were detected with SA-POD (Roche). Finally, plates were washed and developed with TMB substrate kit (BD Biosciences, Oxford, UK) according to the manufacturer's instructions. The reaction was stopped using 0.18 M H₂SO₄, when sufficient colour had developed. The plates were read by a Versa max microplate reader (Molecular Devices) through SoftMax Pro 6.4.2. software at 450 nm, with reference of 570 nm subtracted.

Sample preparation for histology

Proximal colon tissue of *T. muris* infected mice was fixed for 24 hours in 10% neutral buffered formalin (Fisher) containing 0.9% sodium chloride (Sigma-Aldrich), 2% glacial acetic acid (Sigma-Aldrich) and 0.05% alkyltrimethyl-ammonium bromide (Sigma-Aldrich) prior to storage in 70% Ethanol (Fisher) until processing. Fixed tissues were dehydrated through a graded series of ethanol, cleared in xylol and infiltrated with paraffin in a dehydration automat (Leica ASP300 S) using a standard protocol. Specimens were embedded in paraffin (Histocentre2, Shandon). Alternatively, proximal colon tissue was embedded in OCT and snap-frozen on dry ice and stored at -80C until processing.

For naïve and *C. rodentium* infected samples, the full colon or cecum tips were dissected, washed with ice-cold PBS. The colon was rolled into "swiss rolls" as previously described or

a 5 mm piece of the proximal colon was taken.(52) The tissues were fixed in 4% formaldehyde for 24h at RT (Room Temperature). After the fixation, the tissues were embedded into paraffin.

Histological stainings

Paraffin embedded tissues were cut into 4µm sections and placed on glass slides. The slides were heated at 60°C for 20 min prior to deparaffinization in Neo-Clear Xylene Substitute (sigma-aldrich). Rehydration was performed through a decreasing ethanol gradient.

For Hematoxylin and eosin stain, the samples were incubated for 1 min in hematoxylin solution. The tissues were then washed with water until the water ran clear and incubated in Eosin Y solution for 3 min.

For Alcian blue stain, the slides were incubated in alcian blue solution for 30 min. After thoroughly washing the slides with water, the tissues were counter stained with nuclear fast red solution for 5 minutes.

For Alcian blue/PAS stain , the tissues were stained in 1% alcian blue in 3% acetic acid (pH2.5) for 5 min, 1% periodic acid for 5 min, Schiff's reagent for 15 min and finally in Mayer's hematoxylin for 1 minute. After each staining step the slides were washed in distilled water for 5 minutes.

After the staining the tissues were washed, then dehydrated using an alcohol gradient, cleared in Xylene/Neo-Clear and mounted.

Tissue immunostainings

The paraffin-embedded or frozen OCT-embedded tissues were cut into 4 µm sections and placed on glass slides. Paraffin-embedded tissue sections underwent deparaffinization, rehydration, and antigen retrieval using citrate buffer at pH-6.0. Frozen sections were fixed in

-20 °C cold methanol for 10 min before continuing with blocking. Tissues were then blocked and permeabilized with PBS containing 0.2% Triton X-100, 1% BSA, and 2% normal goat serum (NGS) for 1 hr at RT in a humidified chamber.

Primary antibody incubation was performed using a solution containing 0.1% Triton X-100, 0.5% BSA, 0.05 % Tween-20, and 1% NGS in PBS overnight at 4°C. The following anti-mouse primary antibodies were used: anti-RELM-beta (1:500, rabbit polyclonal antibody, Peprotech, 500-p215), anti-MUC2 (1:200, Santa Cruz Biotechnology, sc-15334), anti-CLCA1 (1:200, rabbit monoclonal antibody, Abcam, ab180851), anti-CD68 (1:200, BioRad, MCA1957T), anti-Ki67 (1:200, rabbit monoclonal antibody, Invitrogen, MA5-14520) anti-SMAD4 (for frozen sections, dilution 1:400, Cell signaling, 46535), anti-βGalactosidase (for frozen sections, dilution 1:100, Rabbit polyclonal antibody, Abcam, ab4761), anti-PDGFR-alpha (15 µg/mL, goat polyclonal antibody, R&D systems, AF1062).

Following primary antibody incubation, slides were washed in washing buffer (0.2% Tween-20 in PBS) three times for 10 min each and then incubated with the appropriate Alexa Fluor secondary antibodies, UEA-1 (1:500, Vector Laboratories, RL-1062), anti-SMA-Cy3 antibody (1:500, mouse mAb, Sigma-Aldrich C6198), and counterstained with Hoechst 33342 (1:1000, MERCK, H6024) for 1 hr at RT. After washing the slides three times with washing buffer and once with distilled water, they were mounted in Fluoromount G (Invitrogen, 00-4958-02). Imaging was conducted with a Zeiss Airyscan confocal microscope, using a 10× and 20× objective lens. Images were analyzed using ImageJ software.

Colon crypt isolation

Colon crypts for RNA sequencing and organoid culture were isolated using a previously published method (REF). Briefly, the entire colon was flushed with cold PBS and then cut

into 2-4 mm pieces. These pieces were washed with cold PBS until the supernatant appeared clear and subsequently transferred into cold chelation buffer (PBS containing 2 mM EDTA) for incubation at 4 °C under gentle agitation for 1 h. The chelation buffer was then removed, and the tissue pieces were resuspended in PBS. Crypts were separated from the tissue by vigorously pipetting with a BSA-coated 10 ml pipette or by shaking the tube. The tissue pieces were allowed to settle at the bottom of the tube for approximately 1 min, after which the supernatant was collected into a BSA coated 50 ml tube. The pipetting/shaking process was repeated using fresh PBS until most crypts had detached. The collected supernatant was centrifuged at 200 x g for 3 min, and the resulting crypt pellet was resuspended in basal crypt medium (BCM, see below) and counted. For subsequent experiments, the crypts were either used for RNA isolation, protein extraction or colonoid culture, seeded into 40 µl drops of Matrigel in a P24 well plate (300 crypts/well) and cultured in WNR medium (medium composition is described below) with Rock inhibitor (10 µM) for 24 h at 37 °C and 5% CO₂.

Mouse colon organoid culture

Mouse colon organoids (colonoids) were cultured in WNR medium composed of BCM (advanced Dulbecco's modified Eagle medium-F12 supplemented with penicillin/streptomycin, 10 mM HEPES, 2 mM Glutamax) plus 1× N2 (ThermoFisher Scientific 100×, 17502048), 1× B-27 (ThermoFisher Scientific 50X, 17504044), and 1× N-acetyl-L-cysteine (Sigma, A7250). The medium was overlaid with 50 ng/ml of murine EGF (Thermo Fisher Scientific, PMG8041) and 50% L-WRN (ATCC 3276) cell line conditioned medium, enriched in Wnt, R-sponding, and Noggin.⁽¹⁵⁾ After isolation or splitting the crypts/colonoid pieces were seeded into 40 µl drops of Matrigel in a P24 well plate (300 crypts/well) and cultured in WNR medium (medium composition is described below) with Rock inhibitor (10 µM) for the first 24 h at 37 °C and 5% CO₂. After that the medium was replaced every second or third day. For passaging, Matrigel and organoids were disrupted

mechanically via vigorous pipetting. The suspension was centrifuged at $300 \times g$, 5 min at $4^\circ C$ and the pellet was resuspended in fresh, cold Matrigel to be plated in P24 wells or eight-well ibidi chambers (80821, Ibidi) for immunostainings. For differentiation, the medium was switched to ENR medium consisting of BCM plus $1 \times N2$, $1 \times B-27$, and $1 \times N$ -acetyl-L-cysteine supplemented with 50 ng/ml murine EGF, 20% R-Spondin- conditioned medium (kindly rovided by Calvin Kuo, Stanford University School of Medicine, Stanford, CA, USA), and 10% Noggin-conditioned medium after 3-4 days of culture.

Organoid immunostaining

Organoid immunostaining was performed using a previously described protocol.(15) In brief, organoids were fixed with 4% paraformaldehyde with 2% sucrose for 30 min at room temperature. After washing with sterile PBS, the organoids were permeabilized with 0.2% Triton X 100 in PBS for 30 min at room temperature. Blocking was performed for 1 hour at room temperature in PBS containing 1% BSA, 2% NGS, and 0.2% Triton X 100. Primary antibodies (RELM β (1:200, Peprotech 500-p215)) were diluted in the same blocking buffer and incubated with the organoids over night at $4^\circ C$. After washing, the organoids were incubated with the appropriate Alexa Fluor secondary antibodies, UEA-1 (1:500, Vector Laboratories, RL-1062), and counterstained with Hoechst 33342 (1:1000, MERCK, H6024) over night at $4^\circ C$ in the dark. After incubation, the organoids were washed and 250 μ l Fluoromount G was added to each well. Imaging was conducted with a Zeiss Airyscan confocal microscope, using a $10\times$ and $20\times$ objective lens. Images were analyzed using ImageJ software.

RNA seq of colon crypts

RNAseq data from colon crypts and muscle from Mmp17 KO mice was obtained and analyzed as described in our previous publication.(28) In brief, colon crypts were isolated

using the colon crypt isolation protocol above. The crypts were placed in lysis buffer (RLT, provided in RNeasy® Mini Quiagen Kit, 74104) and RNA was isolated following manufacturer instructions (RNeasy® Mini Kit, Qiagen, 74104). RNA quantification was done by spectrophotometry (ND1000 Spectrophotometer, NanoDrop, Thermo Scientific) and 25 µl with an RNA concentration of 50 ng/µl were used for RNA seq. The library preparation and sequencing was performed by the NTNU Genomic Core facility using a Lexogen SENSE mRNA library preparation kit to generate the library and Illumina NS500 flow cells to sequence the samples at 2 x 75 bp paired end. The STAR aligner was used to align reads to the *Mus musculus* genome build mm10. featureCounts was used to count the number of reads that uniquely aligned to the exon region of each gene in GENCODE annotation M18 of the mouse genome. Genes with less than 10 total counts were filtered out and DESeq2 with default settings was used for differential expression analysis.

All raw sequencing data are available online through ArrayExpress: WT and KO smooth muscle and crypt RNA seq: E-MTAB-9180.

qPCR

RNA was isolated from homogenized colon tissue (fresh, stored in RNAlater or Trizol) or isolated crypts using the Quick-RNA Miniprep Kit (R1055, Zymo Research), or for samples in Trizol, the Direct-zol RNA Miniprep kit (R2051, Zymo Research), following the manufacturer's protocols. Colonoid RNA was isolated using the Quick-RNA Microprep Kit (R1050, Zymo Research), following the manufacturer's protocol. RNA concentration was measured using a spectrophotometer (ND1000 Spectrophotometer, NanoDrop, Thermo Scientific).

The purified RNA was transcribed to cDNA using the Applied Biosystem High-Capacity RNA-to-cDNA Kit. Quantitative real-time PCR was performed with the StepOnePlus Real-

Time PCR System using SYBR Green PCR Master Mix by Applied Biosystem. All primers are listed in supplementary table 1.

Western blot

Pelleted crypts were kept at -80°C and lysed with RIPA buffer supplemented with fresh cComplete™ protease inhibitor cocktail (Roche 11836170001) and PhosSTOP™ phosphatase inhibitor cocktail (Roche 4906837001). Pellets were then lysed using vortexing and ultrasound sonication, then centrifuged to remove debris. Total protein of the lysate was quantified using BCA assay (Pierce 34335). 100ug of total protein was loaded onto each well of a NuPAGE™ 4 to 12%, Bis-Tris gel (Invitrogen WG1402BOX) and run in MOPS buffer for 20 min at 100 V, then 1 h at 185 V. Transfer from gel to nitrocellulose was done with the Invitrogen iBlot2 Gel Transfer Device with 20 V for 7 min. Blots were blocked with 5% BSA or 5% nonfat dry milk in TBS-T according to manufacturers' recommendations, for 1h at room temperature, then primary antibodies (Stat3 (Cell Signaling Technology 9139S; 1:1000 in 5% nonfat dry milk and TBS-T), Stat6 (Cell Signaling Technology 5397S; 1:1000 in 5% BSA and TBS-T), pStat3 (Cell Signaling Technology 9145S; 1:2000 in 5% BSA and TBS-T), pStat6 (Cell Signaling Technology 56554S, 1:1000 5% BSA and TBS-T), and GAPDH (Abcam ab125247; 1:10000 in 5% nonfat dry milk and TBS-T)) were added and incubated with gentle shaking overnight at 4°C. On the following day, blots were washed before adding the secondary antibodies (Polyclonal Swine Anti-Rabbit Immunoglobulins/HRP (Dako p0399; 1:5000 in 1% BSA and TBS-T) and Polyclonal Goat Anti-Mouse Immunoglobulins/HRP (Dako p0447; 1:5000 in 1% BSA and TBS-T)) and incubated for 1 h at room temperature with gentle shaking. After washing the blots were developed for 3 minutes using SuperSignal™ West Femto Maximum Sensitivity Substrate (Thermo Scientific 34094). Chemiluminescence was read using a LI-COR Odyssey Fc Imager with 1 min

exposure for GAPDH, 2 min exposure for total STAT proteins, and 30 min exposure for phospho-STAT proteins.

FIGURES

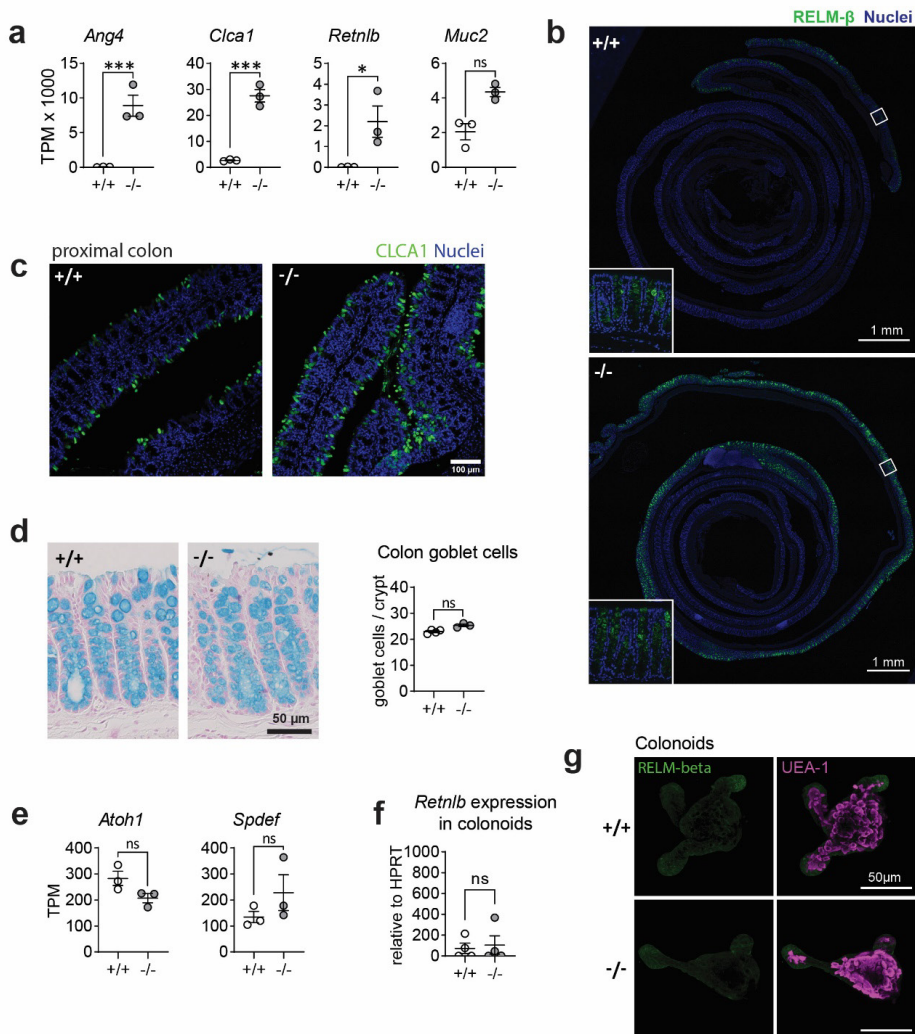


Figure 1: MMP17 controls goblet cell expression in colon. (a) Graphs of RNAseq data of naive mouse colon crypts from WT (+/+) and *Mmp17* KO (-/-) mice depicting the expression levels of *Ang4*, *Clca1*, *Retnlb* and *Muc2*, n=3, padj calculated with DESeq2, * p<0.05, ** p<0.01, *** p<0.001. (b) Immunofluorescence (IF) images of Colon Swiss rolls of naive mouse full-length colon of WT (+/+) and *Mmp17* KO (-/-) mice, for RELM- β (green),

nuclear stain (blue), proximal end on the outside, scale 1 mm. (c) IF stain images of naive mouse proximal colon of WT (+/+) and KO (-/-) mice for CLCA1 (green), nuclear stain (blue), scale 100 μ m. (d) The pictures on the left show Alcian blue stain for goblet cells, on the right is a count of goblets/crypt in proximal colon of naive WT (+/+) (n=4) and KO (-/-) (n=3) mice, 30 crypts counted for each animal. (e) Graphs of RNAseq data of naive mouse colon crypts from *Mmp17* +/+ and -/- mice showing the expression for *Atoh1* and *Spdef*, n=3, padj * p<0.05, ** p<0.01, *** p<0.001. (f) Graph of qPCR data for *Retnlb* of WT (+/+) and KO (-/-) mouse colonoids after one split, Ct value relative to *HPRT*, n=4. (g) IF staining images for RELM- β in WT (+/+) and KO (-/-) mouse colonoids after one split, RELM- β (green) and UEA-1 (magenta), scale 50 μ m. Numerical data are means \pm SEM. Data in (a) and (e) represents p-adjusted value from RNAseq analysis, and data in (d) and (f) was analyzed using Student's unpaired t-test (two-tailed).

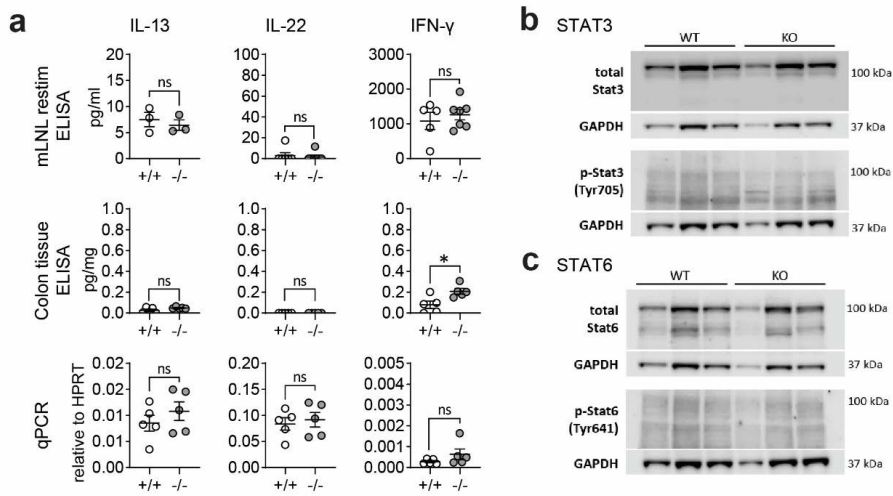


Figure 2: *Mmp17* KO mice do not have increased cytokine levels in the colon. (a) Graphs show cytokine ELISA of mLN restimulations (first row) for IL-13, IL-22 and IFN γ , cytokine ELISA of proximal colon tissue adjusted to mg tissue (second row) for IL-13, IL-22, and IFN γ , and qPCR for *Il13*, *il22* and *Ifng* in proximal colon tissue relative to *Hprt* (third row), n=3-6. (b) Western blots of protein isolates from colon crypts for STAT3 and pSTAT3, GAPDH loading control, n=3. (c) Western blots of protein isolates from colon crypts for STAT6 and pSTAT6, GAPDH loading control, n=3. Numerical data are means \pm SEM. Data were analyzed using Student's unpaired t-test (two-tailed). * p<0.05

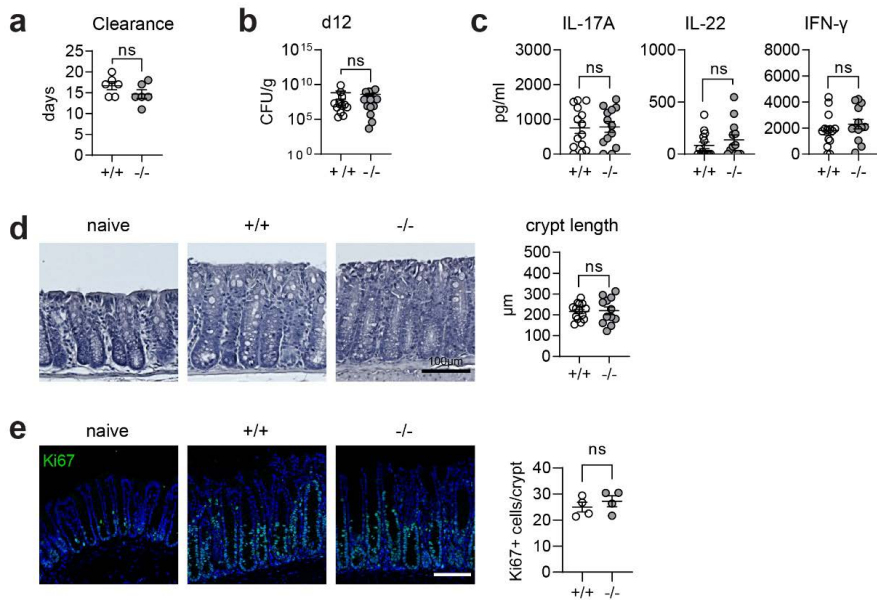


Figure 3: *C. rodentium* infection is not altered in *Mmp17* KO mice. (a) Graph shows days until clearance of *C. rodentium* measured using fecal CFUs, single experiment, n=6. (b) Quantification of fecal CFUs at 12 days post infection (dpi) with *C. rodentium* is depicted in the graph, 2 independent experiments pooled, +/+ (n=14), -/- (n=13). (c) Cytokine levels measured via ELISA of mLNLs restimulations for IL-13, IL-22, and IFN γ . (d) Images depicting hematoxylin and eosin (H&E) staining of naive and *C. rodentium* WT (+/+) and KO (-/-) mouse distal colon 12 dpi, scale 100 μ m (left) and crypt length quantification in μ m (right), 2 independent experiments pooled, +/+ (n=14), -/- (n=13). (e) Confocal maximal projection images showing Ki67 IF stain of naive and *C. rodentium* infected WT (+/+) and KO (-/-) mouse distal colon 12 dpi, scale 100 μ m, Ki67 (green), nuclear stain (blue). Numerical data are means \pm SEM. Data was analyzed using Student's unpaired t-test (two-tailed).

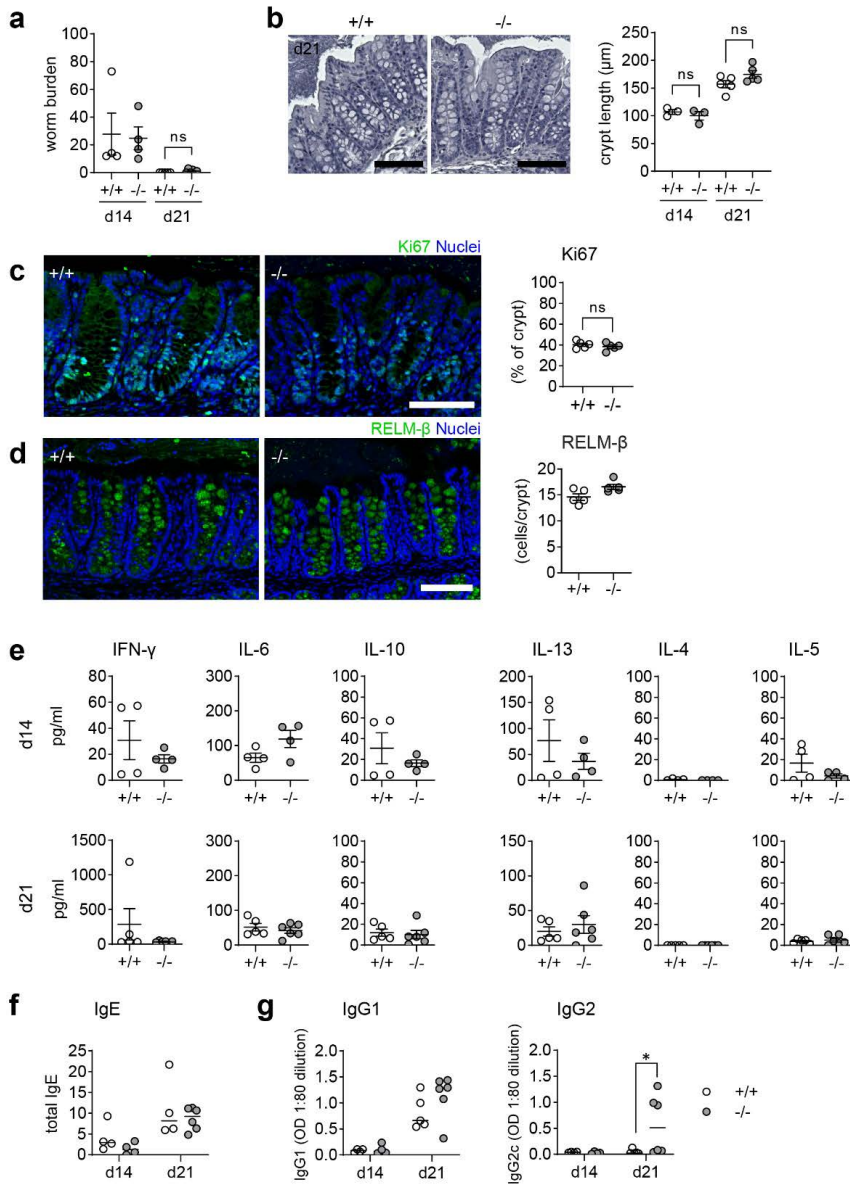


Figure 4: *Mmp17* KO mice show no differences in clearance of high dose *T. muris* infection. (a) Graph shows worm burdens in WT (+/+) and KO (-/-) mice infected with high dose *Trichuris muris* at 14 dpi (d14, 1 experiment n=4) and 21 dpi (d21, 1 experiment, , +/+

(n=5), -/- (n=6)). **(b)** H&E stain of WT (+/+) and KO (-/-) mouse proximal colon (left) and crypt length measurement in μm (right), of naive and *T. muris* infected (21 dpi) mice naive (n=3), +/+ (n=5), -/- (n=5), scale 100 μm . **(c)** Ki67 IF stain of *T. muris* infected WT (+/+) and KO (-/-) mouse proximal colon 21 dpi, scale 100 μm , Ki67 (green), nuclear stain (blue) on the left, Measurement of Ki67 positive area of the crypt (right). **(d)** Cytokine levels measured via cytokine bead array of mLNLS restimulations with E/S antigen at 14 dpi (n=4) and 21 dpi (+/+ (n=5), -/- (n=6)) for the Th1 cytokines IFN γ , IL-6, IL-10, and Th2 cytokines IL-4, IL-5 and IL-13 in pg/ml. **(e)** Graphs show total serum levels of IgE and **(g)** serum levels of parasite specific IgG1 and IgG2c antibodies at 14 (n=4) and 21 (+/+ (n=5), -/- (n=6)) dpi, WT (+/+) mice (empty column and circles), KO (-/-) mice (grey columns and circles). Numerical data are means \pm SEM. Data was analyzed using Student's unpaired t-test (two-tailed) (a,c,d,e) and 2way ANOVA (b,e,f,g).

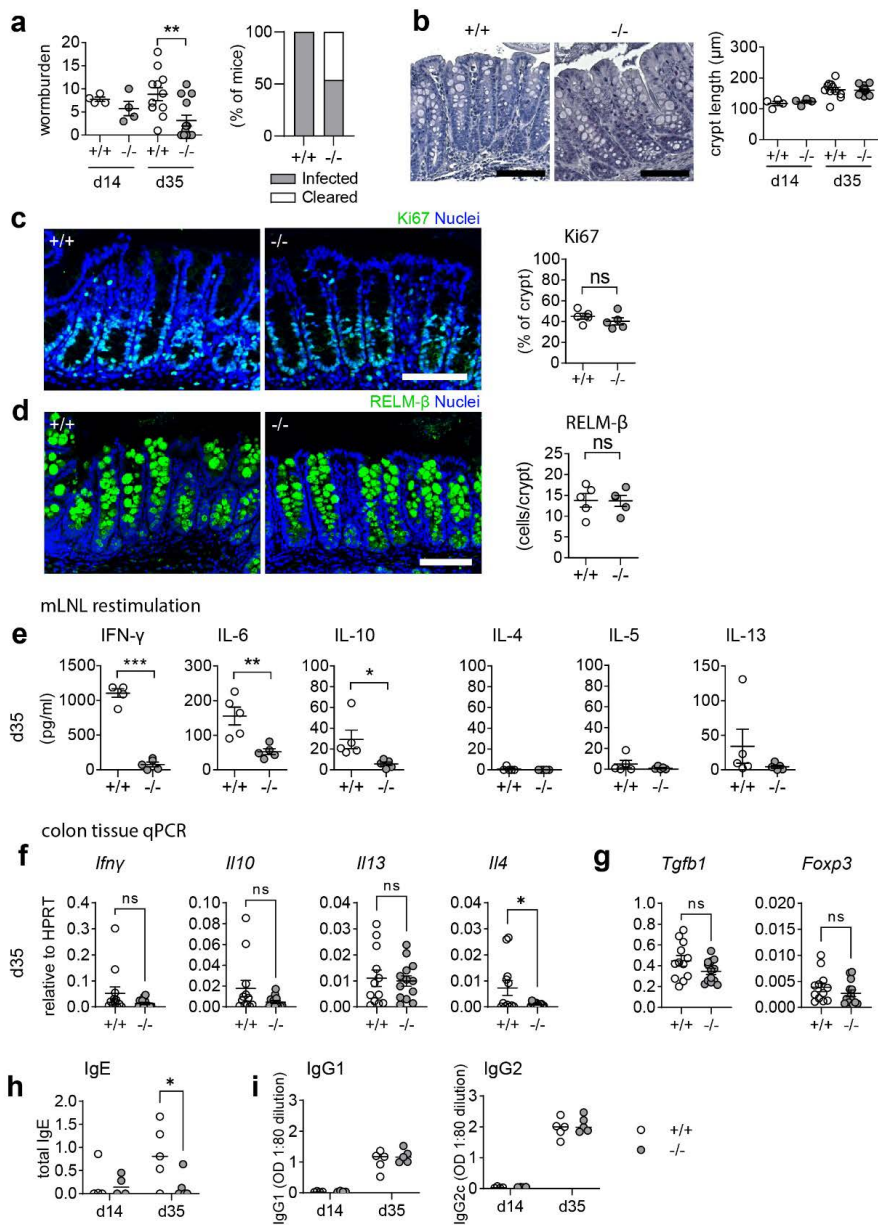


Figure 5: *Mmp17* KO mice exhibit improved clearance in low dose *T. muris* infection. (a)

The left graph shows the worm burden in WT (+/+) and *Mmp17* KO (-/-) mice infected with a low dose of *T. muris* at 14 dpi (d14, 1 experiment n=4) and 35 dpi (d35, 2 independent

experiments pooled, , +/+ : n=12, -/- : n=13). The right one show the percentage of mice that cleared the infection/remained infected at 35 dpi. **(b)** Image of an H&E staining of WT (+/+) and *Mmp17* KO (-/-) mouse proximal colon (left) and crypt length measurement in μm (right), of *T. muris* infected mice at 14 dpi (n=4) and 35 dpi (+/+ (n=12), -/- (n=13)), scale 100 μm . **(c)** IF image of a representative Ki67 stain of *T. muris* infected WT (+/+) and KO (-/-) mouse proximal colon 35 dpi, scale 100 μm , Ki67 (green), nuclear stain (blue) on the left, Graph of measurements of Ki67 positive part of the crypt (right), n=5. **(d)** RELM-beta IF stain of *T. muris* infected *Mmp17* +/+ and -/- mouse proximal colon 35 dpi, scale 100 μm , RELM-beta (green), nuclear stain (blue) on the left, count of RELM-beta positive cells per crypt (right), n=5. **(e)** Cytokine bead array of mLNLs restimulations at 35 dpi (n=5) for the Th1 cytokines IFN- γ , IL-6, IL-10, and Th2 cytokines IL-4, IL-5 and IL-13 in pg/ml, representative data of 1 experiment. **(f)** qPCR of proximal colon tissue at 35 dpi for *Ifn γ* , *Il10*, *Il13*, and *Il4* relative to HPRT, +/+ (n=12), -/- (n=13), pooled from two independent experiments. **(g)** Graphs show mRNA expression data measured using qPCR of proximal colon tissue at 35 dpi for *Tgfb1* and *Foxp3* relative to HPRT, +/+ (n=12), -/- (n=13), pooled from two independent experiments. **(h)** The graphs show total levels of serum IgE antibodies at 14 (n=4) and 35 (n=5) dpi, WT (+/+) mice (empty circles), KO (-/-) mice (grey circles). **(i)** Graphs depict serum levels of parasite specific IgG1 and IgG2c antibodies at 14 (n=4) and 35 (n=5) dpi, WT (+/+) mice (empty circles), KO (-/-) mice (grey circles). Numerical data are means \pm SEM. Data was analyzed using Student's unpaired t-test (two-tailed) (a,c,d,e,f,g) and 2way ANOVA (b,h,i).

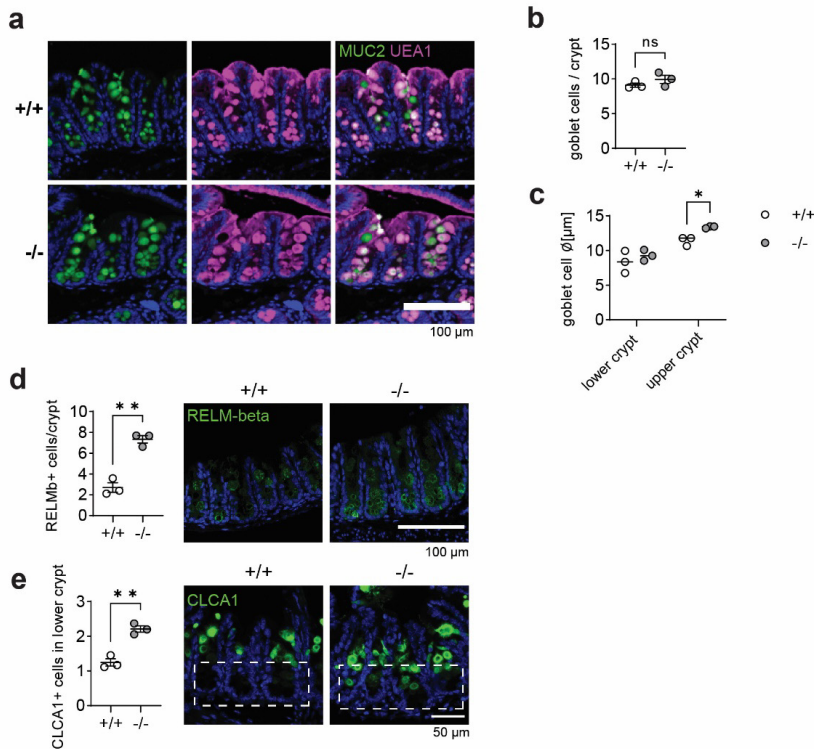


Figure 6: Goblet cells in *Mmp17* KO mouse cecum show increased maturation. (a) Muc2 IF and UEA-1 stain of naive mouse cecum of WT (+/+) and KO (-/-) mice, Muc2 (green), UEA-1 (magenta), nuclear stain (blue), scale bar 100 μ m. (b) Count of goblet cells per cecum crypts of naive WT (+/+) and KO (-/-) mice, n=3. (c) The graph shows the measurement of goblet cell diameter in lower and upper cecum crypts of naive WT (+/+) and KO (-/-) mice, n=3, 40-50 cells measured. (d) RELM-beta IF stain of naive mouse cecum of WT (+/+) and KO (-/-) mice, RELM-beta (green), nuclear stain (blue), scale bar 100 μ m (right) and count of RELM-beta positive cells per crypt, n=3, min 32 crypts counted (left). (e) CLCA1 IF stain of naive mouse cecum of WT (+/+) and KO (-/-) mice, CLCA1 (green), nuclear stain (blue), scale bar 100 μ m (right) and count of CLCA1 positive cells in the lower crypt, n=3, 35 crypts

counted (left). Numerical data are means \pm SEM. Data was analyzed using Student's unpaired t-test (two-tailed) (b,d,e) and 2way ANOVA (c).

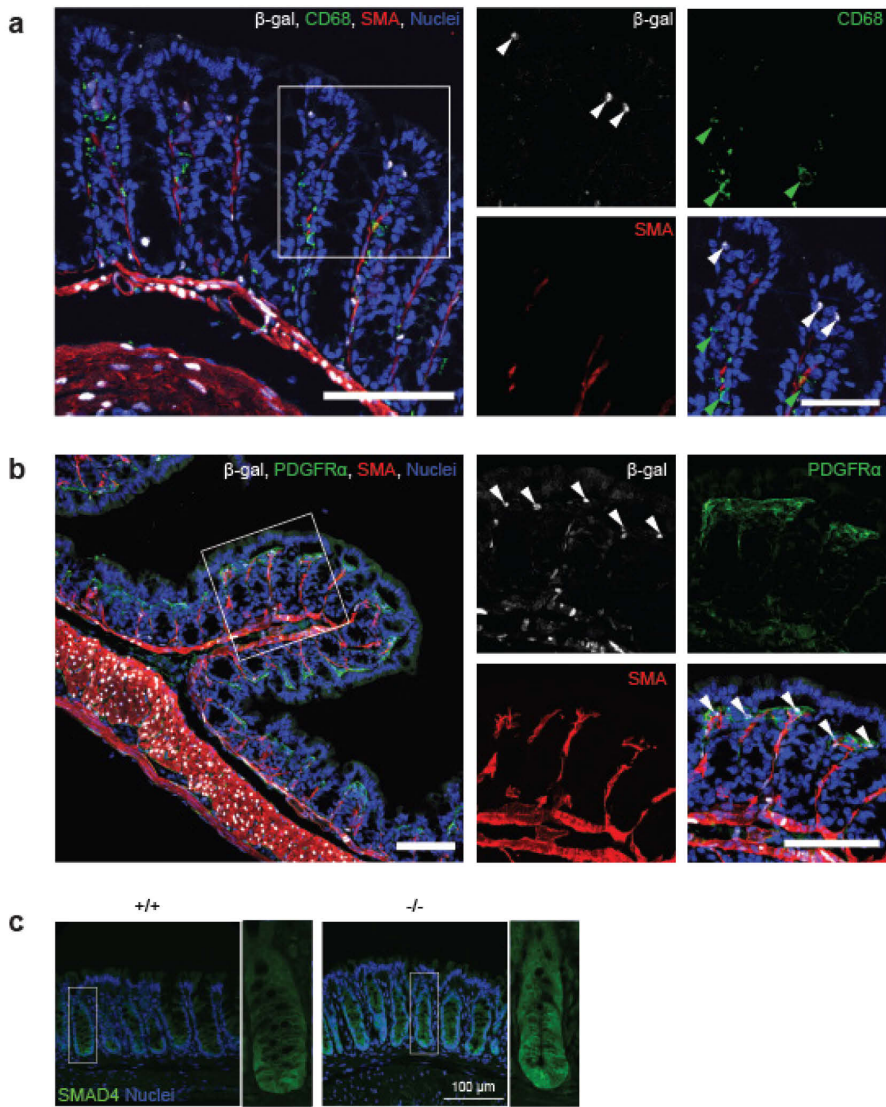


Figure 7: *Mmp17* is expressed in PDGFR α + mesenchymal cells and *Mmp17* KO mice show elevated BMP signaling in colon crypts (a) β -galactosidase in naive *Mmp17* KO mouse proximal colon, β -gal (white), CD68 (green), smooth muscle actin (SMA) (red),

nuclear stain (blue), white arrows point at β -gal⁺ cells at the tip of the colon crypts. Green arrows point at CD68⁺ cells, scale bar 100 μ m, scale bar close up 50 μ m. **(b)** β -gal in naive *Mmp17* KO mouse proximal colon, beta-Gal (white), PDGFR α (green), smooth muscle actin (red), nuclear stain (blue), arrows point at beta-Gal positive cells at the tip of the colon crypts, scale bars 100 μ m. **(c)** SMAD4 IF stain of naive proximal colon of *Mmp17* WT and KO mice, SMAD4 (green), nuclear stain (blue), scale bar 100 μ m.

REFERENCES

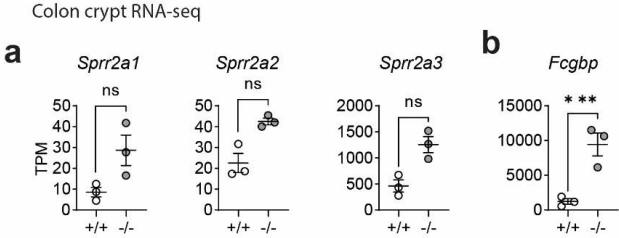
1. Peterson LW, Artis D. Intestinal epithelial cells: regulators of barrier function and immune homeostasis. *Nature Reviews Immunology*. 2014;14(3):141-53.
2. Tetteh PW, Farin HF, Clevers H. Plasticity within stem cell hierarchies in mammalian epithelia. *Trends in Cell Biology*. 2015;25(2):100-8.
3. Barker N, van Es JH, Kuipers J, Kujala P, van den Born M, Cozijnsen M, et al. Identification of stem cells in small intestine and colon by marker gene *Lgr5*. *Nature*. 2007;449(7165):1003-7.
4. Rodriguez-Piñero AM, Bergström JH, Ermund A, Gustafsson JK, Schütte A, Johansson MEV, et al. Studies of mucus in mouse stomach, small intestine, and colon. II. Gastrointestinal mucus proteome reveals *Muc2* and *Muc5ac* accompanied by a set of core proteins. *American Journal of Physiology-Gastrointestinal and Liver Physiology*. 2013;305(5):G348-G56.
5. Ehrencrona E, van der Post S, Gallego P, Recktenwald CV, Rodriguez-Pineiro AM, Garcia-Bonete M-J, et al. The IgGfC-binding protein FCGBP is secreted with all GDPH sequences cleaved but maintained by interfragment disulfide bonds. *Journal of Biological Chemistry*. 2021;297(1):100871.
6. Gustafsson JK, Johansson MEV. The role of goblet cells and mucus in intestinal homeostasis. *Nature Reviews Gastroenterology & Hepatology*. 2022;19(12):785-803.
7. Nyström EEL, Arike L, Ehrencrona E, Hansson GC, Johansson MEV. Calcium-activated chloride channel regulator 1 (*CLCA1*) forms non-covalent oligomers in colonic mucus and has mucin 2-processing properties. *The Journal of biological chemistry*. 2019;294(45):17075-89.
8. Ermund A, Schütte A, Johansson MEV, Gustafsson JK, Hansson GC. Studies of mucus in mouse stomach, small intestine, and colon. I. Gastrointestinal mucus layers have different properties depending on location as well as over the Peyer's patches. *American Journal of Physiology-Gastrointestinal and Liver Physiology*. 2013;305(5):G341-G7.
9. Sharpe C, Thornton DJ, Grenic RK. A sticky end for gastrointestinal helminths; the role of the mucus barrier. *Parasite Immunology*. 2018;40(4):e12517.
10. Artis D, Wang ML, Keilbaugh SA, He W, Brenes M, Swain GP, et al. *RELMβ/FIZZ2* is a goblet cell-specific immune-effector molecule in the gastrointestinal tract. *Proceedings of the National Academy of Sciences of the United States of America*. 2004;101(37):13596-600.
11. Propheter DC, Chara AL, Harris TA, Ruhn KA, Hooper LV. Resistin-like molecule β is a bactericidal protein that promotes spatial segregation of the microbiota and the colonic epithelium. *Proceedings of the National Academy of Sciences*. 2017;114(42):11027-33.
12. Pan Y-R, Wu K-P, Lou Y-C, Liao Y-D, Chen C. Letter to the Editor: ^1H , ^{13}C and ^{15}N resonance assignments and secondary structure of murine angiogenin 4. *Journal of Biomolecular NMR*. 2005;31(2):175-6.
13. Sultana MF, Suzuki M, Yamasaki F, Kubota W, Takahashi K, Abo H, et al. Identification of Crucial Amino Acid Residues for Antimicrobial Activity of Angiogenin 4 and Its Modulation of Gut Microbiota in Mice. *Frontiers in Microbiology*. 2022;13.
14. Forman RA, deSchoolmeester ML, Hurst RJ, Wright SH, Pemberton AD, Else KJ. The goblet cell is the cellular source of the anti-microbial angiogenin 4 in the large intestine post *Trichuris muris* infection. *PLoS One*. 2012;7(9):e42248.
15. Lindholm HT, Parmar N, Drurey C, Campillo Poveda M, Vornewald PM, Ostrop J, et al. BMP signaling in the intestinal epithelium drives a critical feedback loop to restrain IL-13-driven tuft cell hyperplasia. *Sci Immunol*. 2022;7(71):eabl6543.

16. McCarthy N, Manieri E, Storm EE, Saadatpour A, Luoma AM, Kapoor VN, et al. Distinct Mesenchymal Cell Populations Generate the Essential Intestinal BMP Signaling Gradient. *Cell Stem Cell*. 2020;26(3):391-402.e5.
17. Miyoshi H, VanDussen KL, Malvin NP, Ryu SH, Wang Y, Sonnek NM, et al. Prostaglandin E2 promotes intestinal repair through an adaptive cellular response of the epithelium. *Embo j*. 2017;36(1):5-24.
18. Shoshkes-Carmel M, Wang YJ, Wangenstein KJ, Tóth B, Kondo A, Massasa EE, et al. Subepithelial telocytes are an important source of Wnts that supports intestinal crypts. *Nature*. 2018;557(7704):242-6.
19. Roulis M, Kaklamanos A, Schernthanner M, Bielecki P, Zhao J, Kaffe E, et al. Paracrine orchestration of intestinal tumorigenesis by a mesenchymal niche. *Nature*. 2020;580(7804):524-9.
20. Degirmenci B, Valenta T, Dimitrieva S, Hausmann G, Basler K. GLI1-expressing mesenchymal cells form the essential Wnt-secreting niche for colon stem cells. *Nature*. 2018;558(7710):449-53.
21. Greicius G, Kabiri Z, Sigmundsson K, Liang C, Bunte R, Singh MK, et al. PDGFR α (+) pericryptal stromal cells are the critical source of Wnts and RSPO3 for murine intestinal stem cells in vivo. *Proc Natl Acad Sci U S A*. 2018;115(14):E3173-e81.
22. Cosin-Roger J, Ortiz-Masià MD, Barrachina MD. Macrophages as an Emerging Source of Wnt Ligands: Relevance in Mucosal Integrity. *Front Immunol*. 2019;10:2297.
23. Pompili S, Latella G, Gaudio E, Sferra R, Vetuschi A. The Charming World of the Extracellular Matrix: A Dynamic and Protective Network of the Intestinal Wall. *Frontiers in Medicine*. 2021;8.
24. Page-McCaw A, Ewald AJ, Werb Z. Matrix metalloproteinases and the regulation of tissue remodelling. *Nature Reviews Molecular Cell Biology*. 2007;8(3):221-33.
25. Kessenbrock K, Wang C-Y, Werb Z. Matrix metalloproteinases in stem cell regulation and cancer. *Matrix Biology*. 2015;44-46:184-90.
26. Martín-Alonso M, García-Redondo AB, Guo D, Camafeita E, Martínez F, Alfranca A, et al. Deficiency of MMP17/MT4-MMP Proteolytic Activity Predisposes to Aortic Aneurysm in Mice. *Circulation Research*. 2015;117(2):e13-e26.
27. Jakubowska K, Pryczynicz A, Iwanowicz P, Niewiński A, Maciorkowska E, Hapanowicz J, et al. Expressions of Matrix Metalloproteinases (MMP-2, MMP-7, and MMP-9) and Their Inhibitors (TIMP-1, TIMP-2) in Inflammatory Bowel Diseases. *Gastroenterology Research and Practice*. 2016;2016:2456179.
28. Martín-Alonso M, Iqbal S, Vornwald PM, Lindholm HT, Damen MJ, Martínez F, et al. Smooth muscle-specific MMP17 (MT4-MMP) regulates the intestinal stem cell niche and regeneration after damage. *Nature Communications*. 2021;12(1):6741.
29. Hu Z, Zhang C, Sifuentes-Dominguez L, Zarek CM, Propheter DC, Kuang Z, et al. Small proline-rich protein 2A is a gut bactericidal protein deployed during helminth infection. *Science*. 2021;374(6568):eabe6723.
30. Horsnell WGC, Dewals BG. RELMs in the Realm of Helminths. *Trends in Parasitology*. 2016;32(7):512-4.
31. Nair MG, Guild KJ, Du Y, Zaph C, Yancopoulos GD, Valenzuela DM, et al. Goblet Cell-Derived Resistin-Like Molecule β Augments CD4⁺ T Cell Production of IFN- γ and Infection-Induced Intestinal Inflammation. *The Journal of Immunology*. 2008;181(7):4709-15.
32. Forman RA, deSchoolmeester ML, Hurst RJM, Wright SH, Pemberton AD, Else KJ. The Goblet Cell Is the Cellular Source of the Anti-Microbial Angiogenin 4 in the Large Intestine Post *Trichuris muris* Infection. *PLOS ONE*. 2012;7(9):e42248.

33. Mundy R, MacDonald TT, Dougan G, Frankel G, Wiles S. *Citrobacter rodentium* of mice and man. *Cellular Microbiology*. 2005;7(12):1697-706.
34. Symonds EL, Riedel CU, O'Mahony D, Laphorne S, O'Mahony L, Shanahan F. Involvement of T helper type 17 and regulatory T cell activity in *Citrobacter rodentium* invasion and inflammatory damage. *Clin Exp Immunol*. 2009;157(1):148-54.
35. Collins JW, Keeney KM, Crepin VF, Rathinam VAK, Fitzgerald KA, Finlay BB, et al. *Citrobacter rodentium*: infection, inflammation and the microbiota. *Nature Reviews Microbiology*. 2014;12(9):612-23.
36. Klementowicz JE, Travis MA, Grecis RK. *Trichuris muris*: a model of gastrointestinal parasite infection. *Seminars in Immunopathology*. 2012;34(6):815-28.
37. D'Elia R, DeSchoolmeester ML, Zeef LA, Wright SH, Pemberton AD, Else KJ. Expulsion of *Trichuris muris* is associated with increased expression of angiogenin 4 in the gut and increased acidity of mucins within the goblet cell. *BMC Genomics*. 2009;10:492.
38. Artis D. New weapons in the war on worms: identification of putative mechanisms of immune-mediated expulsion of gastrointestinal nematodes. *Int J Parasitol*. 2006;36(6):723-33.
39. Nyström EEL, Birchenough GMH, van der Post S, Arike L, Gruber AD, Hansson GC, et al. Calcium-activated Chloride Channel Regulator 1 (CLCA1) Controls Mucus Expansion in Colon by Proteolytic Activity. *EBioMedicine*. 2018;33:134-43.
40. Datta R, deSchoolmeester ML, Hedeler C, Paton NW, Brass AM, Else KJ. Identification of novel genes in intestinal tissue that are regulated after infection with an intestinal nematode parasite. *Infect Immun*. 2005;73(7):4025-33.
41. Bancroft AJ, Else KJ, Grecis RK. Low-level infection with *Trichuris muris* significantly affects the polarization of the CD4 response. *European Journal of Immunology*. 1994;24(12):3113-8.
42. Yousefi Y, Haq S, Banskota S, Kwon YH, Khan WI. *Trichuris muris* Model: Role in Understanding Intestinal Immune Response, Inflammation and Host Defense. *Pathogens*. 2021;10(8).
43. Beumer J, Puschhof J, Yengej FY, Zhao L, Martinez-Silgado A, Blotenburg M, et al. BMP gradient along the intestinal villus axis controls zoned enterocyte and goblet cell states. *Cell Reports*. 2022;38(9):110438.
44. Clemente C, Rius C, Alonso-Herranz L, Martín-Alonso M, Pollán Á, Camafeita E, et al. MT4-MMP deficiency increases patrolling monocyte recruitment to early lesions and accelerates atherosclerosis. *Nature Communications*. 2018;9(1):910.
45. Hasnain SZ, Evans CM, Roy M, Gallagher AL, Kindrachuk KN, Barron L, et al. Muc5ac: a critical component mediating the rejection of enteric nematodes. *J Exp Med*. 2011;208(5):893-900.
46. Herbert DR, Yang JQ, Hogan SP, Groschwitz K, Khodoun M, Munitz A, et al. Intestinal epithelial cell secretion of RELM-beta protects against gastrointestinal worm infection. *J Exp Med*. 2009;206(13):2947-57.
47. Liu C-L, Shi G-P. Calcium-activated chloride channel regulator 1 (CLCA1): More than a regulator of chloride transport and mucus production. *World Allergy Organization Journal*. 2019;12(11):100077.
48. Hasnain SZ, Thornton DJ, Grecis RK. Changes in the mucosal barrier during acute and chronic *Trichuris muris* infection. *Parasite Immunol*. 2011;33(1):45-55.
49. Rikimaru A, Komori K, Sakamoto T, Ichise H, Yoshida N, Yana I, et al. Establishment of an MT4-MMP-deficient mouse strain representing an efficient tracking system for MT4-MMP/MMP-17 expression in vivo using β -galactosidase. *Genes to Cells*. 2007;12(9):1091-100.

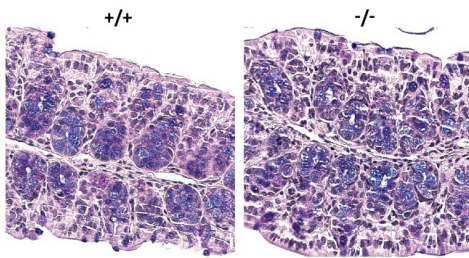
50. Bergstrom KS, Kisooson-Singh V, Gibson DL, Ma C, Montero M, Sham HP, et al. Muc2 protects against lethal infectious colitis by disassociating pathogenic and commensal bacteria from the colonic mucosa. *PLoS Pathog.* 2010;6(5):e1000902.
51. Forman R, Logunova L, Smith H, Wemyss K, Mair I, Boon L, et al. *Trichuris muris* infection drives cell-intrinsic IL4R alpha independent colonic RELM α + macrophages. *PLOS Pathogens.* 2021;17(7):e1009768.
52. Moolenbeek C, Ruitenber EJ. The 'Swiss roll': a simple technique for histological studies of the rodent intestine. *Laboratory Animals.* 1981;15(1):57-60.

SUPPLEMENTARY MATERIALS

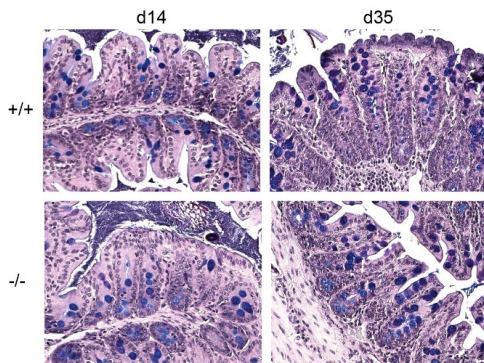


Supplementary figure 1: MMP17 controls goblet cell gene expression in Colon. (a) RNAseq data of naive mouse colon crypts from WT (+/+) and MMP17 KO (-/-) mice showing the expression of for *Sprr2a1*, *Sprr2a2*, *Sprr2a3* and *Fcgbp* (b), n=3, pa dj * p<0.05, ** p<0.01, *** p<0.00. Numerical data are means ± SEM. Data represents p-adjusted value from RNAseq analysis.

a Alcian blue/PAS stain in naive proximal colon



b Alcian blue/PAS stain in proximal colon of mice infected with a low dose *T. muris*



Supplementary Figure 2: Alcian blue/PAS stain of naive mouse proximal colon of WT (+/+) and MMP17 KO (-/-) mice at 14 dpi and 35 dpi.

Supplementary table 1: Primers used for qPCR

target gene	forward primer	reverse primer
<i>il4</i>	ATCATCGGCATTTTGAACGAGGTC	ACCTTGGAAGCCCTACAGACGA
<i>il10</i>	CGGGAAGACAATAACTGCACCC	CGGTAGCAGTATGTTGTCCAGC
<i>il13</i>	CCTGGCTCTTGCTTGCCTT	GGTCTTGTGTGATGTTGCTCA
<i>il22</i>	CATTGCCTTCTAGGTCTCCTCA	CCTGCTTGCCAGTGCAAAAT
<i>ifng</i>	GGATGCATTCATGAGTATTGCC	CCTTTTCCGCTTCCTGAGG
<i>foxp3</i>	CCTGGTTGTGAGAAGGTCTTCG	TGCTCCAGAGACTGCACCACTT
<i>tgfb1</i>	CTGCTGACCCCCACTGATAC	AGCCCTGTATTCCGTCTCCT
<i>retnlb</i>	CGTCTCCCTTCTCCCACTGA	GACAACCATCCCAGCAGGAC
<i>bmp4</i>	AGGAGGAGGAGGAAGAGCAG	CACCTCATTCTCTGGGATGC
<i>hprt</i>	CCTCCTCAGACCGCTTTTT	AACCTGGTTCATCATCGCTAA

ISBN 978-82-326-7290-5 (printed ver.)
ISBN 978-82-326-7289-9 (electronic ver.)
ISSN 1503-8181 (printed ver.)
ISSN 2703-8084 (online ver.)